

DOCTORAL THESIS

Physics-Preserving Model Order Reduction for Stability Analysis of Converter-Dominated Power Systems

Nathalia De Morais Dias Campos

TALLINNA TEHNIKAÜLIKOOL TALLINN UNIVERSITY OF TECHNOLOGY TALLINN 2025

TALLINN UNIVERSITY OF TECHNOLOGY DOCTORAL THESIS 92/2025

Physics-Preserving Model Order Reduction for Stability Analysis of Converter-Dominated Power Systems

NATHALIA DE MORAIS DIAS CAMPOS



TALLINN UNIVERSITY OF TECHNOLOGY School of Engineering Department of Electrical Power Engineering and Mechatronics

The dissertation was accepted for the defence of the degree of Doctor of Philosophy on 6 November 2025

Supervisor: Prof. Dr. Jako Kilter

Department of Electrical Power Engineering and Mechatronics

Tallinn University of Technology

Tallinn, Estonia

Opponents: Prof. Dr. Glauco Nery Taranto

Department of Electrical Engineering Federal University of Rio de Janeiro

Rio de Janeiro, Brazil

Prof. Dr.-Ing. Kai Strunz

Institute of Energy and Automation Technology

Technical University Berlin

Berlin, Germany

Defence of the thesis: 15 December 2025, Tallinn

Declaration:

Hereby I declare that this doctoral thesis, my original investigation and achievement, submitted for the doctoral degree at Tallinn University of Technology, has not been submitted for any academic degree elsewhere.

Nathalia	de Mora	ais Dias	Campos

signature

This research was financially supported by Elering AS (Project "Study of Renewable Energy Source Penetration Capacity in Estonian Power System") contract no. LEEE21002/1.1-4/2020/802, by Nordic Energy Research (Project "Nordic-Baltic Co-Simulation Platform Towards Increasing the Stability of AC/DC Transmission Grids") grant no. 105476 – COSPACT, and by the European Union and co-funded by the Estonian Ministry of Education and Science (Project no. TemTa-134).







Copyright: Nathalia de Morais Dias Campos, 2025 ISSN 2585-6898 (publication)

ISBN 978-9916-80-429-2 (publication)

ISSN 2585-6901 (PDF)

ISBN 978-9916-80-430-8 (PDF)

DOI https://doi.org/10.23658/taltech.92/2025

De Morais Dias Campos, N. (2025). Physics-Preserving Model Order Reduction for Stability Analysis of Converter-Dominated Power Systems [TalTech Press]. https://doi.org/10.23658/taltech.92/2025

TALLINNA TEHNIKAÜLIKOOL DOKTORITÖÖ 92/2025

Füüsikalisi omadusi säilitav mudeli järgu alandamise metoodika muunduripõhiste elektrisüsteemide stabiilsusanalüüsiks

NATHALIA DE MORAIS DIAS CAMPOS



Contents

Lis	t of Pu	ublicatio	ons	. 8
Au	thor's	Contrik	outions to the Publications	9
Ab	brevia	ations		. 10
Int	roduc	tion		. 11
1	Dyna	amic Mo	odelling of Converter-Dominated Power Systems	. 14
	1.1		ty Challenges in Converter-Dominated Grids	
		1.1.1	Converter-Driven Stability	
		1.1.2	Resonance Stability	
	1.2	Compo	onent Models	. 22
		1.2.1	Synchronous Generators	. 22
		1.2.2	Transmission Lines	. 24
		1.2.3	Loads	. 27
		1.2.4	Converters	. 29
	1.3	Model	ling Frameworks and Simulation Tools	. 32
		1.3.1	Electromagnetic Transient Programs	
		1.3.2	Transient Stability Programs	. 36
		1.3.3	Framework Comparison and Discussion	. 38
		1.3.4	Alternatives to Offline Simulations	
	1.4		Order Reduction	
	1.5	Conclu	sion	. 45
2	Mod	el Orde	r Reduction through Balanced Truncation	47
	2.1		uction to Model Order Reduction	
		2.1.1	State-Space Representation of a Physical System	
		2.1.2	System Solution	. 48
		2.1.3	Formal Problem Definition	. 49
	2.2	Theore	etical Foundations: Controllability, Observability, and Realisation	. 49
		2.2.1	Non-Uniqueness of State Selection	. 49
		2.2.2	Controllability	. 51
		2.2.3	Observability	. 51
		2.2.4	Minimal Realisation	. 52
	2.3	Balanc	ed Truncation Method	. 53
		2.3.1	Impulse-Response Matrix and its Decomposition	
		2.3.2	Controllability and Observability Gramians	
		2.3.3	Geometrical Interpretation of Controllability and Observability	. 58
		2.3.4	Method Description	
	2.4	Case S	tudy: Voltage Source Converter	. 60
		2.4.1	Model Description	. 60
		2.4.2	Model Implementation	
		2.4.3	Application of Balanced Truncation	. 65
	2.5	Conclu	sion	. 68
3	Meth	nodolog	ies for Physics-Preserving Model Reduction	69
	3.1	Metho	d 1: Event-Based Model Reduction	. 69
		3.1.1	Controllability and Observability Operators	. 70

		3.1.2	Approximation of the System's Response	71
		3.1.3	Calculation of the Approximation Error	72
		3.1.4	Participation of State in Input-Output Behaviour	74
		3.1.5	Physical Interpretation	
		3.1.6	Model Reduction Algorithm	
	3.2		od 2: Model Reduction for Different Frequency Ranges	
		3.2.1	Frequency-Limited Gramians	78
		3.2.2	Participation of a State Over a Frequency Range	79
		3.2.3	Model Reduction Algorithm	
	3.3		tudy: Voltage Source Converter	79
	5.5	3.3.1	Dynamic Analysis of the System	
		3.3.2	· · · · · · · · · · · · · · · · · · ·	
			Application of Method 1	
	0.4	3.3.3	Application of Method 2	
	3.4	Conciu	ısion	88
4	Taal	6 N 1	delline and Analysis of Dayyou Cystone Dynamics	00
4			delling and Analysis of Power System Dynamics	89
	4.1		escription	
	4.2		tudy 1: Converter-Dominated 9-Bus System	
		4.2.1	Model Description	
		4.2.2	Model Implementation	
		4.2.3	Dynamic Analysis of the System	
		4.2.4	Application of Model Reduction Method 1	
		4.2.5	Application of the Model Reduction Tool	
	4.3	Case S	tudy 2: Modified 39-Bus System	97
		4.3.1	Model Description	97
		4.3.2	Model Implementation	100
		4.3.3	Dynamic Analysis of the System	100
		4.3.4	Application of Model Reduction Method 1	101
		4.3.5	Application of the Model Reduction Tool	
	4.4	Conclu	ısion	
Coi	nclusi	ons and	f Future Work	104
List	t of Fi	gures		107
List	t of Ta	bles		108
Ref	ferenc	es		109
Acl	knowl	edgeme	ents	119
Ab	stract			120
Kol	kkuvõ	te		122
Ар	pendi	х A — II	ncluded Publications	125
			I	
	Publi	cation	II	139
			III	
			IV	

Appendix B — Transformations	179
abc to $lphaeta\gamma$ and its Inverse	
Appendix C — Eigendecomposition	183
Appendix D — Singular Value Decomposition	185
Appendix E — Hardy Spaces	187
Appendix F — Control Tuning Inner Current Control Phase-Locked Loop Active and Reactive Power Controls Voltage Feed-Forward Filter	189 190 191
Curriculum Vitae	192
Elulookirjeldus	194

List of Publications

The present Ph.D. thesis is based on the following publications that are referred to in the text by Roman numbers.

- I G. Grdenić, F. J. C. García, N. M. D. Campos, F. Villella, and J. Beerten, "Model order reduction of voltage source converters based on the ac side admittance assessment: From EMT to RMS," *IEEE Transactions on Power Delivery*, vol. 38, no. 1, pp. 56–67, 2023.
- II N. M. D. Campos, T. Sarnet, and J. Kilter, "Novel Gramian-based structure-preserving model order reduction for power systems with high penetration of power converters," *IEEE Transactions on Power Systems*, vol. 38, no. 6, pp. 5381–5391, 2023.
- III P. De Rua, T. Roose, O. C. Sakinci, N. M. D. Campos, and J. Beerten, "Identification of mechanisms behind converter-related issues in power systems based on an overview of real-life events," *Renewable and Sustainable Energy Reviews*, vol. 183, pp. 1–16, 2023.
- IV N. M. D. Campos, T. Sarnet, and J. Kilter, "A Gramian-based tool for modeling converter-dominated power systems," in 2024 IEEE PES Innovative Smart Grid Technologies Europe (ISGT Europe), 2024, pp. 1–5.

Author's Contributions to the Publications

- In I, Nathalia Campos contributed to the development of the approach for determining model validity ranges by comparing full and reduced-order models using frequency-domain admittance analysis. She also contributed to the revision of the manuscript.
- II In II, Nathalia Campos was the main author. She developed the proposed model-order reduction methodology based on controllability and observability Gramians, implemented the method in MATLAB/Simulink, conducted case studies and simulations, analysed the results, prepared the figures, and wrote the manuscript.
- III In III, Nathalia Campos conducted a bibliographic review of real-world stability events, contributed to the classification of these events, and participated in the writing and revision of the manuscript.
- IV In IV, Nathalia Campos was the main author. She developed the model-order reduction tool in MATLAB/Simulink, implemented the case study, analysed the results, wrote the manuscript, and presented the work at the IEEE ISGT Europe 2024 conference.

Abbreviations

AC. **Alternating Current**

AVR **Automatic Voltage Regulator**

DC **Direct Current**

DFIG **Doubly-Fed Induction Generator FMT Electromagnetic Transients**

EMTP Electromagnetic Transients Program FACTS Flexible AC Transmission Systems

HIL Hardware-in-the-loop HSV Hankel Singular Value **HVDC High-Voltage Direct Current** Insulated Gate Bipolar Transistor **IGBT** IGE **Induction Generator Effect** LCC Line-Commutated Converter

Linear Time-Invariant LTI

MIMO Multiple-Input Multiple-Output MMC Modular Multilevel Converter Model Order Reduction MOR Multi-Terminal DC MTDC **OWF** Offshore Wind Farm PCC **Point of Common Coupling** ы Proportional and Integral PH Phase-Locked Loop

PMSG Permanent Magnet Synchronous Generator

PMU Phasor Measurement Unit PSS Power System Stabilizer

PV Photovoltaic

Pulse Width Modulation PWM RMS Root Mean Square

RTDS® Real-Time Digital Simulator

SCR **Short Circuit Ratio**

SCTL Series-compensated transmission line

SISO Single-Input Single-Output

SSCI Subsynchronous Control Interaction SSDC Subsynchronous Damping Controller

SSO Subsynchronous Oscillation SSR Subsynchronous Resonance

SSTI Subsynchronous Torsional Interaction

SVC Static VAR Compensator SVD Singular Value Decomposition TSO **Transmission System Operator** VSC **Voltage Source Converter**

WF Wind Farm

Introduction

Power systems have experienced substantial transformations in recent years, primarily driven by government policies aimed at reducing greenhouse gas emissions and promoting renewable energy sources. To achieve ambitious climate targets, renewables are expected to supply up to 90% of electricity by 2050, with wind and photovoltaic sources projected to account for approximately 63% of total electricity generation [1]. At the same time, power systems are increasingly interconnected. For example, Europe's cross-border transmission capacity is projected to grow by 35 GW by 2025, with an additional 93 GW anticipated by 2040 [2]. To enable long-distance transmission and renewable interconnections, High-Voltage Direct Current (HVDC) technology has emerged as a key solution, offering improved operational flexibility compared to traditional Alternating Current (AC) connections.

A common consequence of these trends is the increased reliance on power electronic converters. However, the integration of these devices introduces complex stability issues. Despite extensive stability studies during planning and commissioning phases, several unexpected instability events have occurred. Notably, in 2017, ERCOT observed Subsynchronous Oscillation (SSO) events involving wind farms that had previously undergone stability analyses and employed damping controls, yet these measures failed to adequately predict and mitigate instability risks. Similarly, in 2019, the Australian Energy Market Operator (AEMO) identified persistent voltage oscillations at multiple solar farms, leading to prolonged generation curtailment and delayed project commissioning.

One significant reason for these undetected instability risks is the inherent complexity and limited understanding of power electronic device interactions within the system. Traditional Root Mean Square (RMS) modelling assumes near steady-state operating conditions, significantly simplifying the dynamic representation of power electronic converters and their interactions. This simplification can result in inadequate representation of dynamic phenomena, particularly oscillatory behaviours distant from steady-state frequencies, potentially leading to inaccurate stability assessments.

Conversely, Electromagnetic Transients (EMT) simulations provide higher accuracy in capturing dynamic phenomena. However, EMT simulations pose challenges related to computational complexity and the requirement for detailed component models, which are often unavailable due to proprietary constraints or incomplete information from manufacturers. For instance, after a sub-synchronous incident involving wind farms in 2009, ERCOT lacked sufficient EMT models to predict and mitigate instability events effectively.

Thus, a critical challenge emerges: identifying the minimum modelling details required for an accurate stability assessment while accounting for the unique dynamic behaviour introduced by converters. Understanding these requirements is essential to ensure that Transmission System Operators (TSOs) and other stakeholders can request appropriate models in various studies, thereby ensuring system reliability and operational security. This thesis addresses that challenge, aiming to establish a clear and systematic framework to determine the minimal necessary model complexity for accurate stability assessments in converter-dominated power systems.

Main Objectives of the Thesis

To address the modelling and stability assessment challenges introduced by the increasing penetration of power electronic converters in modern power systems, this thesis sets out to achieve the following objectives:

• Investigate the modelling and simulation methodologies for converter-dominated power systems, as well as their limitations.

- Develop methodologies to simplify power system models in order to enhance computational efficiency without compromising dynamic stability accuracy.
- Create and implement software tools to help determine the necessary level of accuracy for modelling various power system components.
- Validate the effectiveness of proposed methodologies through case studies demonstrating computational efficiency improvements and model accuracy.

Contribution of the Thesis

This thesis presents a novel, automated, and physics-preserving Model Order Reduction (MOR) framework designed to address the increasing complexity of stability analysis in converter-dominated power systems. The contributions are grouped below under theoretical and practical aspects.

Theoretical Novelty

- Review of emerging stability challenges in converter-dominated networks, including
 a comparison of modelling frameworks and a summary of the different models
 available for representing various power system components.
- Development of a methodology based on controllability and observability Gramians to quantify the contribution of individual states to system dynamics.
- Extension of Gramian-based MOR theory that preserves the physical interpretability of reduced-order models without requiring coordinate transformation, thereby making the results intuitive and directly applicable.
- Extension of the newly developed participation coefficient through the introduction of frequency-limited Gramians, enabling the quantification of each state's contribution within specific frequency ranges.
- Introduction of a frequency-specific model reduction technique that effectively isolates relevant dynamic behaviour across distinct frequency ranges.

Practical Originality

- Development of an automated model reduction framework for identifying the minimal model complexity required for stability studies.
- Creation of a user-friendly software tool based on MATLAB/Simulink that integrates
 the proposed MOR algorithms and provides a visual summary of model reduction
 outcomes.
- Demonstration of the tool's effectiveness through case studies, confirming its ability to identify critical system components and reduce the computational burden.

Thesis Outline

The thesis is organised as follows: **Chapter 1** introduces the stability challenges encountered in modern power systems increasingly dominated by power electronic converters. It reviews newly emerging stability issues, summarises the various models available for representing different power system components, and evaluates existing modelling frameworks, highlighting their strengths and limitations when applied to stability analysis. The chapter

concludes by presenting MOR as a valuable technique for determining the appropriate level of detail needed in models for different types of studies.

Chapter 2 presents the theoretical foundations of MOR, focusing particularly on the balanced truncation method. It explores fundamental concepts such as controllability, observability, and minimal realisation. The chapter then introduces the balanced truncation method and presents a case study to demonstrate its advantages and limitations. A notable limitation identified is the lack of physical interpretability of the method, which makes it difficult to understand which parts of the model are most relevant to the study.

Chapter 3 addresses this limitation by adapting the balanced truncation method. It proposes two novel physics-preserving MOR methodologies specifically developed for converter-dominated systems: the event-based and frequency-limited approaches. This chapter details their algorithms, provides physical interpretations, and demonstrates their effectiveness through a case study.

Finally, **Chapter 4** introduces a practical MATLAB/Simulink-based software tool that implements one of the MOR methodologies described in Chapter 3. The chapter presents detailed validation of the tool's functionality and efficacy through case studies involving a converter-dominated 9-bus system and a modified 39-bus system, highlighting practical applications and benefits.

1 Dynamic Modelling of Converter-Dominated Power Systems

This chapter examines how the increasing penetration of power-electronic converters is reshaping modern power systems and challenging the classical rotor-angle, frequency, and voltage stability classifications. It introduces the newly recognised converter-driven and resonance stability categories, then reviews the most widely adopted models for generators, transmission lines, loads, and converters, highlighting the assumptions and simplifications that influence accuracy in dynamic studies. Next, the chapter reviews the simulation tools currently used for stability assessment, comparing their capabilities and inherent limitations. It concludes by introducing Model Order Reduction (MOR) techniques applied to power systems, which have the potential to serve as tools for determining the appropriate level of detail required in models for different types of studies. The content of this chapter is partially based on the results presented in Publications 1 and 111.

1.1 Stability Challenges in Converter-Dominated Grids

Power systems are currently transitioning from traditional generation, which mainly relies on synchronous machines, to systems that incorporate a high number of power electronic devices. This shift is primarily driven by the use of renewable energy sources and HVDC transmission. The dynamic behaviour of these devices, characterised by fast-acting control systems and limited short-circuit capability, sets them apart from the devices comprising the traditional grid. This new dynamic behaviour presents both challenges and opportunities.

One significant challenge involves changes in system stability. New system conditions can push converters into unstable operation and increase the potential for interactions between converters and other grid components. These stability issues have been documented in the literature and observed in existing grids. Such problems can result in equipment damage, brownouts (a condition where the system voltage is decreased to reduce the load and potentially avoid further disruption to the system), or even blackouts in severe cases. To address these challenges, significant research efforts are underway to understand their causes and how to best study them. These concerns have motivated a recent review [3] of the widely accepted stability classification published in 2004 by the IEEE/CIGRE Joint Task Force on Stability Terms and Definitions [4]. The newly proposed classification, illustrated in Figure 1, features two additional categories of stability issues primarily observed in systems with a high penetration of converters, namely, converter-driven stability and resonance stability.

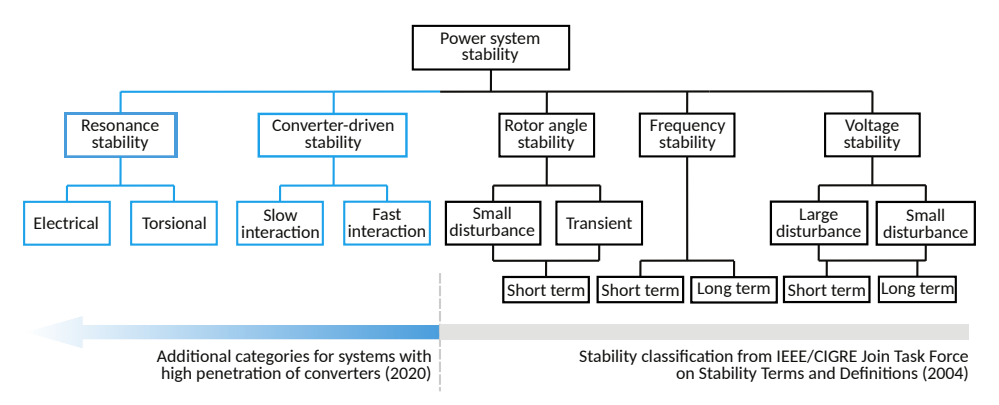


Figure 1: Power system stability classification [3, 4].

Table 1 offers a more detailed view of the new stability categories, including the fre-

quency range of oscillations, the instability phenomena involved in each category, and examples of practical scenarios where they may occur. It can be observed that these new stability issues impact most converter-based systems such as Wind Farms (WFs), Photovoltaics (PVs), and HVDC. The remainder of this section explores the various oscillation phenomena involved. Given the recent emergence of some stability issues, the terminology used to describe different phenomena in the literature is not always consistent. Various terms may be applied to the same phenomena, and different interpretations exist in their classification. In addition to the aforementioned stability reclassification effort, other ongoing initiatives aim to reclassify different phenomena [5]. The following discussion tries to align with recent developments in terminology while still mentioning industry-accepted terms.

Table 1: Instability phenomena and examples resulting from the new stability categories.

Category	Subcategory	Phenomenon	Example
	Slow interaction (<10 Hz)	Instability due to power transfer limits	WF limited voltage support due to current limits [6]
Converter-driven stability		Instability in weak grids	Phase-Locked Loop (PLL) losing synchronism during faults [7]
Stability		Low-frequency oscillations	Interaction among transmission-level PVs [8]
	Fast interaction (>10 Hz)	Harmonic interaction	Interaction of fast HVDC controls with passive grid [9]
	Torsional resonance	Subsynchronous torsional interaction	Wind turbine generator interacting with HVDC controls [10]
Resonance		Induction generator effect	Induction generator effect in WFs [11]
stability	Electrical resonance	Subsynchronous control interaction	WF connected to series compensated lines [12]
		Amplification of harmonics	Amplification of harmonics from distribution-level PVs [13]

1.1.1 Converter-Driven Stability

Converter-driven stability issues include system-wide stability problems caused by the dynamics of power converters. This oscillatory behaviour occurs across all frequency ranges, which can be either slow (typically up to 10 Hz) or fast (greater than 10 Hz) [3]. Converter-driven stability serves as an umbrella term that encompasses several emerging and well-known instability phenomena, such as *instability in weak grids*, *low-frequency oscillations*, and *harmonic interaction*. Table 2 presents chronological examples of real-life converter-driven stability events.

Instability in Weak Grids

Low system strength is linked to various stability issues. According to the Australian Energy Market Commission [25], system strength is defined as "a characteristic of an electrical power system that relates to the size of the change in voltage following a fault or disturbance on the power system." In other words, a weak system exhibits high sensitivity to voltage changes, both in magnitude and phase angle, when there is a change in active and reactive power injection or consumption [6]. System strength can be assessed by the short-circuit current level at a specific location. Elevated short-circuit current levels are typically found in a strong power system, whereas low levels indicate a weak power system. Reduced system strength can elevate the risk of system instability and converter interactions, impacting numerous systems that employ converters.

For example, wind farms face various challenges linked to weak grid conditions, including subsynchronous oscillations. These oscillations arise from the interaction between the controls of wind farm converters and the grid, a situation often aggravated by low system strength. However, system strength is merely one of several factors that determine if a system experiences instability or oscillations. When a system is weak, the likelihood of subsynchronous oscillations is also influenced by factors such as the wind farm's operational mode, control design, controller tuning, and communication delays [7, 26]. The fulfilment of grid code requirements poses another significant challenge for wind farms. During normally cleared faults, they are expected to remain connected to the grid. Once the fault is cleared, they may also be expected to provide active and reactive power to support grid stability [27]. Wind farms face several difficulties in fulfilling fault ride-through requirements. For example, if a wind farm fails to regulate its terminal voltage, it risks disconnection due to the protection functions being triggered [27]. Additionally, disconnection can occur if the controls cannot synchronise with the grid voltage, often due to limitations in the PLL or inadequate tuning. Low system strength conditions may also trigger harmonic oscillations [28] and increase the risk of the wind farm becoming islanded, requiring the design of special anti-islanding schemes [27].

The operation of HVDC systems is also influenced by system strength. Like wind farms, instability cannot be attributed solely to system strength but typically involves multiple other factors. Low Short Circuit Ratio (SCR) not only poses challenges for HVDC operation, such as influencing power transfer limits, but it also amplifies the effect of control tuning, including PLL [29] and power controls [30], on system stability.

Several significant real-life instability events have occurred in the past involving weak grid conditions [16, 31–33]. One notable incident was the 2019 blackout in the United Kingdom, initiated by subsynchronous oscillations at the Hornsea One wind farm. This incident impacted over a million customers and disrupted train services [31]. A lightning strike triggered the tripping of a transmission line, weakening the system at its connection point, which led to the wind farm experiencing subsynchronous oscillations [24]. Subsequent investigations revealed that prior to the blackout, the voltage control at the wind

2014 · · · · •	Nanao Modular Multilevel Converter (MMC)-based Voltage Source Converter (VSC)-HVDC project, Guangdong, CN Low freq. Oscillations observed when increasing output power [15].
2014 - 2015 · · · · •	Permanent Magnet Synchronous Generator (PMSG) wind farm, Xinjiang, CN weak grid Wind farms tripped 111 times in one year [16].
2015 · · · · •	Xiamen MMC-based VSC-HVDC project, CN Low freq. Low-frequency oscillations in the DC-side currents [17].
2015 · · · · •	INELFE MMC-based VSC-HVDC project, FR and ES Harmonic Interaction between converter and grid [9].
2015 · · · · •	Xiamen MMC-based VSC-HVDC project, CN Harmonic Oscillations on the DC side resulting from the interaction between converter controls and DC resonances [18, 19].
2016 ⋯⋯•	VSC-HVDC connecting offshore wind farm, DE Harmonic Oscillations involving offshore network and wind farm controls after blocking HVDC converter [20].
2016 · · · · •	Luxi HVDC project, CN Harmonic Three parallel back-to-back HVDC composed of one MMC and two Line-Commutated Converter (LCC) links [21].
2016 · · · · •	Zhoushan five-terminal VSC-HVDC project, CN Harmonic Oscillations after one of the terminals switched to islanded mode [15].
2018 · · · · •	Transmission-level photovoltaics, CA Harmonic Multiple events at harmonic frequencies [22].
2018 - 2019 · · · · •	Yu-E MMC-based VSC-HVDC project, CN Harmonic Blocked converter station and damaged lighting arrester triggered oscillations [23].
2018 · · · · •	Transmission-level photovoltaics, CA Low freq. Oscillations involving three PV plants connected to same feeder when capacitor is energized [22].
2019 · · · · •	Transmission-level photovoltaics, West Murray, AU Low freq. Oscillations among PV plants led to restrictions on operation and commissioning of units [8].
2019 · · · · •	Hornsea One wind farm, UK Weak grid Instability led to blackout affecting more than 1 million customers [24].

farm presented a damped oscillatory response. During the event, however, the voltage and power oscillations lacked sufficient damping, triggering overcurrent protections and resulting in the wind farm's tripping. Another significant example of weak grid oscillations in real life took place in Xinjiang, China, in 2014 and 2015. Multiple occurrences of oscillations at various subsynchronous and supersynchronous frequencies were observed involving a PMSG-based wind farm in Northwest China [16, 32, 33]. In one of the cases, three turbine generators tripped due to torsional modes coinciding with the oscillations. After implementing protection devices to detect these oscillations, the wind farms tripped 111 times over the course of a year.

Low-Frequency Oscillations

Another form of instability caused by converters is low-frequency oscillations. These oscillations occur at subsynchronous frequencies and can arise from the interaction between the control systems of a power electronic device and the network, or from the interaction between several power electronic devices [5].

A notable instance of oscillation involving a single converter interacting with the grid was recorded at the Nanhui MMC-based VSC-HVDC link, which connects a Doubly-Fed Induction Generator (DFIG)-based Offshore Wind Farm (OWF) to the shore. During the initial testing phase, voltage and current oscillations in the range of 20 to 30 Hz were observed, particularly during fluctuations in transmitted power [15]. Another example occurred in 2019, in West Murray, Australia, where multiple devices experienced oscillations, notably involving several transmission-level PV plants. The oscillations imposed limitations on the generation of solar farms already in operation and further restrictions on commissioning new units. Research indicated that reducing the number of connected PV plants would decrease oscillation amplitudes while lowering the power output of individual plants would be ineffective [8].

Most low-frequency interactions have been observed on the AC network. However, there are also instances of oscillations on the Direct Current (DC) side. This was the case, for example, in 2015, when the Xiamen MMC-HVDC project in China recorded DC current oscillations of approximately 25 Hz [17].

Harmonic Interaction

The final type of issue related to converter-driven stability is harmonic interaction. This term describes high-frequency oscillations, typically between hundreds of hertz and several kilohertz, that arise from the interaction between converter controls and grid dynamics, synchronous machines, or other converters. These oscillations have been observed in wind farms, photovoltaic systems, and HVDC links. The term can sometimes be ambiguous, as it may be used to describe phenomena with varying physical causes. Alternative terms like harmonic resonance or supersynchronous interaction can also be found in the literature [34].

Harmonic interactions can have negative effects at the component level, such as diminishing the effectiveness of power electronics or damaging equipment insulation. They can also lead to system-wide issues, including overheating of equipment connected to the network, interference with communication circuits, and even system instability [35]. This phenomenon arises from the interaction between control loops and passive grid components, resulting in high-frequency oscillations. This occurs when the system, including the converter and the remaining network, contains areas in the frequency spectrum where oscillations have low or negative damping. At these frequencies, oscillations may either be inadequately damped or significantly amplified.

One of the earliest instances of harmonic interaction occurred in 2013 at the BorWin1 VSC-HVDC link in Germany, connecting an OWF to shore. The oscillations started after a switching operation that connected a second OWF to the same HVDC station. Subsequent investigations determined that the primary cause of the oscillations was the interaction between the control loops of the VSC-HVDC converter and the resonant frequencies of the grid [36]. A separate incident took place in 2015, when a high-frequency oscillation was recorded, resulting in the tripping of the INELFE France-Spain MMC-based VSC-HVDC link. This 1.7 kHz oscillatory phenomenon, characterised as an interaction between the HVDC link and the surrounding AC network, could only be reproduced by control replicas [9].

1.1.2 Resonance Stability

Resonance stability is a newly recognised category of stability issues that has emerged alongside converter-driven stability. It occurs when series-compensated AC transmission lines interact with turbine generators. By adding series capacitors to AC transmission lines, the net reactive power transferred through the line is decreased, which increases power transfer capability and improves transient stability [37]. However, these devices change the harmonic impedance of the network, causing natural resonant frequencies to shift, which may potentially interact with other devices in the system. Resonance stability can manifest in two forms: *torsional resonance*, which is related to mechanical components, and *electrical resonance*, as observed in the induction generator effect. Table 3 presents chronological instances of real-life resonance stability events.

Electrical Resonance

Electrical resonance occurs due to various phenomena. One such phenomenon is the Induction Generator Effect (IGE), which refers to the interaction between the electrical grid and turbine generators [37]. This interaction can occur in type 3 wind turbines and arises from the negative resistance of the turbine rotor, potentially aggravated by the turbine controls. When induction machines operate at supersynchronous speeds, the rotor behaves as if it has negative resistance from the perspective of the stator terminals [11], and such negative resistance may result in undamped or even unstable oscillations.

A real-world example of this issue occurred in 2007, when interactions were detected between wind farms and a series compensated line in a 345 kV system in Minnesota, United States [39, 45]. These interactions occurred in the subsynchronous frequency range and were attributed to the induction generator effect. The oscillatory modes ranged from 10.95 to 15.78 Hz, with the damping ratio varying from 3.8% to 2.1%. Two separate events showed oscillations: the first involving a series compensated line and the second occurring after the series compensation was bypassed.

A related, yet different phenomenon is Subsynchronous Control Interaction (SSCI), characterised by electrical oscillation in the subsynchronous frequency range. These oscillations are often observed in wind farms when connected radially to the grid via a SCTL. They may be triggered, for example, by a network topology change due to a line outage following a fault. The oscillations primarily arise from the interaction between wind farm controls and the network impedance.

SSCI is a phenomenon that has been observed multiple times in power systems [12, 42, 46]. For example, in 2017, South Texas experienced three distinct events with oscillations ranging from 20 to 30 Hz. Two of these incidents led to the disconnection of wind farms. These occurrences were significant as all wind farms had undergone SSCI studies and were equipped with controls for subsynchronous oscillation damping. Nevertheless, this proved not to be sufficient to fully eliminate the risk of interaction [12]. Another notable example

1977 · · · · •	Square Butte LCC-HVDC project, Montana, US Torsional First Subsynchronous Torsional Interaction (SSTI) oscillations observed in an HVDC project [38].
2004 · · · · •	Distribution-level photovoltaics, NL Electrical Harmonic emissions amplified by network resonances in residential area [13].
2007 · · · · •	Wind farm, Buffalo Ridge, Minnesota, US Electrical Wind farm located near Series-compensated transmission lines (SCTLs) [39].
2009 · · · · •	DFIG wind farms, Texas, US Electrical Following a permanent fault, the wind farms were connected to SCTL, resulting in subsynchronous currents. [40].
2011 · · · · •	LCC-HVDC link, CN Torsional Torsional oscillations involved the converter controls, SCTLs and multiple synchronous generators [41].
2012 - 2013 · · · · •	DFIG wind farms, Hebei, CN Electrical Oscillations observed in several events resulting from the interaction between the wind farms and SCTLs [42].
2014 ⋯⋯•	Wind farms connected by an HVDC line, Santanghu, CN Torsional Torsional modes of DFIG wind farm were excited by the LCC-HVDC controls [10].
2014 - 2017 · · · · •	VSC-HVDC connecting offshore wind farm, DE Electrical Harmonics observed on the onshore station after a switching event [43].
2016 · · · · •	LCC-HVDC, DK [Electrical] Amplification of 11^{th} harmonics after cable energization [44].
	Wind farms near SCTL, Texas, US Electrical Wind farms were equipped with SSCI damping controls [12].

occurred between 2012 and 2013 in Hebei province, China, where 23 DFIG wind farms with a total installed capacity of over 3,000 MW were commissioned. Several events during this period revealed subsynchronous oscillations caused by the interaction of these wind farms with nearby series compensated lines [42, 46]. The frequency of these oscillations ranged from 6 to 8 Hz but changed over time during the events. The analysis indicated that oscillations can arise for transmission line compensation levels as low as 6.67%. This experience from China highlights the necessity of conducting appropriate studies to assess the risk of SSCI even when transmission lines are not significantly compensated.

Lastly, electrical resonance can occur as an amplification of harmonic emissions when

harmonics are injected into the grid by switching elements present in power electronic converters. When these harmonics interact with the impedance in the network, they can be amplified, leading to high-frequency oscillations that are poorly damped. This phenomenon can affect single power electronic-based devices and may worsen when multiple converters are involved [28, 47].

Torsional Resonance

Torsional resonance is a specific type of resonance stability that can occur due to the interaction between generator shafts and either the electrical network or connected devices [5]. The first type is known as Subsynchronous Resonance (SSR) with torsional characteristics, arising from the interaction between a series-compensated network and the generator's shaft system. Oscillations occur when the subsynchronous frequency induced in the generator matches one of the natural oscillatory modes of the generator shaft. Certain generator types, particularly those found in thermal plants with long shafts, are more susceptible to experiencing this issue [48].

The second form, commonly referred to as SSTI, involves electromechanical oscillations that occur between converter controls and the torsional modes of rotating machine shafts. This device-dependent phenomenon can arise from any control device that responds rapidly to power and speed variations in the subsynchronous frequency range [37]. Examples of such control systems include those found in HVDC converters, Flexible AC Transmission Systems (FACTS) devices, Static VAR Compensators (SVCs), wind turbines, and synchronous generators.

Certain types of generators, particularly those used in steam turbines, are more vulnerable to SSTI because of their natural mechanical modes in the subsynchronous frequency range [49]. Manufacturers measure the modal frequencies of turbine generators, which have been used to predict whether the unstable excited modes arise from the generator itself [39]. When there is a detection of a potential risk of SSTI oscillations, an additional Subsynchronous Damping Controller (SSDC) can be integrated into the existing current controller. This controller increases the damping at critical frequencies by sending a signal to the rectifier controller, which makes slight modifications to the firing angle of the converter switching elements [34].

SSTI oscillations involving LCC-HVDC and synchronous generators have been extensively studied. The LCC converter topology creates currents across a broad frequency range, potentially exciting subsynchronous mechanical modes in generator turbines. LCC-HVDC systems do not solely interact with traditional synchronous generation. The increase of renewable energy introduces new challenges, as SSTI has also been detected between LCC-HVDC systems and wind turbines [10]. Sometimes, multiple generators are involved in an SSTI event. According to [50], both wind turbines and traditional synchronous machines contribute to these oscillations, highlighting the importance of accurately modelling devices that are at risk when assessing SSTI.

Research has indicated that VSC topologies can negatively impact the damping of generator torsional modes under constant active power control [51]. Despite this, the overall risks associated with SSTI are relatively minor when compared to those of LCC-HVDC. In certain situations, the VSC can even contribute to slightly improved damping.

The initial observation of SSTI oscillations in an HVDC project occurred during the commissioning of the Square Butte project in Montana, United States, in 1977. During the event, oscillations were recorded at approximately 14 Hz between the HVDC controls and a turbine generator, which required the implementation of additional damping controls [38, 52]. More recently, in 2014, China experienced multiple oscillation events caused by the inter-

action of wind turbine generators with the controls of a nearby HVDC link. Measurement results showed that these oscillations occurred at lower frequencies (between 0 and 3 Hz for DFIGs) compared to traditional SSTI events involving classic generators. Furthermore, the measured frequency was inconsistent, varying according to the operating mode of the wind turbines [10].

1.2 Component Models

This section summarises the most commonly used models for dynamic studies of power systems. The review includes models for synchronous generators, transmission lines, loads, and power electronics converters.

1.2.1 Synchronous Generators

Models of synchronous generators must accurately represent the mechanical and electromagnetic dynamics of the machine. This section provides an overview of synchronous generator modelling. For more details, please refer to [53–56].

Prime Mover

Modelling a synchronous generator begins with the representation of the prime mover, which includes the turbine and its speed-governing system. This system converts the primary energy source into the mechanical power that acts on the generator shaft. A typical turbine-governor model consists of three main components: (i) a speed governor that detects the rotor speed (or frequency) and generates a command for the valve or wicket gate, (ii) a servo mechanism that drives the flow-controlling element, and (iii) one or more turbine stages that translate the admitted fluid into torque.

The turbine-governor model is usually represented as a block diagram. In this model, the governor introduces a steady-state droop R, along with time constants ranging from 0.1 to 0.5 s, while the turbine stages add extra delays whose magnitudes depend on the energy source [55]. In multi-mass shaft systems, the turbine stages are often modelled as separate inertias that are elastically coupled to the generator, allowing for the analysis of torsional modes [54].

The output from the prime mover model is a time-varying mechanical torque, denoted as T_m . This mechanical torque, together with the electrical torque T_e , can be used to formulate the equation of motion for the generator, as will be demonstrated next.

Swing Equation

The motion of the machine rotor is described based on the angular position δ of the rotor relative to the synchronous reference frame. The relationship between the mechanical torque T_m and the electromagnetic torque T_e determines the angular position of the rotor. When there is an imbalance between these torques, the rotor experiences either acceleration or deceleration. This change in motion is governed by the swing equation [4], which can be expressed as follows:

$$\frac{2H}{\omega_0}\frac{d^2\delta}{dt^2} = T_m - T_e - \frac{K_D}{\omega_0}\frac{d\delta}{dt},\tag{1}$$

where H is the inertia constant, K_D represents the damping factor and ω_0 denotes the rated electrical speed of the rotor.

Electromagnetic Dynamics

The electrical torque T_e , which appears alongside the mechanical torque T_m in Equation (1), originates from the electromagnetic model of the synchronous generator. This model employs the dq-frame to represent three-phase electromagnetic quantities through the use of the Park transformation. Details regarding the Park transformation can be found in Appendix B.

In the dq-frame, there are two defined axes: the direct axis (d-axis), which is aligned with the field windings, and the quadrature axis (q-axis), which is positioned at a right angle (90°) to the d-axis, in line with the rotor [56]. This representation offers several advantages, which have contributed to its popularity. First, under steady-state conditions, the currents and fluxes in both the stator and rotor maintain constant values, behaving similarly to DC quantities. Second, the d- and q-axis circuits can be decoupled, enabling independent analysis of each circuit.

The d-axis model features two terminals: one for the armature winding and the other for the field winding. The direct axis can be represented in varying degrees of complexity [56]:

- Field circuit f: this is the simplest representation, which considers that the only current path in the d-axis is the flux linkage within the armature windings and field windings. This model is regarded as a first-order representation.
- Field circuit f and one damper circuit 1d: this is the most common representation, which expands on the previous model by incorporating not only the field winding but also an additional damper circuit 1d that accounts for the effects of the damper windings. As a result, this model is categorised as a second-order representation. Figure 2 illustrates the corresponding circuit diagram.

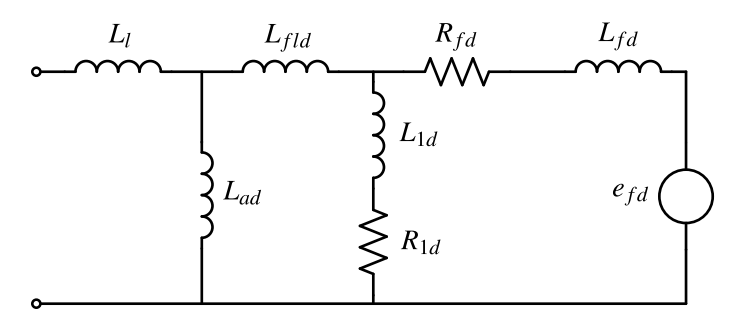


Figure 2: Circuit diagram for second-order d-axis representation [56].

• Field circuit f and two damper circuits 1d and 2d: in this third-order model, the field winding and two damper windings are considered.

In the d-axis models discussed earlier, there is an internal voltage source labelled e_{fd} , which corresponds to the field voltage. In simplified generator models, it can be assumed that the field voltage remains constant. However, more detailed models must account for the effects of the Automatic Voltage Regulator (AVR). The AVR regulates the field voltage based on the difference between the machine's measured terminal voltage and a fixed reference. It uses this error signal to adjust the field voltage; for instance, it increases the voltage whenever the terminal voltage begins to dip and decreases it when the terminal voltage rises, thereby maintaining the desired generator terminal voltage [55].

Because the AVR can lower the damping of rotor-angle oscillations, modern excitation systems typically include a Power System Stabilizer (PSS). This supplementary controller

extracts the rotor speed and feeds it through additional control blocks as a stabilising signal into the AVR. By adding an extra voltage component that is in phase with the generator speed, the PSS introduces damping torque, which helps stabilise small-signal oscillations [54].

Subsequently, models for representing the q-axis will be addressed. Similar to the d-axis, the representation of q-axis dynamics can vary in complexity. It is typically depicted as a circuit with a single terminal. The following variations exist:

• One damper circuit 1q: in this first-order model, a single damper circuit 1q, which corresponds to the amortisseur winding, is considered for the quadrature axis, as shown in Figure 3.

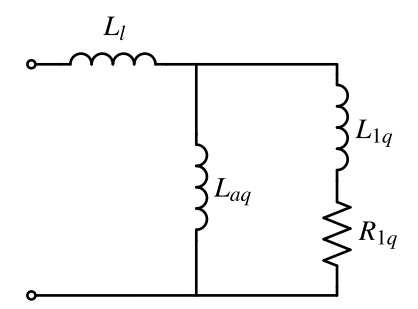


Figure 3: Circuit diagram for first-order q-axis representation [56].

• Two damper circuits 1q and 2q: for this model, two damper circuits are taken into account. The first corresponds to the amortisseur winding 1q, while the second, 2q, represents the eddy currents in the rotor, making it a second-order model. Figure 4 illustrates the circuit diagram for this model.

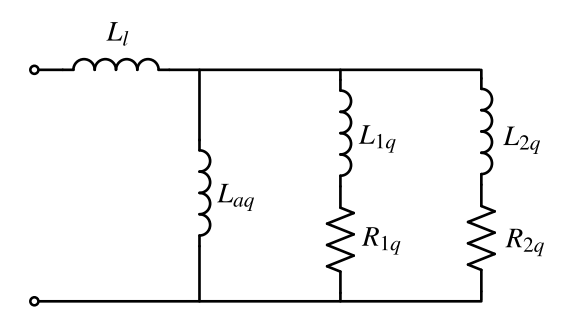


Figure 4: Circuit diagram for second-order q-axis representation [56].

Synchronous machine models are typically named to indicate the order of their d- and q-axis representations, using the notation N for the d-axis and M for the q-axis. This is typically presented in the format "Model N.M" [56]. The selection of appropriate models depends on the specific studies being conducted as well as the rotor structure of the synchronous machine.

1.2.2 Transmission Lines

Transmission line models can be classified into two main categories: lumped-parameter models and distributed-parameter models. These models differ in detail based on the

length of the transmission line and the desired level of accuracy. This section will provide a brief overview of the most commonly used models.

Lumped-Parameter Short Line Model

The short line model consists of a lumped parameter circuit that represents the total line resistance and reactance, obtained by multiplying the per-phase per unit length resistance R and inductance L by the total length l of the line. For lines shorter than 80 km, the line capacitance can be neglected without introducing significant approximation errors [57]. Figure 5 illustrates this model. The total line impedance Z is defined as follows:



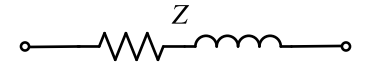




Figure 5: Short line model [57].

Lumped-Parameter Medium Line Model

Lines with lengths between 80 km and 250 km are considered medium-length lines. In this case, a recommended model consists of a lumped parameter circuit similar to that of short transmission lines. However, the effect of charging currents becomes significant and must be represented by a shunt admittance [57]. Half of the shunt capacitance is represented at each end of the line, as illustrated in Figure 6. The admittance value is obtained by multiplying the per-phase per unit length shunt conductance G and shunt capacitance G by the total length G of the line. This configuration is known as the *nominal* G model. The total line impedance G is defined by the same expression as given in Equation (2) for short transmission line impedance, and the total line admittance is calculated as follows:



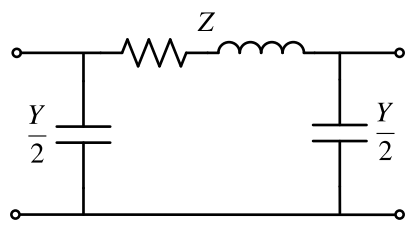


Figure 6: Medium line model [57].

Lumped-Parameter Long Line Model

For transmission lines longer than 250 km, it is important to consider that the line parameters are distributed uniformly along the line rather than being lumped [57]. Assuming

a transmission line of length l with a per unit series impedance $R+j\omega L$ and a per unit shunt admittance $G+j\omega C$, it is possible to define a complex constant γ , known as the line propagation constant and calculated as follows:

$$\gamma = \alpha + j\beta = \sqrt{(R + j\omega L)(G + j\omega C)},\tag{4}$$

where α is the attenuation constant and β is the phase constant.

A lumped parameter circuit can be derived to account for the effects of parameter distribution, yielding accurate results that align with the measurements taken at the ends of the transmission line [58]. This circuit is referred to as the *equivalent* π *model*, as shown in Figure 7.

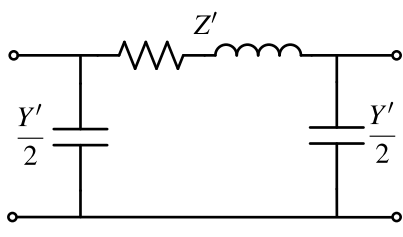


Figure 7: Long line model [57].

The total series line impedance Z' and shunt admittance Y' can be expressed in terms of the impedance Z and admittance Y of the medium transmission line, as well as the previously defined propagation constant γ . A comprehensive demonstration of how to derive these equations can be found in [57]. This results in the following expressions:

$$Z' = Z \frac{\sinh \gamma l}{\gamma l},\tag{5}$$

$$Y' = Y \frac{\tanh \frac{\gamma l}{2}}{\frac{\gamma l}{2}}.$$
 (6)

Distributed-Parameter Model

When studying transmission line transients, it may be necessary to use more detailed models than those previously presented. This section discusses the fundamental mathematical modelling required to derive distributed models of transmission lines. To simplify the analysis, a lossless transmission line is considered.

Consider a section of length Δx along a transmission line, as illustrated in Figure 8. In this segment, the distance from the line element to the sending end is represented by x. The relationships that describe the voltage u and the current i along the transmission line are expressed by partial differential equations as follows [58]:

$$\frac{\partial u}{\partial x} \Delta x = -\left(Ri + L\frac{\partial i}{\partial t}\right) \Delta x,\tag{7}$$

$$\frac{\partial i}{\partial x}\Delta x = -\left(Gu + L\frac{\partial u}{\partial t}\right)\Delta x. \tag{8}$$

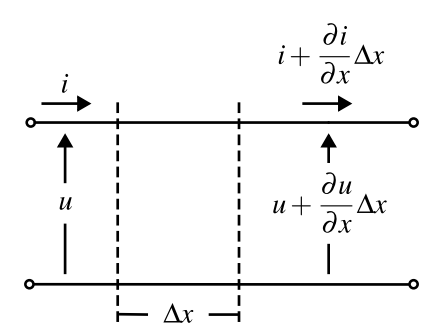


Figure 8: Section of distributed line model [58].

When both Equations (7) and (8) are divided by Δx , and the constants R and G are set to zero, assuming the line is lossless, the following expressions are obtained:

$$\frac{\partial u}{\partial x} = -L\frac{\partial i}{\partial t},\tag{9}$$

$$\frac{\partial i}{\partial x} = -C \frac{\partial u}{\partial t}.$$
 (10)

Finally, combining Equations (9) and (10) leads to an expression known as the *travelling* wave equation. This expression is represented as:

$$\frac{1}{LC}\frac{\partial^2 u}{\partial u^2} = \frac{\partial^2 u}{\partial t^2}.$$
 (11)

The solution to the travelling wave equation can be expressed as a voltage u = f(x - vt). This voltage u represents a wave travelling in the positive direction of x at a speed v [58]. The speed is given by the following expression:

$$v = \frac{1}{\sqrt{LC}}. (12)$$

When the voltage u is applied at the sending end of the transmission line, it travels toward the receiving end, where it may be partially reflected. When the reflected wave reaches the sending end, it can also be partially reflected again. This series of wave reflections in the transmission line leads to the occurrence of transients.

1.2.3 Loads

To describe how electrical loads behave in the grid, engineers typically use two complementary types of load models: static and dynamic. Static load models represent the relationship between active and reactive power consumed by a load as an algebraic function of the voltage and frequency across the load. In contrast, dynamic load models utilise differential equations to describe the relationships between power, voltage and frequency at the load.

Static Load Models

Static load models are used to represent loads that present time-invariant and near-instantaneous changes in power demand when there is a variation in voltage or frequency at the connecting bus. As previously mentioned, these models represent the dependence between active P and reactive Q powers as a function of the voltage U and frequency f as follows:

$$P = f_P(U, f) \tag{13}$$

$$Q = f_O(U, f) \tag{14}$$

where f_P and f_O are algebraic time-independent functions.

Static load models are primarily used to represent resistive loads, residential loads, and other types of loads that do not significantly involve induction motors or electrical drives. These models are mainly utilised for power flow and voltage stability studies [59]. Depending on the form of the functions f_P and f_Q , the model can be classified as an exponential, polynomial, linear, comprehensive, induction motor, and power-electronic interfaced load model.

The *exponential load model*, for example, is one of the most frequently utilised static load models [59] and is represented by the non-linear Equations (15) and (16):

$$P = P_n \left(\frac{U}{U_n}\right)^{k_{pu}} \left(\frac{f}{f_n}\right)^{k_{pf}} \tag{15}$$

$$Q = Q_n \left(\frac{U}{U_n}\right)^{k_{qu}} \left(\frac{f}{f_n}\right)^{k_{qf}} \tag{16}$$

where P_n and Q_n represent, respectively, the nominal active and reactive powers drawn by the load, k_{pu} , k_{qu} , k_{pf} and k_{qf} are the exponents that describe the load's response.

The dependency of the power with respect to the frequency is often neglected because variations in voltage are more common and more significant than changes in frequency. As a result, the model can be simplified to:

$$P = P_n \left(\frac{U}{U_n}\right)^{k_{pu}} \tag{17}$$

$$Q = Q_n \left(\frac{U}{U_n}\right)^{k_{qu}} \tag{18}$$

The exponents k_{pu} and k_{qu} represent the sensitivity of active and reactive power to voltage changes. When these exponents are set to 0, 1, or 2, the model behaves according to constant power, constant current, or constant impedance characteristics, respectively [54].

Another widely used static model is the *polynomial load model*, often referred to as the *ZIP model*. This model includes three load components: constant impedance (Z), constant current (I), and constant power (P). Mathematically, it can be expressed as:

$$P = P_n \left[p_1 \left(\frac{U}{U_n} \right)^2 + p_2 \left(\frac{U}{U_n} \right) + p_3 \right]$$
 (19)

$$Q = Q_n \left[q_1 \left(\frac{U}{U_n} \right)^2 + q_2 \left(\frac{U}{U_n} \right) + q_3 \right]$$
 (20)

where the parameters p_1 and q_1 represent the contribution of the constant impedance load, p_2 and q_2 represent the participation of the constant current load and p_3 and q_3 represent the proportion of the constant power load. The participation of each load component ranges from 0 to 1 p.u., and the sum of all three components must equal 1 p.u.

Dynamic Load Models

Dynamic load models share a similar general mathematical representation with static models; however, the functions that describe power consumption also vary with time. This can be expressed as:

$$P = f_P(U, f, t) \tag{21}$$

$$Q = f_O(U, f, t) \tag{22}$$

where f_P and f_Q are time-dependent functions.

Dynamic load models are primarily used to represent loads that involve a significant number of induction motors and electrical drives. These loads can be categorised into several types, including exponential loads, induction motors, transfer function-based induction motors, composite loads, distribution loads, bulk power bus loads, and distributed energy storage system loads. For further details, refer to [59].

1.2.4 Converters

There are several topologies available for power converters, but this section will focus specifically on the modelling of VSCs for the sake of brevity. VSC technology is based on self-commutating switches, typically Insulated Gate Bipolar Transistors (IGBTs). By employing Pulse Width Modulation (PWM) techniques, it is possible to control the firing pulses sent to the switching devices which in turn generates a controlled AC waveform at the converter's terminals. This waveform comprises a sinusoidal component at the fundamental frequency along with harmonics that are multiples of the switching frequency [60]. VSCs come in various topologies, generally classified based on the number of voltage levels they incorporate: two-level, three-level, and multi-level converters.

Figure 9 illustrates a single phase of a *two-level converter* that uses IGBTs. As the name implies, this converter can produce only two distinct voltage levels at its terminals. One advantage of this topology is the reduced number of switching elements required. However, it is essential for the DC capacitor to be sufficiently large to maintain a constant DC voltage, and IGBTs must withstand significant voltage differentials [60].

Building upon the two-level VSC, researchers developed a *three-level diode-clamped converter*. This design is capable of producing three different voltage levels, which helps lower the switching frequency of the IGBTs and reduces the voltage differentials during switching.

Continuing the trend of enhancing VSC performance by increasing the number of voltage levels, the *Modular Multilevel Converter (MMC)* topology was introduced as an alternative. The MMC generates a relatively high number of voltage levels, resulting in a synthesised voltage waveform with fewer harmonics, a reduced need for filtering, and a lower switching frequency per device [61]. The MMC, illustrated in Figure 10 for a single phase, features a scalable topology composed of submodules that can assume different structures. The most common configurations are the full bridge and the half bridge, also shown in Figure 10.

After examining the most common VSC topologies, the next step is to explore how to model their behaviour. The VSC models used for dynamic studies can be categorised into two main types: switching models and average models. Switching models can either represent the switches individually or in an aggregated form. These models require smaller solution time steps because they need to effectively capture fast-switching phenomena. On the other hand, average models focus on the low-frequency behaviour of the converter, omitting the high-frequency switching details. They simplify a discrete and discontinuous model into a continuous one by averaging the state variables of the converter or the waveforms at the converter terminals that result from the switching elements [62].

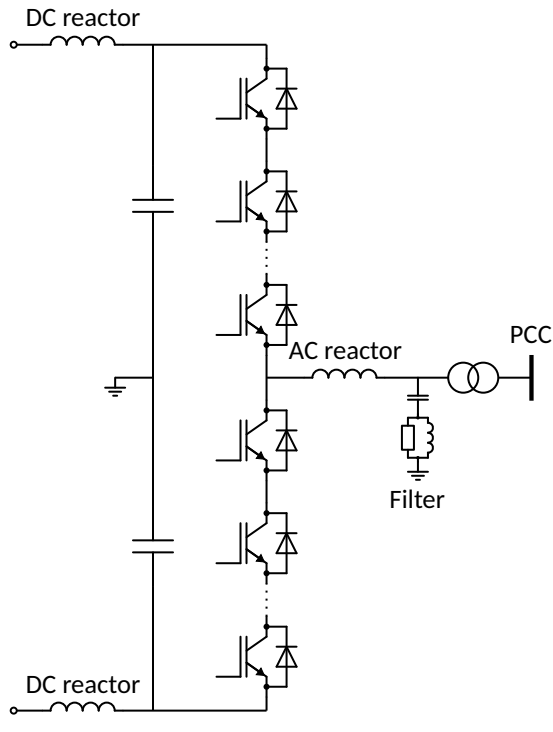


Figure 9: Two-level VSC topology [60].

Full Discrete Switching Model

Each switching device is represented individually in this model. The IGBTs are modelled as ideal controlled switches, while the diodes are treated as nonlinear resistances. This model requires the full converter control to be included, as the firing pulses are input to the IGBTs. A drawback of this approach is that it may not be suitable for real-time simulation due to its complexity, which can become prohibitive [63]. For instance, when modelling a MMC, the large number of switches in this topology leads to significant computational demands. A half-bridge converter with 200 submodules, for example, contains 4800 IGBTs and 4800 diodes. Therefore, this model is primarily recommended for validating simplified models or analysing abnormal behaviour in the converter [64].

Switchable Resistance Model

This model is similar to the previous one. However, the IGBTs and diodes are represented as resistances with two different values: a low value when the device is closed and a high value when it is open. This model still has a high computational cost due to the number of elements to be represented. Similar to the previous model, this model is primarily suited for validating simplified models or analysing abnormal behaviour in the converter [64].

Average Switching Model

In this model, the switching behaviour is averaged in the time domain. One practical application of this model is in representing MMCs, as these devices contain a large number of switches. By reducing the number of switches, simulation efficiency can be significantly improved [63]. This model is developed by representing the MMC arm by a detailed equivalent circuit, which drastically reduces the number of elements that need to be represented.

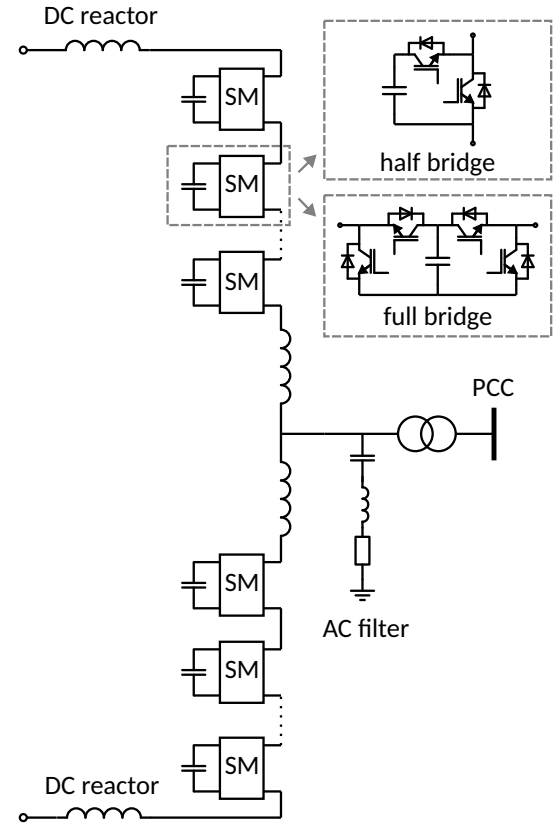


Figure 10: Multi-level MMC-based VSC topology [60].

The equivalent circuit is illustrated in Figure 11, where the values of R_1 and R_2 depend on the switching state of the submodules. Due to this significant reduction in the number of elements represented, models using detailed equivalent circuits are particularly suitable for simulating HVDC grids and can be implemented in real-time simulation platforms [64].

Averaged Value Model

Average-value models can use larger time steps, as they do not need to represent fast-switching events explicitly. Instead, these models replicate the average response of the converter switches using controlled sources and switching functions. The most detailed type of average model incorporates the harmonic content of the switching elements into the AC waveform produced by the controlled voltage source [64]. On the AC side, controlled voltage sources connect directly to the grid. On the DC side, current sources represent current injections from the grid [65]. This model is illustrated in Figure 12.

Simplified Averaged Value Model

This model is similar to the previous average value model but preserves only the fundamental component of the voltage in the controlled voltage sources, omitting the effects of switching [64]. By using the averaged model, the control scheme can be simplified by excluding the inner current control dynamics. Consequently, the output current signals from outer control loops are injected directly into the grid via current sources.

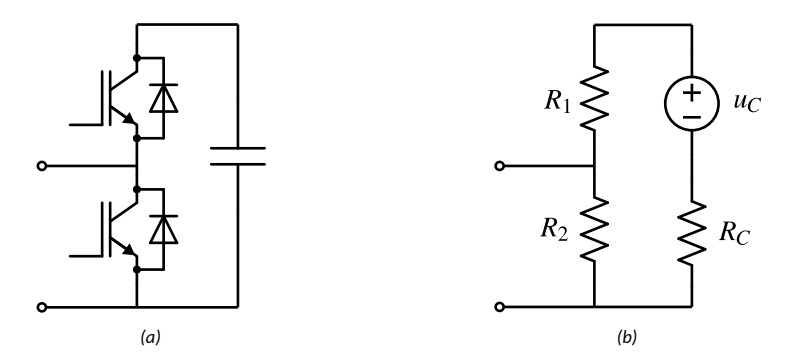


Figure 11: Detailed equivalent circuit representing an MMC arm [64].

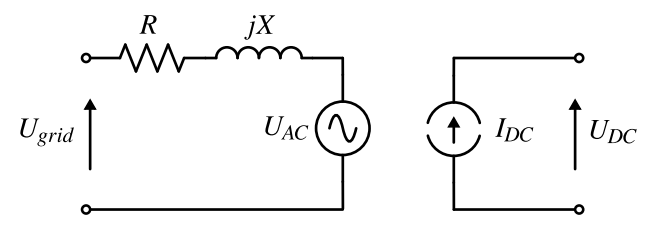


Figure 12: Averaged value model of a VSC.

1.3 Modelling Frameworks and Simulation Tools

When disturbances occur in the power system, system variables experience variations, known as transients, resulting from the energy exchange among components, which can be predominantly electromechanical or electromagnetic [66]. Electromagnetic transients result from the interaction between the magnetic fields of inductive elements and the electric fields of capacitive elements. In contrast, electromechanical transients are related to the interaction between the mechanical energy stored in the rotating machine parts and the electrical energy stored in the network.

The timeframes for different types of transients vary significantly. Electromagnetic transients are associated with faster phenomena and shorter time constants, whereas electromechanical transients exhibit slower response times and larger time constants. Figure 13 illustrates the various oscillation phenomena in power systems along with their corresponding timescales.

This distinction between electromagnetic and electromechanical transients naturally creates a corresponding separation in the modelling frameworks and tools utilised for studying each transient type. Historically, two distinct types of programs and their corresponding modelling frameworks were developed to analyse each transient category: EMT programs for electromagnetic transients and RMS programs for electromechanical transients. To better understand the limitations of each type of simulation tool, it is important to clarify how EMT and RMS programs model power system components.

1.3.1 Electromagnetic Transient Programs

The advent of digital computers motivated the creation of methods for digitally simulating electromagnetic transients, which largely replaced earlier techniques like the Transient Network Analyser that used scaled-down analogue models for power system simulation [66]. In the 1960s, H. W. Dommel devised a technique that employed difference equations

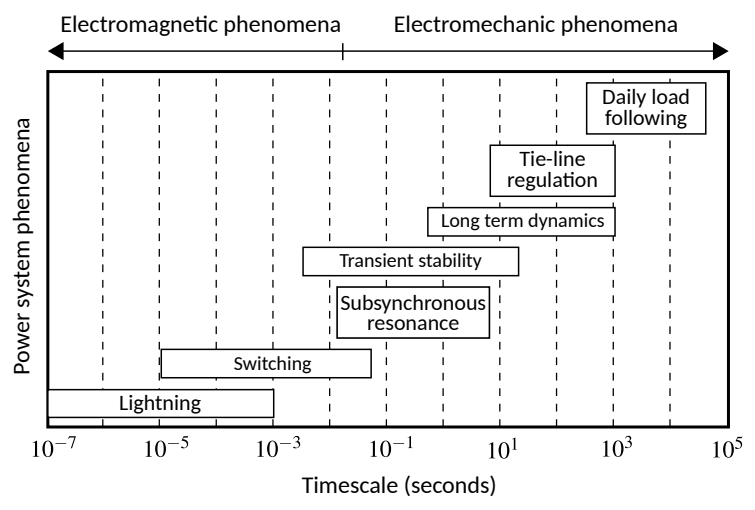


Figure 13: Timescale for power system phenomena [66].

to solve the differential and algebraic equations representing power systems. This approach was incorporated into a program for the digital simulation of electromagnetic transients, known as the Electromagnetic Transients Program (EMTP).

In EMT, variables are represented by real signals, and power system components, including the network, are modelled using a set of differential-algebraic equations. These equations are solved to determine the instantaneous values of the variables. By using appropriate models, it is possible to obtain an accurate response over a wide frequency range. The solution implemented in EMT programs involves converting continuous power system differential equations into discrete algebraic equations, known as difference equations [67]. Discretisation of the differential equations that relate voltage and current produces a convenient discrete-time equivalent circuit composed of an equivalent resistance in parallel with a current source. This process is accomplished using numerical integration methods and it is essential because computers can only perform calculations at discrete time intervals.

Numerical Integration Methods

Numerical integration allows for the determination of an approximation to the definite integral of a function f(t). This approximation corresponds to the area under the curve f(t) over the interval $[t-\Delta t,t]$ as illustrated in Figure 14. The process of discretisation can introduce errors, causing the numerical solution to differ from the continuous-time solution. Additionally, the choice of numerical integration method affects the performance and stability of the solution [67]. Two commonly used integration methods in EMT programs will be discussed: the *trapezoidal rule of integration* and the *backward Euler method*.

The backward Euler method approximates the integral using the area of the rectangle *EBDC*. In mathematical terms,

$$\int_{t-\Delta t}^{t} f(t) dt = f(t) \Delta t.$$
 (23)

In the case of the trapezoidal integration rule, the function f(t) is approximated for the interval $[t - \Delta t, t]$ by the straight line segment \overline{AB} . Therefore, the integral corresponds

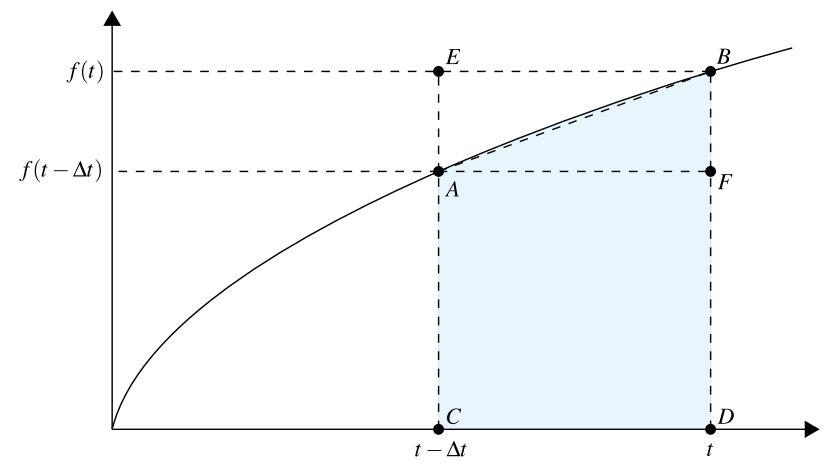


Figure 14: Numerical integration.

to the area of the trapezoid *ABCD*, which is expressed as:

$$\int_{t-\Delta t}^{t} f(t) dt = \frac{\Delta t}{2} [f(t) + f(t - \Delta t)]. \tag{24}$$

Example: Modelling of Circuit Components

By applying integration methods to the differential equations associated with circuit components, it is possible to derive the corresponding discrete-time equivalent circuits that form the basis for digital simulations. Note that numerical integration methods can also be employed to discretise equations that involve differentiation. To accomplish this, both sides of the equation are integrated, resulting in an expression containing only integration operations. The numerical integration method is then applied to this expression. Therefore, it can be said that integration methods, despite their name, function as either integrators or differentiators, depending on the original relationship between the variables in the differential equation.

In the remainder of this section, the trapezoidal integration method will be used to illustrate how to obtain the difference equations representing the resistor, capacitor, and inductor. Starting with the resistor, the relationship between its current i_{km} and the voltage u_{km} across its terminals is given by:

$$u_{km}(t) = Ri_{km}(t). (25)$$

Since Equation (25) is already presented in algebraic form, there is no need to apply an integration method, and the resistor's representation remains unchanged.

For the capacitor, the following relationship holds:

$$i_{km}(t) = C\frac{du_{km}(t)}{dt}. (26)$$

By integrating both sides of Equation (26) over the interval $[t - \Delta t, t]$ and applying the trapezoidal method, it is possible to obtain the following result:

$$i_{km}(t) = \frac{1}{R_C} u_{km}(t) + I_C(t - \Delta t),$$
 (27)

where

$$R_C = \frac{\Delta t}{2C},\tag{28}$$

$$I_C(t - \Delta t) = -\frac{2C}{\Delta t} u_{km}(t - \Delta t) - i_{km}(t - \Delta t). \tag{29}$$

As shown in Figure 15, the capacitor is modelled using a resistance R_C in parallel with a current source I_C .

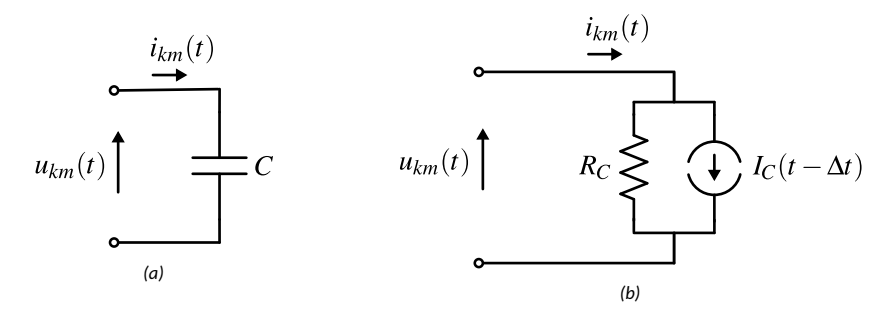


Figure 15: The (a) capacitor and (b) its discrete equivalent.

The procedure for the inductor is identical. The relationship between voltage and current is expressed by the equation:

$$u_{km}(t) = L\frac{di_{km}(t)}{dt}. (30)$$

By integrating both sides of Equation (30) over the interval $[t - \Delta t, t]$ and utilising the trapezoidal integration method, the following expression is obtained:

$$i_{km}(t) = \frac{1}{R_L} u_{km}(t) + I_L(t - \Delta t),$$
 (31)

where

$$R_L = \frac{2L}{\Delta t},\tag{32}$$

$$I_L(t - \Delta t) = \frac{\Delta t}{2L} u_{km}(t - \Delta t) + i_{km}(t - \Delta t). \tag{33}$$

Like the capacitor, the inductor is represented by a discrete equivalent circuit featuring a resistor R_L in parallel with a current source I_L as shown in Figure 16.

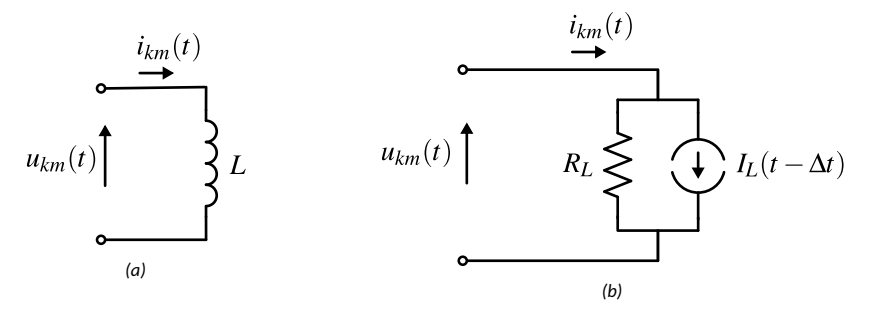


Figure 16: The (a) inductor and (b) its discrete equivalent.

1.3.2 Transient Stability Programs

Unlike EMT programs, which represent variables as real signals, transient stability programs, often referred to as RMS programs, use complex numbers through phasor-based modelling to represent these variables. This approach decreases the computational effort needed in simulations and is commonly employed in stability studies of large power systems.

A key factor in achieving this is the approximation of system variables, including voltages, currents, and electromagnetic fluxes by quasi-stationary phasors. This technique assumes that network signals experience only slight frequency variations around the nominal frequency. By filtering out the nominal frequency component, it becomes possible to focus solely on the frequency deviations. These deviations represent the envelope of the original signal as illustrated in Figure 17, and they typically have a significantly lower frequency compared to the original signal. Consequently, this influences the maximum step size Δt_{max} that can be used in simulations, which is determined by the maximum frequency f_{max} present in a signal. The relationship is calculated according to the Nyquist criterion [68]:

$$\Delta t_{max} = \frac{1}{2 f_{max}}. (34)$$

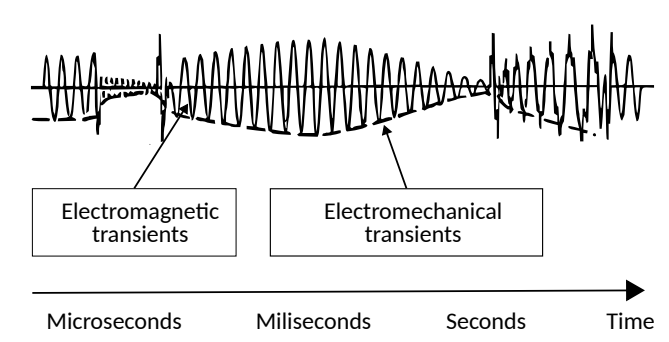


Figure 17: Comparison between instantaneous and phasor variables [69].

In addition to the previously mentioned assumption, RMS simulations typically focus on a narrower frequency range of interest, enabling the use of simplified models for power system components and allowing for larger calculation time steps. Both of these simplifications help reduce computational effort. However, this assumption is only valid when studies are confined to slow dynamic phenomena and may not apply to various stability issues that can arise with converters.

Phasor Representation

A phasor serves as a representation of a sinusoidal signal using complex numbers [70]. For example, consider the sinusoidal voltage u(t), which has magnitude U_m , an angular frequency of ω and a phase of ϕ expressed as follows:

$$u(t) = U_m cos(\omega t + \phi). \tag{35}$$

Using Euler's identity, it is possible to rewrite u(t) in terms of a complex number:

$$u(t) = \operatorname{Re}\{U_m e^{j(\omega t + \phi)}\}. \tag{36}$$

This last expression is equivalent to:

$$u(t) = \operatorname{Re}\{\mathbf{U}e^{j\omega t}\},\tag{37}$$

where U denotes the phasor representation of the sinusoidal signal u(t), given by:

$$\mathbf{U} = U_m e^{j\phi}. \tag{38}$$

For a steady-state signal u(t), the magnitude U_m and phase ϕ remain constant. In contrast, for a quasi-steady-state signal, both magnitude and phasors may change, but only slightly. Thus, the phasor associated with this signal can be viewed as a quasi-stationary phasor.

Example: Modelling of Circuit Components

This section demonstrates how basic circuit components are modelled in RMS. It derives the fundamental equations that represent the resistor, capacitor, and inductor, emphasising the key assumption behind RMS modelling, namely, that the phasors remain quasi-stationary.

Starting with the resistor, its characteristic equation can be represented with instantaneous signals as follows:

$$u(t) = Ri(t). (39)$$

Using the phasor definition from Equation (37), Equation (39) can be rewritten in phasor form:

$$\operatorname{Re}\{\mathbf{U}e^{j\omega t}\} = \operatorname{Re}\{R\mathbf{I}e^{j\omega t}\}. \tag{40}$$

Since Re is a linear operator, the expression can be simplified to a form that involves only complex phasors:

$$\mathbf{U} = R\mathbf{I}.\tag{41}$$

The phasor equation representing the resistor is derived without requiring any special assumptions. A similar relationship can also be established for the capacitor. Consider the characteristic equation that relates current and voltage in a capacitor:

$$i(t) = C\frac{du(t)}{dt}. (42)$$

Using the phasor definition from Equation (37), the derivative term can be developed to produce the following expression:

$$\mathbf{I} = C\frac{d}{dt}\mathbf{U} + j\omega_0 C\mathbf{U}.$$
 (43)

The right-hand side of Equation (43) consists of two terms. Under the assumption that the phasor represents a steady-state signal, the first term simplifies to $d\mathbf{U}/dt=0$, because both the magnitude and phase of the phasor remain constant. A similar simplification can be applied when the magnitude and phase experience only slight variations. In this scenario, the derivative term can be neglected as an approximation, that is, $d\mathbf{U}/dt\approx0$. This is known as the quasi-stationary assumption, which was introduced earlier. It applies to signals whose frequency does not significantly deviate from the nominal value, such as in low-oscillation phenomena [71]. By applying the quasi-stationary assumption to Equation (43), the following expression is obtained:

$$\mathbf{I} = j\omega_0 C\mathbf{U}.\tag{44}$$

Similar procedures can be applied to derive the characteristic phasor equation that defines the behaviour of an inductor, leading to:

$$\mathbf{U} = i\omega_0 L\mathbf{I}.\tag{45}$$

The equations developed for the circuit components using the quasi-stationary phasor assumption are algebraic. These equations can only describe the steady-state behaviour of the components at nominal frequency. However, outside of this frequency range, inaccuracies may arise, which might or might not be acceptable.

1.3.3 Framework Comparison and Discussion

The choice of both the model and the modelling framework can significantly impact the accuracy of simulation results. As previously discussed, EMT and RMS modelling frameworks use distinct solution methods, adopt different typical time steps, and establish the underlying modelling assumptions. Table 4 outlines the key differences between the EMT and RMS approaches.

Table 4: Comparison between EMT and RMS frameworks [72, 73].

	Electromagnetic transient programs	Transient stability programs
Solution method	Instantaneous values of variables are calculated by solving the differential equations	Variables are represented by phasors and sometimes only solved for positive sequence values
Assumptions	No implicit assumptions	Variables do not deviate significantly from nominal frequency
Frequency range of accuracy	Wide frequency range, depending on choice of models	Only accurate around nominal frequency
Simulation time step	Microseconds	A few milliseconds
Generator modelling	Differential equations	Algebraic equations for stator windings
Network modelling	Differential equations	Steady-state network equations
Converter modelling	Model with individual switches or averaged model. Fast controls $< 100~{\rm ms}$ included	Averaged model. Only slower controls included $>10~\mathrm{ms}$
Commercial tools	PSCAD, EMTP-RV, RSCAD, ATP, PowerFactory	PowerFactory, PSS/E, Eurostag

To clarify these differences, examples will be provided to illustrate the various simplifications and assumptions involved in developing power system component models in RMS. Specifically, the focus will be on two cases: the modelling of synchronous generators and

power electronic converters.

Example 1: Generator Modelling in RMS

The generator models used in RMS simulations are based on the principles discussed in Section 1.2.1, but they incorporate certain assumptions that are typically valid in transient stability studies to simplify and speed up calculations. Two primary simplifications can be identified. The first simplification relates to the representation of stator dynamics. As these dynamics are considered relatively fast, the derivatives of the stator flux and current can be neglected. Furthermore, it is assumed that the impact of speed variations on the stator voltage equations is negligible. This assumption arises from the fact that the speed of the machine remains nearly constant during a disturbance, allowing it to be treated as equal to the synchronous speed [74].

The stator electrical equations in the dq-frame are represented as follows [56]:

$$e_d = \frac{d}{dt}\psi_d - \psi_q \omega_r - R_a i_d, \tag{46}$$

$$e_q = \frac{d}{dt}\psi_q + \psi_d \omega_r - R_a i_q, \tag{47}$$

where ψ_d and ψ_q denote the flux linkages, i_d and i_q represent the stator currents, R_a is the armature resistance and ω_r is the rotor speed.

Applying the previously mentioned simplifications to Equations (46)–(47) involves considering the terms $d\psi_d/dt\approx 0$ and $d\psi_q/dt\approx 0$ and $\omega_r\approx 1$. This results in the following equations [75]:

$$e_d = -\psi_q - R_a i_d, \tag{48}$$

$$e_a = \psi_d - R_a i_a. \tag{49}$$

Example 2: Converter Modelling in RMS

RMS simulations typically use averaged models to represent converters, focusing solely on the fundamental frequency component [76]. In a phasor-based representation of an averaged value VSC model, it is assumed that the equations on the AC side of the converter are quasi-stationary phasor equations, thereby neglecting any derivative terms. Whether or not this simplification is applied generally determines if the model is classified as RMS or EMT. Additionally, there are two other simplifications related to converter controls that may be present in RMS converter models. Following is an overview of the VSC simplifications:

- Representing AC side with quasi-stationary phasor equations: as previously mentioned, this approach implies that derivative terms are neglected, leading to a conversion of differential equations into algebraic ones. This simplification aligns with the typical algebraic representation of the network.
- Neglecting or simplifying inner current control: the time constant for current control dynamics is typically shorter than the integration time steps used in RMS simulations. To adapt the VSC model for larger integration time steps, it is common to neglect the current control model and assume that the converter follows current references almost instantaneously. Alternatively, the current control model can be replaced with a time delay [77, 78].
- Neglecting or simplifying the PLL: neglecting the PLL assumes that the converter is
 perfectly synchronised with the grid and instantaneously tracks the Point of Common
 Coupling (PCC) voltage. Alternatively, it can be implemented in place of a detailed
 PLL model.

Simplified models that rely on the assumption of quasi-stationary phasors can enhance simulation speed and reduce modelling complexity. However, this assumption restricts the range of phenomena that can be accurately observed. For many stability issues arising from power electronic converters, this assumption may not hold true and may lead to inaccurate results [3]. Therefore, it is important to carefully analyse new stability phenomena associated with these converters to determine if traditional RMS-based tools are appropriate. If they are not suitable, more accurate models and tools, such as EMT programs, should be employed.

1.3.4 Alternatives to Offline Simulations

The offline EMT and RMS simulation tools discussed previously are widely used in the industry. They can produce accurate results, provided that the models employed adequately represent all relevant behaviours of the system being studied. However, this strong dependence on the models presents a significant limitation and poses a risk of inaccuracy. Additionally, most of these tools do not operate in real time, meaning that simulating just one second of real-time behaviour can take several seconds or even minutes. This limitation restricts the scenarios where these tools can be effectively utilised [79]. In cases where precise models are unavailable or the risk of generating inaccurate results could lead to serious and costly consequences, alternative tools may be necessary.

Real-Time Simulations

Real-time simulation tools utilise high-performance parallel computation to simulate power system models at near real-time speeds. This capability allows for interfacing the model with external hardware devices in a setup known as Hardware-in-the-loop (HIL) simulation. Several commercial tools provide this functionality, including the Real-Time Digital Simulator (RTDS*) developed by RTDS Technologies and Real-Time Lab (RT-LAB) created by OPAL-RT. Some applications of real-time simulations include:

- Testing Control and Protection Systems: The ability to interface hardware and software is advantageous for evaluating the behaviour of devices, such as converter controls or protection systems, before they are deployed in the field. In this context, real-time simulations can closely replicate actual system conditions, providing a more accurate representation of the device under test and its implications for system stability. This methodology has the added benefit of allowing potential issues to be identified and resolved in a testing environment, where making changes is less complicated than in the actual operational environment.
- Large-scale Integration of Renewables: Real-time simulations have been utilised to conduct accurate integration studies for WF and PV projects. For instance, Hydro-Québec employed the Hypersim real-time simulator to assess the integration of 25 wind power plants within a 643-bus model of the Québec power system. The advantage of such a large-scale real-time model extends throughout the lifespan of a project. It can be leveraged in the future to investigate the risks of interactions between the wind farms and the network, as well as converter controls that may be incorporated, possibly through actual hardware implementations of these devices [80].
- Hybrid EMT-RMS Simulations: While large-scale real-time simulations using EMT are beneficial, they require significant computational power, which may not always be available. An alternative approach involves hybrid simulations that combine both

EMT and RMS models, allowing for reduced computational demands. Figure 18 shows a hybrid simulation setup where a detailed representation of the wind park and HVDC system under study is implemented in RTDS®, while the majority of the remaining power system is modelled using RMS. This approach effectively decreases the overall computational power needed.

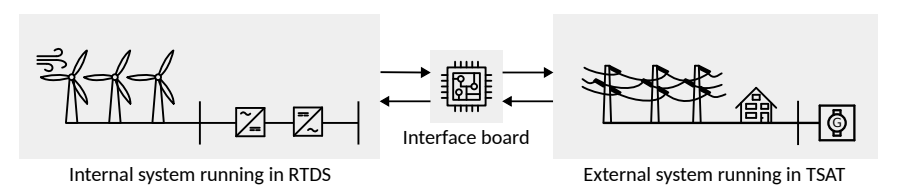


Figure 18: Hybrid RTDS*/RMS simulation setup for wind and HVDC studies [81].

Replicas

Offline EMT models are commonly used for system studies, but they have certain limitations. Onsite updates to controls and protection systems for projects involving power electronic devices may not always be accurately reflected in the offline EMT model. As a result, over the course of a project's lifetime, the model can diverge from the actual system, which compromises the accuracy of system studies that rely on it. Furthermore, the real control and protection systems implemented onsite are often highly complex. To speed up simulations, EMT models may omit certain details present in the actual system, potentially leading to incorrect results.

To address these limitations, real-time simulators have been utilised alongside replicas of control and protection systems for high-fidelity grid simulation. This approach aims to reduce the risks associated with the deployment and operation of new projects. There are two types of control replicas: (a) full replicas, which are exact copies of the installed control panels and include redundancy and auxiliary systems, and (b) study replicas, which replicate the functionality of the actual controls but are significantly less expensive because they lack redundancy and auxiliary systems [82].

Due to the advantages of using replicas and the stability risks associated with power electronic-based devices, system operators around the world have shown interest in acquiring replicas for new projects to incorporate them into their studies. For example, in New Zealand, the HVDC Pole 3 project utilised RTDS® simulations in off-site tests to verify the performance of control and protection systems with a non-redundant set of actual controls [83]. This setup was also intended for future grid studies involving the HVDC link. In Scotland, the National HVDC Centre installed control replicas for the multi-terminal Caithness-Moray HVDC project [82]. Among other benefits, the availability of these replicas enabled the testing of whether converters from different vendors could operate as part of a single HVDC network while still protecting the intellectual property of each vendor. In France, the transmission system operator RTE created the SMARTE laboratory in 2011 for real-time simulations to address the challenges associated with modelling and simulating the increasing number of power electronic devices in the grid [9]. As of 2018, this laboratory contained nine replicas of SVC and HVDC projects. A notable instance of a study where these replicas were used occurred during the analysis of a harmonic instability event involving the INELFE HVDC link in 2015. The behaviour during the event could not be reproduced using the EMT models provided by the manufacturer [9]. Oscillations were detected only when replicas were employed in a HIL setup, as illustrated in Figure 19.

Although replicas have gained popularity in HVDC projects, they are also utilised for

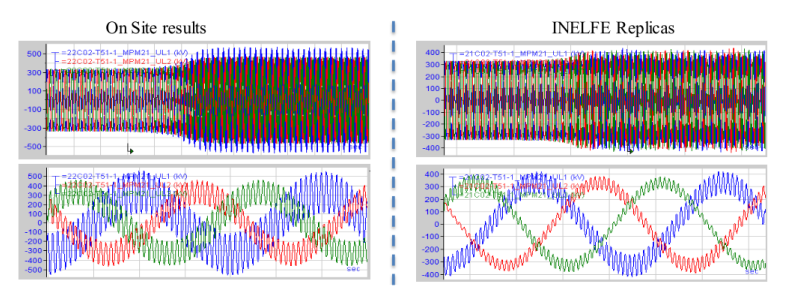


Figure 19: Simulation results using replicas to reproduce the 2015 INELFE HVDC link incident [9].

other types of power electronic devices within the grid. For example, the Korean system operator obtained a control replica of a thyristor-controlled series compensator (TCSC), and their experience is detailed in [84]. Similarly, the transmission operator FURNAS in Brazil describes their experience in [85] regarding the installation of a control replica for an SVC project and development of system studies based on it. Some of the benefits of using control replicas are:

- Network Integration: Replicas can be utilised alongside detailed models of the network and other surrounding power electronic devices to conduct system-wide interaction studies. However, the supplier may not perform this detailed integration study and might rely on simplified AC network models [82].
- Operation: Replicas provide system operators with an accurate model that can be
 trusted to deliver reliable results for future testing and studies. This reliability is
 particularly important given that the grid is continuously evolving and the risk of
 unexpected interactions is increasing with the addition of more power electronic
 devices.
- Commissioning Tests: Replicas enable system operators to offer support during the commissioning process. This includes conducting tests prior to onsite commissioning to anticipate expected behaviour and provide recommendations.
- Operator Training: Replicas can be employed for training control room operators, allowing for hands-on experience where operators can interact with a real-time simulation and immediately observe the effect of their actions. This enhances their confidence and practical knowledge.

1.4 Model Order Reduction

Recent stability issues arising from the integration of power electronic converters into the grid have led to several challenges regarding the models and modelling frameworks necessary for accurately assessing stability risks. Key questions include: how should the system be modelled to effectively represent these new issues? Additionally, how should the modelling of traditional stability categories, namely rotor-angle, voltage, and frequency stability, be revised to properly account for the behaviour of converters?

To address these questions, *Model Order Reduction (MOR)* emerges as a valuable technique for determining the appropriate level of detail required in models for different types of studies. It offers systematic methods to simplify high-dimensional models while preserving their essential dynamic characteristics, leading to significant improvements

in computational efficiency. By focusing on the most relevant aspects of the system and eliminating or simplifying components that are not crucial to the study, MOR methods manage to reduce computational costs while maintaining the accuracy necessary for simulating the phenomena of interest. The accuracy of the results depends on careful selection of which system components should be represented by detailed models.

MOR methods can be classified into two main categories: Singular Value Decomposition (SVD)-based and Krylov-subspace-based approaches [86]. The SVD-based methods originated from the singular value decomposition operation defined in Appendix D. The singular values are then used to determine how to find a reduced-order approximation for a model. This method can ensure that the approximation error remains within an upper bound. However, its main disadvantage is the computational complexity, which can be prohibitive [87]. Krylov-subspace methods, on the other hand, are based on the moment matching of the impulse response of a system [86]. However, the approximation error is not guaranteed to be bound.

The remainder of this section will provide an overview of the applications of MOR in power systems.

Control Design

When designing control systems and evaluating their impact on the surrounding power system, it can be advantageous to use a reduced-order model to speed up simulations and allow for efficient evaluation of the system's response to control parameter changes.

An example of effort in this direction is a parametric MOR method proposed in [88], which can preserve selected parameters in the reduced-order model. The method consists of selecting device parameters to be preserved in the reduced-order model. Thus, it facilitates tasks such as control design because the reduced model does not need to be recalculated whenever the parameters change. The method divides the system into an internal system containing all the selected parameters and an external system that is reduced using an implementation of the balanced truncation method. The paper successfully demonstrated the method for preserving the parameters of PSSs.

Similarly, in [89], the authors propose a model reduction technique based on cross-Gramians to achieve the online tuning of PSSs to reduce inter-area oscillations. A reduced model reduces the time and computational effort to perform online PSS tuning.

System Identification

Typical model reduction techniques require the availability of a full-order model to which the method is applied to obtain a simplified model. System identification techniques, however, allow the derivation of a reduced model based on measurements or simulation data obtained from black-box models.

An example of such use is provided in [90], where the authors propose a system identification and model reduction framework based on the Loewner matrix that can be applied to available frequency response data. Another system identification method is proposed [91] to obtain reduced-order models from Phasor Measurement Unit (PMU) measurements while preserving the identity of selected buses from the full-order model.

Synchronous Generator Coherency

Coherence of a synchronous generator is a property whereby two or more generators present the same or a very similar rotor angle response to a disturbance. This allows the grouping of several generators, resulting in model simplifications. Coherency-based reduction methods have long been popular among power utilities [92].

For example, in [93], the authors present a model reduction technique that leverages the relationship between generator synchrony and the lack of observability and controllability of states associated with the generators. The method allows for the reduction of the order of a model based on the synchrony of generators with respect to a selected mode.

Another instance of such an application is highlighted in [94], where the authors propose a method for identifying generator coherency linked to slow oscillatory modes, which is subsequently applied in dynamic model reduction. This method is based on the normalised cuts approach used for graph segmentation.

Large-Scale Simulations

Numerous model reduction techniques aim to enhance the computational speed of large-scale simulations, particularly in time-domain applications. One widely used method is modal truncation, which applies exclusively to linear systems. This technique reduces the system's order by decomposing the original system into modal components and discarding certain modes. A critical step in this process is deciding which modes to retain and which to remove. Various strategies exist for this selection, including analysing the time constants associated with each mode. For example, modes with rapid time constants can be eliminated, resulting in a system that focuses primarily on slower dynamics. The concept of model reduction through modal decomposition using participation factors was first introduced in [95].

Another technique that targets the physical interpretability of reduced models, inspired by the balanced truncation method, uses the projection of the Hankel Singular Values (HSVs) to measure the importance of the original state variables in the system's input-output behaviour. Additionally, a method has been developed that goes beyond offline models. This model reduction technique, based on measurement data, retains the physical interpretability of key selected parameters [96].

In scenarios where a power system can be divided into a detailed study area and an external area requiring a simplified model, structured model reduction becomes particularly relevant. In [97], a structured model reduction that preserves the network topology is proposed. This approach extends the balanced truncation method by dividing the system into subsystems. In this method, the subsystem that retains the network structure remains unchanged, while the others are individually reduced. Another technique, introduced by [92], employs coherent clustering balanced truncation. This approach partitions the entire system into three areas: a study area, a buffer area, and an external area. The buffer and external areas are subsequently divided into clusters, with each cluster undergoing reduction through balanced truncation.

Some MOR methods have been specifically developed for converter-dominated systems. For instance, in [98], a model reduction strategy is presented that relies on state residualisation. This method identifies connections between states and modes, facilitating the creation of a reduced model by eliminating groups of states, while minimising the error. However, this technique is not automatic, meaning that identifying closely coupled eigenvalues and states can be a manual and time-consuming task, especially in large systems. Another example is a strategy for deriving reduced-order models for Multi-Terminal DC (MTDC) grids proposed in [99]. This method employs an Interactive Rational Krylov algorithm, applied individually to each wind farm connected to the MTDC grid in the study area. However, this study does not address other grid configurations.

Lastly, most MOR methods rely on reducing the order of the system by neglecting certain state variables and excluding them from the state-space equations. An alternative approach to achieving computational efficiency is to approximate the system matrix with a

sparser matrix as proposed in [100]. Since matrix sparsity impacts the speed of calculations, this leads to improved computational efficiency.

Summary

Given the numerous MOR methods that find application in power systems, Table 5 summarises those that can be used to guide decisions on the modelling details necessary for an accurate assessment of different aspects of power system stability.

Table 5: Comparison of selected model reduction methods in power systems.

Method	Advantages	Disadvantages
Modal truncation based on participation factors [95]	Simple, widely used, clear physical interpretation	Requires manual selection of relevant modes
State importance ranking via HSV projection [101]	Clear state ranking, retains interpretability	No guarantee of stability preservation
Subsystem-based structure-preserving balanced truncation [97]	Maintains physical meaning of study area, preserving network structure	Requires dividing the system into study and external areas
Data-Driven Reduction preserving physical parameters [96]	Strong physical interpretability, practical for parameter sensitivity	Limited by available data, requires preselection of modes
State residualisation based on state-mode associations [98]	Preserves physical interpretability	Requires manual identification of groups of coupled modes and states
Krylov subspace method for MTDC grid components [99]	Efficient for MTDC grids, tailored to specific applications	Limited generalizability, complex setup for diverse systems

1.5 Conclusion

The increasing number of power-electronic converters has altered the dynamic behaviour of power systems and introduced new challenges in stability assessment. One challenge involves the emergence of new categories of stability issues and how to effectively model them. Another challenge is determining how to accurately account for the dynamic behaviour of converters within the traditional stability categories, which include rotor angle, voltage, and frequency stability. Addressing these questions requires a reevaluation of existing modelling guidelines and stability analysis tools. Although efforts are underway to tackle these issues, the selection of appropriate models and tools for various stability studies remains complex and uncertain. This complexity is expected to intensify in the future due to the gradual phasing out of synchronous generators, the rise of converter-interfaced

generation, and the increasing use of HVDC for interconnections.

The chapter began by examining the newly recognised stability categories in converter-dominated power systems, specifically converter-driven stability and resonance stability. It provided a review of different phenomena associated with these categories and presented examples of real-life instability events. The chapter then analysed the most widely adopted models for generators, transmission lines, loads, and converters, emphasising the assumptions and simplifications that impact accuracy in dynamic studies.

The chapter then reviewed the simulation tools currently used for stability assessment, evaluating their capabilities and inherent limitations. It concluded by introducing MOR techniques applied to power systems, highlighting their potential as tools for determining the appropriate level of detail needed in models for various types of studies.

In Chapter 2, the fundamentals of model order reduction will be introduced, with particular focus on the balanced truncation method. This technique is essential for guiding modelling simplifications in order to enhance computational efficiency without compromising dynamic stability accuracy.

2 Model Order Reduction through Balanced Truncation

This chapter introduces the fundamentals of model order reduction, with particular focus on the balanced truncation method as a promising approach for addressing the challenges associated with modelling and simulation of converter-dominated power systems. MOR methods aim to reduce computational costs while maintaining accuracy in the simulation of relevant phenomena by eliminating or simplifying parts of the system that are not essential to the study at hand. The accuracy of the results depends on appropriately choosing which system components should be represented using detailed models.

These techniques offer systematic approaches to simplify high-dimensional models while preserving their essential dynamic characteristics, significantly improving computational efficiency. Among them, balanced truncation stands out as an established and widely adopted method, providing a criterion for identifying and eliminating states with minimal impact on system dynamics.

The chapter begins by introducing key concepts and foundational theory underlying model order reduction. It then discusses the concepts of controllability, observability and minimal realisation theory, which guide the development of exact reduced-order models. The balanced truncation methodology is subsequently explained, and the chapter concludes with a case study of a VSC system, demonstrating the method's applicability while also highlighting its limitations in providing practical modelling guidelines.

2.1 Introduction to Model Order Reduction

This section introduces the foundational theory underlying model order reduction. It starts by addressing the fundamental question of how to mathematically represent a physical system, specifically through the definition of state-space representation applicable to Linear Time-Invariant (LTI) systems. Next, it discusses how to obtain the system's response, outlining essential concepts that will be referenced throughout the chapter. Finally, the section concludes with a formal definition of model order reduction.

2.1.1 State-Space Representation of a Physical System

Consider a high-dimensional physical system with m inputs $\mathbf{u}(t) \in \mathbb{R}^m$ and p outputs $\mathbf{y}(t) \in \mathbb{R}^p$, as illustrated in Figure 20. In addition to these external variables, the system is represented by n internal variables $\mathbf{x}(t) \in \mathbb{R}^n$, known as states. The number of states in the system reflects its dimensionality and characterises its complexity [102].

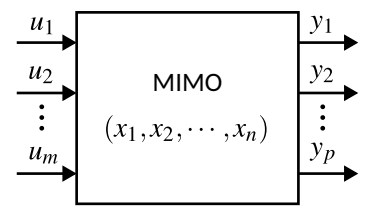


Figure 20: Representation of a Multiple-Input Multiple-Output (MIMO) system showing system inputs and outputs.

Assuming this system is LTI, the relationship among inputs, outputs, and states is governed by differential equations and can be represented in a generic form known as the

state-space representation:

$$\dot{\mathbf{x}}(t) = \mathbf{A}\mathbf{x}(t) + \mathbf{B}\mathbf{u}(t),\tag{50}$$

$$\mathbf{y}(t) = \mathbf{C}\mathbf{x}(t) + \mathbf{D}\mathbf{u}(t), \tag{51}$$

where $\mathbf{A} \in \mathbb{R}^{n \times n}$, $\mathbf{B} \in \mathbb{R}^{n \times m}$, $\mathbf{C} \in \mathbb{R}^{p \times n}$ and $\mathbf{D} \in \mathbb{R}^{m \times m}$ are the state-space matrices.

2.1.2 System Solution

The general solution of the state-space system represented by Equations (50) and (51) can be defined through a few key concepts that will be introduced next. These concepts include the state-transition matrix, the impulse-response matrix, and the transfer function matrix.

State-Transition Matrix

The state-transition matrix, denoted as $\Phi(t,t_0)$ establishes a relationship between the state $\mathbf{x}(t_0)$ of a system at an initial time $\tau=t_0$ to the state $\mathbf{x}(t)$ at a later time $\tau=t$. In the absence of any input, this relationship can be expressed as:

$$\mathbf{x}(t) = \mathbf{\Phi}(t, t_0)\mathbf{x}(t_0). \tag{52}$$

More generally, assuming the system has the initial state $\mathbf{x}(t_0)$ and is subject to an input $\mathbf{u}(t)$, the state-transition matrix can be employed to derive the general solution of the system states as follows:

$$\mathbf{x}(t) = \mathbf{\Phi}(t, t_0)\mathbf{x}(t_0) + \int_{t_0}^t \mathbf{\Phi}(t, \tau)\mathbf{B}\mathbf{u}(\tau)d\tau, \tag{53}$$

where the first term represents the zero-input response, and the second term corresponds to the zero-state response.

For time-invariant systems, the state-transition matrix can be expressed in terms of the state matrix A as:

$$\mathbf{\Phi}(t,t_0) = e^{\mathbf{A}(t-t_0)}. (54)$$

Impulse-Response Matrix

The result presented in Equation (53) illustrates how the system states can be determined at any given time. Likewise, the general solution for the system output needs to be calculated. To achieve this, the concept of the *impulse-response matrix*, represented as $\mathbf{S}(t,t_0)$, is introduced. This matrix reflects the system's response when an impulse signal is applied to each of its inputs. The impulse-response matrix can then be used, along with the state-transition matrix discussed earlier, to compute the output response to a general input through the convolution operation. This is achieved by substituting Equation (53) into Equation (51) [103], resulting in:

$$\mathbf{y}(t) = \mathbf{C}\mathbf{\Phi}(t, t_0)\mathbf{x}(t_0) + \int_{t_0}^t \mathbf{S}(t, \tau)\mathbf{u}(\tau)d\tau + \mathbf{D}\mathbf{u}(t).$$
 (55)

The impulse-response matrix can be calculated directly from the state space parameters and the state-transition matrix [104], as follows:

$$\mathbf{S}(t,\tau) = \begin{cases} \mathbf{C}\mathbf{\Phi}(t,\tau)\mathbf{B}, & t \ge \tau \\ \mathbf{0}, & t < \tau \end{cases}$$
 (56)

For time-invariant systems, and assuming that au=0, the previous expression can be further simplified as:

$$\mathbf{S}(t) = \mathbf{C}e^{\mathbf{A}t}\mathbf{B}.\tag{57}$$

Transfer Function Matrix

The impulse response matrix serves as a clear representation of the relationship between a system's inputs and outputs in the time domain. To analyse this relationship in the frequency domain, the *transfer function matrix*, denoted as $\mathbf{H}(s)$, is utilised. This transfer function is derived from the Laplace transform of the state-space representation of the system [105]. Mathematically, it can be defined as:

$$\mathbf{H}(s) = \mathbf{C}(s\mathbf{I} - \mathbf{A})^{-1}\mathbf{B} + \mathbf{D}.$$
 (58)

By employing these two formulations, it becomes possible to fully characterize the system's response in both the time and frequency domains. The results obtained will be applied later in the analysis.

2.1.3 Formal Problem Definition

Given the high-dimensional state-space realisation of order n described by Equations (50) and (51), the goal of model order reduction is to find an alternative representation of order q such that q < n [87]:

$$\dot{\tilde{\mathbf{x}}}(t) = \tilde{\mathbf{A}}\tilde{\mathbf{x}}(t) + \tilde{\mathbf{B}}\mathbf{u}(t), \tag{59}$$

$$\tilde{\mathbf{y}}(t) = \tilde{\mathbf{C}}\tilde{\mathbf{x}}(t) + \tilde{\mathbf{D}}\mathbf{u}(t),$$
 (60)

where $\tilde{\mathbf{A}} \in \mathbb{R}^{q \times q}$, $\tilde{\mathbf{B}} \in \mathbb{R}^{q \times m}$, $\tilde{\mathbf{C}} \in \mathbb{R}^{p \times q}$ and $\tilde{\mathbf{D}} \in \mathbb{R}^{m \times m}$ and $\mathbf{y}(t)$ are approximately equal.

A reduced-order model is obtained by eliminating or simplifying parts of the system that contribute the least to the system's response while ensuring the results remain within an acceptable error margin. To evaluate the accuracy of the results, it is common practice to compare the full-order model transfer function matrix $\mathbf{H}(s)$ from Equation (58) with the approximate transfer function matrix $\tilde{\mathbf{H}}(s)$ computed using the reduced order system parameters and given by:

$$\tilde{\mathbf{H}}(s) = \tilde{\mathbf{C}}(s\mathbf{I} - \tilde{\mathbf{A}})^{-1}\tilde{\mathbf{B}} + \tilde{\mathbf{D}}.$$
 (61)

A reduced order model is assumed to be accurate when Equation (62) holds for an acceptable value of error ε :

$$\|\mathbf{H}(s) - \mathbf{\tilde{H}}(s)\| < \varepsilon.$$
 (62)

2.2 Theoretical Foundations: Controllability, Observability, and Realisation

In the previous section, model order reduction was introduced as the process of finding a reduced-order representation of a system while ensuring that the error remains within established limits. This section presents the key concepts of *minimal realisation theory*, which allows for obtaining a reduced-order model without any errors by carefully selecting an appropriate coordinate system for the states and eliminating any states that are neither controllable nor observable, if such states exist.

2.2.1 Non-Uniqueness of State Selection

The concept of state is an abstract notion. A state does not necessarily represent a physical quantity, and it is not necessarily measurable or observable. The system states can be regarded as the information about the past history of the system, which is needed to predict how the inputs will affect the system in the future [104]. In other words, knowing

the states at $t = t_0$ and the inputs for $t \ge t_0$ completely determines the future behaviour of the system for $t \ge t_0$ [106].

The values of the state variables in a state vector $\mathbf{x}(t) = \begin{bmatrix} x_1 & x_2 & \cdots & x_n \end{bmatrix}$ can be understood as coordinates in a coordinate system. Consequently, it is possible to choose many different coordinate systems, each leading to a unique state-space representation that models the same physical system. In this context, each of these state-space representations is referred to as a *realisation* of the system described by the impulse-response matrix $\mathbf{S}(t)$.

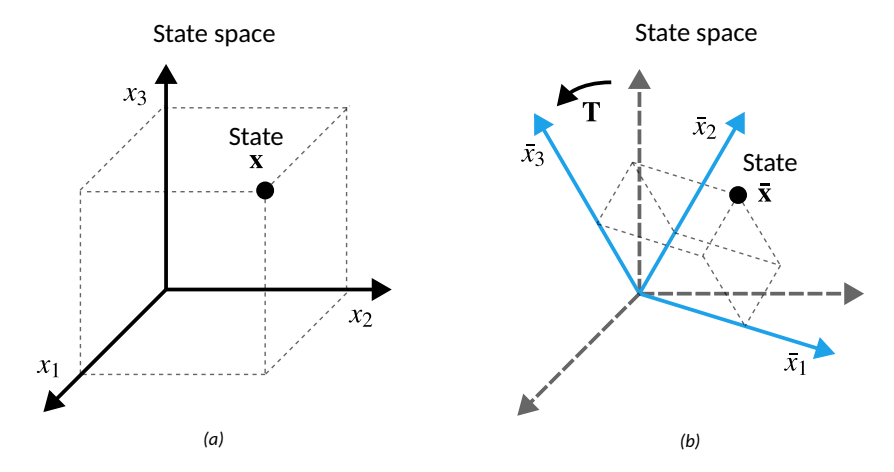


Figure 21: State space, showing a single state represented (a) in the original coordinates x and (b) new coordinates \bar{x} obtained using the transformation T.

Suppose a coordinate transformation $\mathbf{T} \in \mathbb{R}^{n \times n}$ is applied to the original state vector $\mathbf{x}(t)$, yielding a new state vector $\bar{\mathbf{x}}(t)$ in the new coordinate system as illustrated in Figure 21. Mathematically, this is represented as:

$$\bar{\mathbf{x}}(t) = \mathbf{T}\mathbf{x}(t) \tag{63}$$

The state-space representation in the new coordinate system is obtained by substituting $\mathbf{x}(t)$ from Equation (63) into Equations (50) and (51), and is given by:

$$\dot{\bar{\mathbf{x}}}(t) = \bar{\mathbf{A}}\bar{\mathbf{x}}(t) + \bar{\mathbf{B}}\mathbf{u}(t), \tag{64}$$

$$\mathbf{y}(t) = \bar{\mathbf{C}}\bar{\mathbf{x}}(t) + \bar{\mathbf{D}}\mathbf{u}(t), \tag{65}$$

where $\bar{\mathbf{A}} = \mathbf{T}\mathbf{A}\mathbf{T}^{-1}$, $\bar{\mathbf{B}} = \mathbf{T}\mathbf{B}$, $\bar{\mathbf{C}} = \mathbf{C}\mathbf{T}^{-1}$, and $\bar{\mathbf{D}} = \mathbf{D}$.

The new state-space representation $(\bar{A},\bar{B},\bar{C},\bar{D})$ is algebraically equivalent to the original representation (A,B,C,D), meaning that both systems are identical from the perspective of the input-output relationship. Indeed, starting from the transfer function matrix of the new state-space representation and substituting the state-space matrices in the original coordinate system,

$$\mathbf{\bar{H}}(s) = \mathbf{\bar{C}}(s\mathbf{I} - \mathbf{\bar{A}})^{-1}\mathbf{\bar{B}} + \mathbf{\bar{D}},$$
(66)

$$\bar{\mathbf{H}}(s) = \mathbf{C}\mathbf{T}^{-1}(s\mathbf{I} - \mathbf{T}\mathbf{A}\mathbf{T}^{-1})^{-1}\mathbf{T}\mathbf{B} + \mathbf{D},$$
(67)

$$\bar{\mathbf{H}}(s) = \mathbf{C}(s\mathbf{I} - \mathbf{A})^{-1}\mathbf{B} + \mathbf{D},$$
(68)

$$\bar{\mathbf{H}}(s) = \mathbf{H}(s). \tag{69}$$

It is then shown that the transfer function matrices $\mathbf{H}(s)$ and $\bar{\mathbf{H}}(s)$ are equivalent. In other words, the input-output behaviour of the system is independent of the states' coordinate system. If the system is initially represented by a set of states $\mathbf{x}(t)$, it is possible to apply a change of coordinates to represent the states in a new coordinate system without changing the input-output response.

2.2.2 Controllability

Suppose a transformation exists that, when applied to the state-space system represented by Equations (50) and (51), divides the states into two groups, $\mathbf{x}^1(t)$ and $\mathbf{x}^2(t)$, with each group of states forming a subsystem denoted by subsystem 1 and 2, respectively. This is illustrated in Figure 22.

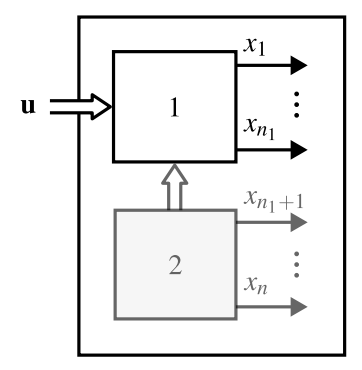


Figure 22: Representation of a system containing a controllable and an uncontrollable group of states [104].

Mathematically, the resulting state-space representation would be given by:

$$\frac{d}{dt} \begin{bmatrix} \mathbf{x}^{1}(t) \\ \mathbf{x}^{2}(t) \end{bmatrix} = \begin{bmatrix} \mathbf{A}^{11} & \mathbf{A}^{12} \\ \mathbf{0} & \mathbf{A}^{22} \end{bmatrix} \begin{bmatrix} \mathbf{x}^{1}(t) \\ \mathbf{x}^{2}(t) \end{bmatrix} + \begin{bmatrix} \mathbf{B}^{1} \\ \mathbf{0} \end{bmatrix} \mathbf{u}(t), \tag{70}$$

$$\mathbf{y}(t) = \begin{bmatrix} \mathbf{C}^1 & \mathbf{C}^2 \end{bmatrix} \begin{bmatrix} \mathbf{x}^1(t) \\ \mathbf{x}^2(t) \end{bmatrix} + \mathbf{D}\mathbf{u}(t). \tag{71}$$

While the states $\mathbf{x}^1(t)$ in subsystem 1 are affected by both the inputs $\mathbf{u}(t)$ and the states $\mathbf{x}^2(t)$ in subsystem 2, the second subsystem is structured in such a way that its states $\mathbf{x}^2(t)$ cannot be affected either by the inputs $\mathbf{u}(t)$ or by subsystem 1. Therefore, it is said that the states $\mathbf{x}^2(t)$ are uncontrollable and its dynamics will depend solely on the initial conditions $\mathbf{x}^2(0)$. If it is not possible to find such a transformation, the system $(\mathbf{A},\mathbf{B},\mathbf{C},\mathbf{D})$ is said to be completely controllable [104].

2.2.3 Observability

Similarly, suppose it is possible to find a transformation that divides the states into two groups, $\mathbf{x}^1(t)$ and $\mathbf{x}^2(t)$, creating two subsystems as illustrated in Figure 23.

The resulting system would be represented in state-space form as:

$$\frac{d}{dt} \begin{bmatrix} \mathbf{x}^{1}(t) \\ \mathbf{x}^{2}(t) \end{bmatrix} = \begin{bmatrix} \mathbf{A}^{11} & \mathbf{0} \\ \mathbf{A}^{21} & \mathbf{A}^{22} \end{bmatrix} \begin{bmatrix} \mathbf{x}^{1}(t) \\ \mathbf{x}^{2}(t) \end{bmatrix} + \begin{bmatrix} \mathbf{B}^{1} \\ \mathbf{B}^{2} \end{bmatrix} \mathbf{u}(t), \tag{72}$$

$$\mathbf{y}(t) = \begin{bmatrix} \mathbf{C}^1 & \mathbf{0} \end{bmatrix} \begin{bmatrix} \mathbf{x}^1(t) \\ \mathbf{x}^2(t) \end{bmatrix} + \mathbf{D}\mathbf{u}(t). \tag{73}$$

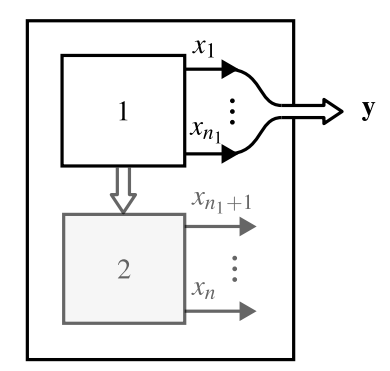


Figure 23: Representation of a system containing an observable and an unobservable group of states [104].

While the states $\mathbf{x}^1(t)$ of subsystem 1 influence the outputs $\mathbf{y}(t)$ and therefore can be measured or observed from outside the system, the same is not true for system 2. The states $\mathbf{x}^2(t)$ do not directly influence the outputs $\mathbf{y}(t)$ and do not influence system 1. Because changes in these states cannot be observed from outside the system, the states $\mathbf{x}^2(t)$ are said to be unobservable. If such a transformation does not exist, it is said that the system $(\mathbf{A}, \mathbf{B}, \mathbf{C}, \mathbf{D})$ is completely observable [104].

2.2.4 Minimal Realisation

The previous definitions of controllability and observability can be used to define a canonical structure for the state-space representation of the system $(\mathbf{A}, \mathbf{B}, \mathbf{C}, \mathbf{D})$. A transformation exists [104] that divides the system states $\mathbf{x}(t)$ into four mutually exclusive groups $\mathbf{x} = (\mathbf{x}^a, \mathbf{x}^b, \mathbf{x}^c, \mathbf{x}^d)$. These groups define four different subsystems, namely:

- Part (a): Completely controllable but unobservable;
- Part (b): Completely controllable and completely observable;
- Part (c): Uncontrollable and unobservable;
- Part (d): Uncontrollable but completely observable.

The state-space matrices rearranged into the canonical structure are given by:

$$\mathbf{A} = \begin{bmatrix} \mathbf{A}^{aa} & \mathbf{A}^{ab} & \mathbf{A}^{ac} & \mathbf{A}^{ad} \\ 0 & \mathbf{A}^{bb} & 0 & \mathbf{A}^{bd} \\ 0 & 0 & \mathbf{A}^{cc} & \mathbf{A}^{cd} \\ 0 & 0 & 0 & \mathbf{A}^{dd} \end{bmatrix}, \tag{74}$$

$$\mathbf{B} = \begin{bmatrix} \mathbf{B}^a \\ \mathbf{B}^b \\ 0 \\ 0 \end{bmatrix}, \tag{75}$$

$$\mathbf{C} = \begin{bmatrix} 0 & \mathbf{C}^b & 0 & \mathbf{C}^d \end{bmatrix}. \tag{76}$$

Minimal realisation theory states that the impulse-response matrix of the system will depend only on the parameters of the completely controllable and completely observable

Part (b) of the system [104], that is,

$$\mathbf{S}(t,\tau) = \mathbf{C}^b \mathbf{\Phi}^{bb}(t,\tau) \mathbf{B}^b,\tag{77}$$

where $\mathbf{\Phi}^{bb}(t,\tau)$ is the state transition matrix corresponding to \mathbf{A}^{bb} .

This result is significant because it demonstrates that the original system representation $(\mathbf{A},\mathbf{B},\mathbf{C},\mathbf{D})$ can be reduced to $(\mathbf{A}^{bb},\mathbf{B}^{b},\mathbf{C}^{b},\mathbf{D})$ while still accurately capturing the system's input-output behaviour. This reduction limits the number of states needed to describe the system dynamics from $\mathbf{x}(t)$ to $\mathbf{x}^{b}(t)$, thus reducing the order of the representation. The reduced-order representation is a minimal order realisation of the system and is algebraically equivalent to $(\mathbf{A},\mathbf{B},\mathbf{C},\mathbf{D})$. Additionally, from another perspective, if a system realisation is both controllable and observable and no transformation exists that separates the states into uncontrollable or unobservable parts, then it qualifies as a minimal realisation [105].

Figure 24 illustrates minimal realisation theory using a simple third-order system. The system is initially represented by three state variables, x_1 , x_2 and x_3 , as shown in Figure 24 (a). In the same figure, it can be observed that among all possible states in the state space, only a limited subset, highlighted in blue, is both controllable and observable. Furthermore, this set of controllable and observable states lies on a plane, indicating that they can be represented in two dimensions rather than the original three-dimensional representation. Consequently, through an appropriate transformation that yields new state variables \overline{x}_1 and \overline{x}_2 , it is possible to reduce the state representation to a second-order system, as depicted in Figure24 (b).

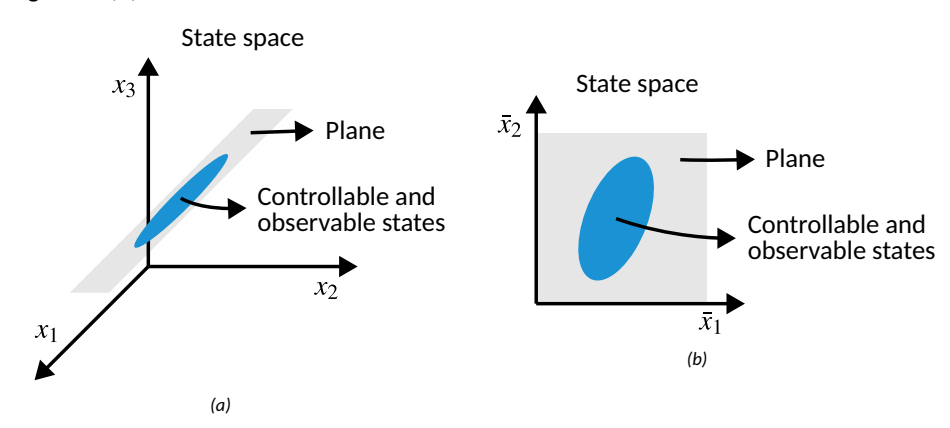


Figure 24: State space containing a set of controllable and observable states represented in (a) third-order state space with coordinates $\mathbf{x} = \begin{bmatrix} x_1 & x_2 & x_3 \end{bmatrix}$ and (b) reduced second-order state space with coordinates $\mathbf{\bar{x}} = \begin{bmatrix} \bar{x}_1 & \bar{x}_2 \end{bmatrix}$.

2.3 Balanced Truncation Method

The previous section defined the concepts of controllability and observability, highlighting that the number of controllable and observable states within a system is influenced by the choice of coordinate system. These concepts were treated as discrete properties, meaning a state is either controllable and observable or it is not. The insights gained from this analysis enabled an exact model reduction based on minimal realisation theory.

This section shifts the focus to controllability and observability as quantifiable properties. This perspective enables not only the determination of whether a state is controllable

or observable but also the measurement of its degree of controllability and observability along a continuum. To begin, the concepts of input-to-state and state-to-output maps will be introduced, followed by the derivation of the Gramians, which serve as metrics for measuring controllability and observability. A geometrical interpretation of these properties will also be provided. Finally, the section will present the balanced truncation method, which generates an approximate realisation of a model within a specified error bound.

2.3.1 Impulse-Response Matrix and its Decomposition

To quantify the controllability and observability, the first step is to decompose the system's impulse-response matrix $\mathbf{S}(t)$, which characterises its input-output behaviour into two parts: an *input-to-state map* $\mathbf{X}(t)$ and a *state-to-output map* $\mathbf{Y}(t)$ as shown in Figure 25. It is considered that the input $\mathbf{u}(t) = \boldsymbol{\delta}(t)$ causes the state $\mathbf{x}(t)$ while the initial conditions $\mathbf{x}(0)$ cause the output $\mathbf{y}(t) = \mathbf{Y}(t)\mathbf{x}(0)$ [86].

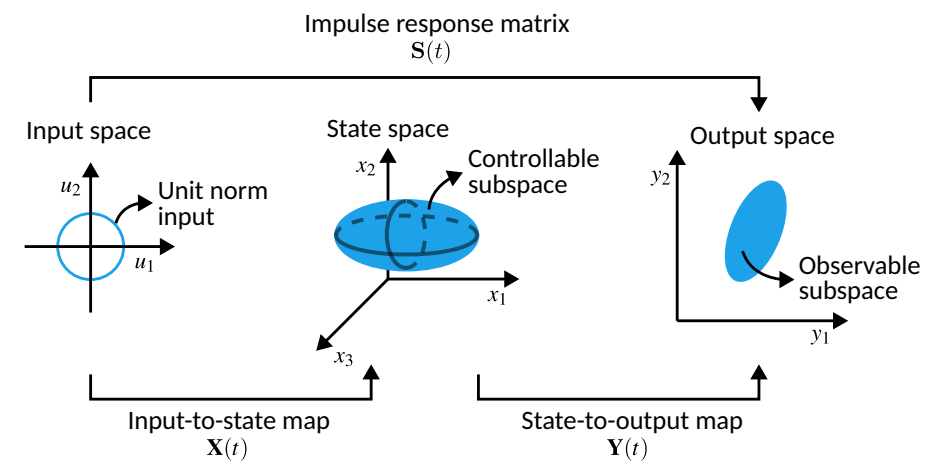


Figure 25: Diagram showing impulse response matrix decomposition for a system with 2 inputs, 2 outputs, and 3 state variables.

For this purpose, consider the modified model of the system originally described by Equations (50) and (51). To facilitate the analysis, it is assumed that $\mathbf{D} = \mathbf{0}$. Additionally, a test input vector $\mathbf{d}(t)$ is included in the state equation to help verify the observability of the system, leading to the following representation:

$$\dot{\mathbf{x}}(t) = \mathbf{A}\mathbf{x}(t) + \mathbf{B}\mathbf{u}(t) + \mathbf{d}(t), \tag{78}$$

$$\mathbf{y}(t) = \mathbf{C}\mathbf{x}(t). \tag{79}$$

The main goal of the following development is to use a test signal, which is chosen as the impulse function $\delta(t)$, to characterise the controllable and observable subspaces. Based on this information, it will be possible to determine the minimal realisation of the system. Note that other scalar functions, such as the unit step, could have been selected as test signals [107].

Suppose a sequence of impulses is applied as an input $\mathbf{u}(t) = \boldsymbol{\delta}(t)$ and the respective state responses are measured as indicated in Figure 26. It is proved in [107] that the set $\mathbf{X}(t)$ of all functions corresponding to the state responses, also known as input-to-state map, is given by:

$$\mathbf{X}(t) = e^{\mathbf{A}t}\mathbf{B}.\tag{80}$$

Using this test system, it is possible to determine the controllable subspace \mathcal{X}_c , which consists of all possible state responses of the model to the input test signals. In mathematical terms, \mathcal{X}_c is determined as the subspace of least dimension that contains the image of $\mathbf{X}(t)$.

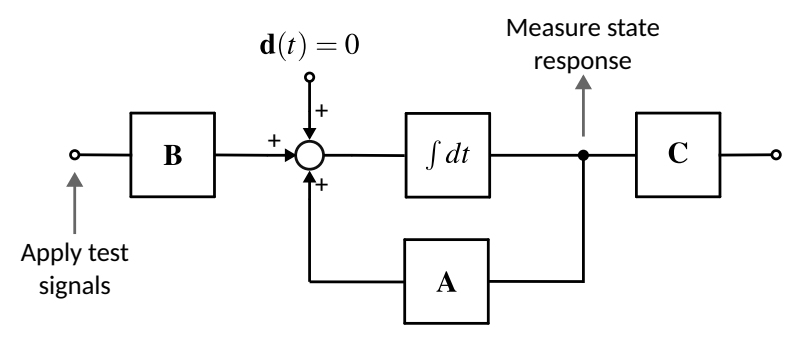


Figure 26: Signal injection test for characterizing the controllable subspace [107].

Similarly, suppose a sequence of impulses is applied to the test point indicated in Figure 27 such that $\mathbf{d}(t) = \boldsymbol{\delta}(t)$. The set $\mathbf{Y}(t)$ of all output responses to the test signals, also known as state-to-output map, is given by:

$$\mathbf{Y}(t) = \mathbf{C}e^{\mathbf{A}t}. ag{81}$$

Based on this test, it is possible to determine the observable subspace \mathcal{X}_o , which is defined as the subspace of least dimension containing the image of $\mathbf{Y}^*(t)$.

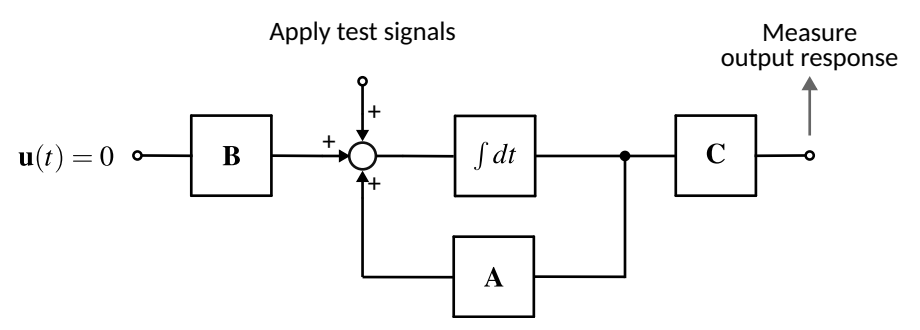


Figure 27: Signal injection test for characterizing the observable subspace [107].

2.3.2 Controllability and Observability Gramians

The input-to-state $\mathbf{X}(t)$ and state-to-output $\mathbf{Y}(t)$ maps can be used to characterise and quantify the controllability and observability of a system by utilising a new operation introduced in this section.

Let $\mathbf{F}(t)$ be a piecewise continuous map $\mathbb{R} \to \mathbb{R}^{n \times m}$. $\mathbf{F}(t)$ can be regarded as a set of n signals, where each signal is represented by a vector involving m variables as follows:

$$\mathbf{F}(t) = \begin{bmatrix} \mathbf{f}^{1}(t) \\ \mathbf{f}^{2}(t) \\ \vdots \\ \mathbf{f}^{n}(t) \end{bmatrix}, \tag{82}$$

where $\mathbf{f}^i(t) = \begin{bmatrix} f^{i1}(t) & f^{i2}(t) & \cdots & f^{im}(t) \end{bmatrix}$ is a row vector of functions corresponding to the *i*-th signal.

An operation known as Gramian and denoted by \mathbf{W}^2 can be defined for $\mathbf{F}(t)$ over the time interval $[t_1, t_2]$. Mathematically, this is represented as [107]:

$$\mathbf{W}^2 = \int_{t_1}^{t_2} \mathbf{F}(t) \mathbf{F}^*(t) dt. \tag{83}$$

Substituting Equation (82) into (83), the Gramian definition can be expanded and rewritten in matrix form as:

$$\mathbf{W}^{2} = \begin{bmatrix} \langle \mathbf{f}^{1}(t), \mathbf{f}^{1}(t) \rangle & \langle \mathbf{f}^{1}(t), \mathbf{f}^{2}(t) \rangle & \cdots & \langle \mathbf{f}^{1}(t), \mathbf{f}^{n}(t) \rangle \\ \langle \mathbf{f}^{2}(t), \mathbf{f}^{1}(t) \rangle & \langle \mathbf{f}^{2}(t), \mathbf{f}^{2}(t) \rangle & \cdots & \langle \mathbf{f}^{2}(t), \mathbf{f}^{n}(t) \rangle \\ \vdots & \vdots & & \vdots \\ \langle \mathbf{f}^{n}(t), \mathbf{f}^{1}(t) \rangle & \langle \mathbf{f}^{n}(t), \mathbf{f}^{2}(t) \rangle & \cdots & \langle \mathbf{f}^{n}(t), \mathbf{f}^{n}(t) \rangle \end{bmatrix},$$
(84)

where $\langle \mathbf{f}^i(t), \mathbf{f}^j(t) \rangle$ is the inner product of the vectors $\mathbf{f}^i(t)$ and $\mathbf{f}^j(t)$.

The matrix elements where i = j in Equation (84) carry a special relevance since the inner product $\langle \mathbf{f}^i(t), \mathbf{f}^i(t) \rangle$ denotes the energy of the signal $\mathbf{f}^i(t)$ and it is defined as:

$$E = \langle \mathbf{f}^{i}(t), \mathbf{f}^{i}(t) \rangle = \int_{t_{1}}^{t_{2}} \|\mathbf{f}^{i}(t)\| dt.$$
(85)

Thus, the total energy in the signal set $\mathbf{F}(t)$ over the interval $[t_1,t_2]$ can be calculated by summing up all the elements in the diagonal of the Gramian \mathbf{W}^2 as illustrated in Figure 28. Mathematically, this corresponds to:

$$\int_{t_1}^{t_2} \|\mathbf{F}(t)\|_F^2 dt = \text{tr}\left(\int_{t_1}^{t_2} \mathbf{F}(t) \mathbf{F}^*(t) dt\right),\tag{86}$$

where $tr(\cdot)$ represents the trace operation, consisting of the sum of all elements on the main diagonal of a square matrix.

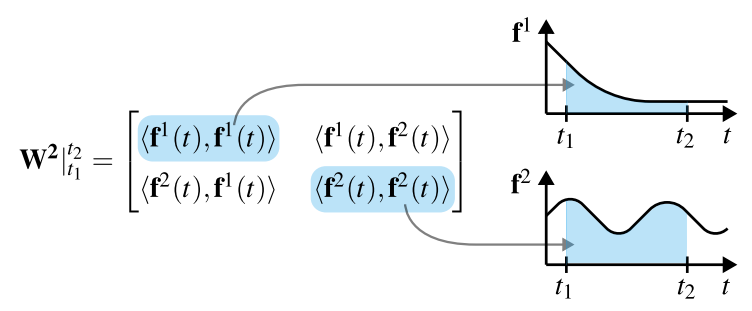


Figure 28: Relationship between Gramian matrix entries of a signal set $\mathbf{F}(t) = \begin{bmatrix} \mathbf{f}^{1}(t) & \mathbf{f}^{2}(t) \end{bmatrix}^{T}$ and the signal energy.

It is possible to define the concepts of controllability and observability Gramians by applying the Gramian definition from Equation (83) to the input-to-state $\mathbf{X}(t)$ and state-to-output $\mathbf{Y}(t)$ maps, respectively [86]. Mathematically, the controllability Gramian \mathcal{P} can be calculated from the input-to-state map $\mathbf{X}(t)$ over the time interval $[t_1,t_2]$ as:

$$\mathcal{P} = \sum_{t} \mathbf{X}(t)\mathbf{X}(t)^* = \int_{t_1}^{t_2} e^{\mathbf{A}t} \mathbf{B} \mathbf{B}^* e^{\mathbf{A}^* t} dt.$$
 (87)

Similarly, the observability Gramian Q is calculated from the state-to-output map Y(t) over the time interval $[t_1, t_2]$ as:

$$\mathcal{Q} = \sum_{t} \mathbf{Y}(t)^* \mathbf{Y}(t) = \int_{t_1}^{t_2} e^{\mathbf{A}^* t} \mathbf{C}^* \mathbf{C} e^{\mathbf{A} t} dt.$$
 (88)

If the Gramians are calculated over the interval $[0,\infty)$, they are termed infinite Gramians and denoted by \mathcal{P}_{∞} and \mathcal{Q}_{∞} . In practice, for stable systems, instead of directly solving the integrals in Equations (87) and (88), the Gramians can be calculated by solving a set of two equations known as the *Lyapunov equations* that are written as follows [86]:

$$\mathbf{A}\mathcal{P} + \mathcal{P}\mathbf{A}^* + \mathbf{B}\mathbf{B}^* = 0, \tag{89}$$

$$\mathbf{A}^* \mathbf{Q} + \mathbf{Q} \mathbf{A} + \mathbf{C}^* \mathbf{C} = 0. \tag{90}$$

The system is said to be controllable or observable at every t_0 in $[t_1,t_2]$ if the respective Gramians are nonsingular and therefore invertible [108]. In addition to that, it is possible to quantify how controllable or observable a state is by measuring, respectively, the energy necessary to drive a state to a value or the energy obtained from the states in the output. The controllability Gramian $\mathcal P$ is associated with the minimal input energy $\mathcal E_c$ required to take the states from $\mathbf 0$ to $\mathbf x$ within an amount of time given by t [86]. Mathematically, it is computed as:

$$\mathcal{E}_c^2(\mathbf{x},t) = \mathbf{x}^* \mathcal{P}^{-1} \mathbf{x}. \tag{91}$$

A high value of \mathcal{E}_c indicates that the state is not easily controllable, as it requires more energy to change its value. The minimum energy needed depends on two factors. The first is the target state that must be reached; states that are further away require more energy to reach, and certain directions in the state space may be more challenging to control than others. The second factor influencing the minimum energy is the time t at which the target state must be reached. This time dependence is implicit in Equation (91) and is related to the controllability Gramian \mathcal{P} . One consequence of this relationship is that a larger set of states can be reached with the same input energy if more time is available, as illustrated in Figure 29. Conversely, reaching a state faster requires more energy.

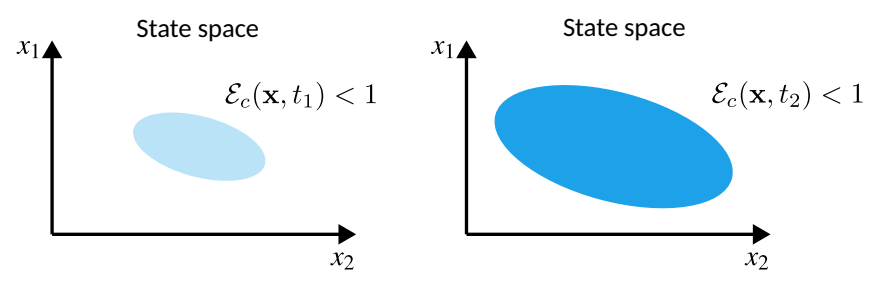


Figure 29: Controllable subspace ellipsoids showing states that are reachable by a unit norm input for $t = t_1$ and $t = t_2$, with $t_2 > t_1$ [109].

Similarly, the observability Gramian Q indicates the maximum amount of energy \mathcal{E}_o obtained from the output caused by the initial condition of a state [86]. The higher the value of \mathcal{E}_o , the more observable a state is. The relationship is given by:

$$\mathcal{E}_o^2(\mathbf{x},t) = \mathbf{x}^* \mathcal{Q} \mathbf{x}. \tag{92}$$

2.3.3 Geometrical Interpretation of Controllability and Observability

The previous discussion emphasised that certain directions within the state space may be more controllable or observable than others. This concept can be further explored by recognising that states with the same level of controllability or observability form an ellipsoid in the state space. The characterisation of this ellipsoid illustrates which directions in the state space are more controllable or observable.

Controllability Characterisation

Considering the input-to-state map $\mathbf{X}(t)$, the image of the unit sphere under this map will provide the set of all points in the state space reachable from the zero-state condition by an input of unit norm. The image of this linear map in the state space will have the form of an ellipsoid as shown in Figure 30 (a), and it represents the set $S_c(\infty)$ of all the states that can be reached with a unit energy input in infinite time [110]. Mathematically,

$$S_c(\infty) = \{ \mathbf{x} \in \mathbb{R}^n ; \mathbf{x}^* \mathcal{P}^{-1} \mathbf{x} \le 1 \}.$$
 (93)

Similar ellipsoids can be obtained, considering the input is applied only for a finite time interval. Since a unit norm input can reach all the states on the ellipsoid's surface, they can be considered equally controllable. However, due to the form of the ellipsoid, some points in the surface representing states will be closer to the origin. This indicates that some directions are more easily reachable than others [111].

The axes of the ellipsoid are determined by applying eigendecomposition to the controllability Gramian and determining its eigenvalues. More information about the eigendecomposition can be found in Appendix C. Let $\lambda_1, \lambda_2, \cdots, \lambda_n$ be the eigenvalues of the controllability Gramian $\mathcal P$ and $\mathbf v_1, \mathbf v_2, \cdots, \mathbf v_n$ its eigenvectors. Based on this transformation, the k-th semi-axis of the controllability ellipsoid is given by $\sqrt{\lambda_k} \mathbf v_k$ [110]. Therefore, the eigenvalues λ_k and eigenvectors $\mathbf v_k$ are said to represent the spatial distribution of the energy in the input-to-state map $\mathbf X(t)$ as illustrated in Figure 30 (a).

Observability Characterisation

A similar analysis can be made considering the state-to-output map $\mathbf{Y}(t)$. The set $S_o(\infty)$ of initial states that result over an infinite time in a unit energy output is given by [110]:

$$S_o(\infty) = \{ \mathbf{x} \in \mathbb{R}^n ; \mathbf{x}^* \mathcal{Q} \mathbf{x} \le 1 \}. \tag{94}$$

Let $\xi_1, \xi_2, \cdots, \xi_n$ be the eigenvalues of the observability Gramian $\mathcal Q$ and $\mathbf w_1, \mathbf w_2, \cdots, \mathbf w_n$ its eigenvectors. Then the k-th semi-axis of the observability ellipsoid is given by $(1/\sqrt{\xi_k})\mathbf w_k$ [110] as illustrated in Figure 30 (b). The directions where the axis is further from the origin represent weekly observable states since a larger state value is needed to produce the same unitary output. This is opposite to the controllability ellipsoid, where the major axis represents strongly controllable states.

2.3.4 Method Description

The controllability and observability Gramians measure how controllable or observable a state is. However, if a state is found to be poorly controllable or observable, no conclusion can be made regarding its contribution to the system's input-output behaviour. This is because a state with low controllability might be highly observable or vice versa. A system where the states have different levels of controllability and observability that do not necessarily match is called *unbalanced*. This situation is illustrated in Figure 31.

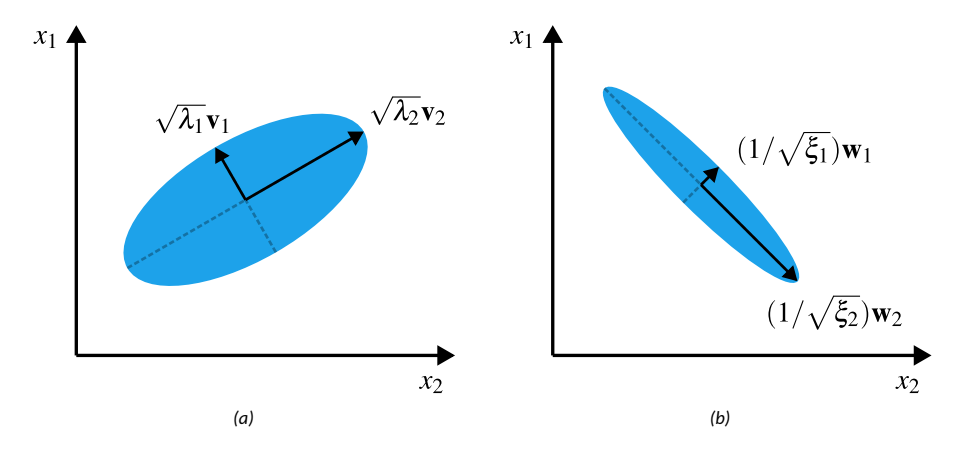


Figure 30: State space containing ellipsoids representing (a) a controllable and (b) an observable subspace with axes characterised by their eigenvalues and eigenvectors.

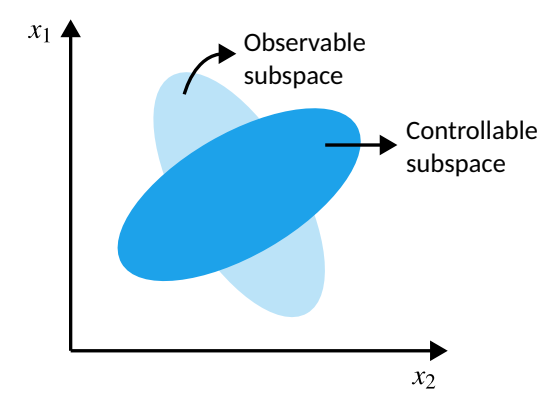


Figure 31: Controllable and observable subspaces for an unbalanced system [105].

The balanced truncation method transforms the state space representation into a balanced system by finding a coordinate transformation T_b such that:

$$\mathbf{x_b} = \mathbf{T_b}\mathbf{x},\tag{95}$$

where x_b is the state vector within the balanced coordinate system, and x indicates the state vector in the original coordinate system.

In the balanced coordinate system, the Gramians are diagonal and equal to the Hankel matrix Σ^2 . Additionally, their diagonal elements represent singular values σ_k referred to as the *Hankel Singular Values* (*HSVs*) [112]. This relationship can be expressed as follows:

$$\mathcal{P}_{\mathbf{b}} = \mathcal{Q}_{\mathbf{b}} = \mathbf{\Sigma}^2 = \operatorname{diag}(\sigma_k).$$
 (96)

This establishes a direct one-to-one correspondence between the HSV and the states in the balanced realisation. For brevity, details on computing T_b are not included, but further information can be found in [86].

Assuming $\mathbf{D} = \mathbf{0}$ for simplicity, the state-space representation from Equations (50) and

(51) can now be realised as:

$$\dot{\mathbf{x}}_{\mathbf{b}}(t) = \mathbf{A}_{\mathbf{b}}\mathbf{x}_{\mathbf{b}}(t) + \mathbf{B}_{\mathbf{b}}\mathbf{u}(t), \tag{97}$$

$$\mathbf{y}(t) = \mathbf{C_b} \mathbf{x_b}(t), \tag{98}$$

where $\mathbf{A_b} = \mathbf{T_b} \mathbf{A} \mathbf{T_b}^{-1}$, $\mathbf{B_b} = \mathbf{T_b} \mathbf{B}$ and $\mathbf{C_b} = \mathbf{C} \mathbf{T_b}^{-1}$.

This balanced realisation can be divided into two interconnected subsystems by rearranging the state variables $\mathbf{x_b}$ such that the singular values of Σ are non-increasing, that is, $\sigma_1 \geq \sigma_2 \geq \ldots \geq \sigma_n \geq 0$. Mathematically,

$$\begin{bmatrix} \dot{\mathbf{x}}_{\mathbf{b}}^{1}(t) \\ \dot{\mathbf{x}}_{\mathbf{b}}^{2}(t) \end{bmatrix} = \begin{bmatrix} \mathbf{A}_{\mathbf{b}}^{11} & \mathbf{A}_{\mathbf{b}}^{12} \\ \mathbf{A}_{\mathbf{b}}^{21} & \mathbf{A}_{\mathbf{b}}^{22} \end{bmatrix} \begin{bmatrix} \mathbf{x}_{\mathbf{b}}^{1}(t) \\ \mathbf{x}_{\mathbf{b}}^{2}(t) \end{bmatrix} + \begin{bmatrix} \mathbf{B}_{\mathbf{b}}^{1} \\ \mathbf{B}_{\mathbf{b}}^{2} \end{bmatrix} \mathbf{u}(t), \tag{99}$$

$$\mathbf{y}(t) = \begin{bmatrix} \mathbf{C_b}^1 & \mathbf{C_b}^2 \end{bmatrix} \begin{bmatrix} \mathbf{x_b}^1(t) \\ \mathbf{x_b}^2(t) \end{bmatrix}. \tag{100}$$

An approximation of the system can be obtained based on the fact that the Hankel matrix Σ^2 is nearly singular; that is, some of the HSVs are approximately zero. Since system order is determined by the number of nonzero singular values of the Hankel matrix [107], an approximate lower-order model is obtained by truncating the portion of the system associated with small HSVs.

2.4 Case Study: Voltage Source Converter

This section demonstrates the use of the balanced truncation method to develop reducedorder models for a VSC converter connected to a grid equivalent. The subsequent subsections will cover the model, its implementation, and the results achieved.

2.4.1 Model Description

The case study consists of a 10th order VSC model connected to an equivalent AC network and a constant DC source. Figure 32 illustrates the modelled system. An averaged-value model is used for the VSC according to details provided in [64]. This model represents the converter's AC and DC sides as controlled voltage and current sources at nominal frequency, neglecting the switching harmonics and lower-level controls. It is suitable for representing both two- and three-level VSCs as well as MMCs. The control system consists of active and reactive power controls; decoupled AC current control implemented in dq reference frame including voltage feed-forward filters; and an $\alpha\beta$ -PLL implemented according to [113]. Figure 33 summarises the control structure. A detailed mathematical description of each component of the system follows.

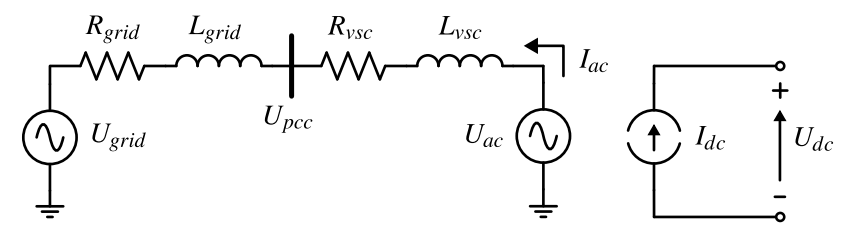
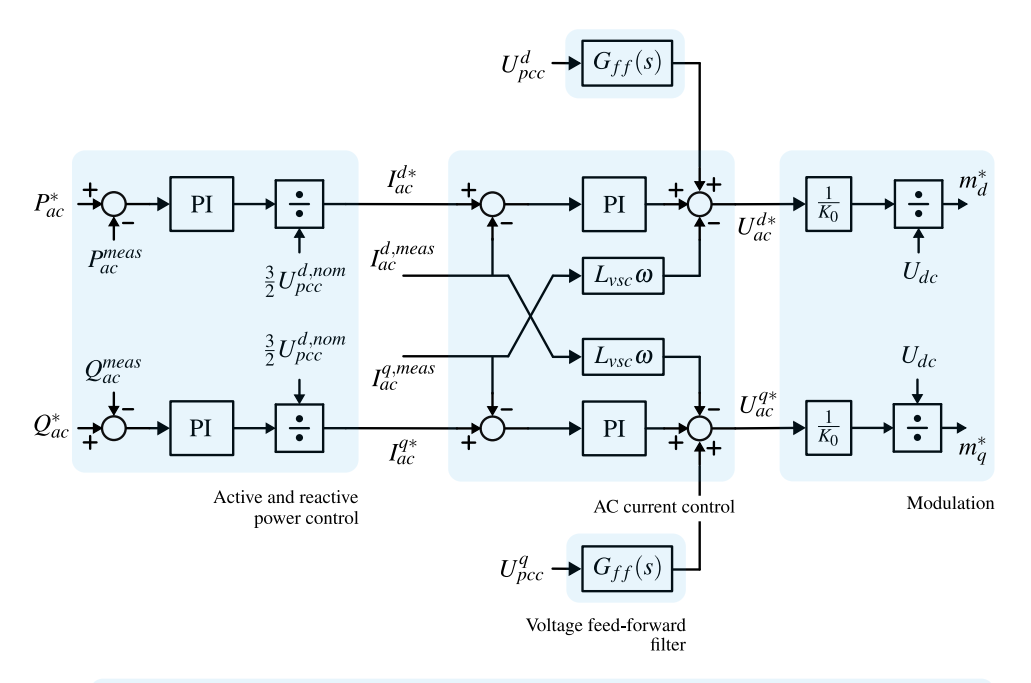
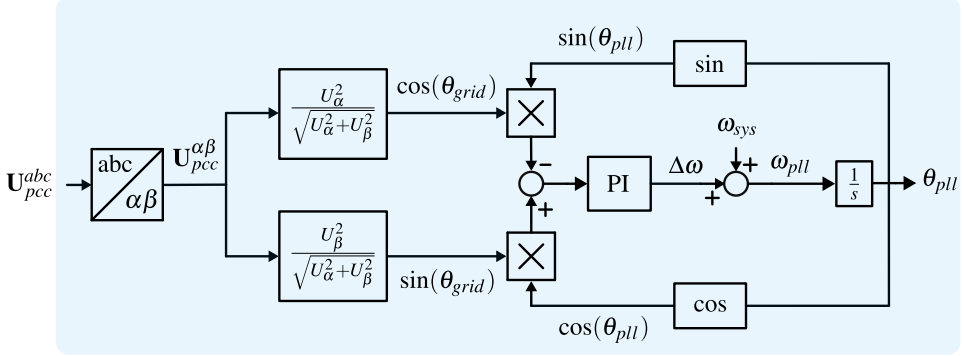


Figure 32: Diagram illustrating the VSC model connected to the AC network.





Phase-locked loop

Figure 33: Diagram illustrating the VSC control system.

Grid Equivalent

The network is represented by a grid equivalent consisting of a voltage source U_{grid} behind an impedance $Z_{grid}=R_{grid}+j\omega L_{grid}$. To facilitate studies involving the impact of the grid strength, the grid impedance is expressed as a function of the desired SCR and X/R ratio. This is achieved by first defining the SCR as the ratio between the short circuit power S_{sc} and the nominal power S_n of the installed converter, expressed as:

$$SCR = \frac{S_{sc}}{S_n}. (101)$$

In the previous equation, the short circuit power can be calculated as a function of the grid nominal voltage U_{grid} and impedance magnitude $|Z_{grid}|$ as:

$$S_{sc} = \frac{U_{grid}^2}{|Z_{grid}|}. (102)$$

Finally, substituting Equation (102) into (101), the grid impedance magnitude $|Z_{grid}|$ and angle θ can be calculated as functions of the SCR and X/R ratio as follows:

$$|Z_{grid}| = \frac{U_{grid}^2}{SCR \cdot S_n},\tag{103}$$

$$\theta = \arctan\left(\frac{X_{grid}}{R_{grid}}\right). \tag{104}$$

AC Side Dynamics

The dynamics of the AC side, which includes the grid equivalent and the converter AC equations, are represented by a set of three equations describing the behaviour of each phase in the *abc* reference frame, shown below in vector notation:

$$\mathbf{U}_{ac}^{abc} - \mathbf{U}_{pcc}^{abc} = R_{vsc} \mathbf{I}_{ac}^{abc} + L_{vsc} \frac{d\mathbf{I}_{ac}^{abc}}{dt}, \tag{105}$$

where \mathbf{U}^{abc}_{ac} is a vector representing the AC-side controlled voltage source, \mathbf{U}^{abc}_{pcc} is the voltage at the PCC, \mathbf{I}^{abc}_{ac} is the AC current and R_{vsc} and L_{vsc} are the equivalent converter resistance and inductance, respectively.

To simplify the design of the converter controls, it is beneficial to express these equations in the dq0 reference frame, which converts sinusoidal voltages and currents into constant values. For reference, Appendix B provides an overview of the various transformations. This conversion is achieved in two phases [114]. Initially, Equation (105) is transformed into the $\alpha\beta\gamma$ reference frame, yielding:

$$\mathbf{U}_{ac}^{\alpha\beta\gamma} - \mathbf{U}_{pcc}^{\alpha\beta\gamma} = R_{vsc} \mathbf{I}_{ac}^{\alpha\beta\gamma} + L_{vsc} \frac{d\mathbf{I}_{ac}^{\alpha\beta\gamma}}{dt}.$$
 (106)

Since this work focuses exclusively on balanced systems, the term γ is omitted. Next, the expression is converted from the $\alpha\beta$ to the dq frame by applying a rotation to each variable. The relationship governing the rotation of a variable x at a rotation speed ω is as follows:

$$x^{\alpha\beta} = x^{dq} e^{j\omega t}. (107)$$

Substituting Equation (107) into (106) results in the following expression describing the dynamics of the AC side in the dq frame:

$$\mathbf{U}_{ac}^{dq} - \mathbf{U}_{pcc}^{dq} = R_{vsc} \mathbf{I}_{ac}^{dq} + L_{vsc} \frac{d\mathbf{I}_{ac}^{dq}}{dt} + j\omega L_{vsc} \mathbf{I}_{ac}^{dq}. \tag{108}$$

where $\mathbf{U}_{ac}^{dq} = \begin{bmatrix} U_{ac}^d & U_{ac}^q \end{bmatrix}^T$ is the AC-side controlled voltage source, $\mathbf{U}_{pcc}^{dq} = \begin{bmatrix} U_{pcc}^d & U_{pcc}^q \end{bmatrix}^T$ is the voltage vector at the PCC, $\mathbf{I}_{ac}^{dq} = \begin{bmatrix} I_{ac}^d & I_{ac}^q \end{bmatrix}^T$ is the AC current and R_{vsc} and L_{vsc} are the equivalent converter resistance and inductance, respectively.

Note that when the $\alpha\beta$ terms are rotated into dq terms this leads to a cross-coupling between d and q axis due to the imaginary term $j\omega L_{vsc}$. This cross-coupling effect needs to be accounted for when designing the AC current control, as will be demonstrated later.

Converter DC Side

The converter's DC side is represented by a current source, with its value derived from the power balance equation. This equation assumes power is transferred between the AC and

DC sides without any losses. Therefore, the total power produced or consumed by the AC side source U_{ac} is equal to the power output from the DC source U_{dc} . This relationship can be expressed as:

$$P_{ac} = \text{Re}\{U_{ac}I_{ac}^*\} = U_{dc}I_{dc} = P_{dc}.$$
 (109)

The value of the DC current source is then obtained by isolating the DC current in Equation (109) as follows:

$$I_{dc} = \frac{U_{ac}^{d} I_{ac}^{d} + U_{ac}^{q} I_{ac}^{q}}{U_{dc}}.$$
 (110)

AC Current Control

A control system must be designed to adjust the AC currents based on a reference value derived from the active and reactive power controls. This control is based on Equation (108), which represents the dynamics of the AC side. It is implemented using a Proportional and Integral (PI) controller in the dq-frame, as illustrated in Figure 33. The key equations that describe the control loop are as follows:

$$U_{ac}^{d*} = (I_{ac}^{d*} - I_{ac}^{d,meas}) \left(K_{p,id} + \frac{K_{i,id}}{s} \right) + U_{pcc}^{d} + I_{ac}^{q,meas} L_{vsc} \omega, \tag{111}$$

$$U_{ac}^{q*} = (I_{ac}^{q*} - I_{ac}^{q,meas}) \left(K_{p,iq} + \frac{K_{i,iq}}{s} \right) + U_{pcc}^{q} - I_{ac}^{d,meas} L_{vsc} \omega, \tag{112}$$

where $K_{p,id}$, $K_{p,iq}$ are the controllers' proportional gains and $K_{i,id}$ and $K_{i,iq}$ are their integral gains.

Phase-Locked Loop

To ensure that the control system operates correctly, it is essential to estimate the voltage angle at the PCC. This can be achieved by using a Phase-Locked Loop (PLL). For this case study, the $\alpha\beta$ -PLL is selected and implemented according to the specifications outlined in [113, 115], as illustrated in Figure 33.

The input for the PI controller is determined based on an approximation that forms the basis of the working principle of the $\alpha\beta$ -PLL. This approximation is mathematically expressed as:

$$\sin(\theta_{grid} - \theta_{pll}) \approx \sin(\theta_{grid})\cos(\theta_{pll}) - \sin(\theta_{pll})\cos(\theta_{grid}), \tag{113}$$

where $heta_{grid}$ is the grid voltage angle and $heta_{pll}$ is the grid angle measured by the PLL.

Using this approximation, the grid frequency measured by the PLL, denoted as ω_{pll} in rad/s, can be formulated as:

$$\omega_{pll} = \left(K_{p,pll} + \frac{K_{i,pll}}{s}\right)\sin(\theta_{grid} - \theta_{pll}),$$
 (114)

where $K_{p,pll}$ and $K_{i,pll}$ are the proportional and integral terms of the PI controller, respectively.

Once the measured frequency ω_{pll} is computed, the measured grid angle θ_{pll} can be derived as:

$$\theta_{pll} = \frac{\omega_{pll}}{s}.\tag{115}$$

Voltage Feed-Forward Filter

Equation (108) illustrates the dynamics of the AC side, indicating that the AC bus voltages U^d_{pcc} and U^q_{pcc} are subtracted from the inner VSC-controlled voltages U^d_{ac} and U^q_{ac} , respectively. The current control system is designed to compensate for these AC bus voltages, which are referred to in control theory as load disturbances. When a transient occurs in the grid voltage, they are injected into the control system, impacting its dynamic performance. To mitigate these effects, a feed-forward filter can be employed [116].

A first-order low-pass voltage-feedforward filter was used, where ω_{ff} represents the filter's cutoff frequency. It can also be regarded as its bandwidth. The filter's transfer function $G_{ff}(s)$ is given by:

$$G_{ff}(s) = \frac{\omega_{ff}}{s + \omega_{ff}}. (116)$$

Active and Reactive Power Control

Active and reactive power controls are derived from the instantaneous power equations in the dq0 frame presented in Appendix B. These equations assume that the zero-sequence components of the voltage are neglected; that is, $U_{pcc}^q=U_{pcc}^0=0$. Consequently, the active P and reactive Q power are expressed as:

$$P = \frac{3}{2} U_{pcc}^d I_{ac}^d, {117}$$

$$Q = -\frac{3}{2} U_{pcc}^d I_{ac}^q. {(118)}$$

The AC current components I_{ac}^d and I_{ac}^q can be isolated from Equations (117) and (118) to derive a control rule as follows:

$$I_{ac}^{d} = \frac{P}{\frac{3}{2}U_{pcc}^{d}},\tag{119}$$

$$I_{ac}^{q} = -\frac{Q}{\frac{3}{2}U_{pcc}^{d}}.$$
 (120)

In order to avoid potential issues with measuring the PCC voltage U^d_{pcc} and feeding it forward to the control loop, the nominal value $U^{d,nom}_{pcc}$ for the voltage is instead used. Equations (119) and (120) then become:

$$I_{ac}^{d} = \frac{P}{\frac{3}{2}U_{pcc}^{d,nom}},\tag{121}$$

$$I_{ac}^{q} = -\frac{Q}{\frac{3}{2}U_{pcc}^{d,nom}}.$$
 (122)

Finally, the main equations describing the active and reactive power controls are derived as:

$$I_{ac}^{d*} = \frac{1}{\frac{3}{2} U_{pcc}^{d,nom}} (P_{ac}^* - P_{ac}^{meas}) \left(K_{p,P} + \frac{K_{i,P}}{s} \right), \tag{123}$$

$$I_{ac}^{q*} = -\frac{1}{\frac{3}{2}U_{pcc}^{d,nom}}(Q_{ac}^* - Q_{ac}^{meas})\left(K_{p,Q} + \frac{K_{i,Q}}{s}\right),\tag{124}$$

where P^*_{ac} and Q^*_{ac} are the active and reactive power references, respectively, P^{meas}_{ac} and Q^{meas}_{ac} are the measured active and reactive power, $K_{p,P}$, $K_{p,Q}$ are the controllers' proportional gains and $K_{i,P}$ and $K_{i,Q}$ are their integral gains.

Modulation

The internal converter AC voltage \mathbf{U}_{ac}^{dq} is regulated using the modulation indexes m_d and m_q in the rotating dq frame [64]. This can be expressed as:

$$U_{ac}^{d} = \frac{\sqrt{3}}{2\sqrt{2}} U_{dc} m_d, \tag{125}$$

$$U_{ac}^{q} = \frac{\sqrt{3}}{2\sqrt{2}} U_{dc} m_{q}. \tag{126}$$

Thus, the control can be implemented by isolating the m_d and m_q in Equations (125) and (126), yielding the reference modulation indexes m_d^* and m_q^* :

$$m_d^* = \frac{2\sqrt{2}}{\sqrt{3}} \frac{U_{ac}^{d*}}{U_{dc}},\tag{127}$$

$$m_q^* = \frac{2\sqrt{2}}{\sqrt{3}} \frac{U_{ac}^{q*}}{U_{dc}}. (128)$$

2.4.2 Model Implementation

The model introduced earlier serves as the full-order model for the analysis in this section. It was implemented using MATLAB/Simulink, and a state-space representation was obtained by linearising the system based on the chosen active and reactive power setpoints of $P_{ac}^*=0.9$ p.u. and $Q_{ac}^*=0.2$ p.u., respectively. Details regarding the parameters used in the case study can be found in Table 6 for the VSC and grid equivalent. The control tuning for the VSC is specified as a function of the response time τ and the damping ratio ζ . For more information on the tuning of each controller, refer to Appendix F.

2.4.3 Application of Balanced Truncation

The state-space model of the original full-order system consists of 10 state variables \mathbf{x} , as follows:

$$\mathbf{x} = \begin{bmatrix} y_{ffd} & I_{ac}^d & I_{ac}^q & \theta_{pll} & y_q & y_{iq} & y_{ffq} & y_p & y_{id} & y_{pll} \end{bmatrix}^T, \tag{129}$$

where y_p and y_q represent the states corresponding to the active and reactive power controller integrators, y_{ffd} and y_{ffq} are associated with the voltage feedforward states, y_{id} and y_{iq} are the states associated with the current control integrators, and θ_{pll} and y_{pll} denote the states connected to the PLL.

The analysis begins with the original state-space realisation of the system, where the controllability and observability Gramians are calculated using Equations (87) and (88). The results are presented in Table 7, showing values rounded to two decimal places. Each row of the table represents the controllability and observability associated with a state variable. It is clear that some states exhibit high controllability while being poorly observable, and vice versa. This indicates an imbalance in the system's original state-space realisation, as the states have varying levels of controllability and observability that do not align.

Table 6: VSC case study reference parameters.

System	Name	Symbol	Value
VSC	Rated apparent power	S_{rated}	1 GVA
	DC bus voltage	U_{dc}	640 kV
	AC bus voltage	U_{pcc}	192 kV
	VSC equivalent inductance	L_{vsc}	$82.70 \mathrm{mH}$
	VSC equivalent resistance	R_{vsc}	1.03Ω
	Active/reactive power control time const.	$ au_{pq}$	$100\mathrm{ms}$
	AC current control time constant	$ au_{idq}$	10 ms
	AC current control damping ratio	ζ_{idg}	0.7
	PLL time constant	$ au_{pll}$	50 ms
	PLL damping ratio	$\dot{\zeta}_{pll}$	0.7
	Voltage feed-forward bandwidth	ω_{ff}	3000 rad/s
Grid equivalent	Equivalent resistance	R_{grid}	1.47 Ω
	Equivalent inductance	L_{grid}	$46.90 \mathrm{mH}$
	Short-circuit ratio	SCR	2.49
	X/R ratio	XR	10

According to the balanced truncation method, a balancing transformation T_b can be derived to change the state space coordinates, ensuring that the Gramians become balanced. By applying this transformation, the states are expressed in a new coordinate system, denoted as x_b . The transformation is achieved using Equation (95).

With the states now expressed in this new coordinate system, the state-space realisation is reformulated according to Equations (97) and (98). The Gramians have been recalculated, and the results are presented in Table 8. The first column of this table lists the states in the new coordinate system. Unlike the states shown in Table 7, which are directly related to different components of the converter and its controls, the states in Table 8 do not correspond to specific components of the physical system. This difference occurs due to the application of the balancing coordinate transformation. Additionally, the new state-space realisation is balanced, as demonstrated by the fact that the controllability and observability Gramians for each state have the same value. As mentioned earlier, these values correspond to the HSVs.

Reduced order models can be obtained by first ranking the states in descending order based on their corresponding HSV as shown in Table 8. States with higher HSV have more impact on the system's response. Consequently, reduced order models can be created by eliminating the states with lower HSVs, which are found at the bottom rows of the table. To demonstrate this method and validate the results, two reduced-order models have been developed. The first is a second-order model that retains the first two states from the balanced model realization:

$$\mathbf{x}_{\mathbf{b}}^{\mathbf{red},\mathbf{1}} = \begin{bmatrix} x_1 & x_2 \end{bmatrix} \tag{130}$$

The second model is a fourth-order model, which incorporates the first four states:

$$\mathbf{x}_{\mathbf{b}}^{\mathbf{red},2} = \begin{bmatrix} x_1 & x_2 & x_3 & x_4 \end{bmatrix} \tag{131}$$

The responses of the full model and the two derived reduced-order models are compared, as shown in Figure 34. This figure displays the active power response of all models

Table 7: Controllability and observability Gramians for the VSC state-space model in the original state space coordinates.

State variables x	Controllability $\mathcal{P}^{(k,k)}$	Observability $\mathcal{Q}^{(k,k)}$
y_{ffd}	0.00	225.78
I_{ac}^{d}	67.10	0.00
$I^d_{ac} \ I^q_{ac}$	116.92	0.00
$ heta_{pll}$	115.72	0.01
y_q	2.41	0.07
y_{iq}	5.92	0.00
y_{ffq}	0.00	251.12
y_p	18.11	0.05
Уid	1.46	0.00
y_{pll}	0.00	0.00

Table 8: Controllability and observability Gramians for the VSC state-space model in the balanced state space coordinates.

State variables x_b	Controllability $\mathcal{P}^{(k,k)}$	Observability $\mathcal{Q}^{(k,k)}$
x_1	1.25	1.25
x_2	0.89	0.89
x_3	0.32	0.32
x_4	0.15	0.15
x_5	0.10	0.10
x_6	0.08	0.08
x_7	0.06	0.06
x_8	0.03	0.03
<i>X</i> 9	0.02	0.02
x_{10}	0.01	0.01

to a step change of $\Delta P_{ac}^*=0.02$ p.u. It is clear that the second-order model exhibits considerable deviation from the full-order model, particularly during the initial response from 0.1 seconds to 0.3 seconds. In contrast, the fourth-order model demonstrates better performance, especially at the beginning of the response.

It can be concluded that the system response can be reasonably approximated by a model of order as low as four. From a computational standpoint, this approach is advantageous as it simplifies the model complexity, leading to improved computational speed. However, when it comes to gaining a better understanding of the system's behaviour and identifying which components influence the system's response, the method is not suitable. This is because, after applying the balancing transformation, the state variables lose their physical interpretation. Consequently, while the method may indicate that the first four states $\begin{bmatrix} x_1 & x_2 & x_3 & x_4 \end{bmatrix}$ are the most relevant to the system dynamics, this information is purely mathematical and lacks physical significance. It does not reveal which parts of the VSC models are relevant.

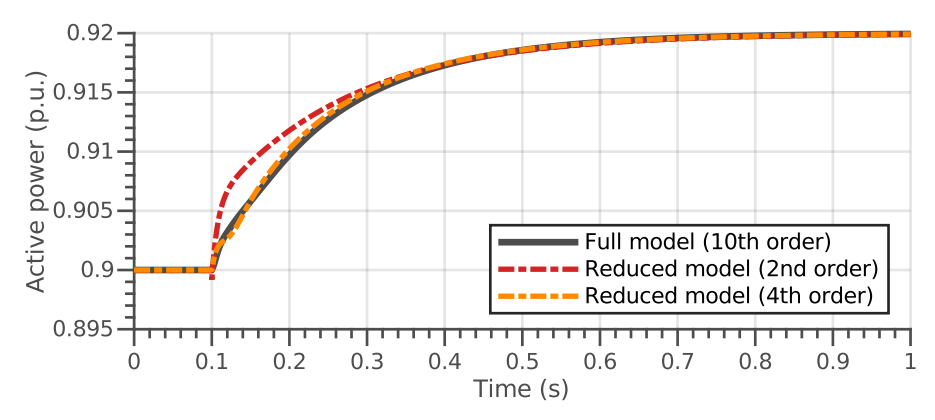


Figure 34: Time-domain response of the measured active power to a step in the active power reference for full and reduced models.

2.5 Conclusion

This chapter provided a comprehensive overview of the fundamental concepts of model order reduction, with a specific emphasis on the balanced truncation method. It began by introducing the state-space representation for linear systems, emphasising that the choice of a coordinate system for representing a system's internal states is arbitrary. The concepts of controllability and observability were then presented, demonstrating how one can achieve a minimal realisation of a system, that is, a representation with the lowest possible order, by selecting a coordinate frame that maximises the number of uncontrollable or unobservable states, which can then be neglected.

The chapter also introduced the controllability and observability Gramians as tools to measure the controllability and observability of states across a continuum. This led to the balanced truncation method, which identifies a balancing transformation such that, in the newly defined coordinate system, the states exhibit equal controllability and observability. The method then truncates states that contribute the least to the system's overall response, as illustrated by a case study of a VSC system.

It is important to note that implementing the balancing transformation results in state variables that have only mathematical significance and are no longer directly related to the physical system. This lack of association makes it difficult for power system experts to apply these methods to understand which components and control models to use in practical system studies. While this technique generally offers high computational efficiency and scalability, aiming to achieve a near-optimal reduction in the number of states in the model, the downside is that the results often become less intuitive and harder to interpret, as the mathematical models lose their physical meaning.

Chapter 3 addresses these limitations by adapting the balanced truncation method and introducing two novel MOR methods that can be used to determine the modelling details required for converter-dominated systems, taking into account dynamics across various time scales. The proposed methods aim to enhance the interpretability of results and facilitate direct model reduction, eliminating the need for a coordinate system transformation, thereby preserving the relationship between the states and the physical system.

3 Methodologies for Physics-Preserving Model Reduction

This chapter introduces two methodologies that aim to systematically address the challenge of determining the appropriate level of modelling detail required for stability studies in converter-dominated power systems. Traditional MOR techniques, while effective in reducing complexity, often obscure the direct physical interpretation of states and system components, making practical application challenging.

To overcome this limitation, two novel physics-preserving MOR methods are proposed, which adapt the balanced truncation approach introduced in Chapter 2. Method 1, the Event-Based Model Reduction, allows identifying states that significantly contribute to system dynamics following specific disturbances, thus ensuring accurate simulations without unnecessary computational complexity. Method 2, Model Reduction for Different Frequency Ranges, extends this approach by evaluating the contribution of system states across specific frequency intervals, enabling targeted and efficient model simplifications tailored to particular dynamic phenomena. Both methods retain the physical meaning of states, facilitating their direct integration into practical power system stability studies.

The chapter provides a detailed theoretical foundation for both methodologies, describes the algorithms used, and explains their physical interpretation. To illustrate the effectiveness and applicability of these methods, the chapter concludes with a case study that demonstrates the application of these techniques. Part of this chapter draws on the findings published in II.

3.1 Method 1: Event-Based Model Reduction

Method 1 for model order reduction offers a technique to create generic reduced models based on how the system responds to an event. These models are chosen according to the degree of each state's impact on the overall response, focusing on the frequency range that is most significantly excited by the event. Figure 35 demonstrates the method. Subsequent sections will outline the essential mathematical background and the development of the model reduction algorithm.

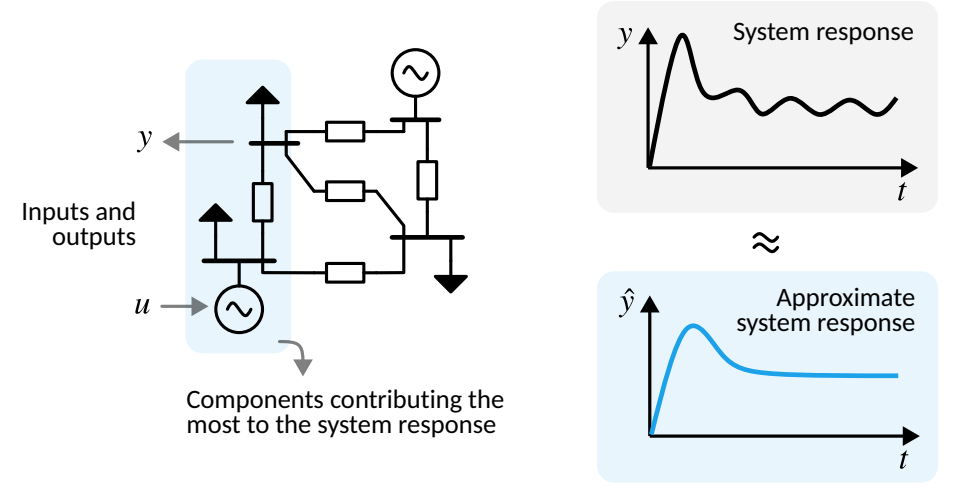


Figure 35: Diagram illustrating the application of Method 1 for model order reduction.

3.1.1 Controllability and Observability Operators

The main idea behind the proposed method is to leverage the concepts of controllability and observability to quantify the importance of a state to the system's response. This approach, however, does not require a coordinate transformation, which distinguishes it from the balanced truncation method presented in Chapter 2. This section introduces the concepts of *controllability and observability operators*, which are fundamental to the development of the proposed MOR approach. These operators establish a relationship between inputs, initial conditions, and outputs.

Consider the system represented in state-space by the Equations (50) and (51). For simplicity, assume the system has only one input and one output and is, therefore, a Single-Input Single-Output (SISO) system described by:

$$\dot{\mathbf{x}}(t) = \mathbf{A}\mathbf{x}(t) + \mathbf{B}u(t),\tag{132}$$

$$y(t) = \mathbf{C}\mathbf{x}(t) + \mathbf{D}u(t), \tag{133}$$

where $\mathbf{A} \in \mathbb{R}^{n \times n}$, $\mathbf{B} \in \mathbb{R}^{n \times 1}$, $\mathbf{C} \in \mathbb{R}^{1 \times n}$ and $\mathbf{D} \in \mathbb{R}^{1 \times 1}$ are the state-space matrices.

Controllability Operator

Let u(t) be an input applied to this system during the time interval $t \in (-\infty, 0]$. The value $\mathbf{x_0}$ of the states at the instant t = 0 can be calculated using the controllability operator $\mathbf{\Psi_c}$ as follows:

$$\mathbf{x_0} = \mathbf{\Psi_c} u(t), \tag{134}$$

where $\Psi_{\mathbf{c}} = [\Psi_c^{(1)} \ \Psi_c^{(2)} \ ... \ \Psi_c^{(n)}]^T$ is a column vector and $\Psi_c^{(k)}$ represents the controllability operator associated with the k-th state.

Furthermore, the controllability operator $\Psi_c: L_2(-\infty,0] \to \mathbb{R}^n$ can be defined in relation to the input and the state space matrices as follows [105]:

$$u \mapsto \int_{-\infty}^{0} e^{-\mathbf{A}\tau} \mathbf{B} u(\tau) d\tau. \tag{135}$$

This operator can be understood as a mapping that translates inputs defined in the past ($t \le 0$) to the initial condition $\mathbf{x_0}$ at t = 0.

Observability Operator

Next, let y(t) be the output of the system resulting from the initial condition $\mathbf{x_0}$ over the interval $t \in [0, \infty)$. The output is determined using the observability operator $\mathbf{\Psi_0}$ as follows:

$$y(t) = \mathbf{\Psi}_0 \mathbf{x}_0, \tag{136}$$

where $\Psi_o = [\Psi_o^{(1)} \ \Psi_o^{(2)} \ ... \ \Psi_o^{(n)}]$ is a row vector and $\Psi_o^{(k)}$ is the observability operator associated with the k-th state.

Additionally, the observability operator Ψ_0 : $\mathbb{R}^n \to L_2[0,\infty)$ is computed from the initial conditions and the state space matrices using the following expression [105]:

$$\mathbf{x_0} \mapsto \begin{cases} \mathbf{C}e^{\mathbf{A}t}\mathbf{x_0}, & \text{for } t \ge 0\\ \mathbf{0}, & \text{otherwise} \end{cases}$$
 (137)

This operator maps the initial condition $\mathbf{x_0}$ to the output of the system for t > 0, when no input is applied.

Finally, an important consequence of these operators is that they can be derived from the respective controllability and observability Gramians defined in Equations (87) and (88). This is achieved as follows:

$$\mathcal{P} = \Psi_{\mathbf{c}} \Psi_{\mathbf{c}}^*, \tag{138}$$

$$Q = \Psi_0^* \Psi_0. \tag{139}$$

Hankel Operator

The controllability operator maps a past input to the initial state, while the observability operator relates the initial state to the output. By combining these two operators, it is possible to define an operator that maps a past input to a future output [105] as illustrated in Figure 36. This combination is known as the *Hankel operator*, denoted as Γ_G , and it enables the analysis of the system's input-output behaviour. Mathematically,

$$\Gamma_{\rm G} = \Psi_{\rm o} \Psi_{\rm c}. \tag{140}$$

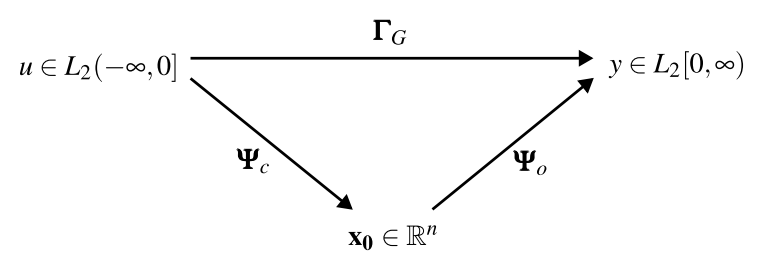


Figure 36: Relationship between the controllability and observability operators and the Hankel operator [105].

3.1.2 Approximation of the System's Response

The Hankel operator, defined in the previous section by means of the controllability and observability operators, is used to relate a system's input u(t) to its output y(t) as follows:

$$\mathbf{v}(t) = \mathbf{\Psi}_{\mathbf{c}} \mathbf{\Psi}_{\mathbf{c}} \mathbf{u}(t). \tag{141}$$

Equation (141) can be developed by expanding the vectors representing the operators, making the components of the operators associated with each state explicit. This expression highlights the contributions of the system's state variables:

$$y(t) = \left[\Psi_o^{(1)}\Psi_c^{(1)} + \Psi_o^{(2)}\Psi_c^{(2)} + \dots + \Psi_o^{(n)}\Psi_c^{(n)}\right]u(t), \tag{142}$$

where $\Psi_o^{(k)}\Psi_c^{(k)}$ represents the product between the observability and controllability operators associated with the k-th state.

Equation (142) shows that the system output can be broken down into n components, each linked to a state variable as illustrated in Figure 37. The output component corresponding to the k-th state variable is described by $\Psi_o^{(k)}\Psi_c^{(k)}u(t)$. Additionally, the impact of each component on the overall output differs based on the product value $\Psi_o^{(k)}\Psi_c^{(k)}$, with higher values leading to a larger contribution to the total output. Consequently, the system input-output behaviour can be decomposed among the state variables, making it possible to identify and evaluate the contribution of each individual state.

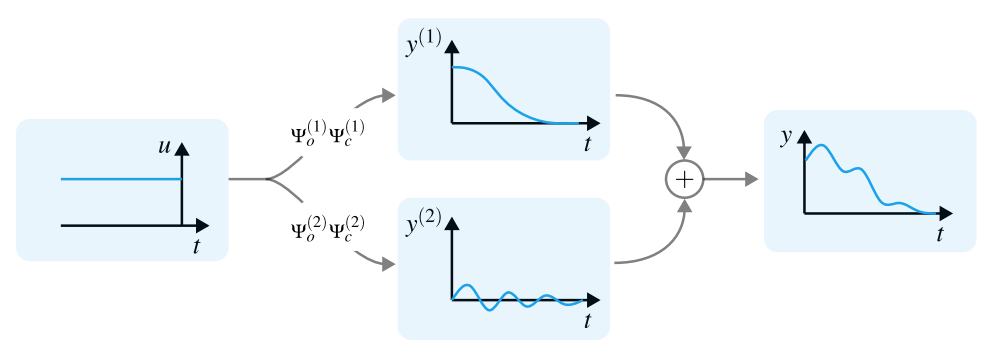


Figure 37: Example of a second-order system showing the decomposition of the outputs into the components associated with each state.

Assuming the state vector is arranged in descending value of the term $\Psi_o^{(k)}\Psi_c^{(k)}$, it is possible to reduce the order of the system from n to r with r < n by eliminating n - r states denoted by $x^{(r+1)}, x^{(r+2)}, \ldots, x^{(n)}$. The output $\hat{y}(t)$ of the reduced model is obtained from Equation (142) by removing the components associated with the states that are being eliminated, resulting in:

$$\hat{y}(t) = \left[\Psi_o^{(1)} \Psi_c^{(1)} + \Psi_o^{(2)} \Psi_c^{(2)} + \dots + \Psi_o^{(r)} \Psi_c^{(r)} \right] u(t). \tag{143}$$

3.1.3 Calculation of the Approximation Error

The approximation error incurred by reducing the model order can be defined as the difference between the outputs of the full and reduced-order models. It is quantified using the L_2 norm as follows:

$$\|y - \hat{y}\|_2 = \left\| \sum_{k=r+1}^n \Psi_o^{(k)} \Psi_c^{(k)} u(t) \right\|_2.$$
 (144)

Based on the submultiplicative and triangle inequality properties, Equation (144) can be rewritten as:

$$\|y - \hat{y}\|_2 \le \sum_{k=r+1}^n \|\Psi_o^{(k)}\|_2 \|\Psi_c^{(k)}\|_2 \|u(t)\|_2.$$
 (145)

In order to develop the right-side term of Equation (145), the controllability $\|\Psi_c^{(k)}\|_2$ and observability $\|\Psi_o^{(k)}\|_2$ norms associated with the k-th state must be calculated. To achieve that, the definition of the \mathbf{H}_{∞} norm of bounded operators [117] is used. More information on Hardy spaces is found in Appendix E. The norm is defined as follows:

$$\|\Phi\|_{\infty} = \sup\{\|\Phi x\|_2 : \|x\|_2 = 1\},\tag{146}$$

where Φ is a bounded operator and $\Phi \in \mathbf{H}_{\infty}$ and $x \in \mathbf{H}_2$.

Let the $\Psi_o^{(k)}$ be the component of the observability operator associated with the k-th state variable. Using the \mathbf{H}_{∞} norm from Equation (146), it is possible to write an expression representing the norm of the k-th component of the observability operator. This results in:

$$\|\Psi_o^{(k)}\|_{\infty} = \sup\{\|\Psi_o^{(k)} x_0^{(k)}\|_2 : |x_0^{(k)}| = 1\}.$$
 (147)

The term in the right-side of Equation (147) can be expanded into:

$$\|\Psi_o^{(k)} x_0^{(k)}\|_2^2 = x_0^{(k)*} \Psi_o^{(k)*} \Psi_o^{(k)} x_0^{(k)}.$$
(148)

Using the result from Equation (148) and knowing that $|x_0^{(k)}|=1 \to x_0^{(k)}=\pm 1$, the right side term from Equation (147) is evaluated as:

$$\|\Psi_o^{(k)}\|_{\infty} = \sqrt{\Psi_o^{(k)*}\Psi_o^{(k)}}.$$
(149)

Similarly, let $\Psi_c^{(k)}$ be the component of the controllability operator associated with the k-th state variable. It follows from Equation (146) that:

$$\|\Psi_c^{(k)}\|_{\infty} = \sup\{\|\Psi_c^{(k)}u\|_2 : \|u\|_2 = 1\}.$$
 (150)

To evaluate the right-side term of Equation (150), it is useful to leverage the fact that the following two sets are equal [105, 111]:

$$\{\Psi_c u : u \in L_2(-\infty, 0] \text{ and } \|u\|_2 \le 1\},$$
 (151)

$$\{(\mathbf{\Psi}_{c}\mathbf{\Psi}_{c}^{*})^{\frac{1}{2}}x_{c}: x_{c} \in \mathbb{C}^{n} \text{ and } |x_{c}| \leq 1\}.$$
 (152)

Equation (150) can then be rewritten, resulting in:

$$\|\Psi_c^{(k)}\|_{\infty} = \sup\{\|(\Psi_c^{(k)}\Psi_c^{(k)*})^{\frac{1}{2}}x_c\|_2 : |x_c| = 1\}.$$
 (153)

The right side term in Equation (153) can be expanded as follows:

$$\|(\Psi_c^{(k)}\Psi_c^{(k)*})^{\frac{1}{2}}x_c\|_2^2 = x_c^*\Psi_c^{(k)}\Psi_c^{(k)*}x_c.$$
(154)

Substituting Equation (154) into (153) and knowing that $|x_c|=1 \rightarrow x_c=\pm 1$ results in:

$$\|\Psi_c^{(k)}\|_{\infty} = \sqrt{\Psi_c^{(k)} \Psi_c^{(k)*}}.$$
 (155)

It follows from the property $\|\Phi\|_{\infty} \leq \|\Phi\|_2$ that the L_2 norms of the controllability and observability operators are given, respectively, by:

$$\|\Psi_c^{(k)}\|_2 \le \sqrt{\Psi_c^{(k)}\Psi_c^{(k)*}},$$
 (156)

$$\|\Psi_o^{(k)}\|_2 \le \sqrt{\Psi_o^{(k)*}\Psi_o^{(k)}}.$$
(157)

The operator norms in Equations (156) and (157) are related to the diagonal terms of the controllability and observability Gramians as $\Psi_o^{(k)*}\Psi_o^{(k)}=\mathcal{Q}^{(k,k)}$ and $\Psi_c^{(k)}\Psi_c^{(k)*}=\mathcal{P}^{(k,k)}$. Taking that into consideration and substituting Equations (156) and (157) into (145), results in:

$$\|y - \hat{y}\|_2 \le \sum_{k=r+1}^n \sqrt{\mathcal{Q}^{(k,k)}\mathcal{P}^{(k,k)}} \|u(t)\|_2.$$
 (158)

If the input is an impulse, that is, $u(t) = \delta(t)$, then the output y(t) is the impulse response denoted by h(t). The previous equations show that the norm of the impulse response error $\|h - \hat{h}\|_2$ is bounded by:

$$||h - \hat{h}||_2 \le \sum_{k=r+1}^n \sqrt{\mathcal{Q}^{(k,k)} \mathcal{P}^{(k,k)}}.$$
 (159)

A reduced system is obtained when the error associated with removing a certain number of states only has a negligible impact compared to the states remaining in the model. Similarly to the model reduction by balanced truncation, the reduced-order model is obtained by eliminating the states that have the lowest values of $\sqrt{\mathcal{Q}^{(k,k)}\mathcal{P}^{(k,k)}}$.

Mathematically, this requirement can be formulated following Moore [107]. A reduced system exists if there is an internally dominant subsystem of order r that satisfies the following equation:

$$\sum_{k=1}^{r} \sqrt{\mathcal{Q}^{(k,k)} \mathcal{P}^{(k,k)}} \gg \sum_{k=r+1}^{n} \sqrt{\mathcal{Q}^{(k,k)} \mathcal{P}^{(k,k)}}.$$
 (160)

Based on these conclusions, it is possible to define an error E_r heuristic that measures how close the reduced system is to the full system. Mathematically,

$$E_r = \frac{\sum_{k=r+1}^{n} \sqrt{\mathcal{Q}^{(k,k)} \mathcal{P}^{(k,k)}}}{\sum_{k=1}^{r} \sqrt{\mathcal{Q}^{(k,k)} \mathcal{P}^{(k,k)}}}.$$
 (161)

This error measures the impact of removing certain states from the model. In other words, state variables that produce significant errors when removed have high participation in the system response.

3.1.4 Participation of State in Input-Output Behaviour

Equation (161), which quantifies the error in approximating a full-order model with its reduced-order equivalent, measures not only the error from neglecting a group of states but can also be used to assess the influence of individual states on model accuracy. When considering the removal of a single state, specifically the k-th state, the resulting error can be derived from Equation (161) as follows:

$$E_r^{(k)} = \frac{\sqrt{Q^{(k,k)}\mathcal{P}^{(k,k)}}}{\sum_{i=1, i \neq k}^{n} \sqrt{Q^{(i,i)}\mathcal{P}^{(i,i)}}}.$$
 (162)

This last expression shows the magnitude of the k-th state's contribution relative to others in the system. The system can be visualized as depicted in Figure 38, where the resulting output is derived from each state's contribution, which is proportional to the term $\sqrt{\mathcal{Q}^{(k,k)}\mathcal{P}^{(k,k)}}$.

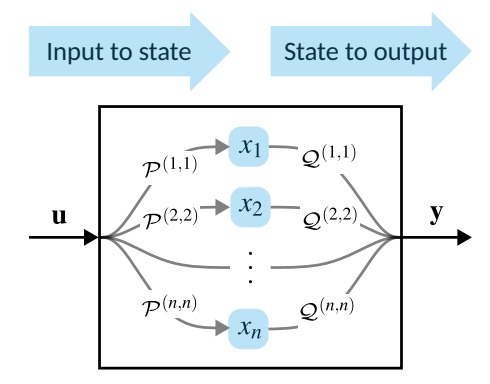


Figure 38: Contribution of state variables to input-output system response.

Thus, Equation (162) can be extended by normalising the contribution of a single state in relation to all states within the system, including the one under analysis. This normalisation process highlights the significance of an individual state. Consequently, it is possible to define the participation $p^{(k)}$ of the k-th state variable in the system's input-output behaviour as:

$$p^{(k)} = \frac{\sqrt{Q^{(k,k)}\mathcal{P}^{(k,k)}}}{\sum_{i=1}^{n} \sqrt{Q^{(i,i)}\mathcal{P}^{(i,i)}}}.$$
 (163)

Equation (163) provides valuable insights about the modelling details necessary for system studies by evaluating the contribution of each model component to the system's response. This can be approached broadly by examining how various elements like transmission lines, converters, or generators influence oscillations. Alternatively, a single component can be inspected, such as a converter, to reveal how specific parts of its model affect the system response, guiding the necessary accuracy of the model.

3.1.5 Physical Interpretation

This section provides the physical interpretation of the Equation (163) from a signal point of view, highlighting the relationship between Gramians and energy transfer across the system from input to output. A MIMO system as described by Equations (50) and (51) is considered.

To begin, it is important to revisit the meaning of signal energy, which was briefly addressed in Chapter 2. The energy of a signal is a purely mathematical concept that may be related to the definition of energy in physics but does not necessarily correspond to it. Mathematically, the energy E of a signal vector $\mathbf{s}(t)$ over the interval $[t_1, t_2]$ is defined as:

$$E = \langle \mathbf{s}(t), \mathbf{s}(t) \rangle = \int_{t_1}^{t_2} \|\mathbf{s}(t)\|_2^2 dt.$$
 (164)

The signal energy is related to both the controllability and observability Gramians. As discussed in Chapter 2, the controllability Gramian $\mathcal P$ is associated with the energy required to drive the states from 0 to x_0 . In contrast, the observability Gramian $\mathcal Q$ is a measure of the energy obtained from the outputs caused by the initial condition x_0 .

Based on that, consider the physical system illustrated in Figure 38. Suppose unitary impulses are successively applied to each system input, and each state's response is observed. The set of state response signals is represented by the matrix $\mathbf{X}(t) \in \mathbb{R}^{n \times m}$ as:

$$\mathbf{X}(t) = \begin{bmatrix} \mathbf{x}_1(t) \\ \mathbf{x}_2(t) \\ \vdots \\ \mathbf{x}_n(t) \end{bmatrix}, \tag{165}$$

where $\mathbf{x}_k(t) \in \mathbb{R}^m$ is a row vector containing the response of the k-th state to each of the inputs.

The vector $\mathbf{X}(t)$ is the input-to-state map and can be used to obtain the controllability Gramian \mathcal{P} over the interval $[t_1, t_2]$ as:

$$\mathcal{P} = \int_{t_1}^{t_2} \mathbf{X}(t) \mathbf{X}(t)^* dt.$$
 (166)

Based on that, the controllability Gramian matrix from Equation (166) can be expanded,

resulting in:

$$\mathcal{P} = \begin{bmatrix} \langle \mathbf{x}_{1}, \mathbf{x}_{1} \rangle & \langle \mathbf{x}_{1}, \mathbf{x}_{2} \rangle & \cdots & \langle \mathbf{x}_{1}, \mathbf{x}_{n} \rangle \\ \langle \mathbf{x}_{2}, \mathbf{x}_{1} \rangle & \langle \mathbf{x}_{2}, \mathbf{x}_{2} \rangle & \cdots & \langle \mathbf{x}_{2}, \mathbf{x}_{n} \rangle \\ \vdots & \vdots & & \vdots \\ \langle \mathbf{x}_{n}, \mathbf{x}_{1} \rangle & \langle \mathbf{x}_{n}, \mathbf{x}_{2} \rangle & \cdots & \langle \mathbf{x}_{n}, \mathbf{x}_{n} \rangle \end{bmatrix}, \tag{167}$$

where $\langle \mathbf{x}_k, \mathbf{x}_j \rangle$ denotes the inner product between the vectors \mathbf{x}_k and \mathbf{x}_j . When these vectors are equal, their inner product $\langle \mathbf{x}_k, \mathbf{x}_k \rangle$ represents the total energy of the signal \mathbf{x}_k as defined in Equation (164).

In other words, the k-th diagonal element of the controllability Gramian measures the total energy contained in the response of the k-th state to each of the inputs. A significant energy value indicates that the impulse had a greater effect on the state. This input-to-state energy transfer is illustrated in the left portion of Figure 39.

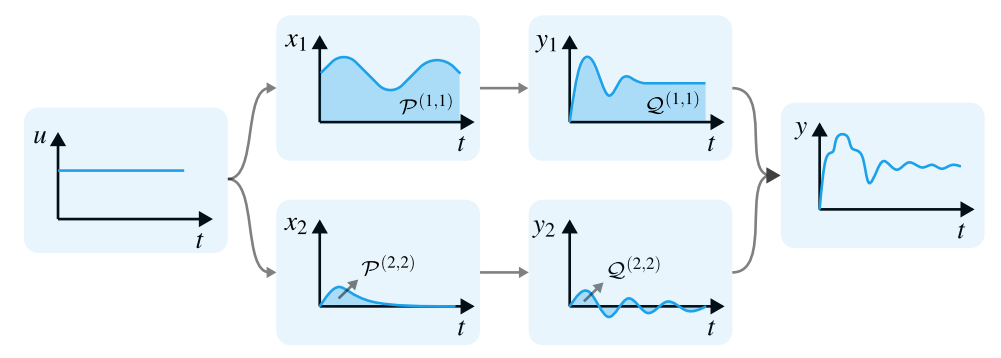


Figure 39: Signal analysis of a second-order system with responses decomposed by state.

Suppose a unitary initial condition is imposed on each state, and the system's output signal is observed. This set of signals is represented by the matrix $\mathbf{Y}(t) \in \mathbb{R}^{p \times n}$ as:

$$\mathbf{Y}(t) = \begin{bmatrix} \mathbf{y}_1(t) & \mathbf{y}_2(t) & \cdots & \mathbf{y}_n(t) \end{bmatrix}, \tag{168}$$

where $\mathbf{y}_k(t) \in \mathbb{R}^p$ is a column vector containing the response of all outputs to the initial condition imposed to the k-th state.

The vector $\mathbf{Y}(t)$ is the output-to-state map, and it can be used to calculate the observability Gramian \mathbf{Q} over the interval $[t_1, t_2]$ as:

$$\mathbf{Q} = \int_{t_1}^{t_2} \mathbf{Y}^*(t) \mathbf{Y}(t) dt.$$
 (169)

Based on that, the observability Gramian matrix defined in Equation (169) can be expanded as:

$$Q = \begin{bmatrix} \langle \mathbf{y}_{1}, \mathbf{y}_{1} \rangle & \langle \mathbf{y}_{1}, \mathbf{y}_{2} \rangle & \cdots & \langle \mathbf{y}_{1}, \mathbf{y}_{n} \rangle \\ \langle \mathbf{y}_{2}, \mathbf{y}_{1} \rangle & \langle \mathbf{y}_{2}, \mathbf{y}_{2} \rangle & \cdots & \langle \mathbf{y}_{2}, \mathbf{y}_{n} \rangle \\ \vdots & \vdots & & \vdots \\ \langle \mathbf{y}_{n}, \mathbf{y}_{1} \rangle & \langle \mathbf{y}_{n}, \mathbf{y}_{2} \rangle & \cdots & \langle \mathbf{y}_{n}, \mathbf{y}_{n} \rangle \end{bmatrix}$$
(170)

Similar to what was observed with the controllability Gramian, the diagonal terms in the matrix represent the signal energy measure as defined in Equation (164). In this case, $\langle \mathbf{y}_k, \mathbf{y}_k \rangle$ measures the total energy of the outputs resulting from a unitary initial condition

applied to the *k*-th state. The greater the energy, the more a state affects the output. This state-to-output energy distribution is illustrated in the right portion of Figure 39.

The diagonal terms from the controllability and observability Gramians for each state are combined into the product $\mathcal{P}^{(k,k)}\mathcal{Q}^{(k,k)}$. Figure 39 illustrates the energy transfer from input to output in a physical system, taking into account how the signal energy is distributed across the states before reaching the output. The contribution of each state is reflected by the product $\mathcal{P}^{(k,k)}\mathcal{Q}^{(k,k)}$. If this term is large, the state will likely impact the input-output system behaviour for a selected frequency range. In absolute terms, it may be difficult to derive meaningful conclusions from the product of the Gramian elements. When all states are considered, however, the terms can be normalised. The results of this normalisation outline the relative importance of an individual state.

3.1.6 Model Reduction Algorithm

The steps illustrated in Algorithm 1 should be followed to obtain a reduced-order model using the proposed method. First, the power system non-linear model should be linearised around an operating point, resulting in a linear state-space model.

Algorithm 1 Event-Based Model Reduction

Select system inputs $\mathbf{u}(t)$, outputs $\mathbf{y}(t)$ and operating point of the full-order model **Linearise** model to obtain a state-space representation according to Equations (50) and (51)

Choose a Gramian computation algorithm

Calculate the controllability ${\cal P}$ and observability ${\cal Q}$ Gramians

Calculate participation $p^{(k)}$ of states according to Equation (163)

Choose a participation threshold ε value serving as a boundary between states that will be included in the model and those that will be neglected

Residualise states with a participation lower than a selected threshold ε

Return reduced state-space model

The system's inputs and outputs are selected according to the study intended to be performed or based on the application the reduced-order model will have. This choice is essential as it directly affects the results. This is because the controllability is highly dependent on the inputs since it measures how those inputs can drive the system. Similarly, the observability depends on the choice of outputs because it measures the response "observed" from those outputs.

Care must be taken when selecting an algorithm for calculating the controllability and observability Gramians. The algorithm implemented in this thesis uses the MATLAB library function gram [118], which calculates the Gramians using Lyapunov equations with a full Gramian approach. This approach has a high computational cost $O(n^3)$ [119] and may not be appropriate for realistic large-scale systems. In this case, one of the several techniques proposed in the literature [120], [121] may be used to speed up computation as the proposed method is independent of the algorithm used to compute Gramians.

After computing the controllability and observability Gramians, one can assess how each state contributes to the system's input-output behaviour. A threshold needs to be established, which determines the minimum level of participation required for states to be incorporated into the model. Ultimately, the reduced model is derived by excluding the states that exhibit low participation based on this criterion.

3.2 Method 2: Model Reduction for Different Frequency Ranges

Method 2 for model reduction builds upon Method 1, enabling the analysis of the contribution of different components of the system broken down into frequency ranges as illustrated in Figure 40. Since this method shares some mathematical principles with Method 1, the fundamental theory will not be repeated here. Readers are encouraged to consult the previous section for those fundamentals.

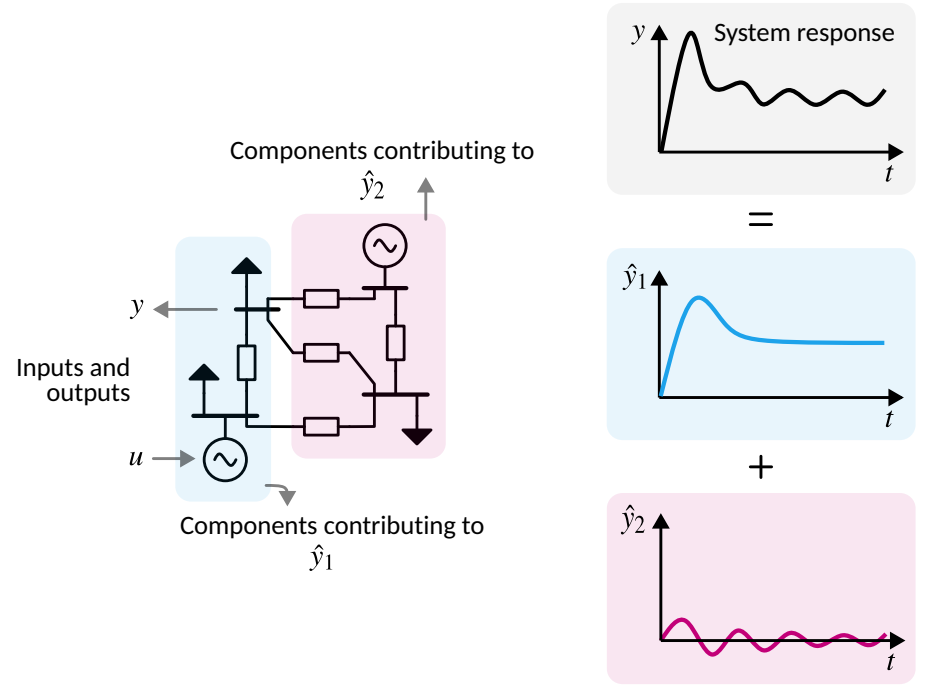


Figure 40: Diagram illustrating the application of Method 2 for model order reduction.

The participation defined in Equation (163) describes the impact of the state over the entire frequency range. When studying oscillation phenomena in specific frequency ranges, it is helpful to understand the participation of the states as a function of the frequency. Certain state variables may be more closely linked to faster or slower phenomena. For example, state variables related to the network tend to be associated with high-frequency transients; thus, models for quasi-steady-state studies discard those states. To this end, the concept of frequency-limited Gramians can be used to define the participation of the states in specific frequency ranges.

3.2.1 Frequency-Limited Gramians

Time-frequency duality and Parseval's theorem can be utilised to formulate the Gramians in the frequency domain based on their time-domain representations in Equations (87) and (88) [122]. The frequency-limited controllability and observability Gramians over the interval $[\omega_1, \omega_2]$, are derived as follows:

$$\mathcal{P}_{\omega} = \int_{\omega_1}^{\omega_2} (j\omega \mathbf{I} - \mathbf{A})^{-1} \mathbf{B} \mathbf{B}^* (-j\omega \mathbf{I} - \mathbf{A}^*)^{-1} d\omega, \tag{171}$$

$$\mathbf{Q}_{\omega} = \int_{\omega_1}^{\omega_2} (-j\omega \mathbf{I} - \mathbf{A}^*)^{-1} \mathbf{C}^* \mathbf{C} (j\omega \mathbf{I} - \mathbf{A})^{-1} d\omega.$$
 (172)

When the entire frequency range $(-\infty,\infty)$ is used, the calculation results in the *infinite* frequency-domain Gramians, defined as:

$$\mathcal{P}_{\infty}^{\omega} = \int_{-\infty}^{\infty} (j\omega \mathbf{I} - \mathbf{A})^{-1} \mathbf{B} \mathbf{B}^* (-j\omega \mathbf{I} - \mathbf{A}^*)^{-1} d\omega, \tag{173}$$

$$\mathbf{Q}_{\infty}^{\omega} = \int_{-\infty}^{\infty} (-j\omega \mathbf{I} - \mathbf{A}^*)^{-1} \mathbf{C}^* \mathbf{C} (j\omega \mathbf{I} - \mathbf{A})^{-1} d\omega, \tag{174}$$

where \mathcal{P}_{∞} and \mathcal{Q}_{∞} correspond to the infinite controllability and observability Gramians defined over the time interval $(-\infty, \infty)$.

Lastly, the relationship between time and frequency domain Gramians is expressed as [122]:

$$\mathcal{P}^{\omega}_{\infty} = 2\pi \mathcal{P}_{\infty},$$
 (175) $\mathcal{Q}^{\omega}_{\infty} = 2\pi \mathcal{Q}_{\infty}.$ (176)

$$\mathcal{Q}_{\infty}^{\omega} = 2\pi \mathcal{Q}_{\infty}.\tag{176}$$

3.2.2 Participation of a State Over a Frequency Range

By using Equations (171) and (172), the controllability and observability of a state can be measured in specific frequency intervals. They can then be used, in conjunction with Equation (163) to define the participation $p_{\omega}^{(k)}$ of the k-th state variable to the input-output system behaviour over the interval $[\omega_1, \omega_2]$. This results in:

$$p_{\omega}^{(k)} = \frac{\sqrt{\mathcal{Q}_{\omega}^{(k,k)} \mathcal{P}_{\omega}^{(k,k)}}}{\sum_{i=1}^{n} \sqrt{\mathcal{Q}_{\omega}^{(k,k)} \mathcal{P}_{\omega}^{(k,k)}}}.$$
(177)

Equation (177) provides a measure of which states have the highest participation in a frequency range and can thus be used to derive reduced-order models appropriate for studies of oscillations within a frequency range. This result is obtained without applying any coordinate changes to the state space.

3.2.3 Model Reduction Algorithm

A summary of the steps needed for obtaining a reduced order model is provided by Algorithm 2. As in Method 1, the inputs and outputs must be selected to define an event for which the system should be modelled. The system is linearised over an operating point, and the linearised system is represented in state space.

When obtaining a model for a specific frequency range, this range must be defined and used during the calculation of the Gramians according to Equations (171) and (172). The Gramians can then be used to calculate each state's participation in the input-output behaviour based on Equation (177). Based on the relative difference between the participation of the states, a set of the most relevant states can be chosen to represent the reduced-order model.

The states with the highest participation should be included in the models, while the remaining states may be safely neglected. In other words, Equation (177) provides a guideline for which parts of the physical system correspond to the most relevant states and must be modelled in detail and which ones can be simplified.

3.3 Case Study: Voltage Source Converter

This section revisits the case study presented in Chapter 2 to demonstrate how the proposed model reduction approaches can be applied to derive reduced-order models for a VSC

Algorithm 2 Model Reduction for Different Frequency Ranges

Select system inputs $\mathbf{u}(t)$, outputs $\mathbf{y}(t)$ and operating point of the full-order model **Linearise** model to obtain a state-space representation according to Equations (50) and (51)

Define the frequency interval of interest $[\omega_1, \omega_2]$

Choose a Gramian computation algorithm

Calculate the controllability \mathcal{P}_{ω} and observability \mathcal{Q}_{ω} Gramians within the frequency interval $[\omega_1, \omega_2]$

Calculate participation $p_{\omega}^{(k)}$ of states according to Equation (177)

Choose a participation threshold ε value serving as a boundary between states that will be included in the model and those that will be neglected

Residualise states with a participation lower than a selected threshold ε

Return reduced state-space model

converter connected to a grid equivalent. By applying the methods, the correspondence between states and the physical system is maintained, allowing for practical modelling insights to be derived from the analysis. This helps identify which aspects of the model are relevant for phenomena occurring in different frequency ranges.

3.3.1 Dynamic Analysis of the System

This section provides an initial analysis to better understand the expected dynamic behaviour of the system. The analysis reveals that the system has ten eigenvalues, all of which are well-damped. This is illustrated in Table 9, where the damping ratios are highlighted. For this study, an eigenvalue is considered well-damped if its damping ratio exceeds 5%. This criterion is determined based on the generally accepted damping ratio standards established by transmission system operators, which typically range from 3% to 5% [12, 123].

Eigenvalue	Natural frequency (Hz)	Damping ratio (%)	
$-1760.5 \pm j145.2$	281.1	99.7	
$-217.3 \pm j218.5$	49.2	70.3	
$-181.4 \pm j240.4$	47.9	60.2	
$-33.6 \pm j41.9$	8.5	62.6	
-8.7	1.4	100	
-5.8	0.9	100	

Table 9: List of eigenvalues for the reference VSC case study.

Sensitivity to PLL Tuning

Subsequently, the sensitivity of the system to PLL tuning is examined. This evaluation is conducted by altering the PLL response time and assessing its impact on the system modes. For the assessment, the PLL response time $t_{r,pll}$ is modified from 50 ms, the original value, to 5 ms, which represents a substantially faster response time. Figure 41 illustrates the complex plane, where eigenvalues corresponding to various values of the PLL response time $t_{r,pll}$ are plotted. Each response time is represented by a distinct colour, as indicated by the colourmap on the right of the figure. As the PLL response time decreases, certain modes appear to be improved, shifting toward the left side of the complex plane. However,

one system mode, indicated by a dashed rectangle in the figure, moves to the right side of the complex plane. Initially, this mode becomes poorly damped, and at the lowest response time values, it transitions to an unstable state.

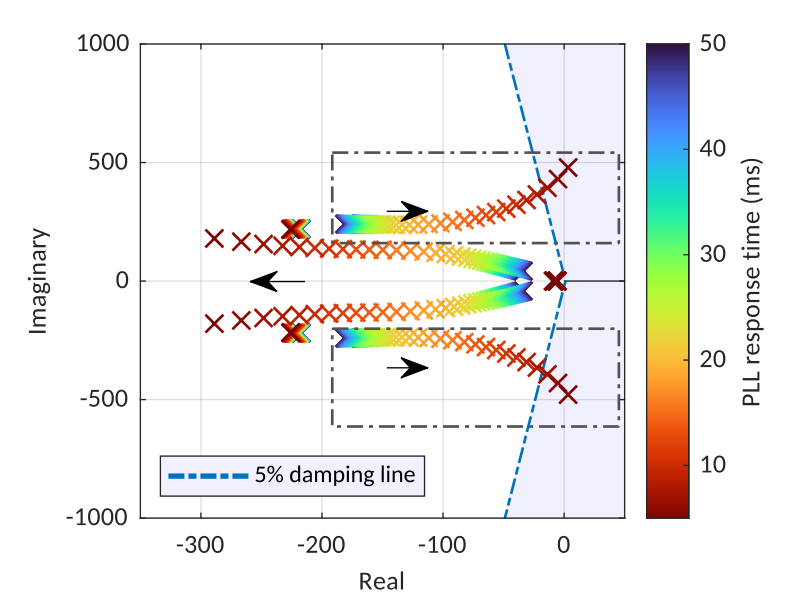


Figure 41: Complex plane illustrating the variations in eigenvalues across different values of PLL response time.

System Behaviour for Fast PLL Tuning

Understanding that variations in the PLL response time have implications for certain modes, the system characteristics are subsequently analysed immediately before instability arises, specifically at a response time of $t_{r,pll}$ equal to 6 ms. Under these conditions, the system features ten eigenvalues, as detailed in Table 10. The eigenvalues marked in green demonstrate improved damping ratios in comparison to the reference case results outlined in Table 9. Notably, one pair of eigenvalues, denoted in red, exhibits inadequate damping with a ratio of 1.2%.

Table 10: List of eigenvalues for the VSC case study corresponding to a faster PLL response time of $t_{r,pll}$ equal to 6 ms.

Eigenvalue	Natural frequency (Hz)	Damping ratio (%)	
$-1740.9 \pm j149.5$	278.1	99.6	
$-5.0 \pm j430.2$	68.5	1.2	
$-226.0 \pm j218.0$	50.0	72.0	
$-266.6 \pm j166.1$	50.0	84.9	
-8.5	1.4	100	
-5.9	0.9	100	

In order to examine which modes experienced improvements in damping and which modes encountered deteriorations, as well as to gain an understanding of the components associated with each oscillation mode, an analysis of participation factors is conducted. The participation factors of the eigenvalues that suffered significant changes in damping, as highlighted in Table 10, are illustrated in Figure 42. The participation factors indicate that the mode $-5.0\pm j430.2$, which demonstrated a worsening in damping, is predominantly linked to the states associated with the PLL and with the AC current. Conversely, the other mode that exhibited improved damping, $-226.0\pm j218.0$, is associated with the AC current and AC inner current control. Lastly, $-266.6\pm j166.1$ has also shown improvements in damping and is associated with the PLL, AC currents, and current control.

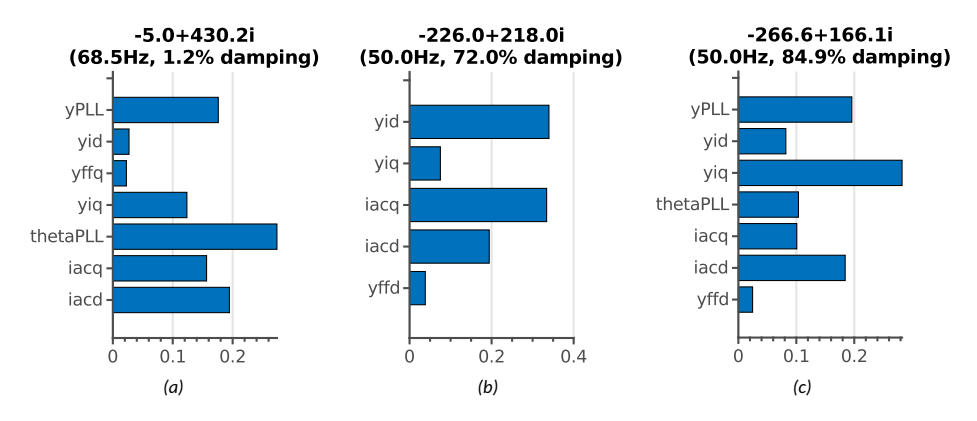


Figure 42: Participation factors showing states involved in the (a) mode whose damping has become worse and the (b) and (c) modes which experienced improved damping.

The detrimental effect of increasing the PLL response time can be attributed to the fact that the system is weak at the PCC, with an SCR of 2.49. Consequently, this situation increases the likelihood of oscillations arising from the PLL.

Finally, to assess the system's time-domain response, an active power step of 0.02 p.u. was applied at t=0.1 s. Figure 43 illustrates both the active power setpoint P_{ac}^* and the measured active power P_{ac}^{meas} . The measured active power follows the reference value. However, it is important to note that the power response displays oscillations, which can be attributed to the inadequately damped mode identified previously.

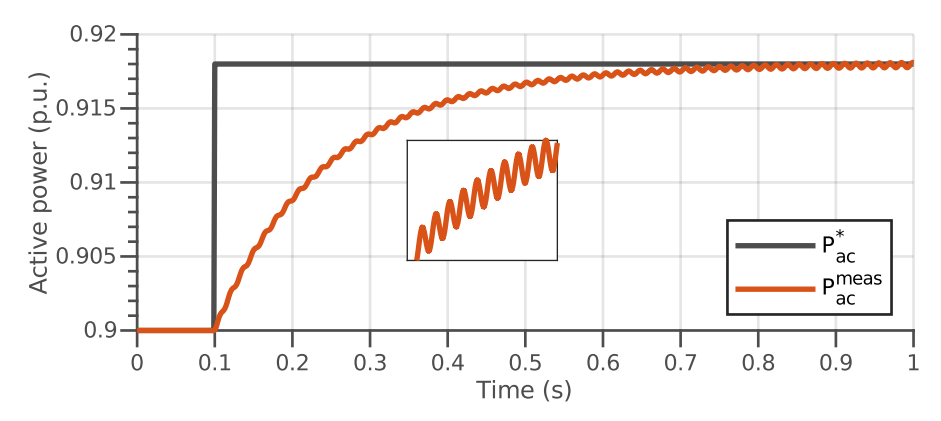


Figure 43: Time-domain response of the measured active power to a step in the active power reference.

3.3.2 Application of Method 1

In this subsection, Method 1 is applied to both system conditions analysed previously: one with a slow PLL characterised by a rise time of $t_{r,PLL} = 50$ ms and another with a fast PLL corresponding to $t_{r,PLL} = 6$ ms. The results are then compared.

To implement Method 1 of model order reduction, the first step is to derive a state space representation of the model. This requires selecting the appropriate inputs and outputs. In this context, the dq frame grid voltages U^d_{grid} and U^q_{grid} are designated as the model inputs, while the measured AC currents in the dq frame I^d_{ac} and I^q_{ac} are selected as the outputs. The state space model consists of 10 state variables \mathbf{x} , as follows:

$$\mathbf{x} = \begin{bmatrix} y_{ffd} & I_{ac}^d & I_{ac}^q & \theta_{pll} & y_q & y_{iq} & y_{ffq} & y_p & y_{id} & y_{pll} \end{bmatrix}^T, \tag{178}$$

where y_p and y_q represent the states corresponding to the active and reactive power controller integrators, y_{ffd} and y_{ffq} are associated with the voltage feedforward states, y_{id} and y_{iq} are the states associated with the current control integrators, and θ_{pll} and y_{pll} denote the states connected to the PLL.

The method is initially demonstrated for the system with a slow PLL. As introduced in Section 3.1, it is necessary to calculate the controllability and observability Gramians in accordance with Equations (87) and (88), respectively. The diagonal elements of the Gramians corresponding to each state are presented in the second and third columns of Table 11. Utilising these two values, one can compute the product $\sqrt{\mathcal{Q}^{(k,k)}\mathcal{P}^{(k,k)}}$ for each state, which is shown in the fourth column of the same table. This product serves as an indicator of the effectiveness with which signals are transferred from input to output via each of the states. Upon normalisation, these results yield the participation of each state in the input-output behaviour, as defined in Equation (163). The table illustrates that a state's participation is influenced by both its controllability and observability. A state exhibiting high controllability, yet lacking observability, or vice versa, will produce a low participation coefficient. The steps outlined here correspond to those in Algorithm 1.

In Table 11, the states that significantly influence the system's input-output behaviour are highlighted for the scenario involving slow PLL tuning. Meanwhile, Table 12 provides a similar analysis for the system with fast PLL tuning. Comparing the results from these two tables reveals several important observations. Firstly, in the case of slow PLL tuning, the dynamics of the active and reactive power controls are more pronounced, as indicated by the high participation of the states y_p and y_q . Although there are no poorly damped modes in this scenario, the PLL states, θ_{pll} and y_{pll} , play a significant role in the system dynamics. Conversely, in the scenario with fast PLL tuning, the active and reactive power controls have a negligible impact. However, there is an increased participation from the PLL states, along with contributions from the grid currents and inner current control loops. This observation aligns with findings from modal analysis, which suggest the presence of a poorly damped mode resulting from the interaction between the PLL, inner current controls, and grid elements, represented by the AC currents.

3.3.3 Application of Method 2

Method 2 of model order reduction facilitates the identification of the appropriate level of modelling details necessary across various frequency ranges. This section will illustrate the process.

Initially, the controllability and observability Gramians are computed using frequency intervals of 10 rad/s, which are deemed sufficiently small for the intended analysis. The diagonal elements of the Gramians are combined according to Equation (163) to calculate the participation of each state in the input-output behaviour across frequencies from 1 to

Table 11: Step-by-step calculation of states' participation in the input-output behaviour for a system with a slow PLL tuning characterised by $t_{r,PLL} = 50$ ms.

State variable	Controllability $\mathcal{P}^{(k,k)}$	Observability $\mathcal{Q}^{(k,k)}$	$\frac{Product}{\sqrt{\mathcal{Q}^{(k,k)}\mathcal{P}^{(k,k)}}}$	Participation $p^{(k)}$
y_{ffd}	0.00	225.78	0.16	0.04
$Y_{ffd} \ I_{ac}^d \ I_{ac}^q$	67.10	0.00	0.33	0.08
I_{ac}^{q}	116.92	0.00	0.45	0.12
$ heta_{pll}$	115.72	0.01	0.98	0.23
y_q	2.41	0.07	0.42	0.10
y_{iq}	5.92	0.00	0.14	0.03
y_{ffq}	0.00	251.12	0.17	0.04
y_p	18.11	0.05	0.98	0.23
Уid	1.46	0.00	0.06	0.02
y_{pll}	123530.00	0.00	0.54	0.13

Table 12: Step-by-step calculation of states' participation in the input-output behaviour for a system with a fast PLL tuning characterised by $t_{r,PLL} = 6$ ms.

State variable	Controllability $\mathcal{P}^{(k,k)}$	Observability $\mathcal{Q}^{(k,k)}$	$\frac{Product}{\sqrt{\mathcal{Q}^{(k,k)}\mathcal{P}^{(k,k)}}}$	Participation $p^{(k)}$
y_{ffd}	0.00	4185.33	1.67	0.02
I_{ac}^{d}	9307.15	0.04	20.04	0.19
$I^d_{ac} \ I^q_{ac}$	16454.82	0.02	16.94	0.16
$ heta_{pll}$	29910.56	0.03	28.29	0.27
y_q	21.47	0.10	1.49	0.01
Уiq	3873.90	0.04	13.15	0.12
y_{ffq}	0.00	7725.36	2.53	0.02
y_p	25.94	0.07	1.33	0.01
Уid	332.77	0.02	2.88	0.03
\mathcal{Y}_{pll}	2260445905.17	0.00	18.27	0.17

 10^4 rad/s. The results are presented in Figure 44 and are grouped according to the parts of the physical system that the states represent. Furthermore, the frequency is measured from the stationary dq reference frame, indicating that, for example, 0 rad/s in the results corresponds to the nominal system frequency.

In Figure 44, the frequency spectrum was divided into three parts, highlighting low, medium, and high-frequency ranges to facilitate the analysis. In the initial portion of the low-frequency range (from 1 to 100 rad/s), highlighted in green in Figure 44, only states associated with active and reactive power controls contribute to the system behaviour. If the model is used to study phenomena in that frequency range, all other controls may be simplified or neglected. In addition to that, the AC equations can be represented by their steady-state formulation. RMS simulations typically use these types of models [124,125] where the frequencies of interest are only those around the nominal frequency. Thus, the results are in line with widely used modelling practices. The upper portion of the low-frequency range becomes increasingly affected by the dynamics of the PLL. This points to the importance of including detailed PLL models even for RMS simulations.

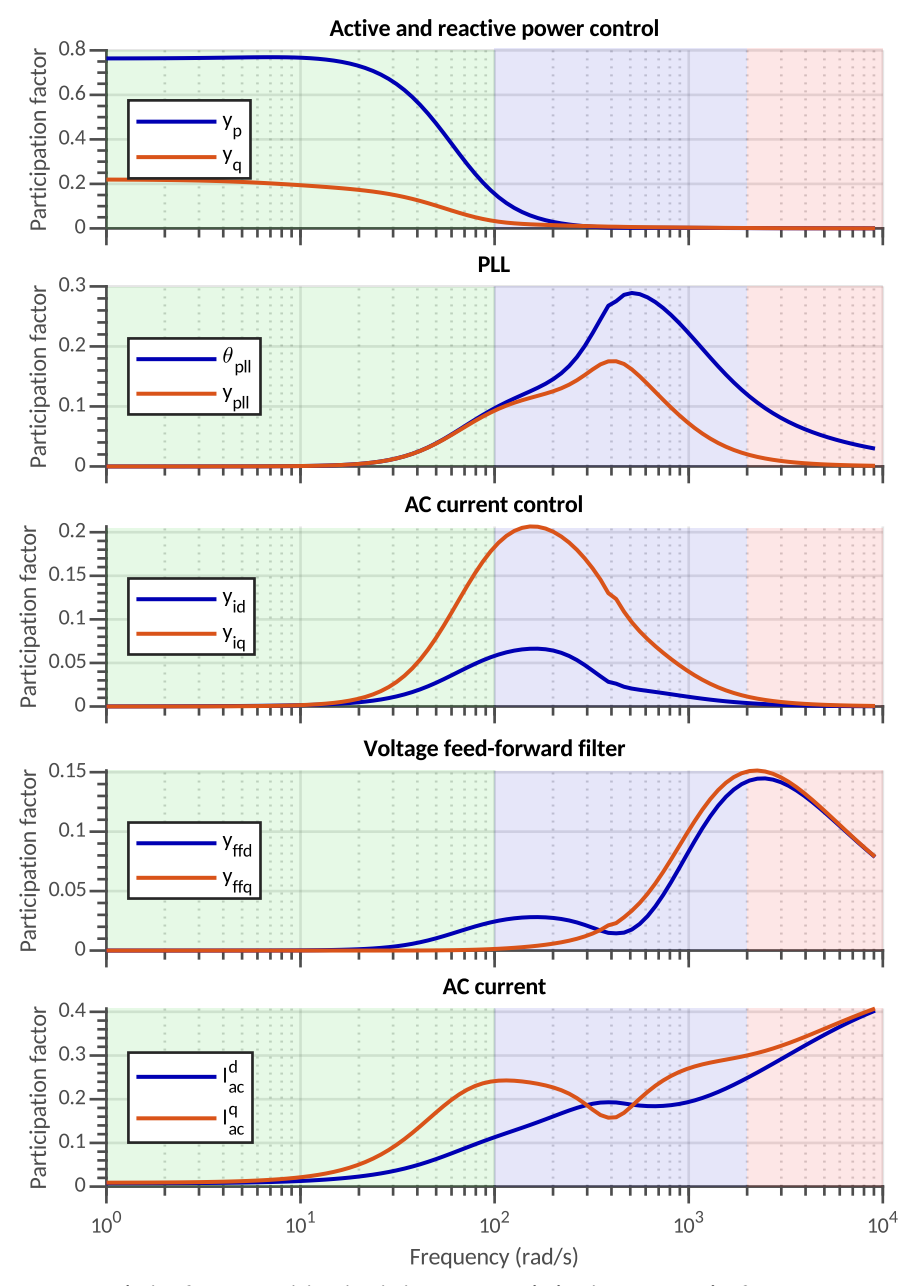


Figure 44: Analysis of state participation in input-output behaviour across the frequency spectrum. The low, medium, and high frequency ranges are indicated in green, blue, and red, respectively, to illustrate their distinct contributions.

The middle-frequency range (100 to 2000 rad/s) highlighted in blue shows varying contributions from several system and control components, except for the power controls. The frequency range in which each of the control loops becomes prominent is in line with the control bandwidths expected considering the tuning parameters used (found in Table 6). This is the frequency range where the RMS models relying on steady-state

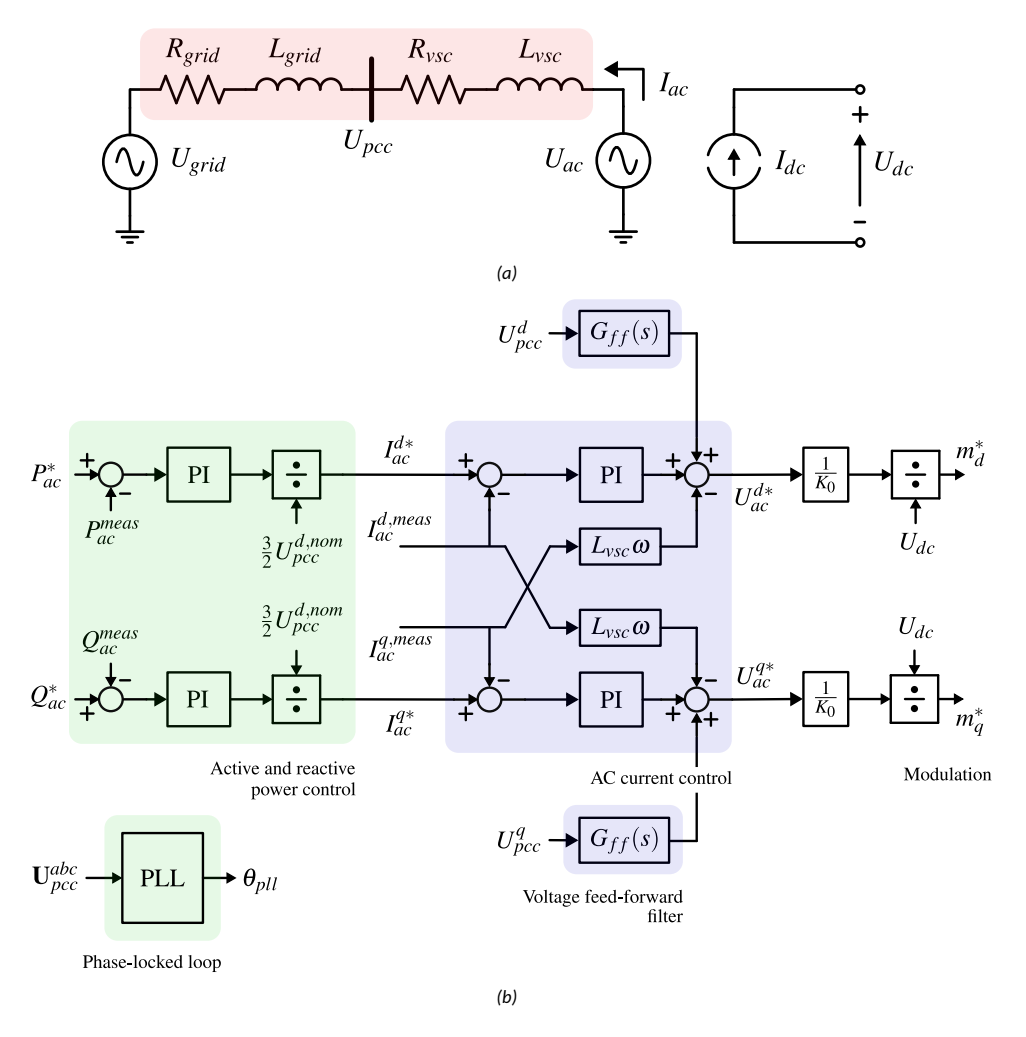


Figure 45: Diagram illustrating the (a) VSC model connected to the AC network and (b) the VSC control system.

network representation might no longer be applicable since the AC current state variable has increased participation in the system behaviour.

Finally, the AC current dominates the system response in the high-frequency range (higher than 2000 rad/s), highlighted in red. However, the full-order model selected for the study case reaches its limitations in this frequency range. More complex models, including PWM and switching elements, should be considered when analysing this frequency region to obtain meaningful conclusions. The study in this paper does not cover this.

As a visual summary, the importance of each part of the VSC model in the three frequency ranges is highlighted in the corresponding colours in Figure 45. This result clearly outlines that the proposed approach can directly provide meaningful insights into the importance of modelling each part of a system for different frequency applications.

Reduced-Order Model Development

To illustrate the application of Method 2, a reduced-order model is derived with the assumption that it will be employed for studies in the low-frequency range. The results from Figure 44 guided the selection of which states to include and which to omit. Based on these results, the reduced model neglects the AC current control and voltage feed-forward filter and represents the AC equations in steady-state. Only the state variables associated with the active and reactive power controls and the PLL are preserved. This procedure was carried out by an algorithm implemented in MATLAB, as detailed in Algorithm 1. The algorithm had a total execution time of 0.788 s, of which 0.002 s was allocated for the computation of the Gramians. By employing this technique, a 4th order VSC reduced model is obtained.

Figure 46 illustrates the response comparison between the full and reduced models to a 5% step increase in active power setpoint applied at t=0.05 s. The response of the full-order model has two components: an exponential term and an oscillatory term with frequency $\omega_{osc} \approx 306$ rad/s.

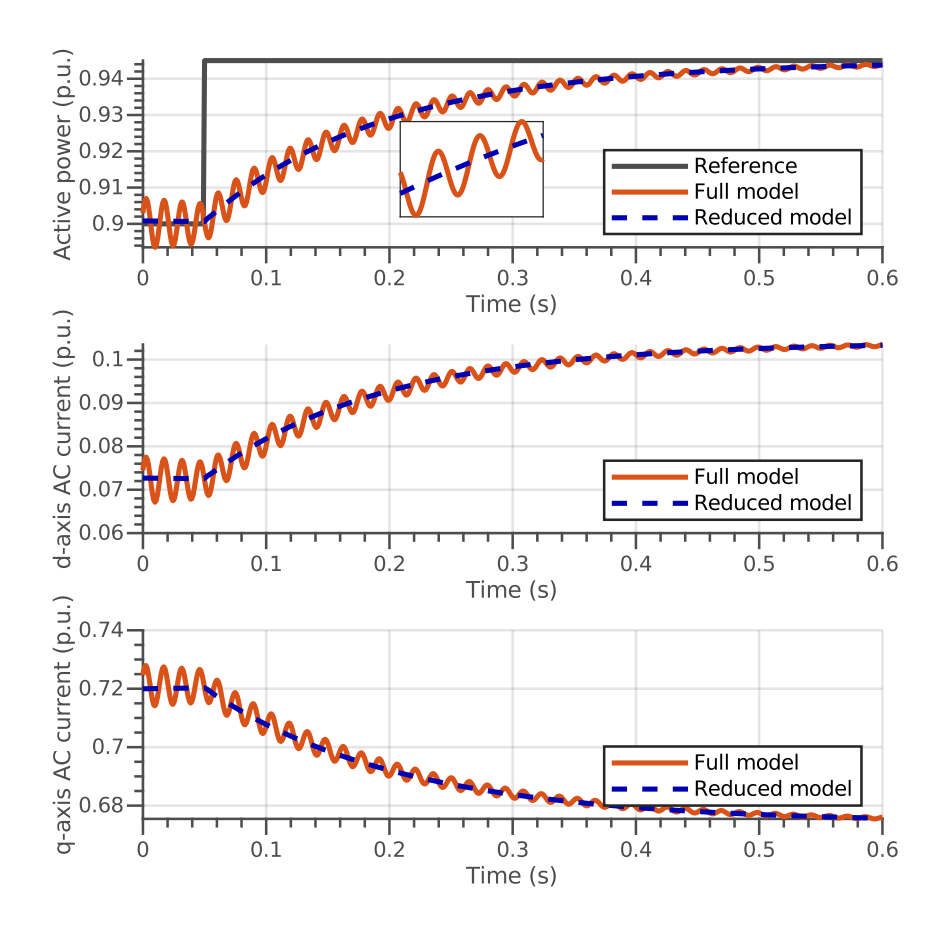


Figure 46: Response comparison between full and reduced models to a 5% step in active power setpoint.

The developed reduced-order model only represents the exponential term of the full model response. The results in Figure 46 indicate that the model reduction technique behaves as expected. The fact that the oscillatory term is not present in the reduced model response is further confirmed by Figure 44 where it is shown that at that frequency value, the AC current, AC current controls, and voltage feed-forward have a significant contribution. These modelling details are not included in the reduced model. These findings indicate that the proposed model reduction approach successfully approximates the full-order model in the low-frequency range.

3.4 Conclusion

This chapter introduced two methods for MOR, adapted from the balanced truncation approach introduced in Chapter 2. Method 1 generates a simplified model that approximates the system's response to a specific disturbance. The chapter explained how to compute the approximation error between the outputs of the full- and reduced-order systems. From this error, a heuristic is derived to assess a state's influence on the system's input-output behaviour, resulting in the definition of a participation coefficient for each state. Additionally, the chapter provides a physical interpretation of the method, along with an algorithm outlining the process of obtaining a reduced-order model.

Method 1 was then extended to consider specific frequency ranges by employing the concept of frequency-limited Gramians. This enabled the measurement of controllability and observability of a state within a particular frequency range, leading to Method 2, for which an algorithm overview was also included.

Subsequently, a case study was developed consisting of a VSC connected to a grid equivalent. The two methods were applied to demonstrate how the participation coefficient can evaluate the importance of different parts of the model in the system's response. Guidelines were established identifying the frequency ranges in which different model components and controls play a critical role. Lastly, a reduced-order model was developed to represent the system's response in low-frequency ranges.

Chapter 4 will illustrate how Method 1 is used to create a tool to visualise the components that most influence system dynamics.

4 Tool for Modelling and Analysis of Power System Dynamics

This chapter presents a MATLAB/Simulink tool developed based on Method 1 for model order reduction discussed in Chapter 3. The tool enables users to visualise and easily determine the level of detail required for modelling each component of a power system. This ensures an accurate stability analysis while avoiding an unnecessary computational burden. This chapter begins by outlining the implementation process of the tool, detailing each step involved. Additionally, two case studies are included to demonstrate the tool's application in analysing converter-dominated power systems. The content of this chapter is based on Publications II and IV.

4.1 Tool Description

The proposed Method 1 of MOR has been implemented as a tool, following the steps illustrated in Figure 47. This section explains how the tool operates, detailing the steps that the user needs to perform, as well as the processes executed independently by the tool to generate the results. The outcome is a visualisation that highlights which parts of the system contribute most significantly to the system response.

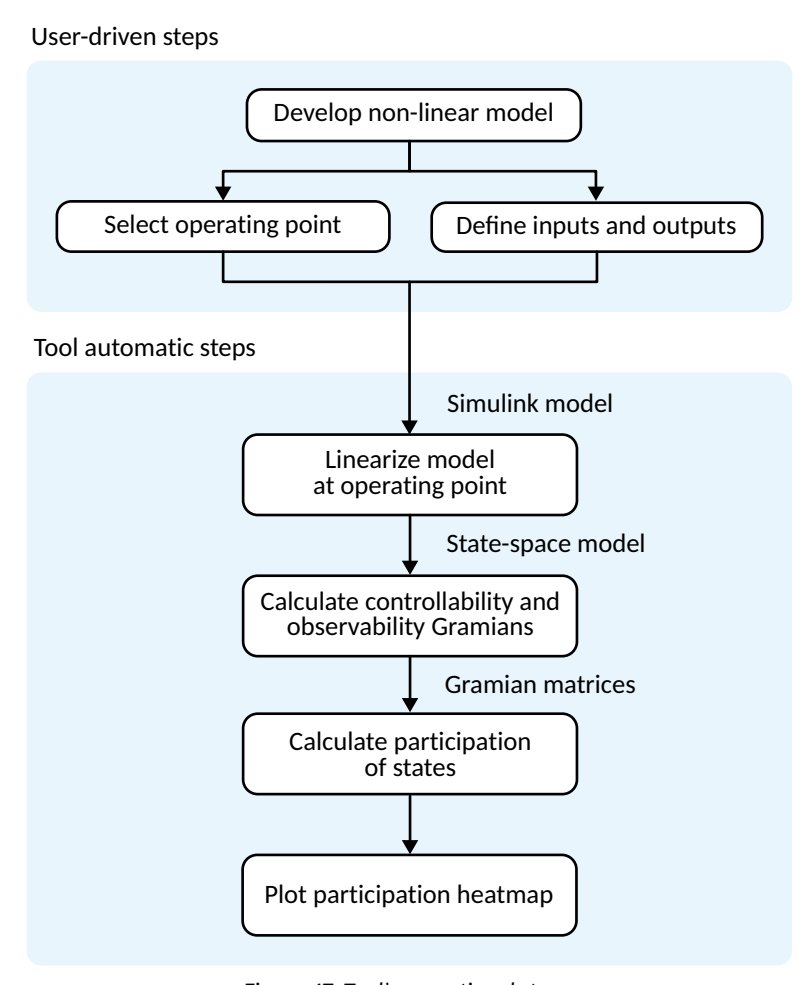


Figure 47: Tool's operational steps.

Model Implementation and Selection of Inputs and Outputs

Users must initially implement the power system model using the Simscape library in Simulink. The model can include both linear and non-linear elements, which will be later linearised.

In Simulink, the inputs and outputs of the system are defined by specifying the linear analysis points. The specification of these inputs and outputs is crucial since the MOR method assesses state participation based on input-output behaviour. Therefore, the selection of inputs and outputs has a significant influence on the results. This is because the controllability is highly dependent on the inputs as it measures how those inputs can drive the system. Similarly, the observability depends on the choice of outputs because it measures the response observed from those outputs. Inputs and outputs should be selected based on the study's objectives or the model's intended application. As a result, the tool may not be suitable for analysing instability due to unobservable or uncontrollable states.

Additionally, this step can be performed programmatically using the linio command in MATLAB [126] followed by the Simulink block name, port number, and type of linear analysis point, that is, input for the system's inputs and output for the system's outputs.

Definition of Operating Point

Because the tool utilises linear analysis, users need to define the operating point for the model linearisation. This operating point can be established either statically by assigning initial values to each component or dynamically by capturing a snapshot of the system's states after a period of simulation.

Model Linearisation

After specifying the inputs and outputs, the non-linear model of the power system must be linearised at the chosen operating point. In the tool implementation, the linearisation is performed by the linearize function [118] from the Control System Toolbox in MATLAB to derive the linear state-space model.

Gramian Calculation

After obtaining the state-space model, the tool determines the matrices corresponding to the observability and controllability Gramians. These matrices are derived by solving the corresponding Lyapunov equations using the gram [118] function available in the MATLAB Control System Toolbox. To compute the controllability Gramian, denoted as \mathcal{P} , the following continuous-time Lyapunov equation needs to be solved:

$$\mathbf{A}\mathcal{P} + \mathcal{P}\mathbf{A}^{\mathbf{T}} = -\mathbf{B}\mathbf{B}^{\mathbf{T}}.\tag{179}$$

In the same way, the observability Gramian ${\cal Q}$ is found by solving the equation:

$$\mathbf{A}^{\mathrm{T}} \mathbf{Q} + \mathbf{Q} \mathbf{A} = -\mathbf{C}^{\mathrm{T}} \mathbf{C}. \tag{180}$$

It is essential to note that the algorithmic complexity and performance of the tool depend significantly on the difficulty of calculating the controllability and observability Gramians. Solving the Lyapunov equations involves a high computational cost of $\mathcal{O}(n^3)$ [119] and does not scale effectively to realistically large systems. Nonetheless, various methods in the literature can help reduce this computational burden [120, 121]. For instance, low-rank Gramian approximations can efficiently compute the Gramians by deriving an approximate Gramian matrix in both time and frequency domains.

Participation of States

After computing the Gramians, the participation of each state is determined using Equation (163). In this process, it is advisable to model the system using per unit (p.u.) values to prevent the emergence of ill-conditioned matrices. This potential issue has been noted during the tool's practical application.

Results Visualization

Finally, the contribution of each component within the system is determined by evaluating the involvement of all state variables in the model associated with that component. This computed value is then normalised and utilised to generate a heatmap, highlighting the areas of the power system most significantly involved in the observed oscillation phenomenon.

4.2 Case Study 1: Converter-Dominated 9-Bus System

This section presents one of two case studies designed to demonstrate the efficacy of the proposed tool and model order reduction method in developing reduced-order models for a converter-dominated 9-bus system.

4.2.1 Model Description

The converter-dominated 9-bus system is derived from [55] and is illustrated in Figure 48. In this modified case study, two synchronous generators were replaced with two-level VSC converters, transforming the test system into one that is primarily converter-based. The modified system contains 84 state variables. The subsequent sections will present an overview of the models employed for the various components.

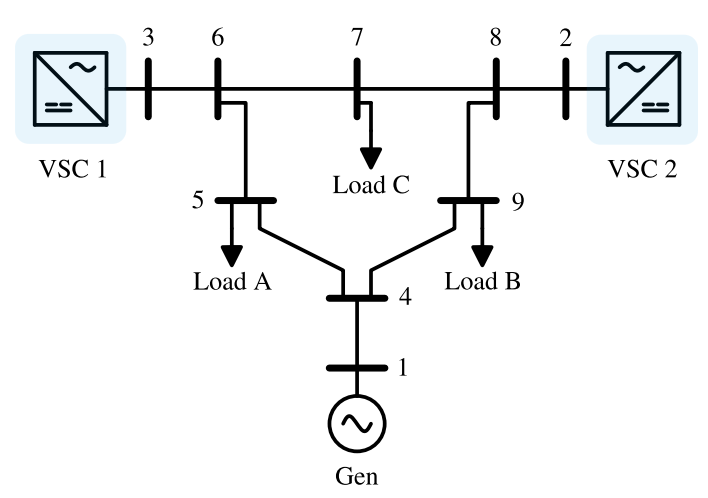


Figure 48: Diagram of the converter-dominated 9-bus system.

Generator

The generator, identified as Gen, was represented using the classical model, which consists of a constant voltage source behind a transient reactance. This model is extensively utilised in screening studies to obtain preliminary insights into the system's performance, particularly for generators located far from the disturbance point. Furthermore, the classical

model neglects electromagnetic dynamics and assumes a constant field voltage, resulting in a constant electromotive force.

Transmission Lines

A lumped-parameter π -circuit model has been selected to represent the behaviour of the transmission lines. This model includes phase resistance, phase self-inductance, lineline mutual inductance and resistance, line-line capacitance, and line-ground capacitance, which makes it appropriate for short to medium-length transmission lines. It assumes that the total line resistance, inductance, and capacitance are concentrated at a single point, thereby neglecting the effects of electromagnetic travelling waves. The parameters are evaluated at the nominal frequency.

Loads

A static load model characterised by constant parameters was employed to represent the loads. In this model, each phase includes a resistance R, inductance L, and capacitance C connected in parallel. The three phases are interconnected in a Y configuration. This model is also referred to as the constant Z load model, and it represents the active and reactive power at any given moment as functions of the frequency and bus voltage magnitudes.

Each phase contains two state variables: the current through the inductor i_l and the voltage across the capacitor v_c . The following equation is applicable:

$$\frac{d}{dt} \begin{bmatrix} i_l \\ v_c \end{bmatrix} = \begin{bmatrix} 0 & \frac{1}{L} \\ -\frac{1}{C} & -\frac{1}{RC} \end{bmatrix} \begin{bmatrix} i_l \\ v_c \end{bmatrix} + \begin{bmatrix} 0 \\ \frac{1}{C} \end{bmatrix} i_{load},$$
(181)

where i_{load} represents the total current in the load branch for a single phase.

Voltage Source Converters

An averaged-value model has been employed for the VSCs, as detailed in Section 2.4.1. In this model, a controlled voltage interfaces with the AC side while a controlled current source is connected to the DC side. Furthermore, the switching harmonics are neglected. The model consists of an AC current control, a PLL, and active and reactive power controls. For simplicity, voltage feed-forward filters were omitted.

4.2.2 Model Implementation

This model was implemented in MATLAB/Simulink, taking into consideration the operation point specified by the active and reactive powers presented in Table 13. This table also lists the parameters utilised for the control systems of both VSCs. It is worth mentioning that VSC 1 exhibits a significantly faster response time compared to VSC 2. This behaviour is due to the more rapid control tuning of VSC 1 with an active and reactive power control time constant τ_{pq} of 10 ms, a PLL time constant τ_{pll} of 6 ms and a current control time constant τ_{idq} of 1 ms.

Finally, an X/R ratio of 20 was employed for the synchronous generator, and the SCR was varied throughout the study. All other system parameters were adopted from the original test system, as detailed in [55].

4.2.3 Dynamic Analysis of the System

The objective of this section is to analyse the system dynamics and the effects of system strength variations on the modelling requirements for the converter-dominated 9-bus

Table 13: VSC parameters for the converter-dominated 9-bus system case study.

Name	Symbol	Values	
	· · · · · · · · · · · · · · · · · · ·	VSC 1	VSC 2
Rated apparent power	S_{rated}	200 MVA	100 MVA
Active power setpoint	P_{ac}^*	163 MW	85 MW
Reactive power setpoint	Q_{ac}^*	-10.9 Mvar	5 Mvar
DC bus voltage	U_{dc}	640 kV	640 kV
AC bus voltage	U_{pcc}	230 kV	230 kV
VSC equivalent inductance	L_{vsc}	82.70 mH	$82.70 \mathrm{mH}$
VSC equivalent resistance	R_{vsc}	1.03Ω	1.03Ω
AC current control time constant	$ au_{idq}$	1 ms	10 ms
AC current control damping ratio	ζ_{idg}	0.7	0.7
PLL time constant	$ au_{pll}$	6 ms	50 ms
PLL damping ratio	$\dot{\zeta}_{pll}$	0.7	0.7
Active/reactive power control time constant	$ au_{pq}$	10 ms	100 ms

system. For this purpose, the internal SCR of the synchronous generator is varied. The SCR values discussed in the subsequent analysis refer to the SCR at the terminals of the generator. Given that the system contains only a single generator, a reduction in the generator's SCR will consequently influence the corresponding SCRs values at the terminals of the VSCs. In other words, decreasing the generator's internal SCR weakens the entire system.

Modal Analysis

Initially, the system behaviour is investigated through modal analysis. As the SCR at the generator terminals is reduced, the system eigenvalues are computed for each SCR level. Figure 49 presents the results of this analysis. The eigenvalues associated with each SCR are plotted in a corresponding colour, allowing the visualisation of how the oscillation modes evolve as the system weakens. The arrows on the graph indicate the movement of specific eigenvalue groups. Additionally, Figure 49 includes the 5% damping ratio line, and the area in blue represents all poorly-damped eigenvalues, defined as those with equal or less than 5% damping. This threshold is defined based on the typical criteria for adequate damping ratios defined by transmission system operators, which range from 3% to 5% [12,123].

Figure 49 illustrates that the system contains several poorly damped modes in the blue area. Two distinct groups of modes are highlighted and identified as Group 1 and Group 2. In Group 1, it can also be observed that the mode is well-damped when the system is strong, shifting to the right side of the complex plane, becoming poorly damped and unstable as the system's strength decreases.

To determine the underlying causes of these poorly damped eigenvalues, the participation factors were computed. For illustration purposes, the participation factors were calculated for the system when the generator's SCR is 4, and the results are displayed in Figure 50. The most significant states are listed for each mode. For brevity, transmission lines are denoted by abbreviations; for instance, TL96 refers to the transmission line connecting buses 9 and 6.

Group 1 is associated with an oscillatory mode with an approximate frequency of 75.6 Hz, which exhibits negative damping, indicating that the mode is unstable. The participation factors reveal that this mode primarily involves the PLL, as illustrated in Figure 50 (a), where

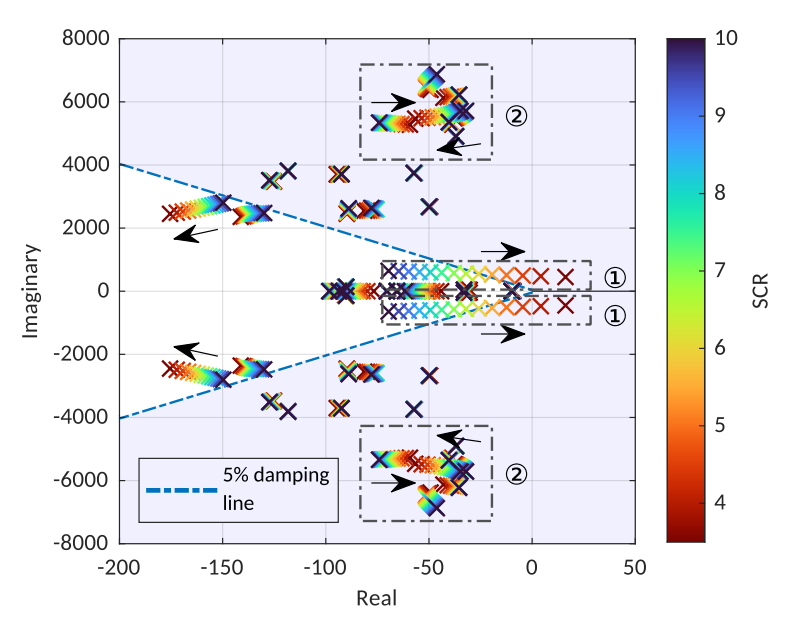


Figure 49: Complex plane illustrating the variations in eigenvalues across different values of SCR. The blue dash line represents the 5% damping line.

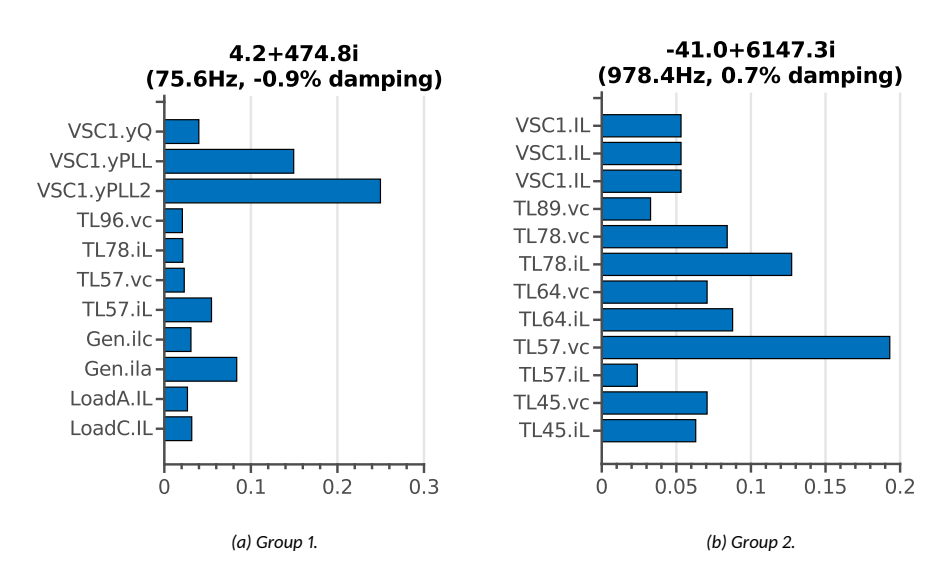


Figure 50: Participation factor of modes associated with (a) PLL instability and (b) network resonant modes.

the PLL state variables show the largest contributions. Group 2 contains high-frequency poorly damped modes characterised by frequencies ranging from 1000 Hz to 800 Hz, with a damping ratio reaching as low as 0.7%. Figure 50 (b) shows the participation factor for the group's lowest damped mode as an example. The findings suggest that these modes are network resonance modes involving converter impedances and impedances of transmission lines.

The results further illustrate that even a relatively simple system, consisting of 9 buses and 84 states, contains a significant number of modes. Many of these modes have poor damping, potentially leading to oscillations in the system. However, modal analysis alone fails to provide clarity regarding which modes are excited or identify those dynamics that may raise concerns. In other words, modal analysis does not lead to conclusions about which modes are relevant and should be modelled and should be complemented with time-domain simulations to understand which modes are actively excited. Moreover, precisely quantifying each element's participation in the overall system dynamics is challenging because modal analysis is focused on specific modes rather than the total behaviour of the system.

Time-Domain Verification

Finally, to validate the results, a time-domain analysis is performed by observing the dynamic behaviour of VSC 1 for different values of Gen's internal SCR. Figure 51 shows the response to a reactive power step change of $\Delta Q=0.05$ p.u. The response contains oscillations that become less damped as the system strength decreases, indicating that some but not all oscillatory modes identified in the modal analysis were excited. By estimating the frequency of oscillations, it is possible to identify that they match the mode associated with the PLL instability.

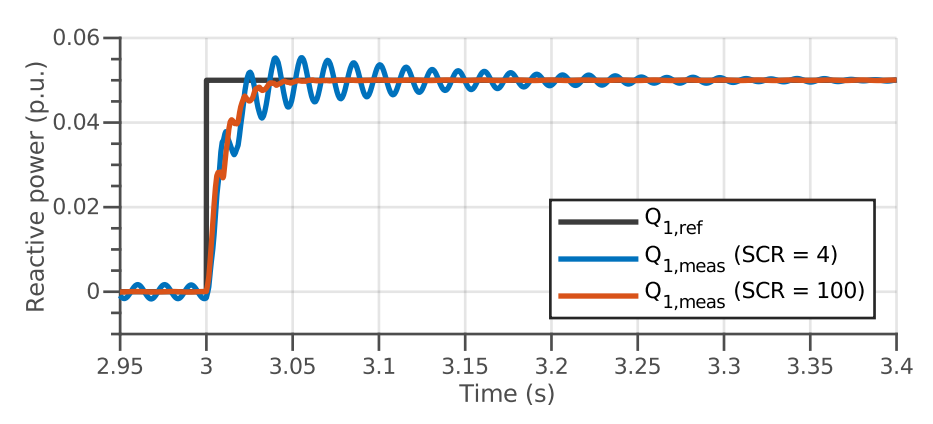


Figure 51: Dynamic behaviour of VSC 1 to a reactive power step.

4.2.4 Application of Model Reduction Method 1

Model reduction Method 1, as outlined in Chapter 3, offers an alternative solution to the challenges encountered in the previous section, quantifying how much each system element contributes to the global dynamics. For illustration, this method was employed in the case study following the procedures detailed in Algorithm 1 presented in Section 3.1.6. The reactive power reference was selected as the input, while the measured reactive power served as the output to linearise the model. Using the state-space model, the

Gramians are computed and subsequently employed to assess the overall participation of each component using Equation (163).

This procedure is applied to determine which models should be used, highlighting the relevant modelling details, particularly as the generator's SCR is lowered. Figure 52 illustrates the contribution of the most significant states in the input-output response of the system across varying SCR levels. It reveals that when the system is strong, its dynamics are primarily influenced by the response of the reactive power controller. However, as the system weakens, the contribution of the reactive power controller becomes less pronounced, and the PLL becomes the dominant factor in the overall dynamic response. In both scenarios, the participation of each transmission line remains relatively low. However, when considering their combined contribution, these lines significantly impact the behaviour of the system. Furthermore, the relative importance of the generator impedance with respect to the network increases significantly when the system is weak.

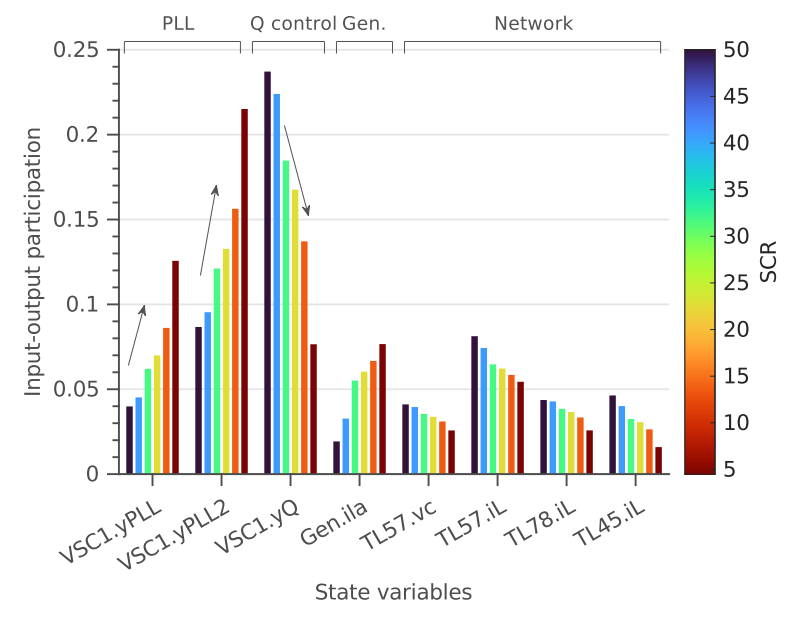


Figure 52: Contribution of state variables to the input-output dynamics according to varying levels of generator SCR.

Subsequently, it is important to consider how these results can guide the selection of appropriate models for system studies. In the scenario of a strong system, the reactive power control must be modelled in detail, while faster controls may be simplified or neglected. Furthermore, the VSC AC-side equations can be expressed by their steady-state formulation, as the states associated with the VSC impedance do not significantly impact the system's behaviour based on the results from Figure 52. This suggests that, in many cases, RMS simulations could be adequate [125] where the frequencies of interest are limited to only those around the nominal frequency. As the system becomes weaker, the PLL assumes greater importance in the system dynamics and should be modelled in detail. It is also likely that the modelling of the generator Gen has an increasing influence, as evidenced by the growing significance of the state associated with the generator reactance. This indicates that EMT studies might be necessary, as these states would not be captured in RMS models due to the representation of reactances through steady-state models, as

discussed in Section 1.3.2.

4.2.5 Application of the Model Reduction Tool

The tool proposed in this chapter is used to investigate the dynamics and modelling requirements of the case study outlined earlier. To make the analysis more intuitive, the tool essentially presents an alternative view of the results found in Figure 52 by generating a colour gradient overlay in the MATLAB/Simulink model that indicates the most relevant components of the system to the phenomenon under investigation. The results are illustrated in Figure 53.

Two scenarios are examined: a strong grid scenario with the generator's internal SCR of 20.2 and a weak grid scenario with an SCR of 4.9. Colours closer to red represent higher participation levels, while those closer to yellow indicate lower participation. This colour map, along with the results in Figure 52, facilitates the process of drawing conclusions regarding the behaviour of the system. It demonstrates that, in the strong grid scenario, the primary factor influencing the response is VSC 1's reactive power control, whereas in the weak grid scenario, a crucial role is played by VSC 1's PLL interaction with the network. Therefore, the colour map can identify which areas of the model should be modelled in high detail and which parts could be simplified. This is particularly useful when analysing more complex systems.

In summary, this example shows which components are actually important in studying the system, including all its dynamics. This methodology systematically identifies the elements that contribute to the system dynamics, eliminating the need for manual intervention. Furthermore, it quantifies each element's impact on the overall system dynamics using a scale ranging from 0 to 1, a capability that traditional power system analysis methods, such as modal analysis, cannot provide. These results can be used for further investigations into appropriate system modelling.

4.3 Case Study 2: Modified 39-Bus System

The application of the tool has been extended to a modified 39-bus system in order to analyse its performance for a more complex grid. The computation times documented in this case study are derived from a system utilising MATLAB R2022a on an Intel i5 processor featuring a 2.40 GHz clock speed and 32 GB of RAM.

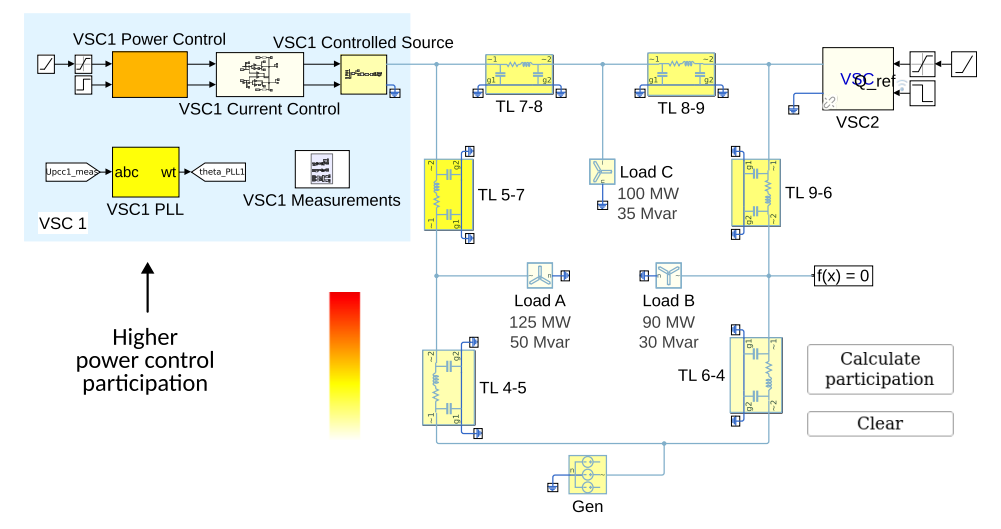
4.3.1 Model Description

Figure 54 illustrates the 39-bus system based on [127], which consists of 396 state variables. The main modification made to the original system is the inclusion of two VSC converters, which are marked in Figure 54. VSC 1 replaces the generator originally connected to bus 30 in the 39-bus system, while VSC 2 connects to bus 26 through the introduction of a new bus 40. The models for generators, transmission lines, and loads follow the description provided in the previous case study outlined in Section 4.2.1. Details regarding the models for the VSCs are presented in the following section.

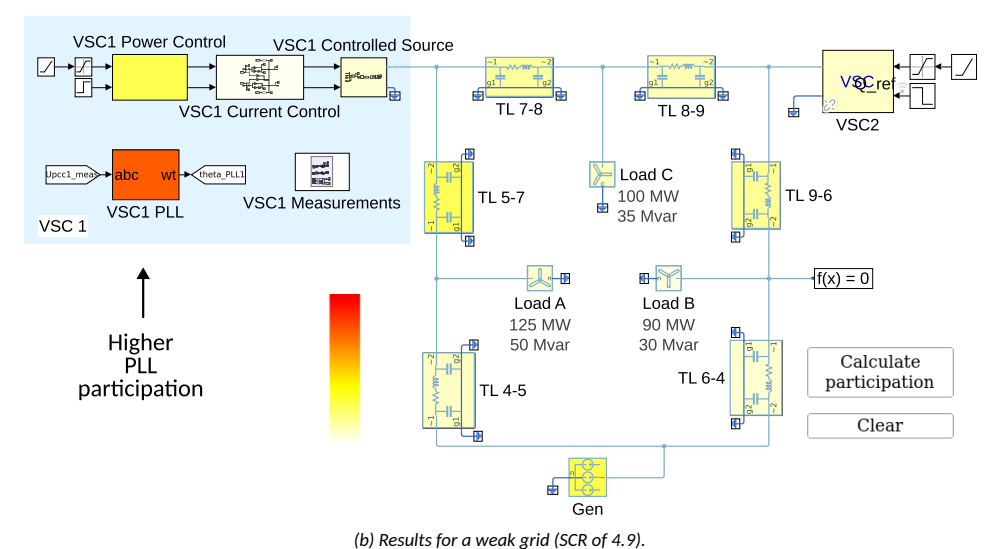
Voltage Source Converters

The model employed for the VSC is based on the two-level averaged converter model detailed in Section 2.4.1. A key distinction is the absence of a voltage feed-forward filter, which has been omitted for the sake of simplicity. Additionally, the model incorporates an AC voltage controller, which replaces the reactive power control. Figure 55 provides an overview of the VSC control system.

The AC voltage control was implemented using a PI controller according to the following



(a) Results for a strong grid (SCR of 20.2).



(b) Results for a weak grid (3CK of 4.7).

Figure 53: Tool developed for MATLAB/Simulink showing the contribution of different parts of the 9-bus system in two scenarios: (a) strong grid, with generator's SCR of 20.2 and (b) weak grid, with generator's SCR of 4.9.

expression:

$$I_{ac}^{q*} = \left(U_{pcc}^* - U_{pcc}^{meas}\right) \left(K_{p,v} + \frac{K_{i,v}}{s}\right),$$
 (182)

where U_{pcc}^* denotes the reference voltage magnitude at the PCC, U_{pcc}^{meas} represents the measured voltage magnitude at the PCC, and $K_{p,v}$ and $K_{i,v}$ are the proportional and integral gains of the controller, respectively.

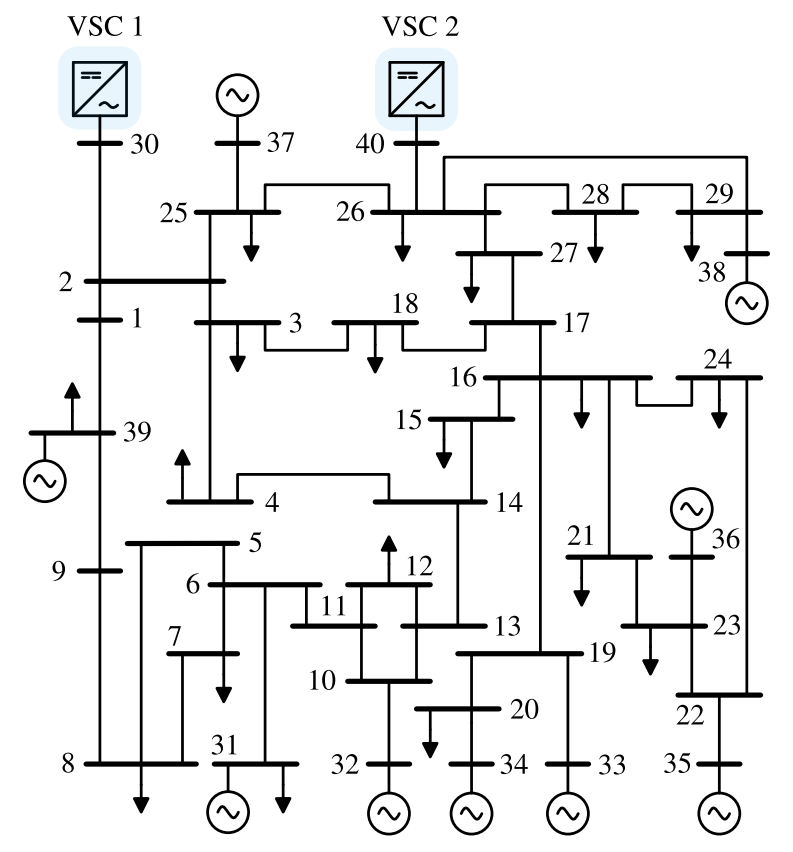


Figure 54: Diagram of the modified 39-bus system.

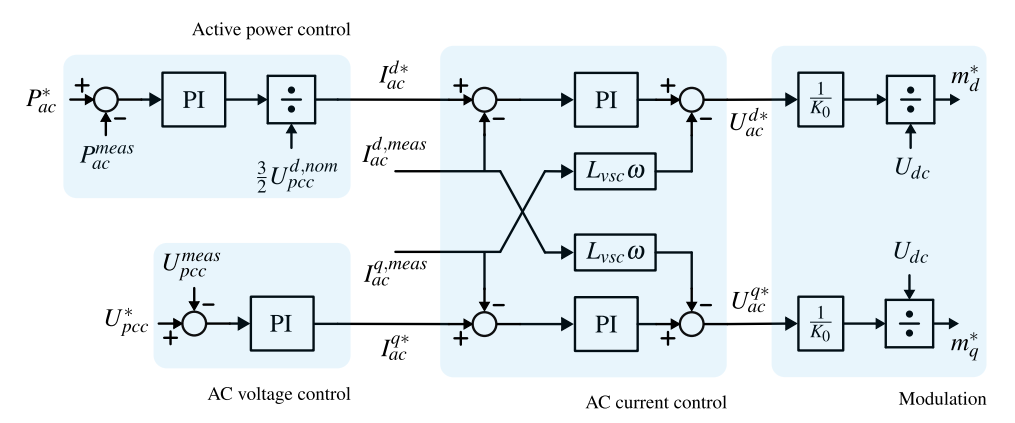


Figure 55: Diagram illustrating the VSC control system employed in the modified 39-bus system case study.

4.3.2 Model Implementation

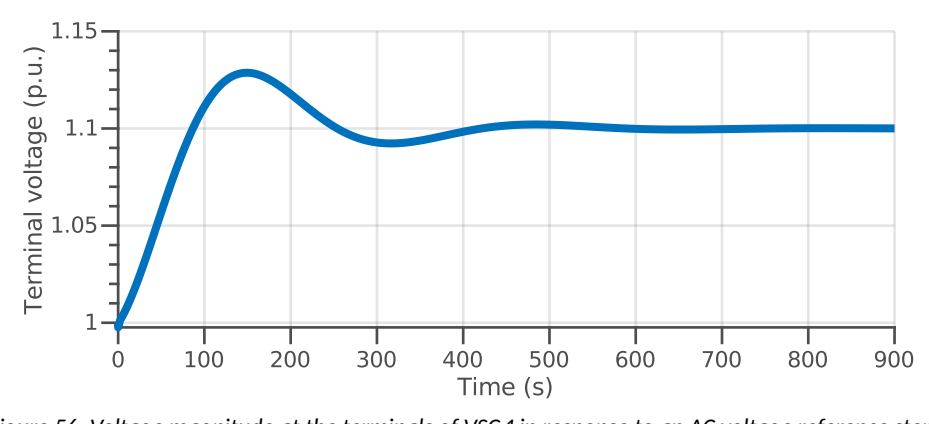
The model described in the preceding section was implemented in MATLAB/Simulink employing both Simscape and custom models. The parameters for the original system components elements were derived from [127]. The VSC parameters are presented in Table 14.

lable 14: VSC parameters for the modified 3	19-bus system case study.

Name	Symbol	Values	
. valle	oysor	VSC 1	VSC 2
Rated apparent power	S_{rated}	1000 MVA	1000 MVA
Active power setpoint	P_{ac}^*	800 MW	700 MW
AC voltage magnitude setpoint	U_{pcc}^*	1.00 p.u.	1.00 p.u.
DC bus voltage	U_{dc}	640 kV	640 kV
AC bus voltage	U_{pcc}	345 kV	345 kV
VSC equivalent inductance	L_{vsc}	82.70 mH	$82.70 \mathrm{mH}$
VSC equivalent resistance	R_{vsc}	1.03Ω	1.03Ω
AC current control time constant	$ au_{idq}$	3 ms	4 ms
AC current control damping ratio	ζ_{idg}	0.7	0.7
PLL time constant	$ au_{pll}$	5 ms	10 ms
PLL damping ratio	$\dot{\zeta_{pll}}$	0.7	0.7
Active power control time constant	$ au_p$	30 ms	40 ms
AC voltage control time constant	$ au_{ u}$	10 ms	10 ms

4.3.3 Dynamic Analysis of the System

To evaluate the system's dynamic response, a voltage reference step of $\Delta U_{pcc}^*=0.1$ p.u. is applied to the voltage control of VSC 1 at t=0 s. Figure 56 illustrates the dynamic response of the converter. Given the relatively short electrical distance between the two converters and the fact that both operate in AC voltage control mode, there exists a potential for interactions between these two converters. This issue will be evaluated utilising the model reduction method proposed in this thesis, alongside the tool described in this chapter.



 $\textit{Figure 56: Voltage magnitude at the terminals of VSC 1} \ in \ response \ to \ an \ AC \ voltage \ reference \ step.$

4.3.4 Application of Model Reduction Method 1

Method 1 of model order reduction, as presented in Section 3.1, is implemented according to the steps outlined in Algorithm 1 to identify the system components that significantly contribute to the observed dynamics. Initially, the model is linearised by designating the AC voltage reference at VSC 1 as the input, while the measured AC voltage serves as the output. This selection of input/output is intentional, as it reveals which elements of the power system are critical for capturing the voltage dynamics at VSC 1. Subsequently, the controllability and observability Gramians are derived from the state space model. Finally, the overall participation of each state is determined using Equation (163).

Figure 57 illustrates the participation of the most significant states in the system's input-output response and is obtained from the aforementioned steps. The participation value not only reflects the significance of each state but also indicates the importance of the associated component in the system's response, given the direct connection between the states and the physical components. Consequently, the findings from the proposed MOR method are directly interpretable, guiding decisions on which system components can be simplified.

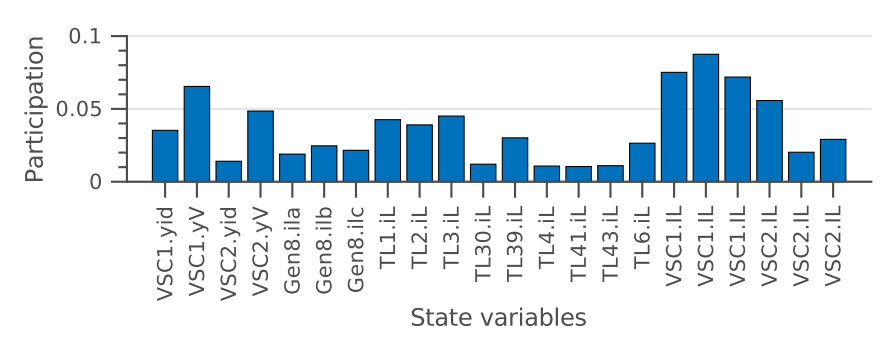


Figure 57: Participation of states in input-output behaviour.

This stands in contrast to MOR methods that depend on transforming the coordinate system to assess which states are most relevant. For instance, the balanced truncation method requires the transformation of the state vector \mathbf{x} using a balancing transformation \mathbf{T}_b , as discussed in Chapter 2. Consequently, any interpretations regarding the relevant states must be reverted back to the original system's frame of reference. This state mapping reduces the interpretability of results and limits its potential to clarify the modelling details needed for studying new dynamics in converter-based power systems.

The results presented in Figure 57 indicate that the primary contributors to the AC voltage dynamics are the voltage controls of the converters, the impedances of the smoothing reactors and the nearby transmission lines. Furthermore, the findings show that while each transmission line shows relatively low participation individually, their combined effect plays a significant role in shaping the system's behaviour.

4.3.5 Application of the Model Reduction Tool

Subsequently, the proposed MATLAB/Simulink tool has been employed to visualise the contributions of various components of the model to the system's response. This tool offers an alternative perspective on the results presented in Figure 57 by employing a colour gradient overlay that emphasises the elements contributing the most to the system dynamics and which, therefore, should be modelled in detail.

Figure 58 presents the results obtained from analysing the modified 39-bus system

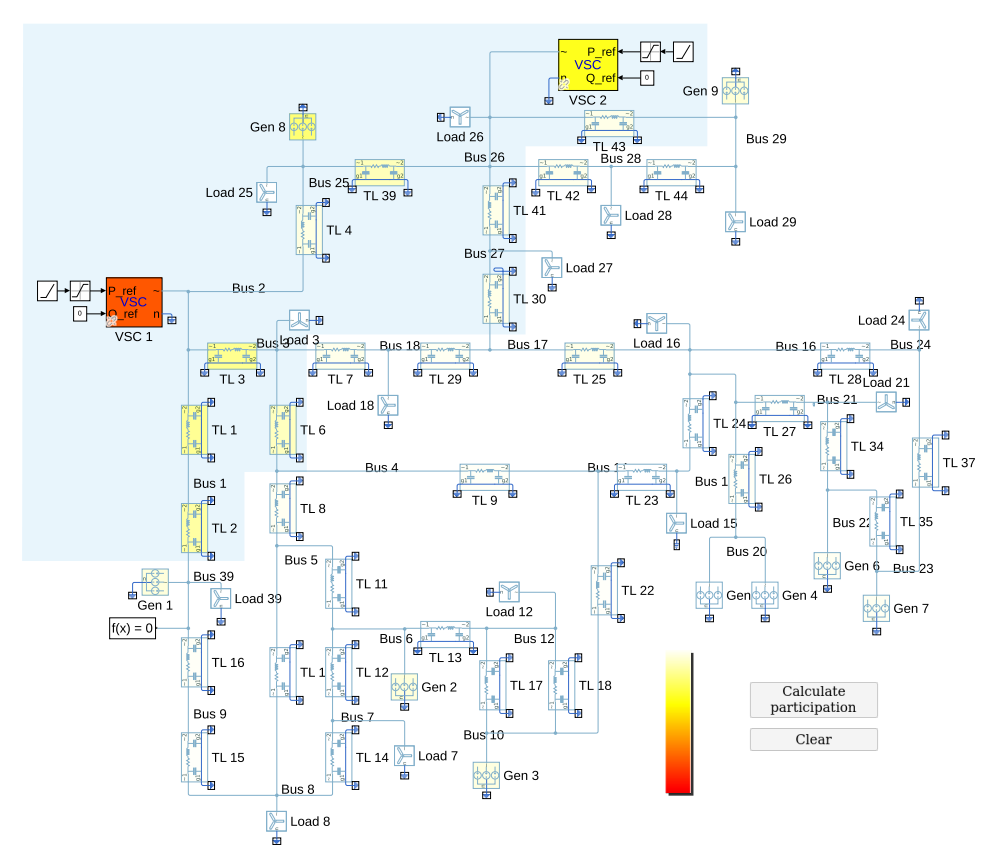


Figure 58: Tool developed for MATLAB/Simulink showing the contribution of different parts of the system in a converter interaction case. The area in blue represents the components that contribute the most to the studied dynamics.

utilising this tool. Components marked in red contribute significantly to the system dynamics, whereas those marked in colours closer to yellow contribute less. This colour mapping enhances the interpretability of the results obtained using the model reduction method. The findings may further assist, for instance, in determining whether the system should be modelled in RMS, EMT, or as a hybrid RMS/EMT simulation. For example, the highlighted area in Figure 58 indicates where the models should be represented in EMT. Conversely, the components situated in the outside area may be simplified and possibly represented in RMS.

Ultimately, a reduced-order model is formed by eliminating states that minimally impact the system's response. This model retains only the states associated with components highlighted in blue in Figure 58. The resulting reduced-order system consists of 48 states, achieving a reduction of approximately 88% in the number of states from the original system. Moreover, the dynamic response closely matches that of the full-order system as demonstrated in Figure 59, suggesting that the unhighlighted area in Figure 58 can be significantly simplified without loss of accuracy. The overall execution time of the algorithm was 24.844 s, with 0.716 s allocated to the computation of the Gramians.

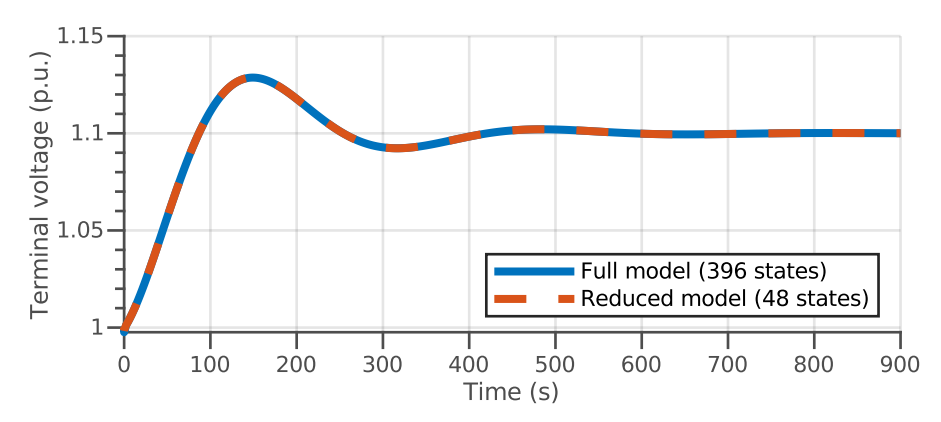


Figure 59: Comparison between full and reduced-order models for a response to a 0.1 p.u. step in the terminal voltage reference.

4.4 Conclusion

This chapter introduced a MATLAB/Simulink tool that automatically computes the contributions of the various components within a model to the input-output system dynamics and highlights which elements of the model need detailed representation. To illustrate the efficacy of this tool, two case studies were developed: a converter-dominated 9-bus system and a modified 39-bus system.

The converter-dominated 9-bus system exemplifies the application of Method 1 for MOR alongside the proposed tool in a scenario characterised by diminishing system strength, which induces control instability, specifically associated with the PLL. The modified 39-bus system extends this analysis by applying the tool to a more complex system to evaluate the tool's performance in such cases. This example clearly demonstrates the advantages of the tool, as it identifies which components and sections of the network must be included in a study to accurately represent the system's behaviour. The findings derived from this tool can be utilised to create guidelines regarding which models to utilise and the extent of the network that requires modelling under various circumstances.

Among the limitations of the proposed tool is that it has been primarily designed for analysing phenomena using small-signal methods. Thus, the studies are confined to those phenomena that can be studied using linearisation without loss of accuracy. Additionally, calculating Gramians may be computationally intensive for exceptionally large systems. Nevertheless, potential solutions for this issue are documented in the literature and referenced within this chapter.

Conclusions and Future Work

This final chapter of the thesis summarises the main findings, highlights contributions, and outlines potential directions for future research.

Conclusions

This thesis examined the challenges of modelling and analysing the stability of converter-dominated power systems. Driven by the rapid expansion of renewable energy sources and the increased reliance on converter-interfaced devices, modern power systems are undergoing fundamental transformations. The unique dynamic behaviour of converters not only introduces new categories of stability issues, but their behaviour must also be taken into account within existing stability categories to ensure that all phenomena are accurately represented in simulation studies. These changes expose limitations in conventional modelling and simulation approaches, and create a need for a reassessment of traditional modelling guidelines and new methods that can support stability assessments under emerging system conditions.

The thesis started by reviewing the emerging stability challenges in converter-dominated power systems, reviewing the most commonly used models for the main power system components, contrasting RMS and EMT tools, which are traditional modelling frameworks for stability studies, and introducing model order reduction as a potential tool for determining the appropriate level of detail required in models for different types of studies.

The thesis then provided an overview of model order reduction, focusing on the balanced truncation method. It began by discussing the state-space representation for linear systems, highlighting the arbitrary nature of choosing a coordinate system. Key concepts such as controllability and observability were introduced, explaining how to achieve a minimal system realisation by carefully selecting an optimal coordinate system. The chapter also presented Gramians as a mathematical tool for measuring the degree of controllability and observability of a state. It introduced the balanced truncation method, a widely used technique for MOR. This method relies on a balancing transformation that enables the identification and truncation of less significant states. However, this transformation leads to state variables that lack physical significance, making it impossible to identify which parts of the physical system are most relevant to the dynamic phenomena.

To address this, the thesis proposed two physics-preserving MOR frameworks based on an adaptation of the balanced truncation method, aimed at simplifying complex power system models while retaining the physical interpretation of state variables. By leveraging controllability and observability Gramians, the proposed methodology systematically identifies system states and components that are most relevant to the system's input-output behaviour. This allows for the systematic reduction of model complexity without sacrificing the accuracy needed for stability studies.

Two complementary approaches were introduced: an event-based method and a frequency-limited method. The event-based approach is designed to capture the system's response to specific disturbances by identifying and retaining the states most active during those events. In contrast, the frequency-limited approach focuses on dynamic behaviour within selected frequency ranges, making it particularly useful for analysing how different model components contribute across varying timescales.

A MATLAB/Simulink-based software tool was developed to automate the model reduction process and help visualise the relative contributions of individual system components. This tool was validated through case studies involving a converter-dominated 9-bus system and a modified 39-bus system. These studies demonstrated the practicality and efficiency

of the proposed methods, showing that reduced-order models can significantly reduce computational requirements while preserving accuracy. A key advantage of the framework is that it avoids coordinate transformations, ensuring that reduced models maintain a clear physical interpretation.

Future Work

Despite the contributions presented in this thesis, several limitations and open questions remain. One such limitation is that the proposed MOR methods are currently restricted to linear time-invariant systems and assume the system is stable. Consequently, they may not be directly applicable to stability issues involving nonlinear behaviour or scenarios operating beyond the system's stability margins. A potential approach to address this limitation is to explore methods for calculating Gramians in unstable systems.

Another challenge concerns the computational cost of Gramian calculation for very large-scale networks, which can limit scalability. Future research could therefore focus on developing or implementing techniques to accelerate Gramian computation, enabling the application of the proposed methods to larger and more complex power system models.

Another promising direction involves the development of hybrid modelling approaches that combine EMT and RMS frameworks. Developing hybrid simulation models that selectively incorporate detailed EMT components within broader RMS simulations could achieve a balance between computational efficiency and modelling accuracy. Investigating the optimal strategies for model partitioning and interface definition of such hybrid models would be particularly beneficial.

Finally, this thesis introduced a framework for identifying the minimal model complexity required for accurate stability assessment in converter-dominated power systems. A logical next step would be to apply this framework toward the development of practical modelling guidelines tailored to specific stability issues and system conditions.

List of Figures

1	Power system stability classification [3, 4]	14
2	Circuit diagram for second-order d-axis representation [56]	23
3	Circuit diagram for first-order q-axis representation [56]	24
4	Circuit diagram for second-order q-axis representation [56]	24
5	Short line model [57]	25
6	Medium line model [57]	25
7	Long line model [57]	26
8	Section of distributed line model [58]	27
9	Two-level VSC topology [60].	30
10	Multi-level MMC-based VSC topology [60].	31
11	Detailed equivalent circuit representing an MMC arm [64]	32
12	Averaged value model of a VSC.	32
13	Timescale for power system phenomena [66]	33
14	Numerical integration.	34
15	The (a) capacitor and (b) its discrete equivalent.	35
16	The (a) inductor and (b) its discrete equivalent.	35
17	Comparison between instantaneous and phasor variables [69]	36
18	Hybrid RTDS® /RMS simulation setup for wind and HVDC studies [81]	41
19	Simulation results using replicas to reproduce the 2015 INELFE HVDC link	
	incident [9]	42
20	Representation of a MIMO system showing system inputs and outputs	47
21	State space, showing a single state represented (a) in the original coor-	
	dinates \mathbf{x} and (b) new coordinates $\bar{\mathbf{x}}$ obtained using the transformation	
	T	50
22	Representation of a system containing a controllable and an uncontrollable	
	group of states [104]	51
23	Representation of a system containing an observable and an unobservable	
	group of states [104].	52
24	State space containing a set of controllable and observable states repre-	
	sented in (a) third-order state space with coordinates $\mathbf{x} = \begin{bmatrix} x_1 & x_2 & x_3 \end{bmatrix}$	
	and (b) reduced second-order state space with coordinates $\bar{\mathbf{x}} = \begin{bmatrix} \bar{x}_1 & \bar{x}_2 \end{bmatrix} \dots$	53
25	Diagram showing impulse response matrix decomposition for a system	
	with 2 inputs, 2 outputs, and 3 state variables	54
26	Signal injection test for characterizing the controllable subspace [107]	55
27	Signal injection test for characterizing the observable subspace [107]	55
28	Relationship between Gramian matrix entries of a signal set $\mathbf{F}(t) = \begin{bmatrix} \mathbf{f^1}(t) & \mathbf{f^2}(t) \end{bmatrix}$	$]^{I}$
	and the signal energy.	56
29	Controllable subspace ellipsoids showing states that are reachable by a	
	unit norm input for $t = t_1$ and $t = t_2$, with $t_2 > t_1$ [109]	57
30	State space containing ellipsoids representing (a) a controllable and (b)	
	an observable subspace with axes characterised by their eigenvalues and	
	eigenvectors.	59
31	Controllable and observable subspaces for an unbalanced system [105]	59
32	Diagram illustrating the VSC model connected to the AC network	60
33	Diagram illustrating the VSC control system	61
34	Time-domain response of the measured active power to a step in the active	
	power reference for full and reduced models	68

35	Diagram illustrating the application of Method 1 for model order reduction.	69
36	Relationship between the controllability and observability operators and the Hankel operator [105]	71
37	Example of a second-order system showing the decomposition of the outputs into the components associated with each state	72
38	Contribution of state variables to input-output system response	74
39	Signal analysis of a second-order system with responses decomposed by state.	76
40	Diagram illustrating the application of Method 2 for model order reduction.	78
41	Complex plane illustrating the variations in eigenvalues across different values of PLL response time	81
42	Participation factors showing states involved in the (a) mode whose damping has become worse and the (b) and (c) modes which experienced im-	
	proved damping.	82
43	Time-domain response of the measured active power to a step in the active	02
73	power reference	82
44	Analysis of state participation in input-output behaviour across the frequency spectrum. The low, medium, and high frequency ranges are indicated in green, blue, and red, respectively, to illustrate their distinct contri-	02
	butions	85
45	Diagram illustrating the (a) VSC model connected to the AC network and	03
10	(b) the VSC control system.	86
46	Response comparison between full and reduced models to a 5% step in	-
	active power setpoint.	87
47	Tool's operational steps.	89
48	Diagram of the converter-dominated 9-bus system.	91
49	Complex plane illustrating the variations in eigenvalues across different values of SCR. The blue dash line represents the 5% damping line	94
50	Participation factor of modes associated with (a) PLL instability and (b) network resonant modes.	94
51	Dynamic behaviour of VSC 1 to a reactive power step	95
52	Contribution of state variables to the input-output dynamics according to varying levels of generator SCR.	96
53	Tool developed for MATLAB/Simulink showing the contribution of different	70
55	parts of the 9-bus system in two scenarios: (a) strong grid, with generator's	
	SCR of 20.2 and (b) weak grid, with generator's SCR of 4.9.	98
54	Diagram of the modified 39-bus system.	99
55	Diagram illustrating the VSC control system employed in the modified	•
	39-bus system case study.	99
56	Voltage magnitude at the terminals of VSC 1 in response to an AC voltage	
	reference step.	
57 50	Participation of states in input-output behaviour.	101
58	Tool developed for MATLAB/Simulink showing the contribution of differ-	
	ent parts of the system in a converter interaction case. The area in blue	400
50	represents the components that contribute the most to the studied dynamics.	102
59	Comparison between full and reduced-order models for a response to a	100
	0.1 p.u. step in the terminal voltage reference	103

List of Tables

1	Instability phenomena and examples resulting from the new stability categories	15
2	Timeline of real-life converter-driven stability events [14]	17
3	Timeline of real-life resonance stability events [14]	20
4	Comparison between EMT and RMS frameworks [72, 73]	38
5	Comparison of selected model reduction methods in power systems	45
6	VSC case study reference parameters	66
7	Controllability and observability Gramians for the VSC state-space model	
	in the original state space coordinates	67
8	Controllability and observability Gramians for the VSC state-space model	
	in the balanced state space coordinates	67
9	List of eigenvalues for the reference VSC case study	80
10	List of eigenvalues for the VSC case study corresponding to a faster PLL	
	response time of $t_{r,pll}$ equal to 6 ms	81
11	Step-by-step calculation of states' participation in the input-output be-	
	haviour for a system with a slow PLL tuning characterised by $t_{r,PLL} = 50$	
	ms	84
12	Step-by-step calculation of states' participation in the input-output be-	
	haviour for a system with a fast PLL tuning characterised by $t_{r,PLL} = 6$ ms	84
13	VSC parameters for the converter-dominated 9-bus system case study	93
14	VSC parameters for the modified 39-bus system case study	100

References

- [1] "World energy transitions outlook: 1.5° pathway," International Renewable Energy Agency, Tech. Rep., 2021.
- [2] "Completing the map Power system needs in 2030 and 2040," European Network of Transmission System Operators for Electricity, Tech. Rep., 2020.
- [3] N. Hatziargyriou, J. Milanovic, C. Rahmann, V. Ajjarapu, C. Canizares, I. Erlich, D. Hill, I. Hiskens, I. Kamwa, B. Pal, P. Pourbeik, J. Sanchez-Gasca, A. Stankovic, T. Van Cutsem, V. Vittal, and C. Vournas, "Definition and classification of power system stability revisited & extended," *IEEE Transactions on Power Systems*, vol. 36, no. 4, pp. 3271–3281, 2021.
- [4] P. Kundur, J. Paserba, V. Ajjarapu, G. Andersson, A. Bose, C. Canizares, N. Hatziargyriou, D. Hill, A. Stankovic, C. Taylor, T. Van Cursem, and V. Vittal, "Definition and classification of power system stability," *IEEE Transactions on Power Systems*, vol. 19, no. 2, pp. 1387–1401, 2004.
- [5] CIGRE Joint Working Group C4/B4.52, "Guidelines for subsynchronous oscillation studies in power electronics dominated power systems," CIGRE, Tech. Rep., June 2023.
- [6] "Integrating inverter-based resources into low short circuit strength systems," North American Electric Reliability Corporation, Tech. Rep., 2017.
- [7] L. Fan and Z. Miao, "An explanation of oscillations due to wind power plants weak grid interconnection," *IEEE Transactions on Sustainable Energy*, vol. 9, no. 1, pp. 488–490, 2018.
- [8] "Power system limitations in north western Victoria and south western New South Wales," Australian Energy Market Operator, Tech. Rep., Dec. 2019.
- [9] H. Saad, Y. Vernay, S. Dennetière, P. Rault, and B. Clerc, "System dynamic studies of power electronics devices with real-time simulation a TSO operational experience," in *Proceedings of the 2018 CIGRE Session, Paris, France*, Aug. 2018.
- [10] W. Qu and J. Jiang, "SSTI and its mitigation in wind farms connected with an HVDC line," *Procedia Computer Science*, vol. 111, pp. 399–405, 2017.
- [11] F. Bizzarri, A. Brambilla, and F. Milano, "Simplified model to study the induction generator effect of the subsynchronous resonance phenomenon," *IEEE Transactions on Energy Conversion*, vol. 33, no. 2, pp. 889–892, 2018.
- [12] IEEE Wind SSO Task Force, "Wind energy systems sub-synchronous oscillations: Events and modeling," IEEE Power & Energy Society, Tech. Rep. PES-TR80, July 2020.
- [13] J. H. Enslin and P. J. Heskes, "Harmonic interaction between a large number of distributed power inverters and the distribution network," *IEEE Transactions on Power Electronics*, vol. 19, no. 6, pp. 1586–1593, Nov. 2004.
- [14] P. De Rua, T. Roose, O. C. Sakinci, N. M. D. Campos, and J. Beerten, "Identification of mechanisms behind converter-related issues in power systems based on an overview of real-life events," *Renewable and Sustainable Energy Reviews*, vol. 183, pp. 1–16, 2023.

- [15] C. Yin, X. Xie, S. Xu, and C. Zou, "Review of oscillations in VSC-HVDC systems caused by control interactions," *The Journal of Engineering*, vol. 2019, no. 16, pp. 1204–1207, 2019.
- [16] T. Bi, J. Li, P. Zhang, E. Mitchell-Colgan, and S. Xiao, "Study on response characteristics of grid-side converter controller of PMSG to sub-synchronous frequency component," *IET Renewable Power Generation*, vol. 11, no. 7, pp. 966–972, June 2017.
- [17] K. Ji, H. Pang, J. Yang, and G. Tang, "DC side harmonic resonance analysis of MMC-HVDC considering wind farm integration," *IEEE Transactions on Power Delivery*, vol. 36, no. 1, pp. 254–266, Feb. 2021.
- [18] X. Guo, Z. Liu, Y. Li, and Y. Lu, "Characteristic analysis of high-frequency resonance of flexible high voltage direct current and research on its damping control strategy," *Proceedings of the Chinese Society of Electrical and Electronics Engineers*, vol. 40, no. 1, pp. 19–40, Jan. 2020.
- [19] H. Ding, Y. Wu, Y. Zhang, Y. Ma, and R. Kuffel, "System stability analysis of Xiamen bipolar MMC-HVDC project," in *Proceedings of the 12th IET International Conference on AC and DC Power Transmission*, Beijing, China, May 2016.
- [20] I. Erlich, B. Paz, M. K. Zadeh, S. Vogt, C. Buchhagen, C. Rauscher, A. Menze, and J. Jung, "Overvoltage phenomena in offshore wind farms following blocking of the HVDC converter," in *Proceedings of the IEEE PES General Meeting*, 2016.
- [21] C. Zou, H. Rao, S. Xu, Y. Li, W. Li, J. Chen, X. Zhao, Y. Yang, and B. Lei, "Analysis of resonance between a VSC-HVDC converter and the AC grid," *IEEE Transactions on Power Electronics*, vol. 33, no. 12, pp. 10 157–10 168, Dec. 2018.
- [22] C. Li, "Unstable operation of photovoltaic inverter from field experiences," *IEEE Transactions on Power Delivery*, vol. 33, no. 2, pp. 1013–1015, 2018.
- [23] Y. Li, H. Pang, M. Kong, J. Lu, K. Ji, and G. Tang, "Compensation control and parameters design for high frequency resonance suppression of MMC-HVDC system," *CSEE Journal of Power and Energy Systems*, vol. 7, no. 6, pp. 1161–1175, 2021.
- [24] "Ørsted technical report for National Grid ESO on the events of 9 august 2019 (appendix of Ofgem technical report on the events of 9 August 2019)," Ørsted, Tech. Rep., 2019.
- [25] H. Gu, R. Yan, and T. Saha, "Review of system strength and inertia requirements for the national electricity market of Australia," *CSEE Journal of Power and Energy Systems (JPES)*, vol. 5, no. 3, pp. 295–305, Aug. 2019.
- [26] L. Fan and Z. Miao, "Wind in weak grids: 4 Hz or 30 Hz oscillations?" *IEEE Transactions on Power Systems*, vol. 33, no. 5, pp. 5803–5804, 2018.
- [27] CIGRE Working Group B4.62, "Connection of wind farms to weak AC networks," CIGRE, Tech. Rep. 671, 2016.
- [28] E. Ebrahimzadeh, F. Blaabjerg, X. Wang, and C. L. Bak, "Harmonic stability and resonance analysis in large PMSG-based wind power plants," *IEEE Transactions on Sustainable Energy*, vol. 9, no. 1, pp. 12–23, 2018.

- [29] J. Z. Zhou, H. Ding, S. Fan, Y. Zhang, and A. M. Gole, "Impact of short-circuit ratio and phase-locked-loop parameters on the small-signal behavior of a VSC-HVDC converter," *IEEE Transactions on Power Delivery*, vol. 29, no. 5, pp. 2287–2296, 2014.
- [30] L. Papangelis, M.-S. Debry, T. Prevost, P. Panciatici, and T. Van Cutsem, "Stability of a voltage source converter subject to decrease of short-circuit capacity: A case study," in *Proceedings of the 2018 Power Systems Computation Conference (PSCC)*, 2018, pp. 1–7.
- [31] "Technical Report on the events of 9 August 2019," National Grid ESO, Tech. Rep. Sept., 2019.
- [32] H. Liu, X. Xie, J. He, T. Xu, Z. Yu, C. Wang, and C. Zhang, "Subsynchronous interaction between direct-drive PMSG based wind farms and weak AC networks," *IEEE Transactions on Power Systems*, vol. 32, no. 6, pp. 4708–4720, Nov. 2017.
- [33] Y. Xu and Y. Cao, "Sub-synchronous oscillation in PMSGs based wind farms caused by amplification effect of GSC controller and PLL to harmonics," *IET Renewable Power Generation*, vol. 12, no. 7, pp. 844–850, May 2018.
- [34] "Interactions between HVDC systems and other connections," European Network of Transmission System Operators for Electricity, Tech. Rep. Mar., 2018.
- [35] H. Saad, S. Dennetière, and B. Clerc, "Interactions investigations between power electronics devices embedded in HVAC network," in *Proceedings of the 13th IET International Conference on AC and DC Power Transmission (ACDC 2017)*, 2017, pp. 1–7.
- [36] C. Buchhagen, C. Rauscher, A. Menze, and J. Jung, "BorWin1 First experiences with harmonic interactions in converter dominated grids," in *Proceedings of the 2015 International ETG Congress*, Bonn, Germany, Nov. 2015, pp. 27–33.
- [37] IEEE Subsynchronous Resonance Working Group, "Reader's guide to subsynchronous resonance," IEEE Transactions on Power Systems, vol. 7, no. 1, pp. 150–157, 1992.
- [38] M. Bahrman, E. V. Larsen, R. J. Piwko, and H. S. Patel, "Experience with HVDC turbine-generator torsional interaction at Square Butte," *IEEE Transactions on Power Apparatus and Systems*, vol. PAS-99, no. 3, pp. 966–975, 1980.
- [39] A. Mulawarman and P. G. Mysore, "Detection of undamped sub-synchronous oscillations of wind generators with series compensated lines," in *Proceedings of the Minnesota Power Systems Conference*, 2011.
- [40] D. Kidd and P. Hassink, "Transmission operator perspective of sub-synchronous interaction," in *Proceedings of the IEEE PES Transmission and Distribution Conference*, Orlando, USA, May 2012.
- [41] C. Luo, X. Xiao, J. Lu, J. Zhang, and C. Yuan, "Analysis and mitigation countermeasures of a new SSO phenomenon," in *Proceedings of the 1st International Future Energy Electronics Conference*, 2013, pp. 553–557.
- [42] X. Xie, X. Zhang, H. Liu, H. Liu, Y. Li, and C. Zhang, "Characteristic analysis of subsynchronous resonance in practical wind farms connected to series-compensated transmissions," *IEEE Transactions on Energy Conversion*, vol. 32, no. 3, pp. 1117–1126, 2017.

- [43] M. Koochack Zadeh, T. Rendell, C. Rathke, and A. Menze, "Operating experiences of HVDC links Behaviour during faults and switching events," in *Proceedings of the CIGRE B4 Colloquium*, Winnipeg, Canada, Oct. 2017.
- [44] J. B. Kwon, C. S. Hansen, and C. F. Flytkjaer, "System-wide amplification of background harmonics due to the integration of high voltage power cables," in *Proceedings of the CIGRE e-Session 2020*, Paris, France, 2020.
- [45] K. Narendra, D. Fedirchuk, R. Midence, N. Zhang, A. Mulawarman, P. Mysore, and V. Sood, "New microprocessor based relay to monitor and protect power systems against sub-harmonics," in *Proceedings of the 2011 IEEE Electrical Power and Energy Conference*, 2011, pp. 438–443.
- [46] L. Wang, X. Xie, Q. Jiang, H. Liu, Y. Li, and H. Liu, "Investigation of SSR in practical DFIG-based wind farms connected to a series-comp. power system," *IEEE Transactions on Power Systems*, vol. 30, no. 5, pp. 2772–2779, Sep. 2015.
- [47] J. He, Y. W. Li, D. Bosnjak, and B. Harris, "Investigation and active damping of multiple resonances in a parallel-inverter-based microgrid," *IEEE Transactions on Power Electronics*, vol. 28, no. 1, pp. 234–246, 2013.
- [48] R. N. Damas, Y. Son, M. Yoon, S.-Y. Kim, and S. Choi, "Subsynchronous oscillation and advanced analysis: A review," *IEEE Access*, vol. 8, pp. 224 020–224 032, 2020.
- [49] A. Abdalrahman, "Experiences from SSTI-studies in HVDC projects," https://energiforskmedia.blob.core.windows.net/media/21928/abdalrahman.pdf, 2016.
- [50] M. Zhang, X. Yuan, and J. Hu, "Mechanism analysis of subsynchronous torsional interaction with PMSG-based WTs and LCC-HVDC," *IEEE Journal of Emerging and Selected Topics in Power Electronics*, vol. 9, no. 2, pp. 1708–1724, 2021.
- [51] N. Prabhu and K. R. Padiyar, "Investigation of subsynchronous resonance with VSC-based HVDC transmission systems," *IEEE Transactions on Power Delivery*, vol. 24, no. 1, pp. 433–440, 2009.
- [52] C. Wu, K. Peterson, R. Piwko, M. Kankam, and D. Baker, "The intermountain power project commissioning-subsynchronous torsional interaction tests," *IEEE Transactions on Power Delivery*, vol. 3, no. 4, pp. 2030–2036, 1988.
- [53] A. Monti, F. Milano, E. Bompard, and X. Guillaud, *Converter-Based Dynamics and Control of Modern Power Systems*, 1st ed. Elsevier, 2020.
- [54] P. Kundur, Power System Stability and Control, 1st ed. New York: McGraw-Hill, 1994.
- [55] P. M. Anderson and A. A. Fouad, *Power Systems Control and Stability*, 2nd ed. New Jersey: Wiley-IEEE Press, 2003.
- [56] Electric Machinery Committee, "IEEE std 1110-2019: IEEE guide for synchronous generator modeling practices and parameter verification with applications in power system stability analyses," IEEE Standards Association, Tech. Rep., 2020.
- [57] H. Saadat, Power System Analysis, 1st ed. New York: McGraw-Hill, 1999.
- [58] J. J. Grainger and S. William D. Jr., *Power System Analysis*, 1st ed. New York: McGraw-Hill, 1994.

- [59] CIGRE Working Group C4.605, "Modelling and aggregation of loads in flexible power networks," CIGRE, Tech. Rep., Feb. 2014.
- [60] D. Jovcic and K. Ahmed, High-Voltage Direct-Current Transmission: Converters, Systems and DC grids, 1st ed. Chichester, UK: Wiley, 2015.
- [61] N. Cherix, "Functional description and control design of modular multilevel converters," Ph.D. dissertation, Ecole Polytechnique Fédérale de Lausanne (EPFL), 2015.
- [62] C. Shah, J. D. Vasquez-Plaza, D. D. Campo-Ossa, J. F. Patarroyo-Montenegro, N. Guruwacharya, N. Bhujel, R. D. Trevizan, F. A. Rengifo, M. Shirazi, R. Tonkoski, R. Wies, T. M. Hansen, and P. Cicilio, "Review of dynamic and transient modeling of power electronic converters for converter dominated power systems," *IEEE Access*, vol. 9, pp. 82 094–82 117, 2021.
- [63] CIGRE Joint Working Group C4/C6.35/CIRED, "Modelling of inverter-based generation for power system dynamic studies," CIGRE, Tech. Rep. May, 2018.
- [64] CIGRE Working Group B4.57, "Guide for the development of models for HVDC converters in a HVDC grid," CIGRE, Tech. Rep., 2014.
- [65] H. A. Pereira, "Modeling of full-converter wind turbine generators for power system studies," Ph.D. dissertation, Universidade Federal de Minas Gerais, 2015.
- [66] N. Watson and J. Arrillaga, *Power Systems Electromagnetic Transients Simulation*, 2nd ed. London: The Institution of Engineering and Technology, 2019.
- [67] H. W. Dommel, Electromagnetic Transients Program (EMTP): Theory Book, 1st ed. Portland: Boneville Power Administration, 1995.
- [68] S. Henschel, "Analysis of electromagnetic and electromechanical power system transients with dynamic phasors," Ph.D. dissertation, The University of British Columbia, Vancouver, Canada, Feb. 1999.
- [69] S. Abourida, J. Bélanger, and V. Jalili-Marandi, "Real-time power system simulation: EMT vs. phasor," OPAL-RT, Montreal, Canada, Tech. Rep., 2016.
- [70] M. N. Alexander, Charles K; Sadiku, *Fundamentals of Electric Circuits Electric Circuits*, 5th ed. New York: McGraw-Hill, 2013.
- [71] W. Liu, J. Liang, N. M. D. Campos, V. Bhardwaj, J. Beerten, D. Van Hertem, H. Ergun, S. Dadjo Tavakoli, E. Prieto, O. Gomis, E. Maggioli, and H. Leite, "Report on the review and evaluation of DC and AC grid operation and interactions in different time frames," Innovative tools for offshore wind and DC grids (InnoDC), Tech. Rep., 2018.
- [72] ——, "Report on dynamic converter interactions and the feasibility of different software routines to represent the problems," Innovative tools for offshore wind and DC grids (InnoDC), Tech. Rep., 2019.
- [73] J. G. Slootweg and W. L. Kling, "Modelling wind turbines for power system dynamics simulations: an overview," *Wind Engineering*, vol. 28, pp. 7–26, 2004.
- [74] P. C. Krause, F. Nozari, T. L. Skvarenina, and D. W. Olive, "The theory of neglecting stator transients," *IEEE Transactions on Power Apparatus and Systems*, vol. PAS-98, no. 1, pp. 141–148, 1979.

- [75] DIgSILENT PowerFactory 2024, "Technical reference synchronous machine ElmSym, TypSym," 2024.
- [76] V. A. Lacerda, E. P. Araujo, M. Cheah-Mane, and O. Gomis-Bellmunt, "Phasor modeling approaches and simulation guidelines of voltage-source converters in grid-integration studies," *IEEE Access*, vol. 10, pp. 51826–51838, 2022.
- [77] S. Liu, Z. Xu, W. Hua, G. Tang, and Y. Xue, "Electromechanical transient modeling of modular multilevel converter based multi-terminal HVDC systems," in *Proceedings* of the 2014 IEEE PES General Meeting, 2014, pp. 1–12.
- [78] P. Chainho, A. Meer, R. Hendriks, M. Gibescu, and M. Meijden, "General modeling of multi-terminal VSC-HVDC systems for transient stability studies," in *Proceedings of the 6th IEEE Young Researchers Symposium in Electrical Power Engineering*, Apr. 2012, pp. 1–6.
- [79] R. Kuffel, J. Giesbrecht, T. Maguire, R. Wierckx, and P. McLaren, "RTDS a fully digital power system simulator operating in real time," in *Proceedings of the 1995 Interna*tional Conference on Energy Management and Power Delivery, 1995, pp. 498–503.
- [80] R. Gagnon, G. Turmel, C. Larose, J. Brochu, G. Sybille, and M. Fecteau, "Large-scale real-time simulation of wind power plants into hydro-quebec power system," in *Proceedings of the 9th Wind Integration Workshop*, Quebec, Canada, 2010, pp. 1–8.
- [81] X. Lin and P. Zadkhast, "Study of transmission/distribution network with large number of power electronic devices using hybrid simulation," *IEEE Power and Energy Magazine*, vol. 18, no. 2, pp. 106–116, 2020.
- [82] I. L. Cowan and S. C. M. Marshall, "Installation and interfacing HVDC control replicas at the national HVDC centre," in *Proceedings of the 15th IET International Conference on AC and DC Power Transmission (ACDC 2019)*, 2019, pp. 1–6.
- [83] D. Crawshay, W. Otto, R. Sherry, and D. Kell, "New Zealand HVDC Pole 3 project testing approach and challenges," in *Proceedings of the 2015 CIGRE Canada Conference*, 2015.
- [84] J. Song, S. Oh, J. Lee, J. Shin, and G. Jang, "Application of the first replica controller in Korean power systems," *Energies*, vol. 13, no. 13, 2020.
- [85] S. D. Espírito Santo, V. A. B. França, E. D. M. Brandi, and H. Meiklejohn, "FURNAS strategy regarding real-time tests: A practical case Campos Static VAr Compensator," Proceedings of the 9th World Multi-Conference on Systemics, Cybernetics and Informatics, pp. 119–124, 2005.
- [86] A. C. Antoulas and D. C. Sorensen, "Approximation of large-scale dynamical systems: an overview," *International Journal of Applied Mathematics and Computer Science*, vol. 11, no. 5, pp. 1093–1121, 2001.
- [87] S. Tan and L. He, *Truncated balanced realization methods for MOR*. Cambridge University Press, Jan. 2010, pp. 37–55.
- [88] Y. G. I. Acle, F. D. Freitas, N. Martins, and J. Rommes, "Parameter preserving model order reduction of large sparse small-signal electromechanical stability power system models," *IEEE Transactions on Power Systems*, vol. 34, no. 4, pp. 2814–2824, 2019.

- [89] S. Ghosh, Y. J. Isbeih, M. S. El Moursi, and E. F. El-Saadany, "Cross-gramian model reduction approach for tuning power system stabilizers in large power networks," *IEEE Transactions on Power Systems*, vol. 35, no. 3, pp. 1911–1922, 2020.
- [90] C. M. Rergis, I. Kamwa, R. Khazaka, and A. R. Messina, "A Loewner interpolation method for power system identification and order reduction," *IEEE Transactions on Power Systems*, vol. 34, no. 3, pp. 1834–1844, 2019.
- [91] S. Nabavi and A. Chakrabortty, "Structured identification of reduced-order models of power systems in a differential-algebraic form," *IEEE Transactions on Power Systems*, vol. 32, no. 1, pp. 198–207, 2017.
- [92] J. Leung, M. Kinnaert, J.-C. Maun, and F. Villella, "Model reduction in power systems using a structure-preserving balanced truncation approach," *Electric Power Systems Research*, vol. 177, pp. 1–9, 2019.
- [93] B. Marinescu, B. Mallem, and L. Rouco, "Large-scale power system dynamic equivalents based on standard and border synchrony," *IEEE Transactions on Power Systems*, vol. 25, no. 4, pp. 1873–1882, 2010.
- [94] I. Tyuryukanov, M. Popov, M. A. M. M. van der Meijden, and V. Terzija, "Slow coherency identification and power system dynamic model reduction by using orthogonal structure of electromechanical eigenvectors," *IEEE Transactions on Power Systems*, vol. 36, no. 2, pp. 1482–1492, 2021.
- [95] I. J. Perez-Arriaga, G. C. Verghese, and F. C. Schweppe, "Selective modal analysis with applications to electric power systems, part I: Heuristic introduction," *IEEE Transactions on Power Apparatus and Systems*, vol. PAS-101, no. 9, pp. 3117–3125, 1982.
- [96] M. K. Transtrum, A. T. Sarić, and A. M. Stanković, "Measurement-directed reduction of dynamic models in power systems," *IEEE Transactions on Power Systems*, vol. 32, no. 3, pp. 2243–2253, 2017.
- [97] C. Sturk, L. Vanfretti, Y. Chompoobutrgool, and H. Sandberg, "Coherency-independent structured model reduction of power systems," *IEEE Transactions on Power Systems*, vol. 29, no. 5, pp. 2418–2426, 2014.
- [98] Q. Cossart, F. Colas, and X. Kestelyn, "A novel event- and non-projection-based approximation technique by state residualization for the model order reduction of power systems with a high renewable energies penetration," *IEEE Transactions on Power Systems*, vol. 37, no. 4, pp. 3221–3229, 2022.
- [99] H. R. Ali and B. C. Pal, "Model order reduction of multi-terminal direct-current grid systems," *IEEE Transactions on Power Systems*, vol. 36, no. 1, pp. 699–711, 2021.
- [100] Y. Levron and J. Belikov, "Reduction of power system dynamic models using sparse representations," *IEEE Transactions on Power Systems*, vol. 32, no. 5, pp. 3893–3900, 2017.
- [101] S. D. Dukić and A. T. Sarić, "A new approach to physics-based reduction of power system dynamic models," *Electric Power Systems Research*, vol. 101, pp. 17–24, 2013.
- [102] W. H. A. Schilders, H. A. van der Vorst, and J. Rommes, *Model Order Reduction Theory, Research Aspects and Applications*. Berlin, Germany: Springer-Verlag, 2008.

- [103] D. Rowell, "Time-domain solution of LTI state equations," https://web.mit.edu/2.14/www/Handouts/StateSpaceResponse.pdf, Oct. 2002.
- [104] R. E. Kalman, "Mathematical description of linear dynamical systems," *Journal of the Society for Industrial and Applied Mathematics*, vol. 1, no. 2, pp. 152–192, 1963.
- [105] G. E. Dullerud and F. G. Paganini, A Course in Robust Control Theory: A Convex Approach. New York: Springer-Verlag, 2000.
- [106] K. Ogata, Modern Control Engineering, 5th ed. New Jersey: Prentice Hall, 2010.
- [107] B. Moore, "Principal component analysis in linear systems: Controllability, observability, and model reduction," *IEEE Transactions on Automatic Control*, vol. 26, no. 1, pp. 17–32, 1981.
- [108] C.-T. Chen, *Introduction to Linear System Theory*, 1st ed. New York, USA: Holt, Rinehart and Winston, Inc, 1970.
- [109] S. Boyd, "Lecture 18: Controllability and state transfer," https://see.stanford.edu/materials/lsoeldsee263/18-contr.pdf, 2007.
- [110] S. Lall, "Lecture 9: Controllability and observability," http://floatium.stanford.edu/engr210a/lectures/lecture9_2001_10_30_01.pdf, pp. 1-20, 2001.
- [111] M. A. Wicks and R. A. DeCarlo, "An energy approach to controllability," in *Proceedings* of the 27th IEEE Conference on Decision and Control, Austin, Texas, Dec. 1988, pp. 2072–2077.
- [112] Q. Cossart, "Tools and methods for the analysis and simulation of large transmission systems using 100% power electronics," Ph.D. thesis, École Nationale Supérieure d'Arts et Métiers, Sept. 2019.
- [113] Z. Ali, N. Christofides, L. Hadjidemetriou, E. Kyriakides, Y. Yang, and F. Blaabjerg, "Three-phase phase-locked loop synchronization algorithms for grid-connected renewable energy systems: A review," *Renewable and Sustainable Energy Reviews*, vol. 90, no. February, pp. 434–452, 2018.
- [114] T. M. Haileselassie, M. Molinas, and T. Undeland, "Multi-terminal VSC-HVDC system for integration of offshore wind farms and green electrification of platforms in the north sea," in *Proceedings of the Nordic Workshop on Power and Industrial Electronics*, 2008.
- [115] DIgSILENT PowerFactory 2017, Technical Reference Documentation Phase Measurement Device ElmPhi_pll, DIgSILENT, 2017.
- [116] K. Sharifabadi, L. Harnefors, H.-P. Nee, S. Norrga, and R. Teodorescu, *Dynamics and Control*. John Wiley & Sons, Ltd, 2016, ch. 3, pp. 133–213.
- [117] B. A. Francis, A course in H_{∞} control theory, 1st ed. Berlin, Germany: Springer-Verlag, 1988.
- [118] The MathWorks, Inc., "MATLAB Control System Toolbox," 2022.
- [119] A. Antoulas, "Approximation of large-scale dynamical systems: An overview," *IFAC Proceedings Volumes*, vol. 37, no. 11, pp. 19–28, 2004.

- [120] P. Benner, P. Ezzatti, D. Kressner, E. S. Quintana-Ortí, and A. Remón, "A mixed-precision algorithm for the solution of Lyapunov equations on hybrid CPU-GPU platforms," *Parallel Computing*, vol. 37, no. 8, pp. 439–450, 2011.
- [121] F. D. Freitas, J. Rommes, and N. Martins, "Low-rank Gramian applications in dynamics and control," in *Proceedings of the International Conference on Communications*, Computing and Control Applications, 2011, pp. 1–6.
- [122] P. Karim Aghaee, A. Zilouchian, S. Nike-Ravesh, and A. H. Zadegan, "Principle of frequency-domain balanced structure in linear systems and model reduction," *Computers & Electrical Engineering*, vol. 29, no. 3, pp. 463 477, 2003.
- [123] J. G. Calderón-Guizar, M. Ramírez-González, and R. Castellanos-Bustamante, "Identification of low frequency oscillation modes in large transmission systems," *Revista Facultad de Ingeniería Universidad de Antioquia*, no. 86, pp. 31–39, 2017.
- [124] R. L. Hendriks, G. C. Paap, R. Völzke, and W. L. Kling, "Model of a VSC transmission scheme for wind farm connection for incorporation in power system stability studies," in *Proceedings of the 16th Power Systems Computation Conference*, 2008, pp. 14–19.
- [125] J. B. Glasdam, L. Zeni, J. Hjerrild, U. Kocewiak, B. Hesselbæk, P. E. Sorensen, A. D. Hansen, C. L. Bak, and P. C. Kjær, "An assessment of converter modelling needs for offshore wind power plants connected via VSC-HVDC networks," in *Proceedings of the 12th Wind Integration Workshop*, 2013, pp. 1–6.
- [126] The MathWorks Inc., "Create linear analysis point for simulink model, linear analysis plots block, or model verification block," https://se.mathworks.com/help/slcontrol/ug/linio.html, 2023, accessed: 07-12-2023.
- [127] M. A. Pai, Energy Function Analysis for Power System Stability, 1st ed. New York: Springer, 1989.
- [128] G. Grdenić, F. J. C. García, N. M. D. Campos, F. Villella, and J. Beerten, "Model order reduction of voltage source converters based on the ac side admittance assessment: From EMT to RMS," *IEEE Transactions on Power Delivery*, vol. 38, no. 1, pp. 56–67, 2023.
- [129] N. M. D. Campos, T. Sarnet, and J. Kilter, "Novel gramian-based structure-preserving model order reduction for power systems with high penetration of power converters," *IEEE Transactions on Power Systems*, vol. 38, no. 6, pp. 5381–5391, 2023.
- [130] N. M. D. Campos, T. Sarnet, and J. Kilter, "A gramian-based tool for modeling converter-dominated power systems," in 2024 IEEE PES Innovative Smart Grid Technologies Europe (ISGT Europe), 2024, pp. 1–5.
- [131] Y. Levron, J. Belikov, and D. Baimel, "A tutorial on dynamics and control of power systems with distributed and renewable energy sources based on the DQ0 transformation," Applied Sciences (Switzerland), vol. 8, no. 9, 2018.
- [132] A. Antoulas, "Frequency domain representation and singular value decomposition," Rice University, Tech. Rep., 2002.
- [133] H. Sandberg, "Introduction to model order reduction lecture notes," https://www.diva-portal.org/smash/get/diva2:1338145/FULLTEXT01.pdf, pp. 1–51, 2019.

Acknowledgements

My PhD was a long journey that began in Belgium, continued for the most part in Estonia, and concluded in Germany. Over the years, several people supported me and made this thesis possible, making the acknowledgements almost as challenging to write as the thesis itself.

First, I would like to thank my supervisor, Jako Kilter, for giving me the opportunity to pursue a PhD. I am grateful for his feedback, guidance, and patience throughout this process. I would also like to thank my colleagues at TalTech: Sajjad, Pradeep, and Madis, for the shared moments together. In particular, I want to thank Tanel. He was the first to plant in me the idea of pursuing a PhD at TalTech. He rooted for my success and spent countless hours of his time supporting me throughout my journey. He helped me with publications, research ideas, and otherwise, serving as a sounding board on many occasions. Without him, my history would probably have been written in a very different way.

I am grateful to the people I met during my time in Belgium, in particular, Philippe, Özgür, Thomas, Firew, Geraint, and Vaishally, among others. Special thanks go to Diyun, who became a friend in unexpected times, from Belgium and beyond. I also thank the InnoDC colleagues for the great and enjoyable moments we shared together.

Finalising this thesis would not have been possible without the flexibility and understanding I received from Diana, Tom, and my colleagues at Fraunhofer IEE, for which I am very grateful.

Finally, I would like to express my gratitude to all the friends and people close to me who listened and offered advice along the way, with whom I shared this journey in both its good and challenging moments. Special thanks go to Anders for his patience and support during the demanding final stages of writing this thesis.

Não poderia terminar esses agradecimentos sem reconhecer e agradecer todo o apoio e torcida que recebi da minha família ao longo do meu doutorado, e na verdade, muito antes mesmo de eu começar essa trajetória. Em especial, quero agradecer ao meu pai, Henriques, que sempre estimulou meu senso crítico desde quando eu era criança. Com suas lições de matemática e seu laboratório cheio de componentes eletrônicos, ele me inspirou e habilitou a seguir o caminho da engenharia. Também sou muito grata à Fabiana, à minha avó, Ana Maria, ao meu avô, Manoel, e à minha irmã, Amandinha, que estiveram ao meu lado durante toda essa jornada que começou há muitos anos.

Abstract

Physics-Preserving Model Order Reduction for Stability Analysis of Converter-Dominated Power Systems

Modern power systems are undergoing rapid change as renewable energy sources and interconnections expand. This evolution is fundamentally reshaping system dynamics, with power electronic converters playing an increasingly central role. The unique dynamic behaviour of these converters not only introduces new categories of stability issues, but must also be accounted for within the established stability categories to ensure that all relevant phenomena are accurately represented in simulation studies. This thesis investigates the modelling and assessment of dynamic stability in converter-dominated power systems, addressing the crucial challenge of balancing model fidelity with computational efficiency.

To begin, the thesis reviews the emerging stability challenges in converter-dominated networks, contrasting Root Mean Square (RMS) and Electromagnetic Transients (EMT) modelling frameworks. A summary of various models available for representing different power system components is provided. Additionally, the concept of Model Order Reduction (MOR) is introduced as a potential tool for determining the appropriate level of detail required in models suited for different types of studies.

The thesis offers an overview of MOR, with a particular focus on the widely adopted balanced truncation method. This method utilises a balancing transformation to identify and truncate less significant states, enabling a near-optimal reduction of the number of states within the model. However, this transformation results in a changed coordinate system that no longer has a direct connection to the physical system, resulting in reduced models that are neither intuitive nor interpretable. Consequently, it becomes impossible to identify which parts of the physical system are most relevant to the dynamic phenomena.

To overcome this limitation, the thesis adapts the balanced truncation method, introducing two systematic MOR methodologies. One methodology focuses on capturing the system's response to specific disturbance events, while the other targets dynamic behaviour within selected frequency ranges. Both methods rely on controllability and observability Gramians to quantify each state's contribution to system dynamics. Unlike other MOR methods, the proposed methodologies preserve original state coordinates to maintain physical interpretability. This feature facilitates the application of these methods to determine which components and control models to incorporate in practical system studies.

Additionally, a software tool based on MATLAB/Simulink was developed to automate the model reduction process and assist users in selecting the appropriate level of modelling detail for different system configurations. This tool provides both visual and quantitative assessments of each component's contribution to the system dynamics. The proposed method and tool were validated through two case studies: the converter-dominated 9-bus system and the modified 39-bus system. These studies demonstrate that the method can significantly reduce model complexity and simulation time while maintaining accuracy in dynamic responses.

Together, the model reduction frameworks and the software implementation offer an effective approach to defining requirements on dynamic models in converter-dominated power systems. These contributions aim to assist system operators, researchers, and engineers in selecting appropriate modelling detail as power systems transition toward higher levels of converter integration.

Keywords

Converter-Dominated Power Systems, Power System Stability, Model Order Reduction, Controllability and Observability Gramians, Electromagnetic Transient Simulation, Root Mean Square Simulation, Dynamic System Modelling, Stability Assessment Tools

Kokkuvõte

Füüsikalisi omadusi säilitav mudeli järgu alandamise metoodika muunduripõhiste elektrisüsteemide stabiilsusanalüüsiks

Tulenevalt taastuvenergiaallikate kiirest lisandumisest ja suurenevast võrkudevahelisest integreeritusest on tänapäeva elektrisüsteemid kiires muutumises. Need põhimõttelised muutused muudavad ka põhjalikult süsteemi dünaamikat ja järjest olulisem osatähtsus selles süsteemis on jõuelektroonikamuunduritel. Sellest tulenevalt on võrguarvutuste teostamisel oluline muundurite korrektne arvestamine, kuna nende seadmete ainulaadne dünaamiline käitumine põhjustab uusi stabiilsusnähtusi ja samuti mõjutavad need olemasolevaid stabiilsuskategooriaid. Käesolev doktoritöö uurib, kuidas adekvaatselt modelleerida ja analüüsida elektrisüsteemi dünaamilise stabiilsusega seotud aspekte muundurpõhistes elektrisüsteemides, käsitledes olulist väljakutset, kuidas leida tasakaal mudeli täpsuse ja arvutuskoormuse vahel.

Doktoritöö algab ülevaatega muundurpõhistes elektrisüsteemides aset leidvatest stabiilsusnähtustest, võrreldakse efektiiv- ja hetkväärtusmodelleerimise raamistikke ning esitatakse kokkuvõte praegustest soovitustest erinevate elektrisüsteemi komponentide kujutamiseks sobivatest mudelitest. Lisaks tutvustatakse mudeli järgu alandamise kontseptsiooni, kui potentsiaalset tööriista erinevat tüüpi uuringuteks sobivate mudelite detailsuse taseme määramiseks.

Doktoritöö esitab ülevaate mudeli järgu alandamise lähenemisviisidest, keskendudes eelkõige laialdaselt kasutusel olevale tasakaalustatud vähendamismeetodile. See meetod kasutab tasakaalustavat teisendust vähemoluliste olekute tuvastamiseks ja eemaldamiseks, võimaldades seeläbi mudeli olekute arvu peaaegu optimaalset vähendamist. Selline lähenemisviis põhjustab aga koordinaatsüsteemi muutuse, mille tulemusena puudub saadaval mudelil otsene seos füüsilise süsteemiga ja seetõttu on tulemuseks lihtsustatud mudelid, mis ei ole ei intuitiivsed ega tõlgendatavad. Selle tulemusena muutub võimatuks määratleda millised füüsilise süsteemi osad on kõige olulisemad elektrisüsteemi dünaamikanähtuste uurimiseks.

Sellest puudusest ülesaamiseks esitatakse doktoritöös tasakaalustatud vähendamismeetodi edasiarendus ja pakutakse välja kaks süstemaatilist mudeli järgu alandamise meetodit. Esimene neist keskendub süsteemi reageeringu tuvastamisele konkreetsete häiringute korral ja teine dünaamikaprotsesside määratlemisele vaadeldavates sagedusvahemikes. Mõlemad lähenemisviisid tuginevad juhitavuse ja vaadeldavuse gramianidele, et kvantifitseerida iga oleku panust süsteemi dünaamikasse. Erinevalt teistest mudeli järgu alandamise lähenemisviisidest säilitavad pakutud meetodid esialgsed oleku koordinaadid ja seeläbi säilitatakse füüsikaline tõlgendatavus. See omadus hõlbustab nende meetodite rakendamist ja aitab määratleda, milliseid komponente ja juhtimismudeleid on praktiliste süsteemiuuringute korral tarvilik kasutada.

Eesmärgiga automatiseerida mudelite järgu alandamise protsessi ja abistamaks kasutajaid erinevate elektrisüsteemi konfiguratsioonide korral sobiliku modelleerimisdetailsuse valikul koostati MATLAB/Simulink keskkonnas vastavasisuline tarkvaratööriist. See tööriist pakub nii visuaalset kui ka kvantitatiivset hinnangut iga komponendi panuse kohta süsteemi dünaamikasse. Arendatud meetodite ja tööriista sobilikkust hinnati kahe juhtumiuuringu näitel, kus kasutati vastavalt muundurpõhist 9-sõlmelist ja muudetud 39-sõlmelist süsteemi. Nende uuringute tulemused näitavad, et arendatud meetodid võimaldavad oluliselt vähendada mudeli keerukust ja simulatsiooniaega, säilitades samal ajal dünaamiliste reaktsioonide täpsuse.

Mudeli järgu alandamise raamistik ja selle tarkvaraline rakendamine pakuvad tõhusa

lähenemisviisi dünaamiliste mudelite nõuete määratlemiseks muundurpõhistes elektrisüsteemides. Uurimustöö tulemused aitavad süsteemihalduritel, teadlastel ja inseneridel valida sobilik modelleerimistäpsus elektrisüsteemide üleminekul muundurpõhistele süsteemidele.

Märksõnad

dünaamiliste süsteemide modelleerimine, efektiivväärtusarvutus, elektrisüsteemi stabiilsus, hetkväärtusarvutus, juhitavuse ja vaadeldavuse gramian, mudeli järgu alandamine, muundurpõhised elektrisüsteemid, stabiilsuse hindamise tööriistad

Appendix A — Included Publications

Publication I

G. Grdenić, F. J. C. García, N. M. D. Campos, F. Villella, and J. Beerten, "Model order reduction of voltage source converters based on the ac side admittance assessment: From EMT to RMS," *IEEE Transactions on Power Delivery*, vol. 38, no. 1, pp. 56–67, 2023

Model Order Reduction of Voltage Source Converters Based on the Ac Side Admittance Assessment: From EMT to RMS

Goran Grdenić , *Member, IEEE*, Francisco J. Cifuentes García , Nathalia de Morais Dias Campos , *Student Member, IEEE*, Fortunato Villella, and Jef Beerten , *Senior Member, IEEE*

Abstract—Time-averaged electromagnetic (EMT) power electronics models can comprise tens of state variables, and in upcoming converter-dominated power systems, this can cause a substantial computational burden. The level of detail in their modeling, however, is typically much greater than what is typically necessary for transient stability (RMS) tools. Hence, there is a reasonable need for using reduced-order models of power electronics devices in accordance with the study needs and the related frequency range of interest. This paper focuses on modeling the time-averaged voltage source converter (VSC) for the application in ac system stability studies where the small-signal assumption holds for converter variables. The impact of simplifications and converter parameters in VSC's model accuracy is evaluated first as observed from the ac-side admittance. Subsequently, based on the previous assessment, a limited set of VSC reduced-order models is established and analyzed – which is the main paper contribution. The parametric sensitivity analysis is conducted to establish the validity boundaries of the proposed models in the frequency domain. Finally, the recommendations for the use in different power system studies are provided.

Index Terms—Ac side equivalent admittance, EMT models, model order reduction, RMS models, time-averaged models, voltages source converters.

I. INTRODUCTION

MATHEMATICAL model of a material system or a process is an approximate representation of physical reality. However, the goal of such approximations is to capture the

Manuscript received 29 October 2021; revised 29 January 2022 and 15 April 2022; accepted 14 May 2022. Date of publication 3 June 2022; date of current version 24 January 2023. This work was supported in part by European Commission's Horizon 2020 Research and Innovation Programme (Marie Skłodowska-Curie Actions) through the project Innovative Tools for Offshore Wind and DC Grids (InnoDC) under Grant 765585, in part by the Research Foundation Flanders (FWO) under Grant G0D2319N, and in part by the Neptune project, supported by the Energy Transition Fund, FOD Economy, Belgium. Paper no. TPWRD-01630-2021. (Corresponding author: Goran Grdenić.)

Goran Grdenić, Francisco J. Cifuentes García, Nathalia de Morais Dias Campos, and Jef Beerten are with the Department of Electrical Engineering, KU Leuven, 3000 Leuven, Belgium, and also with the Energyville, 3600 Genk, Belgium (e-mail: goran.grdenic@fer.hr; franciscojavier.cifuentesgarcia@kuleuven.be; nathalia.campos@taltech.ee; jef.beerten@esat.kuleuven.be).

Fortunato Villella is with Elia Grid International, 1000 Brussels, Belgium (e-mail: fortunato.villella@eliagrid-int.com).

Color versions of one or more figures in this article are available at https://doi.org/10.1109/TPWRD.2022.3179836.

Digital Object Identifier 10.1109/TPWRD.2022.3179836

phenomena of interest accurately. In this regard, various models of power system components have been developed for different types of studies [1].

This paper focuses on time-averaged models of two-level voltage source converters (VSCs), a technology that is increasingly being employed in power systems. In time-averaged models of power electronics devices, discrete-time switching is substituted with continuous-time functions. This simplification enables both the application of larger time steps in running electromagnetic (EMT) simulations, and, forms the basis for further simplifications such that the model can be used in transient stability (RMS) programs [2]. Time-averaged models are applicable in many power system studies: transient and small-signal analysis, tuning of converter high-level control parameters, and a broad range of analysis usually performed in RMS tools [3].

Time-averaged converter models are described by nonlinear time-varying mathematical functions. These properties hinder the application of powerful linear analysis techniques. Several methods are developed for obtaining linear time-invariant (LTI) models, of which the dq-frame, dynamic phasor, and harmonic state-space (HSS) are the most known [4]. This paper concentrates on dq-frame LTI models of VSCs which are extensively being employed in many power system studies. The Park transformation enables the conversion of a balanced steady-state three-phase system into time-invariant dq quantities. The obtained model can easily be linearized around the operating point using Taylor series expansion.

The significant property of dq-frame modeling is the preservation of frequency coupling dynamics of the fundamental frequency. On the downside, it cannot be applied to obtain an LTI model of unbalanced three-phase systems or to study the effects of harmonics, thus necessitating the use of multi-frequency modeling methods (dynamic phasors, HSS) [5]. Besides, the applicability of dq-frame models in the frequency domain is lower than half of the switching frequency. This limitation derives from the use of the moving average operator to obtain a continuous switching function [4].

Various levels of detail can be found in dq-frame two-level VSC models available in the literature. They include the following elements: ac- and dc-side dynamics, inner and outer controls, phase-locked loop (PLL), filter dynamics, converter

0885-8977 © 2022 IEEE. Personal use is permitted, but republication/redistribution requires IEEE permission. See https://www.ieee.org/publications/rights/index.html for more information.

dead time. Timescales of specified components extend from several hundred of microseconds to seconds, therefore requiring a high computational power (small time steps and long horizon). As long the number of converters in a system is small, this might not pose a major issue. However, in envisioned future converter-dominated power systems, removal of the unnecessary modeling details is imperative to obtain the optimal model size for the study of interest.

Previously, a number of model simplifications have been presented or have implicitly been used in power system studies. The most common simplifications are the omission of the inner current control (ICC) [6], [7], [8] and/or the PLL [6], [9], [10]. Although some of the listed research incorporates modular multilevel converters, the same principles regarding the ICC and PLL also hold for two-level converters. The simulation time step in RMS tools is usually higher than the ICC time constant, thus justifying its elimination. However, it has been demonstrated that inner loops also play a relevant role in slow mode dynamics [11], [12]. Alternatively, the ICC loop is sometimes modeled with a first-order time-delay approximation. Yet, following the results from [13], such representation is inadequate for converters connected to the bus with a low short-circuit ratio. The converter dead time is usually not represented in most of the studies. Nevertheless, its modeling becomes essential for the appropriate assessment of converter and grid interactions at higher frequencies [14], [15]. A classical phasor approximation is often used to neglect the dynamics of ac side currents (as for stator currents in synchronous generator models [16]). However, the EMT representation of converter currents may also become important at higher frequencies.

Model-order reduction has been applied to large-scale wind or PV power plants by aggregating the dynamics of many similar units into an equivalent that preserves the main dynamic characteristics, e.g., [17] and [18]. However, such reduction methods are not applicable if converters are spatially distributed in a power grid - thus, necessitating the need for reducedorder models of a single converter. In [19], the reduction of a grid-forming converter model is conducted by residualizing the groups of state variables linked to the fastest eigenvalues. Yet, because of insufficient timescale separation, the formation of disjoint groups of state variables and the associated eigenvalues may be troublesome. An innovative approach was developed in [11], where several fast states are initially discarded, and subsequently, the representation of their participation in slow modes is added back to the converter model. Another reduction method was proposed in [12], in which time constants of fast states are extracted in a transfer function model, while the state-space model is used for dynamics of slow states.

The above-mentioned research, however, do not reflect on the applicability of developed reduced-order models in the frequency domain and suitability for different power system studies. Therefore, the main objectives of this paper are: (a) evaluate the impact of simplifications in the model's accuracy as observed from the ac-side admittance, and (b) establish a limited set of VSC reduced-order models measuring in what frequency ranges the models are valid and thus determining their applicability in different stability studies according to the

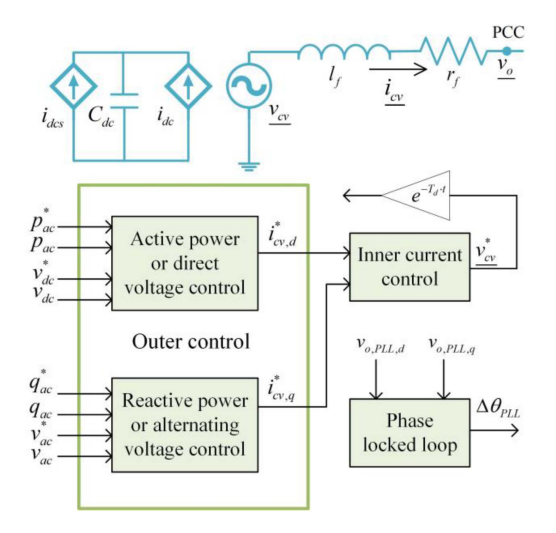


Fig. 1. Time-averaged model of a two-level converter.

frequency of observed phenomena. The proposed reduced-order models consist only of the basic VSC components and preserve the physical meaning of the model variables.

The rest of the article is organized as follows. Chapter 2 provides the complete mathematical description of the detailed dq-frame converter model that will serve as a reference model in this study. The impact of converter parameters and modeling details on the ac side admittance is assessed in chapter 3. In chapter 4, the set of reduced-order models is proposed and evaluated. A parametric sensitivity analysis is conducted in chapter 5 to establish the validity boundaries of the different models in the frequency domain. In addition, recommendations for the application of the proposed VSC reduced-order models in different stability studies are provided. Finally, the main findings are summarized in the conclusion section.

II. REFERENCE VSC MODEL IN DQ-FRAME

The layout of the time-averaged two-level VSC converter model in grid-following operation mode is presented in Fig. 1. It consists of a controllable voltage source on the ac side and a controllable current source on the dc side.

The ac side current $i_{\underline{cv}}$ is described by the following equation:

$$\frac{l_f}{\omega_b} \frac{di_{cv}}{dt} = \underline{v_{cv}} - \underline{v_o} - \underline{i_{cv}} \cdot (r_f + j \cdot \omega_g \cdot l_f) \tag{1}$$

where $\underline{v_{cv}}$ and $\underline{v_o}$ are the converter and point of common coupling (PCC) voltages, l_f and r_f are the aggregated phase reactor and transformer inductance and resistance, ω_b and ω_g are the base and grid per unit angular frequencies. The underbar denotes variables in the dq-reference frame, i.e., $\underline{x} = x_d + jx_q$. The equation governing the behavior of the dc side voltage v_{dc} is:

$$\frac{c_{dc}}{\omega_b} \frac{dv_{dc}}{dt} = i_{dc} - i_{dcs} \tag{2}$$

The dc side current is denoted with i_{dc} , the dc current source with i_{dcs} , and c_{dc} is the dc side capacitance. The ac and the

dc side are linked by the power conservation law (a lossless converter is assumed):

$$v_{cv,d} \cdot i_{cv,d} + v_{cv,q} \cdot i_{cv,q} = v_{dc} \cdot i_{dc} \tag{3}$$

The converter has a hierarchical control structure consisting of outer loops for the active power (or the dc voltage) and the reactive power (or the ac voltage) control, the ICC loop for the regulation of ac side currents, and the PLL that is utilized for synchronization with the ac grid. The employed vector control method enables independent regulation of converter active and reactive power. The mathematical description of control circuits and employed tuning rules are provided in the subsequent sections

A. Inner Current Control and Dead Time

The reference value of the converter voltage $\underline{v_{cv}^*}$ is set in the ICC loop:

$$\underline{v_{cv}^*} = k_{p,ICC} \left(\underline{i_{cv}^*} - \underline{i_{cv,m}} \right) + k_{i,ICC} \cdot \underline{\gamma}
+ \underline{j} \cdot l_f \cdot \omega_{PLL} \cdot \underline{i_{cv,m}} + v_{o,ICC}$$
(4a)

$$\frac{d\gamma}{dt} = \left(\underline{i_{cv}^*} - \underline{i_{cv,m}}\right) \tag{4b}$$

where $i^*_{\underline{cv}}$ and $i_{\underline{cv},\underline{m}}$ are the reference and low-pass filtered (measured) values of converter current, $k_{p,ICC}$ and $k_{i,ICC}$ are the proportional and integral coefficients of the PI controller, $\underline{\gamma}$ is the controller integrator state, and $\underline{v}_{o,ICC}$ is the feedforwarded low-pass filtered PCC voltage. The coefficients of the PI controllers are tuned using the model internal control technique [20] resulting in the two straightforward equations:

$$k_{p,ICC} = \frac{l_f}{\tau_{ICC} \cdot \omega_b} \tag{5a}$$

$$k_{i,ICC} = \frac{r_f}{\tau_{ICC}} \tag{5b}$$

with τ_{ICC} being the desired first-order time response of the ICC.

The ac side driving voltage $\underline{v_{cv}^*}$ is an input to the pulse width modulator that is not presented in time-averaged models. However, the common approach is adding the time delay T_d at the ICC output that accounts for the modulation and computation dead time:

$$\underline{v_{cv,d}^*} = e^{-T_d \cdot t} \cdot \underline{v_{cv}^*} \tag{6}$$

B. Outer Loop Control

The reference value of converter ac side current $\frac{i_{cv}^*}{cv}$ is set in the outer control. The d-component is utilized for the active power or the dc voltage control, and the q-component for the reactive power or the ac voltage control. The outer control loops are described in equations (7) and (8), where a^* and a are the reference and the low-pass filtered values of the active power or the dc voltage, b^* and b are the reference and the low-pass filtered values of the reactive power or the ac voltage, $k_{p,P}$, $k_{i,P}$, ρ_d , $k_{p,Q}$, $k_{i,Q}$ and ρ_q are the coefficients and the integrator states of the corresponding PI controllers.

$$i_{cv,d}^* = k_{p,P} (a^* - a) + k_{i,P} \rho_d$$
 (7a)

$$\frac{d\rho_d}{dt} = a^* - a \tag{7b}$$

$$i_{cv,q}^* = k_{p,Q} (b^* - b) + k_{i,Q} \rho_q$$
 (8a)

$$\frac{d\rho_q}{dt} = b^* - b \tag{8b}$$

In tuning of the active and reactive power control loops, the previously designed first-order response of the ICC is assumed, and the variation of the voltage at the PCC is neglected. Imposing the desired first-order time response with the time constant $\tau_{\rm out}$ leads to the following expressions for the proportional and integral coefficients:

$$k_{p,P(Q)} = \frac{\tau_{ICC}}{\tau_{\text{out}}}$$
 (9a)

$$k_{i,P(Q)} = \frac{1}{\tau_{\text{out}}} \tag{9b}$$

The square of the dc voltage is employed for the dc voltage control, and the PI coefficients are determined by using the expressions from [21]. The ac voltage control has not been utilized in this research.

C. PLL Control

The PLL is an unavoidable element in grid following converters employed for the synchronization with the ac grid. The following set of equations describe the PLL dynamics:

$$\Delta \varphi = \frac{v_{o,PLL,q}}{\sqrt{v_{o,PLL,d}^2 + v_{o,PLL,q}^2}}$$
(10a)

$$\Delta \omega_{PLL} = k_{nPLL} \cdot \Delta \varphi + k_{iPLL} \cdot \varepsilon_{PLL} \tag{10b}$$

$$\frac{d\varepsilon_{PLL}}{dt} = \Delta\varphi \tag{10c}$$

$$\Delta \theta_{PLL} = \int \Delta \omega_{PLL} dt \tag{10d}$$

The phase tracking error is denoted with $\Delta \varphi$, $v_{o,PLL,d}$ and $v_{o,PLL,q}$ are the low-pass filtered components of the PCC voltage, $\Delta \omega_{PLL}$ and $\Delta \theta_{PLL}$ are the frequency and angle deviations, $k_{p,PLL}$, $k_{i,PLL}$ and ε_{PLL} are the PI coefficients and the corresponding integrator state. The coefficients of the PI controller are tuned by using the recommendations from [22]. The angle deviation $\Delta \theta_{PLL}$ is used in the transformations from the global DQ-reference frame to the converter's local dq-reference frame, and vice versa.

Fig. 2 presents the comparison of frequency response estimation using a sinusoidal perturbation of the described VSC model with the linearized model where the 10th order Padé approximation is used for time-delay linearization. The comparison is conducted in terms of an equivalent ac side admittance with PCC voltage $\underline{v_o}$ being the input and the converter currents $\underline{i_{cv}}$ the output signals:

$$\begin{bmatrix} i_{cv,d} \\ i_{cv,q} \end{bmatrix} = \begin{bmatrix} Y_{dd} & Y_{dq} \\ Y_{qd} & Y_{qq} \end{bmatrix} \cdot \begin{bmatrix} v_{o,d} \\ v_{o,q} \end{bmatrix}$$
(11)

Only the dd component is exhibited. MATLAB/Simulink is utilized, as well as in the rest of this research. The converter is in rectifier operation mode, with active and reactive power

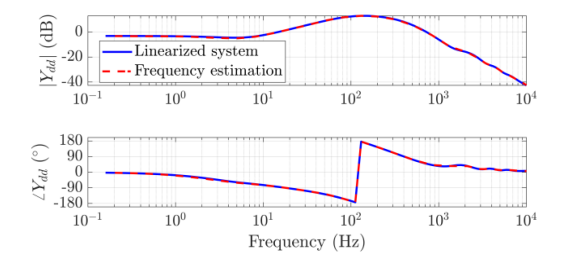


Fig. 2. Comparison of frequency response estimation and linearized VSC model (dd admittance component).

control being implemented in outer loops. An almost perfect matching can be observed even above the frequency of interest, i.e., the half of the switching frequency (1 kHz in this case). Accordingly, the linearized system (with the 10th order Padé time delay approximation) serves as a reference model in the sequel of this research. All parameters of the reference model are provided in Table VI in the Appendix.

III. IMPACT OF CONVERTER PARAMETERS AND MODELING DETAILS ON THE AC SIDE ADMITTANCE

In the following subsections, the influence of different VSC model simplifications and parameters on the ac side equivalent admittance in the dq-reference frame is examined. Because of the limited space, only the dd-component of the admittance is presented (except for the PLL influence where the qq-component is exhibited).

A. Ac and Dc Side Representation

The phasor-based or RMS modeling is the most common simplification in the analysis of power systems. It assumes that the variables are quasi-stationary, i.e., they do not deviate significantly from the nominal frequency. Applying this assumption to the reference EMT model developed in the previous section results in the omission of the derivative term in (1). The differential equation becomes an algebraic (12), consequentially neglecting the high-frequency phenomena in the electromagnetic spectrum. Fig. 3 shows the influence of this simplification for different values of ICC bandwidths on the ac side admittance¹. The better matching of the simplified RMS model is achieved for faster ICC control. Neglecting the derivation term in (1) results in almost instantaneous converter current control.

$$0 = v_{cv} - v_o - i_{cv} \cdot (r_f + j \cdot \omega_g \cdot l_f)$$
 (12)

For the dc side modeling, three different representations are considered: (i) a voltage source, (ii) a capacitance and an ideal current source, and (iii) a capacitance, dc line and a voltage source. The results exhibited in Fig. 4 show the perfect matching of all the three dc side representations when a converter is in the active power control mode. However, for the dc voltage control,

¹The bandwidth of the first-order system is equal to a reciprocal value of the time constant.

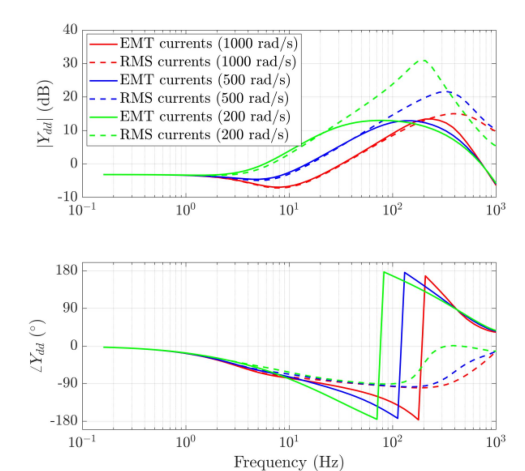


Fig. 3. Influence of the ac side representation on the dd admittance component.

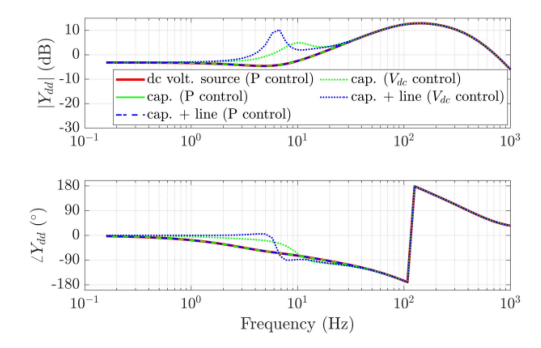


Fig. 4. Influence of the dc side representation on the dd admittance component.

a mismatch appears in the low-frequency region for the different dc side representations.

B. ICC Modeling

The time constant of the ICC is usually smaller than the simulation time step used in RMS simulations. Accordingly, its omission or simplification has been considered in electromechanical stability programs. The resulting simplified model is based on the first-order time delay transfer function:

$$\underline{i_{cv}} = \frac{1}{1 + \tau_{ICCS}} \, \underline{i_{cv}^*} \tag{13}$$

The simplified model and the ICC omission are benchmarked against the reference EMT model in Fig. 5. The neglection of the ICC loop causes a mismatch even in the low-frequency region (below 10¹ Hz). Furthermore, the first-order time delay approximation does not substantially extend the VSC model validity in the frequency domain. Therefore, the simplified ICC model is disregarded in the rest of this paper.

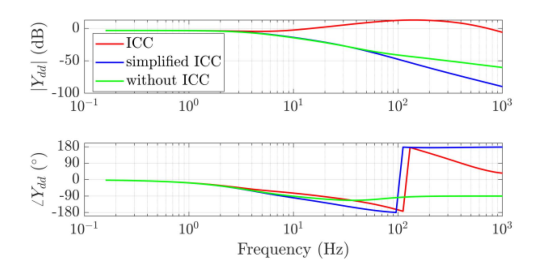


Fig. 5. Influence of the ICC modeling on the dd admittance component.

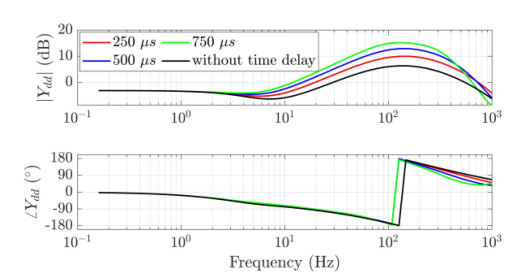


Fig. 6. Influence of the dead time values and its omission on the dd admittance component.

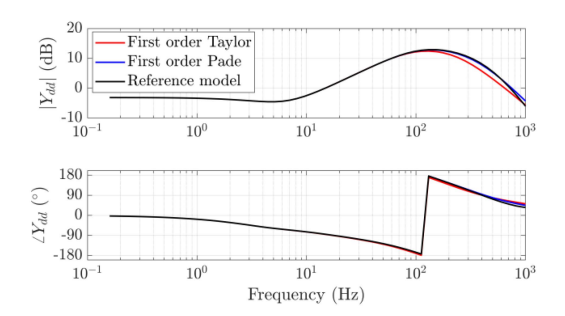


Fig. 7. Influence of the dead time representation on the dd admittance component.

C. Dead Time Modeling

Fig. 6 exhibits the influence of different values of the dead time and its omission. The mismatch to the reference model is more prominent for higher values of the dead time. In the magnitude plot, it is largest above 10^2 Hz. Yet, it is present in the low-frequency range as well. The phase mismatch becomes more pronounced closer to the kHz region. Furthermore, in Fig. 7, two simplified time-delay representations used for the linearization (1st order Taylor and Padé approximations) are compared with the benchmark model. The first-order Padé approximation, although utilizing the same number of state variables as the first-order Taylor approximation, shows better agreement with the benchmark model.

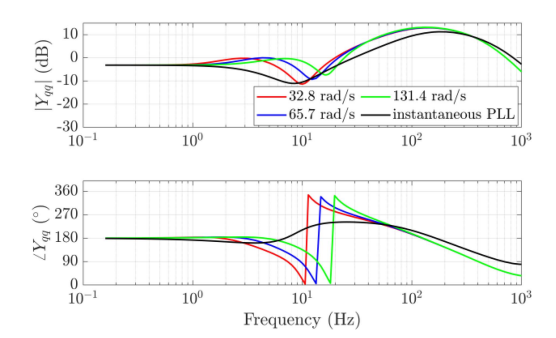


Fig. 8. Influence of the PLL modeling and bandwidth on the qq admittance component.

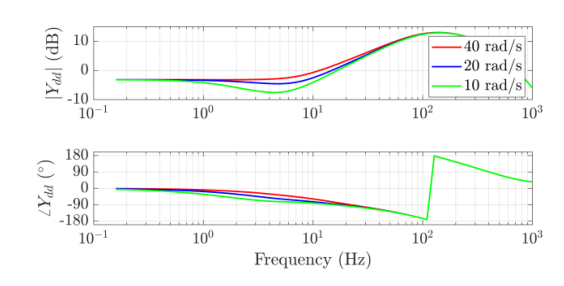


Fig. 9. Influence of the outer loop bandwidth on the dd admittance component.

D. PLL Modeling

The influence of the PLL bandwidth on the ac side admittance is presented in Fig. 8. Moreover, it is compared with an instantaneous PLL in which (10b)–(10d) are replaced with the following expression:

$$\Delta \theta_{PLL} = \sin(\Delta \varphi) \tag{14}$$

The angle deviation $\Delta\theta_{PLL}$ is calculated algebraically, and the PLL dynamics are disregarded. This simplification has a significant impact even at very low frequencies, emphasizing the need for the appropriate PLL modeling to obtain a good representation in the low-frequency region.

E. Outer Loop Bandwidth and Operating Point

Fig. 9 exhibits the influence of outer loop bandwidth on the ac side admittance. This control parameter, expectedly, influences the low-frequency region. The converter operating point affects the low-frequency dynamics and the steady-state admittance value, as observable in Fig. 10.

IV. VSC REDUCED-ORDER MODELS

Based on the analysis from the previous section, different converter parameters and modeling components are presented in Fig. 11, accounting for their influence on the equivalent ac side admittance in the frequency domain. The frequency shift of 50 Hz caused by Park transformation is considered. The outer loop bandwidth and operating point influence the equivalent ac

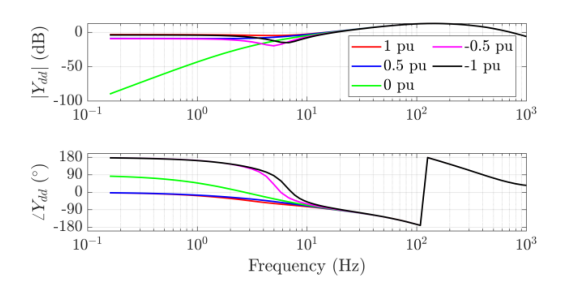


Fig. 10. Influence of the operating point on the dd admittance component.

Outer loop control	Inner current con	trol
Operating point	Phase locked loop	Time delay
De side dy	namics A	c currents dynamics
10 Hz 50	0 Hz 100 Hz	1000 Hz

Fig. 11. Influence of different converter parameters and modeling components in the frequency domain.

 $\begin{tabular}{l} TABLE\ I\\ THE\ PROPOSED\ REDUCED-ORDER\ MODELS\ AND\ THEIR\ CONSTITUENT\\ ELEMENTS \end{tabular}$

	Outer loops	P&Q filter	PLL	PLL filter	ICC	ICC voltage filter	ICC current filter	EMT currents	Dead time	Number of state variables
Model 1	+	+								4
Model 2	+	+	+	+	+	+	+			14
Model 3	+	+	+	+	+	+	+	+	+	18
Model 4			+	+	+	+	+	+	+	14

side admittance in the low-frequency region, including the synchronous frequency. Then, the appropriate PLL and ICC modeling becomes important for phenomena above the synchronous frequency. The suitable dc side representation is also relevant in this frequency region, but only for the dc voltage control mode. Finally, the impact of the ac side representation and the dead time subsequently rises at higher frequencies. Here, it needs to be emphasized that the exhibited frequency distribution of converter parameters and modeling components summarized in Fig. 11 holds under the assumption of the converter's stability as a standalone system that is ensured by applying standard tuning procedures of converter parameters.

Based on the exhibited converter element stratification in Fig. 11, the proposed VSC modeling reduction includes four models with varying levels of detail. The active and reactive power control modes are considered in the sequel of this research. Following the results from Fig. 4, the dc side dynamics can be neglected consequently. The number of state variables and constituent elements of the VSC reduced models are summarized in Table I. Low-pass filters are included together with the corresponding modeling element. Model 1 consists of only outer loops for the active and reactive power control and has

TABLE II VALIDITY LIMITS OF THE REDUCED-ORDER MODELS IN DQ-REFERENCE FRAME (HZ) AND THE NECESSARY PADÉ ORDER TO MEET SPECIFIED TOLERANCES UP TO 1000 HZ

	Model 1	Model 2	Model 3	Model 4*	Padé
5 dB	<3.6	<14.2	<1000	>12.0	1
10 dB	<10.1	<39.9	<1000	>5.8	1
20 dB	<19.1	<48.7	<1000	>2.3	1
5°	< 0.5	< 5.8	<271.2	>55.0	3
15°	<1.7	<8.6	<501.9	>28.9	2
30°	<6.1	<10.1	<760.0	>15.3	2

^{*}Model 4 upper validity limits correspond to model 3 limits provided in the table.

four state variables. Model 2 additionally incorporates the ICC loop, the PLL, and the corresponding low-pass filters. It has 14 state variables overall. Model 3, furthermore, is extended by the EMT representation of the ac side currents and the first order Padé time-delay approximation, resulting in the model with 18 state variables altogether. Model 3 differs from the reference model only in the Padé order utilized for time delay linearization. Finally, the low-frequency dynamics of outer loops are neglected in Model 4, making the model applicable only for high-frequency domain studies. It needs to be emphasized that the proposed composition is certainly not unique. However, the results presented in continuation and the comparison with other reduced-order model configurations justify the selection made.

The comparison of the ac side admittance absolute error for the four reduced-order VSC models w.r.t. to the reference model is presented in Fig. 12. Reduced-order models 1, 2, and 3 match the reference model in the low-frequency region, and the absolute error starts to increase when moving to higher frequencies. A better fitting is accomplished, expectedly, with an increase in the number of model state variables. Model 4 absolute error is significant in the low-frequency region, reduces for higher frequencies, and becomes prominent again while approaching the kHz range (as model 3).

Three different values for the magnitude (5, 10, and 20 dB) and the phase tolerances (5°, 15°, and 30°) are selected to establish quantitative limits of the reduced-order models in a frequency domain. The minimum value of the four admittance components is provided in Table II for models 1, 2, and 3, and the maximum value for model 4. The validity of Model 1 extends slightly above the synchronous frequency for specified tolerances. The validity limits, as might be expected, become higher for less strict tolerances. Model 2 validity does not extend significantly in the frequency domain, although the model includes the ICC and the PLL. The more notable extension is accomplished by model 3. For the set magnitude thresholds, it is accurate in the entire range, i.e., up to half of the switching frequency, and for the set phase thresholds, its validity reaches several hundred Hz. Model 4 becomes suitable for frequencies above the synchronous frequency, and the validity limits become lower for less strict tolerances. Also, model 4 upper validity boundaries correspond to model 3 limits provided in the table because it also includes only the first order Padé approximation for time delay modeling. It is interesting to notice that for the set phase tolerances, there is a gap between validity limits of models

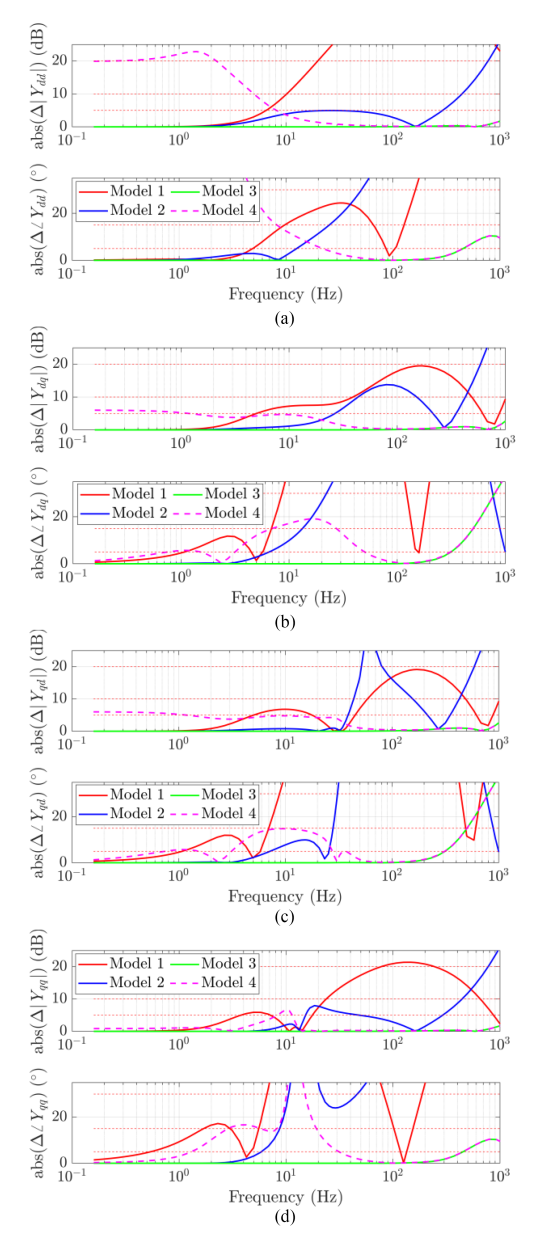


Fig. 12. Comparison of the ac side admittance absolute error of the reducedorder VSC models: (a) dd-component; (b) dq-component; (c) qd-component; (d) qq-component.

2 and 4, thus necessitating the model 3 application to cover this frequency range. Finally, the necessary Padé order for time delay linearization to meet the VSC model accuracy up to half of the switching frequency is provided in the last column of Table II. While the first-order approximation is sufficient for the set magnitude tolerances, the 2nd order is necessary for 15° and 30° phase tolerance, and the 3rd order for the 5° threshold.

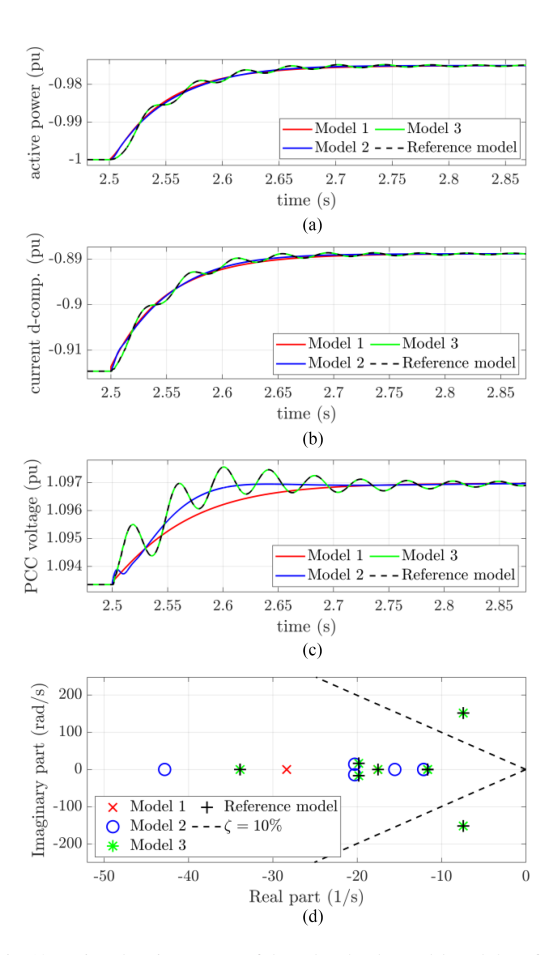


Fig. 13. Time-domain response of the reduced-order models and the reference model following the active power reference step: (a) Active power; (b) d-component of converter current; (c) PCC voltage; (d) Dominant modes.

TABLE III OTHER COMMONLY USED REDUCED-ORDER MODELS AND THEIR CONSTITUENT ELEMENTS

	Outer loops	P&Q filter	PLL	PLL filter	ICC	ICC voltage filter	ICC current filter	EMT currents	Dead time	Number of state variables
Model 2a	+	+	+	+						8
Model 2b	+	+			+	+	+			10
Model 3a	+	+	+	+	+	+	+	+		16
Model 3b	+	+	+	+	+	+	+		+	16

The behavior of the reduced-order models is compared by time-domain simulations of nonlinear models in Figs. 13(a)–(c). The external ac grid consists of a Thevenin equivalent and a capacitance at the connection point. The parameters are provided in Table VII in the Appendix. When the phasor representation is employed for converter currents modeling, the same modeling

TABLE IV VALIDITY RANGES OF THE REDUCED-ORDER MODELS IN DQ-REFERENCE FRAME (HZ)

	Model 1	Model 2	Model 3	Model 4
5 dB	<1.8-11.7	<5.1-71.6	<642.6-1000	>3.7-58.5
10 dB	<4.4-18.7	<8.4-114.4	<887.9-1000	>2.3-36.7
20 dB	<8.9-35.1	<24.8-825.7	<1000	>0-5.1
5°	< 0.2-1.0	<2.2-12.6	<185.5-686.5	>27.4-91.7
15°	<0.8-7.4	<4.0-19.1	<242.0-1000	>6.2-66.9
30°	<2.8-12.6	<4.8-23.1	<304.8-1000	>1.7-52.7

TABLE V
RECOMMENDATIONS FOR THE APPLICABILITY OF THE PROPOSED
REDUCED-ORDER VSC MODELS IN POWER SYSTEM STABILITY STUDIES

Categories of power system stability	Proposed VSC reduced-order model
Classical stability problems (rotor angle oscillations, small-disturbance voltage stability,)	Model 1 or model 2
Resonance stability	Model 2 or model 3
Slow-interaction converter-driven stability	Model 2 or model 3
Fast-interaction converter-driven stability	Model 3, model 4 or the reference model

assumption is also utilized for external grid modeling. The active power reference step $\Delta p^*=0.025$ pu is applied at 2.5 s, and the converter's active power, current (d-component), and PCC voltage are observed. Oscillations present in the reference model time response are not reflected when using reduced-order models 1 or 2. This can also be observed from the eigenvalue plot (Fig. 13d), where the low-damped mode associated to the oscillation is not present for models 1 and 2. Nevertheless, an increase in the size of the reduced model results in better matching with the reference model.

A. Comparison With Other Reduced-Order Models

The absolute admittance errors of the four reduced-order models are compared with other commonly used model configurations (summarized in Table III) to support the previous analysis. First, model 1 (consisting of only outer loops) and model 2 (also including the ICC and PLL) are compared with reduced models that comprise only the PLL or only the ICC (besides the outer loops). The absolute errors of dd- and qq-components are presented in Fig. 14. From Fig. 14a magnitude plot, it can be observed that the model with only PLL does not extend the validity of the converter model compared to model 1. And similarly, the model with only the ICC exhibits an equivalent behavior to model 1 for the qq- admittance phase component (Fig. 14b). Therefore, a VSC model needs to incorporate both the ICC and the PLL to achieve the error improvement compared to the model with only outer loops.

Likewise, in Fig. 15, model 3 is compared with the models in which only time delay or EMT current representation is considered. It can be similarly reasoned that it is necessary to include both modeling components to achieve the actual validity extension in the frequency domain comparatively to model 2 configuration. Additionally, models are analyzed by time-domain simulations for the same input perturbation ($\Delta p^* = 0.025$ pu

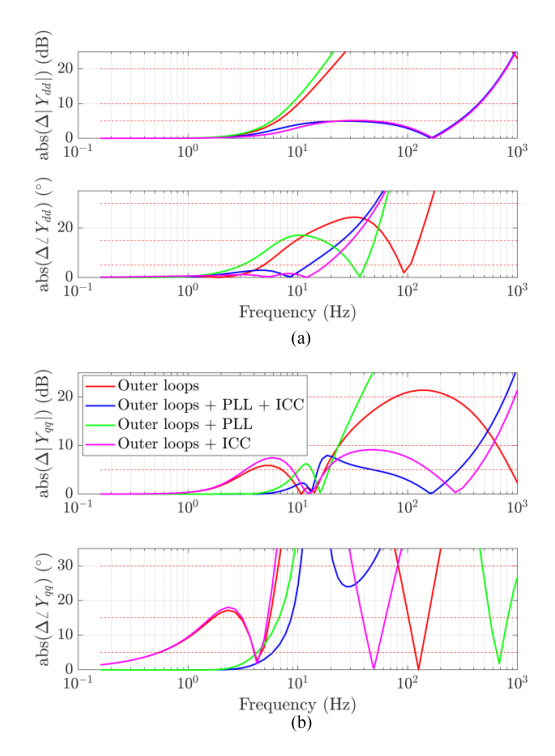


Fig. 14. Comparison of the ac side admittance absolute error of the proposed and other reduced-order VSC models (PLL and ICC influence): (a) dd-component; (b) qq-component.

at 2.5 s). The results presented in Fig. 16 show that both the time delay and EMT current representation are necessary to capture the PCC voltage dynamics. The model with only EMT current representation results in an overdamped response and the model with only time delay results in an unstable response. The more detailed quantitative results for other reduced-order model configurations are provided in Table VIII in the Appendix.

V. PARAMETRIC SENSITIVITY ANALYSIS

A parametric sensitivity analysis is conducted to determine the validity range of the proposed reduced-order models. The following parameters are examined separately for each reduced VSC model:

- Model 1: outer loop, PLL, and ICC bandwidth (27 combinations)
- Model 2: ICC and PLL bandwidth, time delay (27 combinations)
- Model 3: ICC bandwidth and time delay (9 combinations)
- Model 4: outer loop, PLL, and ICC bandwidth (27 combinations)

Parameters are provided in Table IX in the Appendix. Due to limited space, only one of the admittance components and the limited number of combinations are exhibited for the proposed reduced-order models in Figs. 17 to 20. The quantitative results

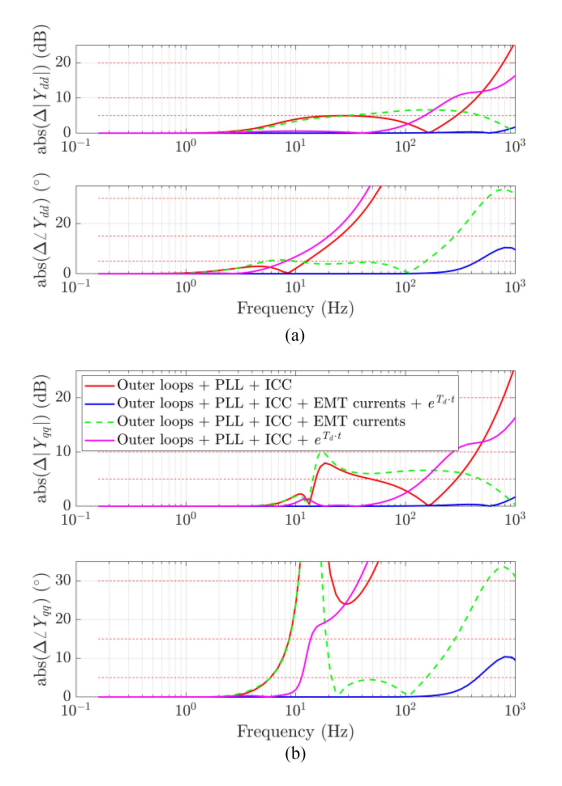


Fig. 15. Comparison of the ac side admittance absolute error of the proposed and other reduced-order VSC models (time delay and EMT current representation influence): (a) dd-component; (b) qq-component.

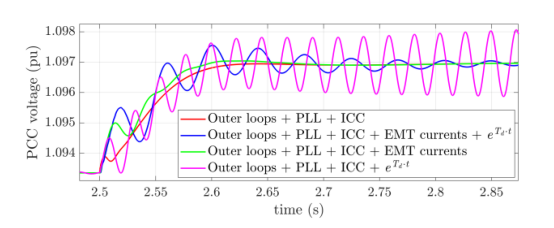


Fig. 16. Active power time-domain response of the proposed and other reduced-order models.

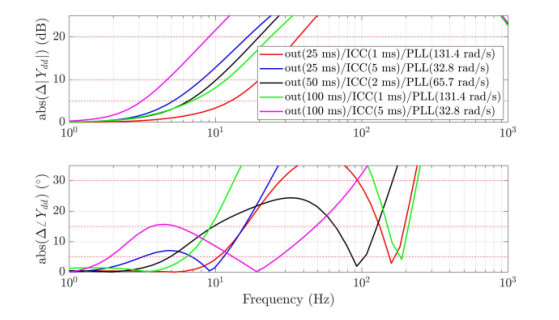


Fig. 17. Influence of the ICC, PLL and outer loops bandwidth on model 1 absolute error (dd-component).

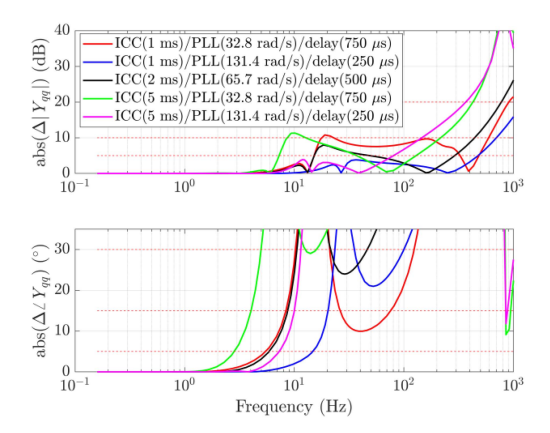


Fig. 18. Influence of the ICC and PLL bandwidth and time delay value on model 2 absolute error (qq-component).

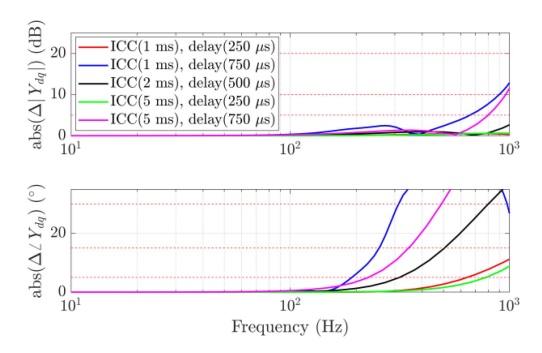


Fig. 19. Influence of the ICC bandwidth and time delay value on model 3 absolute error (dq-component).

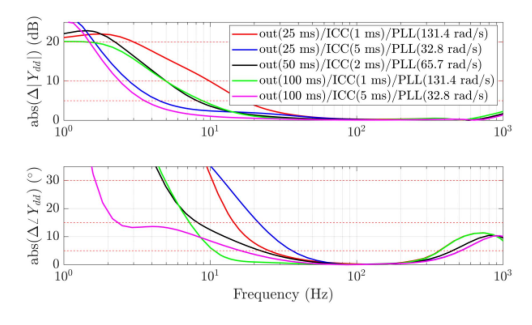


Fig. 20. Influence of the ICC, PLL and outer loops bandwidth on model 4 absolute error (dd-component).

for all examined combinations and accounting for all four admittance components are summarized in Table IV and Fig. 21 (for 5° phase tolerance). A wavy pattern in Fig. 21 presents the sensitivity of upper and lower applicability limits of the proposed reduced-order models for the examined control parameters and the selected tolerance threshold. Different converter parameters, generally, have diverse influences on four admittance components (plus the impact of various magnitude and phase angle

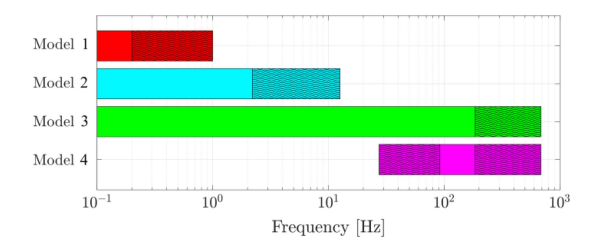


Fig. 21. Validity ranges of the reduced-order models in dq-reference frame (for 5° phase tolerance).

tolerances). In many cases, lower frequency limits are achieved with slower dynamics of control circuits and higher time delay values.

A. Applicability of the Proposed Reduced-Order Models in Power System Stability Studies

Following the results presented in Table IV and Fig. 21, the recommendations for the applicability of the proposed VSC reduced-order models in different stability studies are given in accordance with the latest power system stability classification [23]. It needs to be emphasized that the proposed models are applicable for stability studies where the small-signal assumption holds for the converter and no additional control schemes are active e.g., regulator limits. Furthermore, different power system dynamic phenomena as well as the proposed models do not have strict limits in the frequency domain. Therefore, it is not possible to unambiguously associate a single reduced-order VSC model to study particular phenomena.

For studying the classical dynamic phenomena based on the phasor approximation – such as rotor angle oscillations or small-disturbance voltage stability - model 1 and model 2 are applicable. Resonance stability phenomena (torsional or electrical) appear at subsynchronous frequencies, indicating that the VSC model 2 or model 3 should be included in the system model when studying these dynamics. Slow-interaction converter-driven stability (appearing at subsynchronous frequencies) requires model 2 or model 3 application, while fast-interaction converter-driven stability (arising at super-synchronous frequencies) necessitates the application of model 3 or the reference model. If lowfrequency dynamics is out of interest, model 4 can be used instead of model 3. High-frequency dynamic phenomena including switching dynamics cannot be studied using the timeaveraged models presented in this paper. The recommendations are summarized in Table V.

VI. CONCLUSION

Various simplified VSC models have been employed in power system stability studies without a proper understanding of applicability of such models in the frequency domain. This paper proposes a set of four reduced VSC models for ac system stability studies based on the extensive analysis of different converter parameters and modeling components. The simplest model 1 includes only outer control loops and the corresponding

low-pass filters. The second reduced model has extended applicability in the frequency domain, however not significantly, despite including both the ICC and PLL circuits. It confirms the high coupling of converter slow and fast state dynamics. Thus, a more prominent validity extension is achieved with model 3 which includes both the time delay and the ac side current EMT representation. Reduced model 4 does not include outer loop dynamics and is intended only for high-frequency studies. In the case of a dc voltage control mode, the dc side representation must also be included. Various converter parameters, as well as the specified magnitude and phase tolerances, influence the frequency range of reduced-order model applicability. Finally, the paper discusses the applicability of the obtained set of VSC reduced-order models for different studies in ac power systems based on the frequency of the studied phenomena. These conclusions apply for studies where the small-signal assumption holds for converter variables. Future research directions should include a detailed assessment of filtering dynamics impact to decrease the number of state variables further in the model order reduction process. Also, an establishment of reduced-order models and their frequency validity boundaries for modular multilevel VSC configuration and converters in grid-forming mode is recommended.

APPENDIX

TABLE VI PARAMETERS OF THE REFERENCE CONVERTER MODEL

Parameter	Value
Base frequency ω_b	2π·50 rad/s
Grid frequency ω_g	1 pu
Rated voltage V _{ll,RMS}	220 kV
Rated power S_b	1200 MVA
Filter inductance l_f	0.08 pu
Filter resistance r_f	0.003 pu
Dc side capacitance c_f	4.2 pu
Switching frequency	2 kHz
Time delay T_d	500 μs
ICC time constant τ_{ICC}	2 ms
Outer loop time constant τ_{out}	50 ms
PLL P coefficient $k_{p,PLL}$	50 rad/s
PLL I coefficient $k_{i,PLL}$	833 rad/s ²
Active and reactive power low-	200 rad/s
pass filter cut-off frequency ω_{out}	
PCC voltage low-pass filter cut-	1500 rad/s
off frequency (ICC) ω_{ICC}	
PCC voltage low-pass filter cut-	500 rad/s
off frequency (PLL) ω_{PLL}	
Current measurement low-pass	2π·1200 rad/s
filter cut-off frequency $\omega_{i,cv}$	

TABLE VII
PARAMETERS OF THE EXTERNAL GRID

Parameter	Value
Inductance l_g	0.3 pu
Resistance r_g	0.03 pu
Capacitance c_f	0.5 pu

TABLE VIII
VALIDITY LIMITS OF OTHER REDUCED-ORDER MODELS IN DQ-REFERENCE FRAME (HZ)

	Model 2a	Model 2b	Model 3a	Model 3b
5 dB	< 5.8	<3.1	<14.2	<28.9
10 dB	<8.6	<369.0	<15.9	<32.2
20 dB	<15.9	<501.9	<55.0	<271.2
5°	<2.7	< 0.5	< 5.8	<7.7
15°	<6.1	<1.6	<8.6	<13.3
30°	<8.6	<6.1	<10.1	<28.9

TABLE IX
PARAMETERS OF THE SENSITIVITY ANALYSIS

Parameter	Lower value	Base value	Higher value
Outer loop time constant	25 ms	50 ms	100 ms
$ au_{out}$			
ICC time constant τ_{ICC}	1 ms	2 ms	5 ms
PLL P coefficient $k_{p,PLL}$	25 rad/s	50 rad/s	100 rad/s
(PLL bandwidth)	(32.8 rad/s)	(65.7 rad/s)	(131.4 rad/s)
Time delay T_d	250 μs	500 μs	750 μs

ACKNOWLEDGMENT

The authors would like to thank prof. Marko Delimar for reading the manuscript and providing valuable ideas and comments.

REFERENCES

- G. de Carne, M. Langwasser, and M. Ndreko, "Which deepness class is suited for modeling power electronics?," *IEEE Ind. Electron. Mag.*, vol. 13, no. 2, pp. 41–55, Jun. 2019.
- [2] D. Van Hertem, O. Gomis-Bellmunt, and J. Liang, HVDC Grids: For Offshore and Supergrid of the Future. Hoboken, NJ, USA: Wiley, 2016.
- [3] R. Wachal et al., Guide for the Development of Models for HVDC Converters in A HVDC Grid, Paris, France: CIGRE, 2014.
- [4] X. Wang and F. Blaabjerg, "Harmonic stability in power electronic-based power systems: Concept, modeling, and analysis," *IEEE Trans. Smart Grid*, vol. 10, no. 3, pp. 2858–2870, May 2019.
- [5] J. Sun, "Small-Signal methods for AC distributed power systems—A Review," *IEEE Trans. Power Electron.*, vol. 24, no. 11, pp. 2545–2554, Nov. 2009.
- [6] P.J. D. Chainho, A. A. van der Meer, M. Gibescu, R. L. Hendriks, and M. A. M. M. van der Meijden, "General modeling of multi-terminal VSC-HVDC systems for transient stability studies," in *Proc. 6th IEEE Young Res. Symp. Elect. Power Eng.*, Delft, Netherlands, 2012, pp. 16–17.
 [7] S. Liu, Z. Xu, W. Hua, G. Tang, and Y. Xue, "Electromechanical transient
- [7] S. Liu, Z. Xu, W. Hua, G. Tang, and Y. Xue, "Electromechanical transient modeling of modular multilevel converter based multi-terminal HVDC systems," *IEEE Trans. Power Syst.*, vol. 29, no. 1, pp. 72–83, Jan. 2014.
- [8] R. Irnawan, F. F. da Silva, C. L. Bak, and T. C. Bregnhoj, "Evaluation of half-bridge modular multilevel converter model for VSC-HVDC transient stability studies," in *Proc. 13th IET Int. Conf. AC DC Power Transmiss.*, Manchester, England, U.K., 2017, pp. 1–6.
- [9] S. Cole and R. Belmans, "A proposal for standard VSC HVDC dynamic models in power system stability studies," *Elect. Power Syst. Res.*, vol. 81, pp. 967–973, Apr. 2011.
- [10] S. Zhu et al., "Reduced-order dynamic model of modular multilevel converter in long time-scale and its application in power system lowfrequency oscillation analysis," *IEEE Trans. Power Del.*, vol. 34, no. 6, pp. 2110–2122, Dec. 2019.
- [11] Y. Gu, N. Bottrell, and T. C. Green, "Reduced-order models for representing converters in power system studies," *IEEE Trans. Power Electron.*, vol. 33, no. 4, pp. 3644–3654, Apr. 2018.
- [12] H. Yu, J. Su, H. Wang, Y. Wang, and Y. Shi, "Modelling method and applicability analysis of a reduced-order inverter model for microgrid applications," *IET Power Electron.*, vol. 13, no. 12, pp. 2638–2650, Jun. 2020.
- [13] D. Ramasubramanian et al., "Positive sequence voltage source converter model for use in low short circuit systems," *IET Gener. Transmiss. Distrib.*, vol. 14, no. 1, pp. 87–97, Jan. 2020.

- [14] Y. Lyu, H. Lin, and Y. Cui, "Stability analysis of digitally controlled LCL-type grid-connected inverter considering the delay effect," *IET Power Electron.*, vol. 8, no. 9, pp. 1651–1660, Sep. 2015.
- [15] C. Chen, J. Xiong, Z. Wan, J. Lei, and K. Zhang, "A time delaycompensation method based on area equivalence for active damping of an LCL-type converter," *IEEE Trans. Power Electron.*, vol. 32, no. 1, pp. 762–772, Jan 2017
- [16] P. Kundur, Power System Stability and Control. New York, NY, USA: McGraw-Hill, 1994.
- [17] W. Du, W. Dong, and H. Wang, "A method of reduced-order modal computation for planning grid connection of a large-scale wind farm," *IEEE Trans. Sustain. Energy*, vol. 11, no. 3, pp. 1185–1198, Jul. 2020.
- [18] J. L. Agoretta, M. Borrega, J. Lopez, and L. Marroyo, "Modeling and control of N-paralleled grid-connected inverters with LCL filter coupled due to grid impedance in PV plants," *IEEE Trans. Power Electron.*, vol. 26, no. 3, pp. 770–785, Mar. 2011.
- [19] Q. Cossart, F. Colas, and X. Kestelyn, "Model reduction of converters for the analysis of 100% power electronics transmission systems," in *Proc. IEEE Int. Conf. Ind. Technol.*, Lyon, France, 2018, pp. 1254–1259.
- [20] L. Harnefors and H.-P. Nee, "Model-based current control of AC machines using the internal model control method," *IEEE Trans. Ind. Appl.*, vol. 34, no. 1, pp. 133–141, Jan./Feb. 1998.
- [21] A. Egea-Alvarez, A. Junyent-Ferre, and O. Gomis-Bellmunt, "Active and reactive power control of grid connected distributed generation systems," in Modeling and Control of Sustainable Power Systems. Green Energy and Technology. Berlin, Heidelberg, Germany, Springer, 2012.
- [22] K. Sharifabadi, L. Harnefors, H.-P. Nee, and R. Teodorescu, Design, Control, and Application of Modular Multilevel Converters for HVDC Transision Systems. Hoboken, NJ, USA: Wiley, 2016.
- [23] N. Hatziargyriou, J. Milanović, C. Rahmann, and V. Ajjarapu, "Definition and classification of power system stability - Revisited & extended," *IEEE Trans. Power Syst.*, vol. 36, no. 4, pp. 3271–3281, Jul. 2021.



Goran Grdenić (Member, IEEE) received the B.Sc., M.Sc., and Ph.D. degrees in electrical engineering from the University of Zagreb, Zagreb, Croatia, in 2012, 2014, and 2019, respectively. He is currently a Postdoctoral Researcher with the Faculty of Electrical Engineering and Computing, Department of Energy and Power Systems, University of Zagreb. From 2015 to 2020, he was a Teaching and Research Assistant with the same faculty. From September 2020 to August 2021, he was a Postdoctoral Researcher with KU Leuven and Energy Ville, Belgium. His research

interests include modeling, control and stability analysis of converter-based ac power systems, and high-voltage direct-current transmission.



Francisco J. Cifuentes García received the B.S. (Hons.) degree in energy engineering and M.Sc. degree in industrial engineering specialized in electronics from the Universitat Politècnica de Catalunya (UPC). Barcelona, Spain, in 2018 and 2021, respectively. In 2018, he was a Research Assistant with CITCEA-UPC, Barcelona, Spain, for two years, where he worked on the stability of HVDC converters connected to weak grids and the control of hybrid power plants. During 2020–2021, he completed his master's thesis on the stability of VSCs operating in

weak grids as an Erasmus student with KU Leuven, Leuven, Belgium. During 2021, he was part of the InnoDC project as an Early-Stage Researcher working on Hybrid AC/DC grids hosted by KU Leuven. Since 2022, he has been a Research Associate of KU Leuven - Electa and Energy Ville focusing on the stability of power systems with high penetration of power electronics. His research interests include power system modeling and stability, renewable energy technologies, machine learning, and optimization.



Nathalia de Morais Dias Campos (Student Member, IEEE) received the B.Eng. degree in electrical engineering from the University of Campina Grande, Campina Grande, Brazil, in 2018, and the M.Sc. degree in electrical engineering for sustainable development from the University of Lille 1, Lille, France, in 2017. In 2014, she was a Visiting Student with the University of Manitoba, Winnipeg, MB, Canada. From 2018 to 2020, she was an Early Stage Researcher KU Leuven, Leuven, Belgium, and Elia System Operator, Belgium, within the Marie Curie

project InnoDC. She is currently working toward the Ph.D. degree with Tal-Tech, Tallinn, Estonia. Her research interests include power systems modeling, stability analysis, converter controls, and renewable energy.



Fortunato Villella received the M.S. degree in computer engineering from Università della Calabria (UNICAL), Rende, Italy, in 2005. In the same year, he visited the Department of Automation and Control, Aalborg Universitet, Aalborg, Denmark. From 2006 and 2008, he was with Universiteit Gent, Ghent, Belgium, performing research on modeling and simulation of electrical power networks. He is currently with Elia Grid International, Belgium, as a Principal Power System Expert. His main research interests include integration of power electronics with focus

on offshore wind parks and HVDC, power system modeling, identification, simulation, operation, and control.



Jef Beerten (Senior Member, IEEE) received the M.Sc. degree in electrical engineering and the Ph.D. degree in electrical engineering from the University of Leuven (KU Leuven), Leuven, Belgium, in 2008 and 2013, respectively. He is currently an Assistant Professor with KU Leuven and EnergyVille. His research interests include future power system dynamics, modeling, and control. In 2011, he was a Visiting Researcher with the Royal Institute of Technology (KTH), Stockholm, Sweden, for three months. From April 2014 to March 2015, he was a Visiting Post-

doctoral Researcher with the Norwegian University of Science and Technology (NTNU), Trondheim, Norway. Dr. Beerten was the first winner of the ABB Research Award in Honor of Hubertus von Gruenberg in 2016 and was the recipient of the KBVE/SRBE Robert Sinave Award and the Prix Paul Caseau from the Institut de France - EDF Foundation for his Ph.D. thesis on modeling and control of DC grids. Dr. Beerten is an Active Member of both the IEEE and CIGRE.

Publication II

N. M. D. Campos, T. Sarnet, and J. Kilter, "Novel gramian-based structure-preserving model order reduction for power systems with high penetration of power converters," *IEEE Transactions on Power Systems*, vol. 38, no. 6, pp. 5381–5391, 2023

Novel Gramian-Based Structure-Preserving Model Order Reduction for Power Systems With High Penetration of Power Converters

Nathalia de Morais Dias Campos , *Graduate Student Member, IEEE*, Tanel Sarnet, *Member, IEEE*, and Jako Kilter , *Senior Member, IEEE*

Abstract-Renewable energy and high voltage direct current connections increase the number of power electronic devices in the grid, changing how power systems operate and introducing new dynamic behavior. For this reason, it is fundamental to understand what modeling details are needed to represent the system in this new context. This article proposes a novel model reduction approach using frequency-limited controllability and observability Gramians that preserves the link between the physical structure of the system and the state variables. This method allows understanding and analytically determining how vital each state is to the input-output behavior in different frequency ranges. The primary contribution of this article is an algorithm that can provide intuitive results to help power system experts understand the simulation tools and minimum modeling details needed to perform different stability studies. Two case studies supported the applicability of the developed method, and a tool for MATLAB/Simulink was developed based on the findings, allowing visualization and immediate identification of the model components that are most relevant for the system dynamics under study. This tool can analyze dynamic behaviors where the cause is poorly understood and provide clarity around modeling detail requirements in converter-rich power

 ${\it Index~Terms} \hbox{--} {\it Controllability~and~observability,~Gramians,} \\ {\it model~reduction,~power~electronic~converters,~power~system~modelling,~power~system~simulation.} \\$

I. INTRODUCTION

P OWER systems have seen extensive changes in the past years. Renewable energy sources incentivized by governmental policies are substituting traditional generation. For instance, to reach the 1.5° climate target, renewables should supply 90% of the electricity by 2050. Wind and photovoltaics should dominate with 63% of the total electricity needs [1]. Additionally, power systems are becoming more interconnected. In Europe, there is an expected increase of 35 GW cross-border transmission capacity by 2025 and an additional 93 GW by

Manuscript received 6 April 2022; revised 4 September 2022 and 17 November 2022; accepted 28 November 2022. Date of publication 12 December 2022; date of current version 20 October 2023. Paper no. TPWRS-00491-2022. (Corresponding author: Nathalia de Morais Dias Campos.)

The authors are with the Tallinn University of Technology, 19086 Tallinn, Estonia (e-mail: nathalia.campos@taltech.ee; tanel.sarnet@taltech.ee; jako.kilter@ttu.ee).

Color versions of one or more figures in this article are available at https://doi.org/10.1109/TPWRS.2022.3228458.

Digital Object Identifier 10.1109/TPWRS.2022.3228458

2040 [2]. High voltage direct current (HVDC) technology is especially relevant for long-distance transmission and renewables' interconnection since it provides more operational flexibility than AC transmission. It is believed that the developments in power systems will continue in the following years, with ambitious targets set towards renewable generation and additional interconnection projects planned [2].

These trends have in common that they increase the number of power electronic devices connected to the grid. Determining how to model power electronic-based systems in stability studies is a significant challenge. Despite studies carried out during the planning and operation of new interconnections, several instability events have occurred in recent years. For instance, in 2017, ERCOT observed three subsynchronous oscillation (SSO) events involving wind farms. The wind farms affected had undergone stability studies and were equipped with SSO damping controls [3] but these measures proved insufficient for predicting and avoiding the instability risks. In 2019, studies conducted by AEMO showed five solar farms with sustained voltage oscillations under credible contingencies. This incident led to several months of generation curtailment and delayed commissioning of new units [4].

One reason instability risks can remain undetected during the project's study phase is that power electronic devices may interact unexpectedly with the surrounding system, and their dynamic behavior is not always well understood. Traditional modeling practices based on root mean square (RMS) simulations aggravate this risk as RMS models assume that all system signals are steady-state or near steady-state, leading to simplified network, generator, and converter models. This assumption significantly impacts its ability to represent oscillation phenomena far from the steady-state frequency. In this case, using RMS models could lead to an incorrect stability assessment.

Electromagnetic transient (EMT) simulations, on the other hand, can produce very accurate stability results. However, using EMT simulations still leads to the question of how detailed the model of each component should be. Modeling to a high degree of detail every element of an extensive system leads to computational complexity that is at the very least difficult to handle and often unfeasible. It also requires data that might not be available due to, for instance, manufacturers not having yet supplied a detailed EMT model of their device. For instance, following a sub-synchronous incident involving wind farms in

0885-8950 © 2022 IEEE. Personal use is permitted, but republication/redistribution requires IEEE permission. See https://www.ieee.org/publications/rights/index.html for more information.

2009, [5] reported that ERCOT did not have the required wind farm EMT models for detailed studies that could have detected the subsynchronous oscillations ahead of time.

Thus, it is critical to understand the minimum modeling details required for different stability studies. It allows transmission system operators (TSOs) to demand the correct type of studies and models, ensuring the safe operation of the power system.

Model-order reduction methods are one of the techniques able to address this problem. They reduce computational costs while maintaining the accuracy for given phenomena of interest. A reduced-order model is obtained by eliminating or simplifying parts of the system that are not relevant for the study carried out. The accuracy of the results depends on appropriately choosing which system components are relevant for the study and must therefore be represented by detailed models.

Several model reduction methods have been proposed in the literature and applied in power system analysis. These include modal reduction [6], balanced truncation [7] and reduction by moment matching [8]. These approaches, however, rely on changing the state space coordinate system. Because the analysis occurs on a changed basis, state variables tend only to have mathematical significance and no longer have a direct link to the physical system. This lack of connection makes it difficult for power system experts to apply these methods to understand which components and control models to use in practical system studies. These methods typically offer high computational efficiency and scalability, where the aim is near optimal reduction of the number of states in the model. However, the drawback is that the results become less intuitive and interpretable as the mathematical models can no longer be understood physically.

A parametric model reduction method is proposed in [9], which can preserve selected parameters in the reduced-order model. The article successfully demonstrated the method for preserving the parameters of Power System Stabilizers (PSS). However, the method only preserves the relationship between mathematical and physical models for selected parameters. It also requires knowing the parameters to be preserved beforehand, which limits its application when the instability causes and devices involved are not entirely known.

In [10], the authors propose a model reduction method based on state residualization. They determine the relationship between states and modes and then find a reduced model by removing groups of states, minimizing the error. This method, however, does not directly determine the importance of each state and how this changes in particular frequency ranges.

A method of obtaining reduced-order models of Multi-Terminal DC Grids (MTDC) is proposed in [11]. The approach is based on an Interactive Rational Krylov algorithm and is applied individually to every wind farm connected to the study area consisting of the MTDC grid. This work, however, does not cover other grid configurations.

In [12], the authors propose a model reduction technique inspired by the balanced truncation method and based on the projection of the Hankel Singular Values using the inverse balancing transformation. In [13], the authors propose a structured model reduction that preserves the network topology based on an extension of the balanced truncation method. The technique

first partitions the system into subsystems. The method is applied to each subsystem except the one where the network structure should be preserved. However, these methods have not been explicitly used to determine modeling details necessary in converter-rich systems considering dynamics in different time scales. The method proposed in this article was conceived specifically for this purpose, focusing on the interpretability of results to provide clarity around modeling detail requirements for converter-rich power systems. The proposed model reduction approach can be applied directly without any coordinate system transformation, thus maintaining the connection between the states and the physical system.

The key contributions of this article are: (i) an approach to calculate the contribution of each state to the system behavior based on the controllability and observability Gramians; and (ii) a model reduction technique that highlights which parts of a model are relevant at a given frequency range, and that is applied to obtain models targeted for studies of specific oscillation phenomena. The proposed approach is especially relevant given the new categories of interactions introduced in power systems with high penetration of power electronic devices [14].

This article is organized as follows. Section II provides an overview of the main concepts of model reduction theory. The proposed model reduction approach is described in Section III. Section IV covers two case studies where the method is applied and demonstrates a visualization tool developed on MAT-LAB/Simulink. Finally, Section V discusses conclusions and limitations of the proposed approach.

II. MODEL ORDER REDUCTION

The problem of finding a reduced-order model of a linear system represented in state-space consists in identifying which states are relevant and which ones can be discarded while ensuring the results remain within an acceptable error margin.

Consider a linear time-invariant (LTI) and high-dimensional system with n states, m inputs and p outputs represented in state-space form by

$$\dot{\boldsymbol{x}}(t) = \boldsymbol{A}\boldsymbol{x}(t) + \boldsymbol{B}\boldsymbol{u}(t) \tag{1}$$

$$y(t) = Cx(t) \tag{2}$$

where $\boldsymbol{u}(t) \in \mathbb{R}^m$ is a vector of system inputs, $\boldsymbol{y}(t) \in \mathbb{R}^p$ is a vector of system outputs and $\boldsymbol{x}(t) \in \mathbb{R}^n$ are the state variables and $\boldsymbol{A} \in \mathbb{R}^{n \times n}$, $\boldsymbol{B} \in \mathbb{R}^{n \times m}$ and $\boldsymbol{C} \in \mathbb{R}^{p \times n}$ are the state-space matrices.

The controllability operator $\Psi_c: L_2(-\infty,0] \to \mathbb{C}^n$ is defined as [15]

$$\boldsymbol{u} \mapsto \int_{-\infty}^{0} e^{-\boldsymbol{A}\tau} \boldsymbol{B} u(\tau) d\tau.$$

It can be interpreted as a mapping between inputs defined in the past $(t \le 0)$ to the initial condition x_0 at t = 0.

Similarly, the observability operator $\Psi_o: \mathbb{C}^n \to L_2[0,\infty)$ is defined as [15]

$$x_0 \mapsto \begin{cases} Ce^{At}x_0, & \text{for } t \ge 0\\ 0, & \text{otherwise} \end{cases}$$
 (3)

This operator maps the initial condition x_0 to the output of the system when no input is applied for t > 0.

The controllability and observability of a state can be measured using the concept of Gramians and derived from the respective operators.

The controllability Gramian \mathcal{P} is associated with the minimal energy required to drive the states from $\mathbf{0}$ to x and is defined [15] as

$$\mathcal{P} = \Psi_c \Psi_c^* = \int_{t_1}^{t_2} e^{At} B B^* e^{A^* t} dt.$$
 (4)

where $\Psi_c^*: L_2(-\infty, 0] \to \mathbb{C}^n$ and \mathbf{A}^* denotes the complex conjugate transpose of matrix \mathbf{A} .

The observability Gramian Q is a measure of the maximum amount of energy obtained from the outputs caused by the initial condition x_0 and is defined [15] as

$$\mathcal{Q} = \Psi_o^* \Psi_o = \int_{t_*}^{t_2} e^{\mathbf{A}^* t} \mathbf{C}^* \mathbf{C} e^{\mathbf{A} t} dt.$$
 (5)

where $\Psi_o^*: L_2[0,\infty) \to \mathbb{C}^n$.

A reduced-order model can be obtained by neglecting states with relatively low controllability or observability. However, a state's controllability and observability depend on the coordinate system used. The same model may be completely controllable and observable in one coordinate system and have several uncontrollable or unobservable states when using another basis. It is possible to carefully select a change of coordinate system to result in as many unobservable and uncontrollable states as possible to reduce the order of the system considerably.

Several model reduction approaches in the literature are based on this idea [7]. However, this comes at the cost of mathematical models that can no longer be interpreted physically. This article proposes an approach to calculating a state variable's relative controllability and observability without changing coordinate systems. The following Section covers the mathematical background for the technique proposed.

III. PROPOSED MODEL REDUCTION APPROACH

This section first explains how to calculate the approximation error between the outputs of a full and reduced-order system. Then, a heuristic is obtained from the approximation error that determines a state's participation in the input-output behavior of the system. The heuristic is extended to take into account specific frequency ranges. Finally, it is shown how it can be applied to obtain a reduced-order model, and a physical interpretation for the method is provided.

A. Calculation of Approximation Error

A single-input single-output system (SISO) is adopted to make the derivation clearer. However, extending the same concepts to multiple-input multiple-output (MIMO) systems is possible.

Suppose there is SISO system with n internal states. Let u(t) be an input applied to this system during the time interval $t \in (-\infty, 0]$. The value x_0 of the states at t = 0 can be calculated

using the controllability operator Ψ_c as follows:

$$\boldsymbol{x}_0 = \boldsymbol{\Psi}_c \boldsymbol{u}(t) \tag{6}$$

where $\Psi_c = [\Psi_c^{(1)} \quad \Psi_c^{(2)} \quad \cdots \quad \Psi_c^{(n)}]^T$ is a column vector and $\Psi_c^{(k)}$ is the controllability operator associated with the k-th state.

Now let us observe the system output y(t) caused by the initial condition x_0 during the interval $t \in [0, \infty)$. The output is determined with the help of the observability operator Ψ_o as

$$y(t) = \mathbf{\Psi}_o \mathbf{x}_0 \tag{7}$$

where $\Psi_o = [\Psi_o^{(1)} \quad \Psi_o^{(2)} \quad \cdots \quad \Psi_o^{(n)}]$ is a row vector and $\Psi_o^{(k)}$ is the observability operator associated with the k-th state.

Equations (6) and (7) defining the controllability and observability operators are combined, resulting in an expression that relates a system's input to its output,

$$y(t) = \Psi_o \Psi_c u(t) \tag{8}$$

When expanded, this expression highlights the contribution of the system's state variables:

$$y(t) = \left[\Psi_o^{(1)}\Psi_c^{(1)} + \Psi_o^{(2)}\Psi_c^{(2)} + \dots + \Psi_o^{(n)}\Psi_c^{(n)}\right]u(t) \tag{9}$$

where $\Psi_o^{(k)}\Psi_c^{(k)}$ represents the product between the observability and controllability operators associated with the k-th state.

Equation (9) is essential because it shows that the system input-output behavior can be decomposed among the states variables, allowing to isolate and measure the contribution of individual states.

Suppose the order of the system is reduced from n to r with r < n by eliminating n - r states denoted by $x^{(r+1)}, x^{(r+2)}, \ldots, x^{(n)}$. The output $\hat{y}(t)$ of the reduced model is obtained from (9) by removing the components associated with the states that are being eliminated, resulting in

$$\hat{y}(t) = \left[\Psi^{(1)}\Psi^{(1)} + \Psi^{(2)}\Psi^{(2)} + \dots + \Psi^{(r)}\Psi^{(r)}\right]u(t) \quad (10)$$

The approximation error incurred by reducing the model order can be defined as the difference between the outputs of the full and reduced-order models. It is quantified using the L_2 norm as

$$\|y - \hat{y}\|_{2} = \left\| \sum_{k=r+1}^{n} \Psi_{c}^{(k)} \Psi_{c}^{(k)} u(t) \right\|_{2}$$
 (11)

Based on the submultiplicative and triangle inequality properties, (11) can be rewritten as

$$\|y - \hat{y}\|_{2} \le \sum_{k=r+1}^{n} \|\Psi_{o}^{(k)}\|_{2} \|\Psi_{c}^{(k)}\|_{2} \|u(t)\|_{2}$$
 (12)

In order to develop the right-side term of (12), the controllability $\|\Psi_{o}^{(k)}\|_{2}$ and observability $\|\Psi_{o}^{(k)}\|_{2}$ norms associated with the k-th state must be calculated. In order to achieve that, the following definition of the H_{∞} norm of bounded operators [16] is used:

$$\|\Phi\|_{\infty} = \sup\{\|\Phi x\|_2 : \|x\|_2 = 1\}$$
 (13)

where Φ is a bounded operator and $\Phi \in \mathcal{H}_{\infty}$ and $x \in \mathcal{H}_2$.

Let the $\Psi_o^{(k)}$ be the component of the observability operator associated with the k-th state. Using the definition in (13), it is

possible to write

$$\|\Psi_o^{(k)}\|_{\infty} = \sup\{\|\Psi_o^{(k)}x_0^{(k)}\|_2 : |x_0^{(k)}| = 1\}$$
 (14)

The right-side term from (14) can be expanded into

$$\|\Psi_{o}^{(k)}x_{0}^{(k)}\|_{2}^{2} = x_{0}^{(k)*}\Psi_{o}^{(k)*}\Psi_{o}^{(k)}x_{0}^{(k)} \tag{15}$$

Based on (15) and knowing that $|x_0^{(k)}|=1 \rightarrow x_0^{(k)}=\pm 1$, the right side term from (14) is evaluated as

$$\|\Psi_o^{(k)}\|_{\infty} = \sqrt{\Psi_o^{(k)*}\Psi_o^{(k)}} \tag{16}$$

Similarly, let $\Psi_c^{(k)}$ be the component of the controllability operator associated with the k-th state. It follows from (13) that

$$\|\Psi_c^{(k)}\|_{\infty} = \sup\{\|\Psi_c^{(k)}u\|_2 : \|u\|_2 = 1\}$$
 (17)

Knowing that the following sets are equal [15], [17]:

$$\{\Psi_c u : u \in L_2(-\infty, 0] \text{ and } \|u\|_2 \le 1\}$$
 (18)

$$\{(\Psi_c \Psi_c^*)^{\frac{1}{2}} x_c : x_c \in \mathbb{C}^n \text{ and } |x_c| < 1\}$$
 (19)

the right-side term in (17) is evaluated, resulting in

$$\|\Psi_c^{(k)}\|_{\infty} = \sup\{\|(\Psi_c^{(k)}\Psi_c^{(k)*})^{\frac{1}{2}}x_c\|_2 : |x_c| = 1\}$$
 (20)

The right side term in (20) evaluates to

$$\|(\Psi_c^{(k)}\Psi_c^{(k)*})^{\frac{1}{2}}x_c\|_2^2 = x_c^*\Psi_c^{(k)}\Psi_c^{(k)*}x_c \tag{21}$$

Knowing that $|x_c| = 1 \rightarrow x_c = \pm 1$ results in

$$\|\Psi_c^{(k)}\|_{\infty} = \sqrt{\Psi_c^{(k)}\Psi_c^{(k)*}} \tag{22}$$

It follows from the property $\|\Phi\|_{\infty} \leq \|\Phi\|_2$ that the L_2 norms of the controllability and observability operators are given, respectively, by

$$\|\Psi_c^{(k)}\|_2 \le \sqrt{\Psi_c^{(k)}\Psi_c^{(k)*}} \tag{23}$$

$$\|\Psi_o^{(k)}\|_2 \le \sqrt{\Psi_o^{(k)*}\Psi_o^{(k)}} \tag{24}$$

The operator norms in (23) and (24) are related to the diagonal terms of the controllability and observability Gramians as $\Psi_o^{(k)*}\Psi_o^{(k)}=\mathcal{Q}^{(k,k)}$ and $\Psi_c^{(k)}\Psi_c^{(k)*}=\mathcal{P}^{(k,k)}$. Taking that into consideration and substituting (23) and (24) into (12), results in

$$\|y - \hat{y}\|_2 \le \sum_{k=r+1}^n \sqrt{\mathcal{Q}^{(k,k)} \mathcal{P}^{(k,k)}} \|u(t)\|_2$$
 (25)

If the input is an impulse, that is, $u(t) = \delta(t)$, then the output y(t) is the impulse response denoted by h(t). The previous equations shows that the norm of the impulse response error $\|h-\hat{h}\|_2$ is bounded by

$$\|h - \hat{h}\|_2 \le \sum_{k=n+1}^n \sqrt{\mathcal{Q}^{(k,k)}\mathcal{P}^{(k,k)}}$$
 (26)

A reduced system is obtained when the error associated with removing a certain number of states only has a negligible impact compared to the states remaining in the model. Mathematically, this requirement can be formulated following Moore [7]. A reduced system exists if there is an internally dominant subsystem of order r that satisfies the following equation:

$$\sum_{k=1}^{r} \sqrt{\mathcal{Q}^{(k,k)} \mathcal{P}^{(k,k)}} \gg \sum_{k=r+1}^{n} \sqrt{\mathcal{Q}^{(k,k)} \mathcal{P}^{(k,k)}}.$$
 (27)

Based on these conclusions, it is possible to define an error E_r heuristic that measures how close the reduced system is to the full system. Mathematically,

$$E_r = \frac{\sum_{k=r+1}^{n} \sqrt{Q^{(k,k)} \mathcal{P}^{(k,k)}}}{\sum_{k=1}^{r} \sqrt{Q^{(k,k)} \mathcal{P}^{(k,k)}}}.$$
 (28)

This error measures the impact of removing certain states from the model. In other words, state variables that produce significant errors when removed have high participation in the system response.

B. Participation of State in Input-Output Behavior

Equation (28) not only measures the error associated with removing a group of states but also indicates the impact of individual states on the model accuracy. Therefore, the participation $p^{(k)}$ of the k-th state variable in the system input-output behavior is defined as

$$p^{(k)} = \frac{\sqrt{Q^{(k,k)}\mathcal{P}^{(k,k)}}}{\sum_{i=1}^{n} \sqrt{Q^{(i,i)}\mathcal{P}^{(i,i)}}}.$$
 (29)

Equation (29) allows ranking the importance of individual states. Because each state is associated with a physical component of the power system, the participation $p^{(k)}$ reveals not only the most important states but also the most important components of the system. The next sections show how this property is used to produce a tool for visualizing which components contribute the most to the system dynamics.

The participation defined in (29) describes the impact of the state over the entire frequency range. When studying oscillation phenomena in specific frequency ranges, it is helpful to understand the participation of the states as a function of the frequency. Certain state variables may be more associated with faster or slower phenomena. For example, state variables related to the network tend to be associated with high-frequency transients; thus, models for quasi-steady-state studies discard those states. To this end, the concept of frequency-limited Gramians can be used to define the participation of the states in specific frequency ranges.

Time-frequency duality and Parseval's theorem can be used to define the Gramians in the frequency domain from their time-domain formulation presented in (4) and (5) [18]. The frequency-limited controllability and observability Gramians over the interval $[\omega_1, \omega_2]$ are obtained, respectively, as

$$\mathcal{P}_{\omega} = \int_{\omega_1}^{\omega_2} (j\omega \mathbf{I} - \mathbf{A})^{-1} \mathbf{B} \mathbf{B}^* (-j\omega \mathbf{I} - \mathbf{A}^*)^{-1} d\omega, \quad (30)$$

$$\mathbf{Q}_{\omega} = \int_{0}^{\omega_2} (-j\omega \mathbf{I} - \mathbf{A}^*)^{-1} \mathbf{C}^* \mathbf{C} (j\omega \mathbf{I} - \mathbf{A})^{-1} d\omega.$$
 (31)

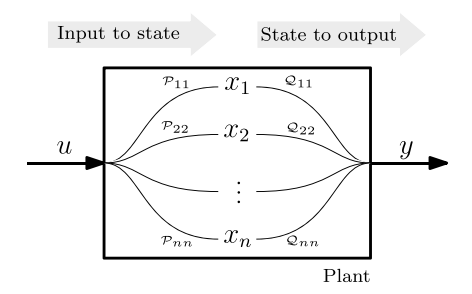


Fig. 1. Contribution of state variables to input-output system response.

By using (30) and (31), the controllability and observability of a state can be measured in specific frequency intervals. They can then be used, in conjunction with (29) to define the participation $p_{\omega}^{(k)}$ of the k-th state variable to the input-output system behavior over the interval $[\omega_1, \omega_2]$. This results in

$$p_{\omega}^{(k)} = \frac{\sqrt{\mathcal{Q}_{\omega}^{(k,k)} \mathcal{P}_{\omega}^{(k,k)}}}{\sum_{i=1}^{n} \sqrt{\mathcal{Q}_{\omega}^{(i,i)} \mathcal{P}_{\omega}^{(i,i)}}}.$$
 (32)

Equation (32) provides a measure of which states have the highest participation in a frequency range and can thus be used to derive reduced-order models appropriate for studies of oscillations within a frequency range. This result is obtained without applying any coordinate changes to the state space.

The states with the highest participation should be included in the models, while the remaining states may be safely neglected. In other words, (32) provides a guideline for which parts of the physical system correspond to the most relevant states and must be modeled in detail and which ones can be simplified.

C. Physical Interpretation

This section provides the physical interpretation of the proposed model reduction method from a signal injection point of view, highlighting the relationship between Gramians and signal energy.

The notion of signal energy is a purely mathematical concept that may be related to the definition of energy in physics but does not necessarily correspond to it. Mathematically, the energy E of a signal \boldsymbol{x} over the interval $[t_1,t_2]$ is defined as

$$E = \langle \boldsymbol{x}(t), \boldsymbol{x}(t) \rangle = \int_{t_1}^{t_2} \| \boldsymbol{x}(t) \|_2^2 dt.$$
 (33)

The signal energy is related to both the controllability and observability Gramians. The controllability Gramian \mathcal{P} is associated with the energy required to drive the states from 0 to x_0 while the observability Gramian \mathcal{Q} is a measure of the energy obtained from the outputs caused by the initial condition x_0 .

Based on that, consider the physical system illustrated in Fig. 1.

Suppose unitary impulses are successively applied to each system input, and each state's response is observed. The set of state response signals is represented by the matrix $X(t) \in$

 $\mathbb{R}^{n\times m}$ as

$$\boldsymbol{X}(t) = \begin{bmatrix} \boldsymbol{x}_1(t) \\ \boldsymbol{x}_2(t) \\ \vdots \\ \boldsymbol{x}_n(t) \end{bmatrix}, \tag{34}$$

where $\boldsymbol{x}_k(t) \in \mathbb{R}^m$ is a row vector containing the response of the k-th state to each of the inputs.

The vector X(t) is the input-to-state map and can be used to obtain the controllability Gramian \mathcal{P} over the interval $[t_1, t_2]$ as

$$\mathcal{P} = \int_{t_1}^{t_2} \boldsymbol{X}(t) \boldsymbol{X}(t)^* dt.$$
 (35)

Based on that, the controllability Gramian matrix from (30) can be expanded resulting in

$$\mathcal{P}_{\omega} = \begin{bmatrix} \langle \boldsymbol{x}_{1}, \boldsymbol{x}_{1} \rangle & \langle \boldsymbol{x}_{1}, \boldsymbol{x}_{2} \rangle & \cdots & \langle \boldsymbol{x}_{1}, \boldsymbol{x}_{n} \rangle \\ \langle \boldsymbol{x}_{2}, \boldsymbol{x}_{1} \rangle & \langle \boldsymbol{x}_{2}, \boldsymbol{x}_{2} \rangle & \cdots & \langle \boldsymbol{x}_{2}, \boldsymbol{x}_{n} \rangle \\ \vdots & \vdots & & \vdots \\ \langle \boldsymbol{x}_{n}, \boldsymbol{x}_{1} \rangle & \langle \boldsymbol{x}_{n}, \boldsymbol{x}_{2} \rangle & \cdots & \langle \boldsymbol{x}_{n}, \boldsymbol{x}_{n} \rangle \end{bmatrix}, \quad (36)$$

where $\langle x_k, x_j \rangle$ denotes the inner product between the vectors x_k and x_j . When these vectors are equal, their inner product $\langle x_k, x_k \rangle$ represents the total energy of the signal x_k as defined in (33).

In other words, the k-th diagonal element of the controllability Gramian measures the total energy contained in the response of the k-th state to each of the inputs. A large energy value indicates that the impulse had a greater effect on the state. This input-to-state energy transfer is illustrated in the left portion of Fig. 1.

Now suppose a unitary initial condition is imposed on each state, and the system's output signal is observed. This set of signals is represented by the matrix $Y(t) \in \mathbb{R}^{p \times n}$ as

$$\boldsymbol{Y}(t) = \begin{bmatrix} \boldsymbol{y}_1(t) & \boldsymbol{y}_2(t) & \cdots & \boldsymbol{y}_n(t) \end{bmatrix},$$
 (37)

where $y_k(t) \in \mathbb{R}^p$ is a column vector containing the response of all outputs to the initial condition imposed to the k-th state.

The vector $\boldsymbol{Y}(t)$ is the output-to-state map and it can be used to calculate the observability Gramian $\boldsymbol{\mathcal{Q}}$ over the interval $[t_1,t_2]$

$$\mathcal{Q} = \int_{t_1}^{t_2} \mathbf{Y}^*(t) \mathbf{Y}(t) dt. \tag{38}$$

Based on that, the observability Gramian matrix defined in (31) can be expanded as

$$\mathcal{Q}_{\omega} = \begin{bmatrix}
\langle y_1, y_1 \rangle & \langle y_1, y_2 \rangle & \cdots & \langle y_1, y_n \rangle \\
\langle y_2, y_1 \rangle & \langle y_2, y_2 \rangle & \cdots & \langle y_2, y_n \rangle \\
\vdots & \vdots & & \vdots \\
\langle y_n, y_1 \rangle & \langle y_n, y_2 \rangle & \cdots & \langle y_n, y_n \rangle
\end{bmatrix}.$$
(39)

Similar to what was observed with the controllability Gramian, the diagonal terms in the matrix represent the signal energy measure as defined in (33). In this case, $\langle y_k, y_k \rangle$

Algorithm 1: Model Reduction Method.

Select system inputs u(t), outputs y(t) and operating point of the full-order model

Linearize model to obtain a state-space representation according to (1) and (2)

Define the frequency interval of interest $[\omega_1, \omega_2]$

Choose a Gramian computation algorithm

Calculate the controllability \mathcal{P}_{ω} and observability \mathcal{Q}_{ω} Gramians within the frequency interval $[\omega_1, \omega_2]$

Calculate participation $p_{\omega}^{(k)}$ of states according to (32) **Choose** a participation threshold ε value serving as a boundary between states that will be included in the model and those that will be neglected

Residualize states with a participation lower than a selected threshold ε

Return reduced state-space model

measures the total energy of the outputs resulting from a unitary initial condition applied to the k-th state. The greater the energy, the more a state affects the output. This state-to-output energy distribution is illustrated in the right portion of Fig. 1.

The diagonal terms from the controllability and observability Gramians for each state are combined into the product $\mathcal{P}_{\omega}^{(k,k)}\mathcal{Q}_{\omega}^{(k,k)}$. Fig. 1 illustrates the energy transfer from input to output in a physical system taking into account how the signal energy is distributed across the states before reaching the output. The contribution of each state is reflected by the product $\mathcal{P}_{\omega}^{(k,k)}\mathcal{Q}_{\omega}^{(k,k)}$. If this term is large, the state is likely to impact the input-output system behavior for a selected frequency range. In absolute terms, it may be difficult to derive meaningful conclusions from the product of the Gramian elements. When all states are considered, however, the terms can be normalized. The results of this normalization outline the relative importance of an individual state.

D. Choice of Relevant States

The steps illustrated in Algorithm 1 should be followed to obtain a reduced-order model using the proposed method. First, the power system non-linear model should be linearized around an operating point, resulting in a linear state-space model.

The system's inputs and outputs are selected according to the study intended to be performed or based on the application the reduced-order model will have. This choice is essential as it directly affects the results. This is because the controllability is highly dependent on the inputs since it is a measure of how those inputs can drive the system. Similarly, the observability is dependent on the choice of outputs because it measures the response "observed" from those outputs.

When obtaining a model for a specific frequency range, this range must be defined and used during the calculation of the Gramians according to (30) and (31). The Gramians can then be used to calculate the participation of each state in the input-output behavior based on (32). Based on the relative difference

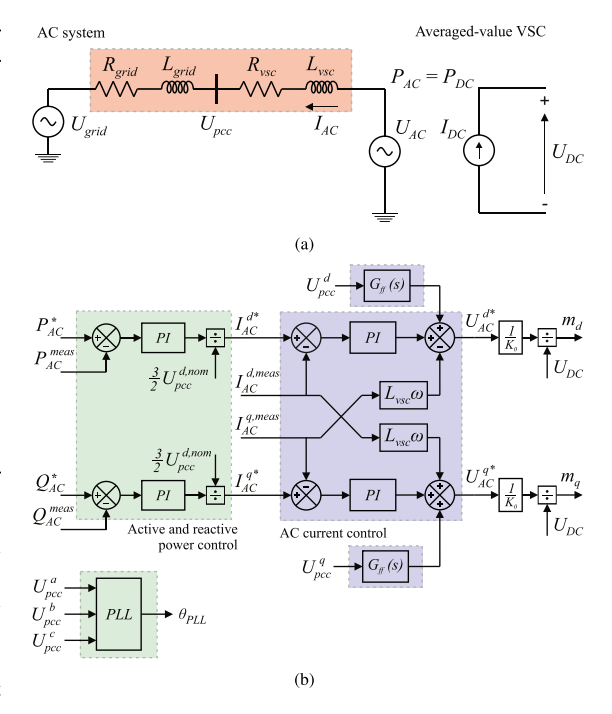


Fig. 2. Diagram illustrating the (a) VSC model connected to the AC network and (b) the VSC control system.

between the participation of the states, a set of the most relevant states can be chosen to represent the reduced-order model.

Care must be taken when selecting an algorithm for calculating the controllability and observability Gramians. This article uses the MATLAB library function 'gram' [19] which calculates the Gramians using Lyapunov equations with a full Gramian approach. This approach has a high computational cost $O(n^3)$ [20] and may not be appropriate for realistic large-scale systems. In this case, one of the several techniques proposed in the literature [21], [22] may be used to speed up computation as the proposed method is independent of the algorithm used to compute Gramians.

IV. APPLICATIONS AND RESULTS

This section covers two study cases showing how the proposed model reduction approach can be applied to derive reduced-order models for (a) a VSC system and (b) a modified 39-bus system with two converters. All computations were conducted using MATLAB R2022a on an Intel i5 processor with a 2.40-GHz clock and 32 GB RAM.

A. VSC System

The study case consists of a 10th order VSC model connected to an equivalent AC network and a constant DC source. Fig. 2(a) illustrates the modelled system. An averaged-value model is used for the VSC according to details provided in [23]. In this model, the converter AC and DC sides are represented as

TABLE I VSC CASE STUDY PARAMETERS

Name	Symbol	Value
Rated apparent power	S_{rated}	1 GW
DC bus voltage	U_{dc}	640 kV
AC bus voltage	U_{pcc}	192 kV
VSC equivalent inductance	L_{vsc}	50 mH
VSC equivalent resistance	R_{vsc}	0.05Ω
Equivalent grid resistance	R_{qrid}	10.19Ω
Equivalent grid inductance	L_{arid}	324.3 mH
Active and reactive power control time constant	τ_{PQ}	100 ms
AC current control time constant	τ_{idq}	10 ms
AC current control damping ratio	ζ_{idq}	0.7
PLL time constant	$ au_{PLL}$	27 ms
PLL damping ratio	ζ_{PLL}	0.7

controlled voltage and current sources at nominal frequency, neglecting the switching harmonics.

The equations describing the converter AC side in the dq0 frame are summarized as:

$$U_{AC}^{dq}-U_{pcc}^{dq}=R_{vsc}I_{AC}^{dq}+L_{vsc}\frac{dI_{AC}^{dq}}{dt}+j\omega L_{vsc}I_{AC}^{dq} \eqno(40)$$

where U^{dq}_{pcc} is the voltage at the point of common coupling (PCC), U^{dq}_{AC} is the AC-side controlled voltage source, I^{dq}_{AC} is the AC current and R_{vsc} and L_{vsc} are the equivalent converter resistance and inductance, respectively.

The control system consists of active and reactive power controls; decoupled AC current control implemented in dq reference frame including voltage feed-forward filters; and an $\alpha\beta$ phase-locked loop (PLL) implemented according to [24]. Fig. 2(b) summarizes the control structure. The parameters used in the study case can be found in Table I.

The inner current controller is implemented in the dq-frame according to Fig. 2(b). The main equations describing the control loop are:

$$\begin{split} U_{AC}^{d*} &= (I_{AC}^{d*} - I_{AC}^{d,meas}) \left(K_{p,d} + \frac{K_{i,d}}{s} \right) \\ &+ U_{pcc}^{d} + I_{AC}^{q,meas} L_{vsc} \omega \end{aligned} \tag{41}$$

$$U_{AC}^{q*} &= (I_{AC}^{q*} - I_{AC}^{q,meas}) \left(K_{p,q} + \frac{K_{i,q}}{s} \right) \\ &+ U_{pcc}^{q} - I_{AC}^{d,meas} L_{vsc} \omega \tag{42}$$

where $K_{p,d}$, $K_{p,q}$ are the controller's proportional gains and $K_{i,d}$ and $K_{i,q}$ are the integral gains.

The $\alpha\beta$ -PLL is implemented as follows:

$$\omega_{\alpha\beta PLL} = \left(K_p + \frac{K_i}{s}\right) sin(\theta_{grid} - \theta_{\alpha\beta PLL})$$
 (43)

$$\theta_{\alpha\beta PLL} = \frac{\omega_{\alpha\beta PLL}}{s} \tag{44}$$

where θ_{grid} is the grid voltage angle, $\theta_{\alpha\beta PLL}$ is the grid angle measured by the PLL, and $\omega_{\alpha\beta PLL}$ is the measured grid frequency in rad/s.

A first-order low-pass voltage-feedforward filter was used, where ω_{ff} represents the filter's cutoff frequency. The filter's

transfer function $G_{ff}(s)$ is given by:

$$G_{ff}(s) = \frac{\omega_{ff}}{s + \omega_{ff}} \tag{45}$$

Finally, the main equations describing the active and reactive power controls are:

$$I_{AC}^{d*} = (P_{AC}^* - P_{AC}^{meas}) \left(K_{p,P} + \frac{K_{i,P}}{s} \right)$$
 (46)

$$I_{AC}^{q*} = -\left(Q_{AC}^* - Q_{AC}^{meas}\right) \left(K_{p,Q} + \frac{K_{i,Q}}{s}\right)$$
 (47)

where P_{AC}^{*} and Q_{AC}^{*} are the active and reactive power reference values, respectively, while P_{AC}^{meas} and Q_{AC}^{meas} are the measured active and reactive power values.

This model is referred to in this article as the full-order VSC model. It was implemented in MATLAB/Simulink, and a state-space representation was obtained from the linearized system considering the arbitrarily selected active and reactive power setpoints of P=0.9 p.u. and Q=0.2 p.u., respectively. The correspondence between states and the physical system was maintained to derive practical modeling insights from the analysis.

1) Application of Model Reduction Approach: The controllability and observability Gramians are calculated to derive a reduced-order model. Frequency intervals of 10 rd/s are used and considered sufficiently small for the intended analysis. The diagonal terms of the Gramians are combined according to (29) to calculate the participation of each state in the input-output behavior of the system for frequencies ranging from 1 to 10⁴ rad/s. The results are presented in Fig. 3 and are grouped according to the parts of the physical system the states represent. Additionally, the frequency is measured from the stationary dq reference frame. This means, for instance, that 0 rd/s in the results correspond to nominal system frequency.

To facilitate the analysis, in Fig. 3 the frequency spectrum was divided into three parts highlighting low, medium, and high-frequency ranges. In the initial portion of the low-frequency range (from 1 to 100 rd/s), highlighted in green on Fig. 3, only states associated with active and reactive power controls contribute to the system behavior. If the model is used to study phenomena in that frequency range, all other controls may be simplified or neglected. In addition to that, the AC equations can be represented by their steady-state formulation. RMS simulations typically use these types of models [25], [26] where the frequencies of interest are only those around the nominal frequency. Thus, the results are in line with widely used modeling practices. The upper portion of the low-frequency range becomes increasingly affected by the PLL dynamics. This points to the importance of including detailed PLL models even for RMS simulations.

The middle frequency range (100 to 2000 rd/s) highlighted in blue shows varying contributions from several system and control components, except for the power controls. The frequency range in which each of the control loops becomes prominent is in line with the control bandwidths expected considering the tuning parameters used (found in Table I). This is the frequency

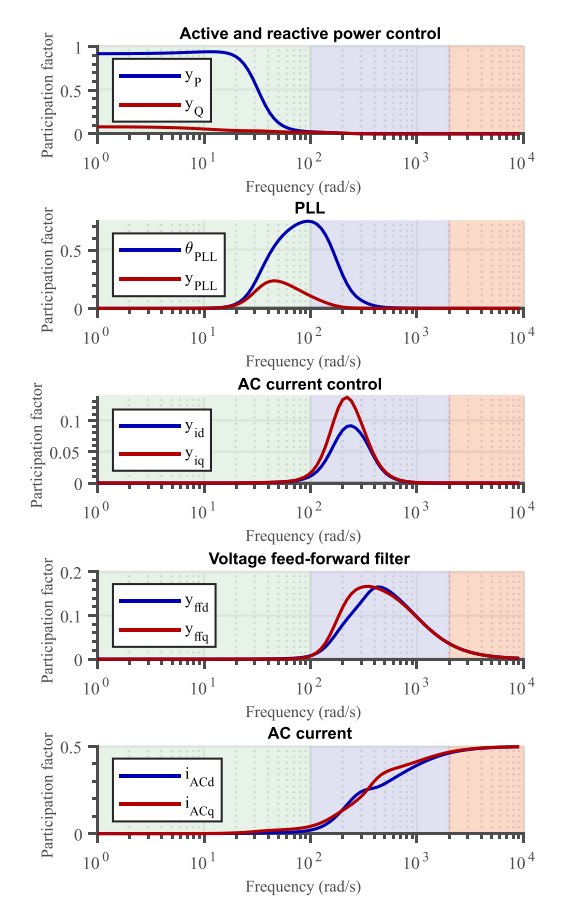


Fig. 3. Participation of states in input-output behavior over the frequency spectrum.

range where the RMS models relying on steady-state network representation might no longer be applicable since the AC current state variable has increased participation in the system behavior.

Finally, in the high-frequency range (higher than 2000 rd/s) highlighted in red, the AC current dominates the system response. However, the full-order model selected for the study case reaches its limitations in this frequency range. More complex models, including PWM and switching elements, should be considered when analyzing this frequency region to obtain more meaningful conclusions. This is not covered by the study in this article.

As a visual summary, the importance of each part of the VSC model in the three frequency ranges is highlighted in the corresponding colors in Fig. 2. This result clearly outlines that the proposed approach can directly provide meaningful insights into the importance of modeling each part of a system for different frequency applications.

2) Reduced Model Development: To further illustrate the application of the proposed approach, a reduced model is obtained

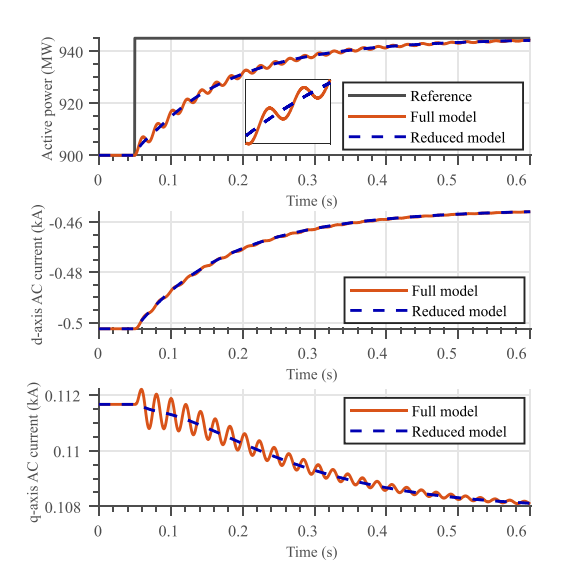


Fig. 4. Response comparison between full and reduced models to a 5% step in active power setpoint.

to verify the conclusions derived in the previous subsection. The full-order VSC model presented in Fig. 2 is simplified, assuming it will be used in the low-frequency range (considered in this article up to 100 rd/s). The algorithm had a total execution time of 0.788 s (of which 0.002 s is the time taken to compute the Gramians). According to the results concluded from Fig. 3, the low frequency reduced model should be obtained by neglecting the AC current control and voltage feed-forward filter and representing the AC equations in steady-state. Only the state variables associated with the active and reactive power controls and the PLL are maintained. These controls are highlighted in green on Fig. 2(b). This results in a 4th order VSC model.

Fig. 4 shows the response comparison between the full and reduced models to a 5% step increase in active power setpoint applied at t=0.05 s. The response of the full-order model has two components: an exponential term and an oscillatory term with frequency $\omega_{osc}\approx 306$ rad/s.

The developed reduced-order model is only intended to represent the exponential term of the full model response. The results in Fig. 4 indicate that the model reduction technique behaves as expected. The fact that the oscillatory term is not present in the reduced model response is further confirmed by Fig. 3 where it is shown that at that frequency value, the AC current, AC current controls, and voltage feed-forward have a significant contribution, and these modeling details are not included in the reduced model. These findings indicate that the proposed model reduction approach successfully approximates the full order model in the desired frequency range.

B. Modified 39-Bus System

The analysis is extended to a modified 39-bus system based on [27] containing 396 state variables. The main modification

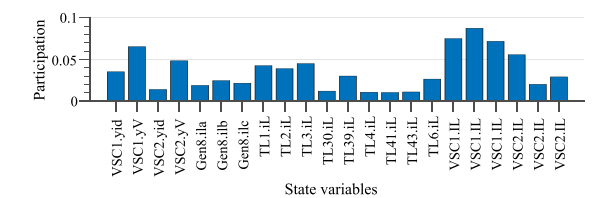


Fig. 5. Participation of states in input-output behavior.

made to the original system was the addition of two VSC converters based on the model described in Subsection IV-A. The models include an additional AC voltage controller replacing the reactive power control. The parameters used for VSC 1 are $\tau_P=30$ ms and $\tau_{PLL}=5$ ms, $\tau_{idq}=3$ ms, $\tau_V=10$ ms. The parameters for VSC 2 are $\tau_P=40$ ms and $\tau_{PLL}=10$ ms, $\tau_{idq}=4$ ms and $\tau_V=10$ ms. VSC 1 replaces generator 10 from the original 39-bus system, and VSC 2 is connected to bus 26.

The electrical distance between the two converters is relatively short, and both are operating in AC voltage control mode. In order to evaluate the dynamic response of the system, a 0.1 p.u. voltage reference step is applied to the voltage control reference of VSC 1. Fig. 7 shows the dynamic response of the converter.

The method proposed in this article is applied following the steps detailed in Algorithm 1 to determine which parts of the system contribute to the observed behavior. First, the model is linearized by selecting the AC voltage reference at VSC 1 as the input while the measured AC voltage is selected as the output. This choice of input/output was deliberate as it will provide insight into which elements of the power system are essential to capture the voltage dynamics at VSC 1. The controllability and observability Gramians are calculated from the state space model. Finally, the overall participation of each state is determined using (29).

Fig. 5 presents the participation of the most significant states in the input-output response of the system obtained from the analysis. Because the states are associated with the physical components of the power system, the participation value measures the relevance of each state and the corresponding component in the system response. Because of that, the results of the model reduction method are directly interpretable and can be used to decide which parts of the system can be simplified. These results can be further used to determine whether the system must be modeled in RMS, EMT, or as a hybrid RMS/EMT simulation. For instance, the highlighted area in Fig. 6 represents the area where the models must be represented in EMT. The components in the outside area, however, can be simplified and even represented in RMS.

This is in contrast to model reduction methods that rely on a transformation of the coordinate system to evaluate which states are most relevant. For instance, the balanced truncation method requires that the state vector \boldsymbol{x} be transformed using a balancing transformation \boldsymbol{Tb} [7]. Thus, any conclusions about the relevant states must be interpreted back to the original system frame of reference. The required mapping of the states decreases

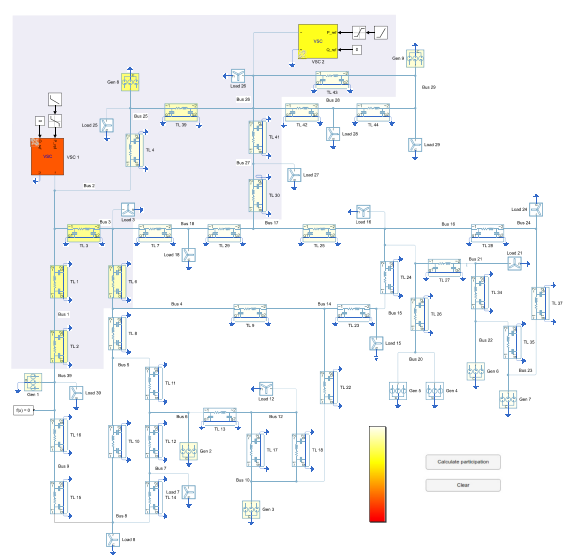


Fig. 6. Tool developed for MATLAB/Simulink showing the contribution of different parts of the system in a converter interaction case. Area in blue represents the components that contribute the most to the studied dynamics.

the interpretability of results and its potential to provide clarity around modeling detail requirements for novel dynamics in converter-rich power systems.

The results on Fig. 5 show that the main factors contributing to the AC voltage dynamics are both of the converters' voltage controls, the smoothing reactor impedances, and the nearby transmission lines. Additionally, the results show that each transmission line has relatively low participation. However, when all of them are taken into account, they contribute significantly to the system's behavior.

The proposed methodology was used to develop a tool for MATLAB/Simulink, which helps visualize the contribution of different parts of a model to the system's response. The tool presents an alternative view of the results found in Fig. 5 by creating a color gradient overlay that highlights the elements that contribute the most and must be modeled in detail.

Fig. 6 shows the results of analyzing the modified 39-bus system with the tool. The red colors indicate a higher participation level, while colors closer to yellow indicate a lower level of participation. This color map contributes to the interpretability of the results obtained using the method.

Finally, a reduced-order model is obtained by residualizing states that do not significantly affect the system response. The only states maintained in the reduced model are those associated with the area highlighted in blue in Fig. 6). The resulting reduced-order system has 48 states. The method achieved a reduction of approximately 88% of the number of states in the original system. In addition to that, the dynamic response closely matches that of the full-order system as shown in Fig. 7, indicating that the area which has not been highlighted in Fig. 6 can

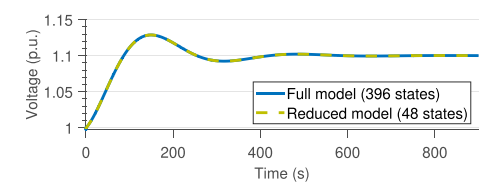


Fig. 7. Comparison between full and reduced-order models for a response to a 0.1 p.u. step in the terminal voltage reference.

be significantly simplified without accuracy loss. The algorithm had a total execution time of 24.844 s (of which 0.716 s is the time taken to compute the Gramians).

The proposed tool has some limitations as it is only suitable for analyzing dynamic phenomena that can be studied using small-signal analysis. In addition to that, the computation of Gramians can be expensive for very large systems.

V. CONCLUSION

This article proposed a novel model reduction approach using frequency-limited controllability and observability Gramians to understand how relevant each state is to the input-output behavior in different frequency ranges. The technique does not rely on any coordinate system transformation, preserving the physical meaning of the states. The approach demonstrated that it is possible to determine the parts of a system that must be modeled in detail in a practical study setting.

The method was applied to analyze two case studies. The first case study used the proposed approach to derive a reduced-order model of a VSC-based system valid for low-frequency studies. The results confirmed the validity of typical model simplifications reported in the literature. The authors propose that this method could be beneficial when applied to scenarios where it is unclear whether the simplifications are valid.

The second case study applied the method to investigate a converter interaction in a modified 39-bus system. The technique was able to identify which parts of the system were associated with the observed voltage dynamics. In addition to that, a tool was created for MATLAB/Simulink, allowing visualization and immediate identification of the power system components that are most relevant for the phenomenon under study. This tool can be beneficial when analyzing oscillatory behaviors where the cause is unknown or poorly understood.

The main limitation of the proposed method is that it applies only to linear time-invariant systems and small-signal studies. The system must have a stable operating point because Gramians are not defined for unstable systems. In addition, a limitation of the proposed algorithm is the potential computational burden of calculating the controllability and observability Gramians for very large systems. Despite the shortcomings mentioned, techniques proposed in the literature [21], [22] may be used to speed up Gramian computation. Also, Gramian definitions may be extended to unstable systems [28]. The extension of the proposed method to account for unstable systems is a topic for future research.

REFERENCES

- IRENA, "World energy transitions outlook: 1.5° pathway," International Renewable Energy Agency, Abu Dhabi, UAE, Tech. Rep., 2021.
- [2] ENTSO-E, "Completing the map-Power system needs in 2030 and 2040," European Network of Transmission System Operators for Electricity, Brussels, Belgium, Tech. Rep. Aug., 2020.
- [3] Y. Cheng and L. Fan, "Wind energy systems sub-synchronous oscillations: Events and modeling," IEEE Power & Energy Society, Tech. Rep. Jul., 2020.
- [4] AEMO, "Power system limitations in north western victoria and south western new south wales," Australian Energy Market Operator, Australia, Tech. Rep. Dec., 2019.
- [5] J. Adams, C. Carter, and S. Huang, "ERCOT experience with subsynchronous control interaction and proposed remediation," in *Proc. IEEE PES Trans. Distr. Conf.*, Orlando, USA, 2012, pp. 1–5.
- [6] I. J. Perez-Arriaga, G. C. Verghese, and F. C. Schweppe, "Selective modal analysis with applications to electric power systems, PART I: Heuristic introduction," *IEEE Trans. Power App. Syst.*, vol. PAS-101, no. 9, pp. 3117–3125, Sep. 1982.
- [7] B. Moore, "Principal component analysis in linear systems: Controllability, observability, and model reduction," *IEEE Trans. Autom. Control*, vol. 26, no. 1, pp. 17–32, Feb. 1981.
- [8] D. Chaniotis and M. A. Pai, "Model reduction in power systems using Krylov subspace methods," *IEEE Trans. Power Syst.*, vol. 2, no. 2, pp. 888–894, May 2005.
- [9] Y. G. I. Acle, F. D. Freitas, N. Martins, and J. Rommes, "Parameter preserving model order reduction of large sparse small-signal electromechanical stability power system models," *IEEE Trans. Power Syst.*, vol. 34, no. 4, pp. 2814–2824, Jul. 2019.
- [10] Q. Cossart, F. Colas, and X. Kestelyn, "A novel event- and non-projection-based approximation technique by state residualization for the model order reduction of power systems with a high renewable energies penetration," *IEEE Trans. Power Syst.*, vol. 37, no. 4, pp. 3221–3229, Jul. 2022.
- [11] H. R. Ali and B. C. Pal, "Model order reduction of multi-terminal directcurrent grid systems," *IEEE Trans. Power Syst.*, vol. 36, no. 1, pp. 699–711, Jan. 2021.
- [12] S. D. Dukić and A. T. Sarić, "A new approach to physics-based reduction of power system dynamic models," *Electric Power Syst. Res.*, vol. 101, pp. 17–24, 2013.
- [13] C. Sturk, L. Vanfretti, Y. Chompoobutrgool, and H. Sandberg, "Coherency-independent structured model reduction of power systems," *IEEE Trans. Power Syst.*, vol. 29, no. 5, pp. 2418–2426, Sep. 2014.
- [14] N. Hatziargyriou et al., "Definition and classification of power system stability-revisited & extended," *IEEE Trans. Power Syst.*, vol. 36, no. 4, pp. 3271–3281, Jul. 2021.
- [15] G. E. Dullerud and F. G. Paganini, A Course in Robust Control Theory: A Convex Approach. New York, NY, USA: Springer, 2000.
- [16] B. A. Francis, A Course in H_∞ Control Theory. New York, NY, USA: Springer, 1988.
- [17] M. A. Wicks and R. A. DeCarlo, "An energy approach to controllability," in *Proc. IEEE 27th Conf. Decis. Control*, 1988, vol. 3, pp. 2072–2077.
- [18] P. K. Aghaee, A. Zilouchian, S. Nike-Ravesh, and A. H. Zadegan, "Principle of frequency-domain balanced structure in linear systems and model reduction," *Comput. Elect. Eng.*, vol. 29, no. 3, pp. 463–477, 2003.
- [19] "MATLAB Control System Toolbox," in *Release 2022a*, Natick, MA, USA: The MathWorks, Inc..
- [20] A. Antoulas, "Approximation of large-scale dynamical systems: An overview," *IFAC Proc. Volumes*, vol. 37, no. 11, pp. 19–28, 2004.
- [21] P. Benner, P. Ezzatti, D. Kressner, E. S. Quintana-Ortí, and A. Remón, "A mixed-precision algorithm for the solution of Lyapunov equations on hybrid CPU-GPU platforms," *Parallel Comput.*, vol. 37, no. 8, pp. 439–450, 2011.
- [22] F. D. Freitas, J. Rommes, and N. Martins, "Low-rank gramian applications in dynamics and control," in *Proc. Int. Conf. Commun.*, *Comput. Control Appl.*, 2011, pp. 1–6.
- [23] CIGRE, "Technical brochure 604: Guide for the development of models for HVDC converters in a HVDC grid," CIGRE Working Group B4.57, Tech. Rep. Dec., 2014.
- [24] Z. Ali, N. Christofides, L. Hadjidemetriou, E. Kyriakides, Y. Yang, and F. Blaabjerg, "Three-phase phase-locked loop synchronization algorithms for grid-connected renewable energy systems: A review," *Renewable Sustain. Energy Rev.*, vol. 90, pp. 434–452, 2018.

- [25] R. L. Hendriks, G. C. Paap, R. Völzke, and W. L. Kling, "Model of a VSC transmission scheme for wind farm connection for incorporation in power system stability studies," in *Proc. 16th Power Syst. Comput. Conf.*, 2008, pp. 14–19.
- [26] J. B. Glasdam et al., "An assessment of converter modelling needs for offshore wind power plants connected via VSC-HVDC networks," in *Proc.* 12th Wind Integration Workshop, 2013, pp. 1–6.
- [27] M. A. Pai, Energy Function Analysis for Power System Stability. New York, NY, USA: Springer, 1989.
- [28] G. Salomon, K. Zhou, and E. Wu, "A new balanced realization and model reduction method for unstable systems," *IFAC Proc. Volumes*, vol. 32, no. 2, pp. 1696–1701, 1999.



Tanel Sarnet (Member, IEEE) received the B.Sc. and M.Sc. degrees in electrical power engineering in 2009 and 2011, respectively, from the Tallinn University of Technology, Tallinn, Estonia, where he is currently working toward the Ph.D. degree. From 2014 to 2015, he was a Visiting Scholar with the KTH Royal Institute of Technology, Stockholm, Sweden, in 2013, and the University of Manitoba, Winnipeg, MB, Canada. He is currently a Power System Dynamics Expert. His research interests include power system modeling, railway power supply systems, renewable energy

generation modeling, FACTS devices, power system stability.



Nathalia de Morais Dias Campos (Graduate Student Member, IEEE) received the B.Eng. degree in electrical engineering from the University of Campina Grande, Campina Grande, Brazil, in 2018, and the M.Sc. degree in electrical engineering for sustainable development from the University of Lille 1, Lille, France, in 2017. She is currently working toward the Ph.D. degree with the Tallinn University of Technology, Tallinn, Estonia. In 2014, she was a Visiting Student with the University of Manitoba, Winnipeg, MB, Canada. From 2018 to 2020, she was an Early

Stage Researcher with KU Leuven, Leuven, Belgium, and Elia System Operator, Belgium, within the Marie Curie project InnoDC. Her research interests include power systems modelling, stability analysis, converter controls, and renewable energy.



Jako Kilter (Senior Member, IEEE) received the Ph.D. degree in electrical power engineering from the Tallinn University of Technology, Tallinn, Estonia, in 2009. He is currently a Professor of power systems and the Head of Power Systems Research Group with the School of Engineering, Tallinn University of Technology, Chairperson of the High Voltage Committee with the Estonian Centre for Standardization and Accreditation, and Co-Chair of ClGRE Estonian National Committee. He is Chartered Engineer in Estonia. Over the years he has been active member

in various ENTSO-E (Grid Code development) and CIGRE (B4, C4) working groups. His research and consultancy work over the years has been split between the areas of power system dynamics, wide-area control and applications, power quality, renewable energy integration, and HVDC.

Publication III

P. De Rua, T. Roose, O. C. Sakinci, N. M. D. Campos, and J. Beerten, "Identification of mechanisms behind converter-related issues in power systems based on an overview of real-life events," *Renewable and Sustainable Energy Reviews*, vol. 183, pp. 1–16, 2023



Contents lists available at ScienceDirect

Renewable and Sustainable Energy Reviews

iournal homepage: www.elsevier.com/locate/rser



Review article

Identification of mechanisms behind converter-related issues in power systems based on an overview of real-life events

Philippe De Rua ^{a,b}, Thomas Roose ^{a,b}, Özgür Can Sakinci ^{a,b}, Nathalia de Morais Dias Campos ^{a,b,c}, Jef Beerten ^{a,b,*}

- a KU Leuven, ESAT/ELECTA, Department of Electrical Engineering, Kasteelpark Arenberg 10, 3001 Leuven, Belgium
- b EnergyVille, Thor Park 8310, 3600 Genk, Belgium
- c TalTech, Department of Electrical Power Engineering and Mechatronics, Ehitajate tee 5, 19086 Tallinn, Estonia

ARTICLE INFO

Keywords: Power-electronic converters Control interactions Power system stability Power quality Classifications Resonance Subsynchronous oscillations

ABSTRACT

Within modern power systems comprising both power-electronic converters and synchronous generators, a sufficiently high power quality and a stable operation can only be guaranteed if the fundamental mechanisms underlying converter-related issues can be thoroughly understood, properly identified and successfully mitigated. In particular, classifications are regarded as essential tools for the identification of converterrelated instabilities and interactions. However, the large variety of emerging events make that proposed classifications have not always been capable of encompassing all observed problems. This paper addresses this issue and presents a bottom-up approach capable of constructing more-encompassing classifications. The approach consists in carrying out a comprehensive literature review of problematic real-life events that have been reported by the electrical power industry, and that have directly or indirectly involved power-electronic converters. The focus is set on five prominent types of systems in which such converters are used: wind farms, photovoltaic systems, electrical railways, LCC-HVDC, and VSC-HVDC/STATCOM systems. Next, patterns are identified among the real-life events in order to pinpoint underlying mechanisms capable of explaining the converter-related issues. Lastly, the underlying mechanisms are discussed in regard to the events, their triggers, modeling requirements and dedicated terminology. The overview of real-life events and the set of underlying mechanisms established in this paper can support the development of new interaction and stability classifications and contribute to ensuring the correct identification and mitigation of converter-related issues in future converter-based power systems.

1. Introduction

With the ongoing energy transition, conventional power systems that have traditionally relied on synchronous generators (SGs) in thermal and hydro power plants, are rapidly evolving to meet future energy needs. Large thermal power plants are being phased out while the share of renewable energy sources (RES) grows fast, for instance with the commissioning of onshore and offshore wind farms (WFs). At the transmission level, flexible AC transmission systems (FACTS) and high-voltage direct current (HVDC) systems are becoming more common [1], while at the distribution level, both the generation from domestic photovoltaic (PV) systems and the demand from electric household appliances continue to increase [2]. Moreover, we see a rising trend in the electrification of transportation, particularly with electric vehicles and railway (RW) systems.

A common feature of the aforementioned systems is that their grid interface generally relies on power-electronic (PE) converters. Despite

offering substantial advantages in terms of control and flexibility, PE converters also significantly impact the dynamic behavior of electrical networks. Since the first converter-based devices were integrated into power systems, numerous events have been reported in which converters contributed to (i) network instabilities, (ii) adverse forms of interactions, or (iii) degradation of power quality. As a consequence, the potentially negative impact that PE converters can have on the network has become a prominent concern within the power system community [3–5]. Within modern power systems comprising both PE converters and SGs, a sufficiently high power quality and a stable operation can only be guaranteed if the fundamental mechanisms underlying converter-related issues are thoroughly understood, properly identified and successfully mitigated. In particular, classifications are regarded as essential tools for identifying converter-related instabilities and interactions.

^{*} Corresponding author at: KU Leuven, ESAT/ELECTA, Department of Electrical Engineering, Kasteelpark Arenberg 10, 3001 Leuven, Belgium. E-mail address: jef.beerten@kuleuven.be (J. Beerten).

Abbreviations

Constant power load DFIG Doubly-fed induction generator FACTS Flexible AC transmission systems Fault ride through FRT GSC Grid-side converter HVDC High-voltage direct current IGE Induction generator effect LCC Line commutated converter MMC Modular multilevel converter OWF Offshore wind farm

PE Power-electronic
PLL Phase locked loop

PMSG Permanent-magnet synchronous generator

PV Photovoltaic

PWM Pulse width modulation RES Renewable energy sources

RW Railway

SCR Short circuit ratio

SCTL Series-compensated transmission line

SG Synchronous generator

SSCI Subsynchronous control interaction

SSO Subsynchronous oscillation SSR Subsynchronous resonance

SSTI Subsynchronous torsional interaction STATCOM Static synchronous compensator

STG Steam turbine generator

VSC Voltage source converter

WF Wind farm
WT Wind turbine

Various classifications have been established over the years, initially dealing with issues that were specific to conventional systems based on SGs [6,7], but progressively evolving towards the inclusion of PE converters in order to accommodate the complexity of modern systems [8]. However, the large variety of emerging converter-related events makes it such that proposed classifications have not always been capable of encompassing all observed problems [9]. Often, reallife issues within modern power systems are cascaded phenomena with multiple causes and consequences, where dynamics of rotating machines, PE converters, and passive grid components are intertwined. This paper addresses the complexity of creating new classifications and presents an approach capable of constructing more-encompassing classifications. The undertaken strategy consists in identifying fundamental mechanisms in a bottom-up approach based on an extensive overview of problematic real-life events involving PE converters. Consequently, the first step is to select or establish such an overview.

Several overviews of converter-related events have been published in the past years. For instance, Hu et al. [10] reviewed events that have occurred within electrical RW networks, while Yin et al. [11] reviewed events related to voltage source converter (VSC)-HVDC systems. Virulkar et al. [12] presented an overview of subsynchronous oscillations (SSOs) in wind power systems, while Shair et al. [13] expanded on this topic to include a more detailed analysis of real-life events and a categorization of instability phenomena. The impact of PV integration on stability was discussed in [14,15].

However, by limiting the discussion to one type of application, these overviews fall short of drawing analogies between similar events observed in different types of systems. Consequently, a comprehensive cross-system overview has been missing to this day, while being

essential for identifying a coherent set of mechanisms. This paper fills this gap by first carrying out a comprehensive literature review to collect examples of problematic real-life events from the electrical power industry that have directly or indirectly involved PE converters. To ensure that the overview covers only real-life events, works in the literature discussing purely theoretical phenomena exclusively observed in simulations are discarded. The focus is set on five prominent types of systems in which PE converters are used: (1) WF systems, (2) PV systems, (3) electrical RW systems, (4) line commutated converter (LCC)-HVDC systems, and (5) VSC-HVDC/static synchronous compensator (STATCOM) systems. In a second phase, patterns are identified among the real-life events in order to pinpoint their fundamental underlying mechanisms, which eventually supports the establishment of new classifications.

The outline of the remaining part of the paper is depicted in Fig. 1. Sections 2 to 6 are dedicated to reviewing problematic real-life events. Each of these sections is assigned to one of the five above-mentioned types of systems. It is noted that several real-life events involve more than one type of system, but these cases are only discussed in one of the sections. Next, Section 7 is dedicated to identifying the fundamental underlying mechanisms. In Section 8, the mechanisms are discussed in regard to the events, their triggers, modeling requirements and dedicated terminology. Section 9 concludes the paper.

Throughout the paper, each event is identified by an acronym and a number, which are listed in Tables 1 to 5. The tables provide main characteristics such as a summary of the observed event, the frequency of oscillations (when relevant), and the terminology used in the original references to describe the issues at hand. The complete list of events is provided in Table 9, which gives additional information such as year, location, and identified mechanisms for each event.

2. Overview of wind farm events

Nowadays, the dominant types of wind turbines (WTs) are either based on doubly-fed induction generators (DFIGs) in which the stator is directly connected to the grid while the rotor is connected through a partial-scale back-to-back converter, or on permanent-magnet synchronous generators (PMSGs) where the stator is connected through a full-scale back-to-back converter [32]. This section provides an overview of real-life events involving PE converters within WFs. A selection of events is presented in detail, and a complete list is provided in Table 1.

2.1. Wind farms and series-compensated transmission lines

A first type of phenomenon that was reported in the literature involved the radial connection of DFIG-based WFs with series-compensated transmission lines (SCTLs). In this configuration, SSOs involving energy exchanges between the WTs and the SCTLs have been observed on several occasions. It was shown that such oscillations are due to a phenomenon called *induction generator effect (IGE)*, in which the equivalent rotor resistance of a rotating machine becomes negative at subsynchronous frequencies, resulting in self-sustained oscillations [40]. In the case of DFIGs, the controls of the rotor-side converter can significantly amplify the negative rotor resistive behavior [40].

Events WF1 [16,17], WF2 [18–22], WF3 [21,23] and WF4 [24,25] are examples of such interactions between DFIGs and SCTLs. In event WF3 for instance, the Texan transmission system operator ERCOT reported that the tripping of a line caused two DFIG-based WFs to become radially connected to a SCTL, leading to SSOs [21]. The series capacitors were bypassed and then reinserted, restarting and further aggravating the oscillations. This event happened even though the WFs were equipped with SSO damping controls and had undergone subsynchronous resonance (SSR) studies prior to their installation [41]. The phenomenon, termed "subsynchronous control interaction (SSCI)" in [21], stopped after the WFs were tripped.

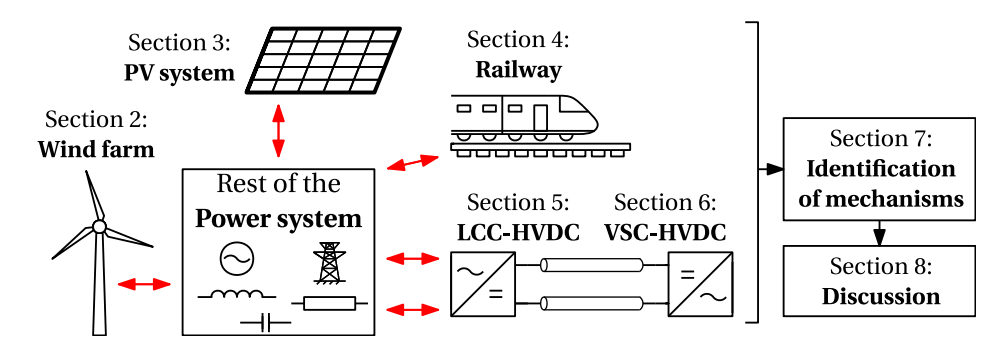


Fig. 1. Outline of the paper: review of real-life events in five types of systems and identification of mechanisms.

Table 1

Events involving	wind farms	S.							
Context	ID	Ref.	Trigger	Outcome	$f_{\rm osc.}$ [Hz]	f_1 [Hz]	Terminology in references		
	WF1	[16,17]	line switching	electrical SSOs	9–16	60	"undamped subsynchronous oscillations"		
	WILI	[10,17]	inie switching		9-10	00	"sustained sub-harmonic oscillations"		
	WF2	[18-20]	fault	electrical SSOs	20-25	60	"subsynchronous control interaction"		
SCTLs	VV1'2	[21,22]	iduit	electrical 330s	20-23	00	"subsynchronous oscillation phenomena"		
OGILD	WF3	[21,23]	line switching	electrical SSOs	25	60	"subsynchronous oscillation phenomena"		
		[21,20]		ercenten 5555			"SSCI phenomena"		
	WF4	[24,25]	power decrease in	electrical SSOs	6–9	50	"DFIG-control participated IGE"		
	****	[21,20]	specific ranges				"subsynchronous resonance"		
				electrical SSOs,	19.4, 29.6		"subsynchronous interaction"		
	WF5	[26–28]	not given or known	excitation of nonlinearity,	39.8, 60.2, 70.4, 80.6	50	"subsynchronous oscillation"		
				electromech. (torsional) osc.	30.6				
	WF6	[21]	fault	electrical SSOs	≤10	60	"subsynchronous control interactions"		
					2–3	60	"voltage stability issues"		
weak grids	WF7	[29]	line switching	electrical SSOs			"temporary overvoltage"		
							"voltage oscillations"		
	WF8	WF8	WF8			electrical SSOs, reached over-			"unexpected WF control system
				[30]	fault	current limit, frequency col-	≈ 8	50	response"
-				lapse					
	WF9	[4]	power fluctuations	voltage collapse	_	60	"weak grid voltage stability issues"		
	****	L-13	power nuctuations				"classical voltage instability conditions"		
FRT issues	WF10	[31]	fault	reached max. allowed	_	50	"activation of protection feature"		
	s WF10	[OI]	iddic	FRTs, frequency collapse		50	"significant sustained power reduction"		

 f_{osc} : oscillations frequency. f_1 : fundamental grid frequency.

2.2. Wind farms and weak grids

Low short-circuit levels have been associated with a higher risk of control interactions between WT converters and the grid. This constitutes a second type of phenomenon that was reported in the literature. A notorious example of control interaction involving WFs within a weak grid is that of event WF5 [26-28]. This event took place in the area of Hami (China), which comprises multiple WFs mostly based on PMSG WTs, as well as traditional thermal plants. In this system, the generated power is collected on an AC grid before being sent over a long distance via an LCC-HVDC link. On several occasions, interactions between the converters of the WTs and the weak grid impedance, termed "subsynchronous interactions" in [28], caused SSOs to appear. In turn, these oscillations had an adverse impact on the WT converter controllers. Specifically, the nonlinear nature of the phase locked loops (PLLs) led the converters to emit additional non-fundamental frequency components when disturbed by the SSOs [26]. Some of the oscillations had frequencies that were complementary to the torsional modes of the turbine-generator shafts of the thermal plants, causing them to trip despite being located hundreds of kilometers away. It is worthwhile noting that the local LCC-HVDC converter was not involved in the event [26].

Similar control interactions were observed in event WF6 [21], involving a DFIG-based WF, and event WF7 [29], involving a PMSG-based WF and in which the WTs tripped as a consequence of the resulting SSOs, thereby ending the event. In both cases, the WFs were in a weak grid configuration when SSOs occurred.

At times, such control interactions have led to a frequency collapse. In event WF8 [30], a large offshore WF in the United Kingdom tripped after a fault left the connection point in a weak grid configuration. Simultaneously, the fault triggered an unexpected control system response within the WF. Post-event analysis showed that the unexpected control response was due to an "insufficiently-damped electrical resonance" in the subsynchronous frequency range. These SSOs caused the WF to trip when the over-current limit was reached. The loss of generation from other plants impacted by the fault was aggravated by the loss of generation from the WF and eventually resulted in a blackout.

Aside from the above-described converter-grid interactions, WFs within weak grids can also be faced with cases of traditional voltage instability. In event WF9 [4], a large WF was connected near the mid-point of a long high-voltage transmission line. The area had the characteristics of a weak grid and presented high sensitivity to changes in active and reactive powers, causing significant voltage fluctuations. After a major wind ramp, the area experienced a voltage collapse. Postevent analysis showed that the WF was operating at unity power factor, while it was expected to provide voltage support.

2.3. Wind farms and fault-ride-through issues

Generally, protection controls rely on monitoring the grid conditions and are capable of disconnecting converters or reducing their power output, thereby preventing damage to the converters themselves.

Table 2 Events involving PV systems

Context	ID	Ref.	Trigger	Outcome	$f_{\rm osc.}$ [Hz]	f_1 [Hz]	Terminology in references
PLL or FRT issues	PV1	[33]	faults	incorrect PLL operation, reached low-frequency, under/over-voltage, and over-current capability limits	-	60	"perceived, though incorrect, low system frequency condition"
	PV2	[34]	faults	reached under/over-voltage and over-current capability limits, slow power restoration, synchronization issues	-	60	"restoration of power output was hindered by ramp limiters"
	PV3	[35]	faults	reached under/over-voltage and over-current capability limits	-	60	"momentary cessation of active and reactive current injection"
harmonics amplified by grid resonances	PV4	[36]	harmonic emissions	electr. supersynchr. osc., converters tripping	1150	50	"power quality problem" "harmonic interference"
	PV5	[37]	faults	electrical SSOs	7	50	"post-fault voltage oscillations"
	PV6	[38]	capacitor energization	electrical SSOs	20	60	"unstable operation at interharmonics" "subsynchronous oscillations"
interactions with the grid	PV7	[39]	PV power generation	electrical SSOs	9	50	"low frequency oscillation"
	PV8			electr. supersynchr. osc.	420	60	"unstable PV operation at low-order harmonics"
	PV9	[38]	not given or known	electr. supersynchr. osc.	780	60	"unstable PV operation at low-order harmonics", "harmonic instability"
	PV10			electr. supersynchr. osc.	2370	60	"unstable operation at high frequency"

In multiple events, the protection systems of WTs and WFs have detected abnormal grid conditions and tripped the converters or reduced their active power output, causing the anomalies to end. However, an excessive limitation of the fault-ride-through capabilities can also be problematic. For instance, in event WF10 [31], a series of faults occurred in Southern Australia over a short period of time. In these circumstances, eight WFs reduced their power output upon activation of a specific protection feature. This unique feature allowed the WTs to withstand only a pre-set maximum number of voltage dips within a two-minute period, thereby limiting their effective fault ride through (FRT) capability. At the moment of the event, the power demand in the South Australian area was also supplied by a single interconnector. Following the reduction of the WFs power generation, the power imported through the interconnector reached a too high level, which caused the interconnector to trip and the South Australian system to enter an islanded operation. The strong power imbalance within the islanded area eventually led to a frequency collapse.

Event WF8, discussed in the previous subsection, is also an example of WF tripping when FRT limits were reached after a fault.

In summary, seven types of events have been observed in WFs:

- SSOs resulting from the radial connection of DFIG-based WFs and SCTLs;
- Oscillations resulting from interactions between WFs or WTs controls and weak grids or natural grid resonances;
- · WTs tripping as a consequence of SSOs;
- Emission of non-fundamental frequency components by WTs converters resulting from the disturbance of control nonlinearities (e.g. PLLs);
- Interactions between WT converters and grid-connected SGs via the excitation of their torsional oscillatory modes;
- Voltage collapse caused by inadequate voltage or reactive power control in a weak grid environment;
- Frequency collapse caused by active power reduction, for instance after reaching low-voltage or over-current protection limits in amplitude or in number of instances.

3. Overview of PV system events

In recent years, a large amount of PV generation has been commissioned and the installed PV capacity continues to increase at a fast pace [42]. The generation capacity is composed of large-scale centralized PV plants and small-scale distributed PV systems, both introducing additional converters into the grid and hence impacting its dynamic behavior. In this section, problematic real-life events involving PE converters within PV systems are reviewed. A selection of events is presented in detail, and a complete list is provided in Table 2.

3.1. PV converters and PLL or fault-ride-through issues

In case of faults in the grid, PV systems and their converters have experienced PLL issues or have reached their fault ride-through capability limits. For example, in event PV1 [33], a series of faults occurred in the transmission grid and resulted in the loss of nearly 1200 MW of PV generation when PV plants decreased their power output as a response to the faults. The largest part of the generation loss, approximately 700 MW, was caused by an incorrectly-measured fundamental frequency: the PLL control mistakenly detected a frequency of less than 57 Hz due to the phase-jump and waveform distortion of the system voltage during the fault transients, to which the converters responded by tripping as the measured frequency exceeded the control limits. Similar synchronization issues were reported in PV2 [34].

Still in PV1, additional generation loss was primarily attributed to the momentary cessation of PV plants as a consequence of reaching the under/over-voltage capability limits of the converters. During momentary cessation, the converters remained connected to the grid, but temporarily suspended their current injection. When the voltage returned to its normal operating range, the converters resumed current injection. Similar issues of PV plants exceeding their under/over-voltage or overcurrent capability limits during faults have also been reported in events PV2 and PV3 [35].

3.2. PV converter harmonics amplified by grid resonances

Another type of converter-related problematic phenomenon is illustrated by event PV4 [36], which refers to the undesired tripping of PV converters in residential areas with high penetration of PV generation. Measurements showed that the harmonic distortion of the grid voltages and currents exceeded the levels specified by power quality standards. This power quality problem was associated with natural resonances amplifying both harmonic emissions of PV converters and background harmonics. In particular, it was also shown that the capacitive behavior of the PV converters contributed to the natural resonance with the inductive behavior of the distribution grid. The most dominant resonance frequency of event PV4 was determined to be around the 23rd harmonic.

3.3. Interactions among PV converters and with the grid

Interactions between the PV converters and the grid impedance may lead to oscillations over a broad frequency range. For example, in event PV5 [37], a subsynchronous voltage oscillation of approximately 7 Hz was observed at the connection points of five PV plants after a fault. Studies showed that reducing the number of online converters would lower the amplitude of the oscillations. However, individually decreasing the total power output of each PV plant, while maintaining all converters online, was ineffective in solving the problem. This indicates that the issue consisted of a form of interaction between the PV plants. SSOs have also been observed in a system with three PV plants connected to the same feeder (event PV6 [38]), and in a distribution grid with small-scale PV systems (event PV7 [39]).

Aside from SSOs, several grid-connected PV plants have also experienced oscillations above the fundamental frequency, even up to several kilohertz, due to interactions between the PV converters and the grid. In event PV8 [38], output current oscillations of about 420 Hz occurred in a PV plant with multiple converters in parallel, and reached 20% of the rated current. Due to the internal protection control, the PV converters restarted, which resolved the distortions. The triggering of these oscillations could not be related to utility switching, outages or faults. Similar phenomena also took place in events PV9 and PV10 [38] where oscillations appeared at 780 Hz and 2.37 kHz, respectively, and disappeared after (partially) shutting down the converters.

In summary, four types of events have been observed in PV systems:

- PV converters tripping after the fundamental grid frequency was mistakenly identified to be outside specified limits following a grid disturbance;
- Momentary cessation of current injection by PV converters after the fundamental voltage amplitude reached the under/over-voltage capability limits, or after the fundamental current amplitude reached the over-current capability limits;
- PV converters tripping due to supersynchronous oscillations resulting from the amplification of converters switching harmonics by grid resonances;
- Subsynchronous or supersynchronous oscillations resulting from interactions between the controls of PV converters and the grid.

4. Overview of railway system events

Nowadays, PE converters play an essential role in electrical RW systems, in particular on board of locomotives where they are used as variable speed drives. Up to this day, grid-side converters (GSCs) have evolved from thyristor-diode rectifiers to pulse width modulation (PWM)-based VSCs with regenerative braking capability.

This section reviews real-life events involving PE converters within electrical RW systems. A selection of events is presented in detail, and a complete list is provided in Table 3.

4.1. Interactions between train converters and rotating machines

A first type of phenomenon reported in RW systems concerns events RW1, RW2 and RW3 [43]. These events show that, from the 1990s, low-frequency oscillations were experienced in RW systems supplied by rotary frequency converters, which are intended to provide traction networks with electrical power at a fraction of the fundamental frequency of the supplying transmission grid. Such events were referred to as "interaction between electric rail vehicles and rotary frequency converter" and can arise when a mechanical oscillatory mode – although not necessarily a torsional mode – of the rotary frequency converters is triggered while the oscillations are negatively damped as a consequence of non-passive behavior of the converters on board the trains [54]. Such non-passive behavior at low frequencies was explained by a constant power load (CPL) operating mode, i.e. when the PE converters consume a fixed amount of power, independently of the supply voltage [55].

4.2. Converter harmonics amplified by natural resonances

A second type of event reported for electrical RW systems involves frequency components generated by PE converters and amplified by natural resonances of the traction network.

For instance, in event RW4 [45], the problematic frequency components were the switching harmonics of mixed thyristor-diode bridges. The harmonics were generated while trains were at a standstill, and were amplified around a frequency of $20f_1$. The phenomenon was described as a "harmonic interaction" between the trains and the network impedance. Similarly, in event RW5 [46], switching harmonics were generated by locomotives with PWM-based VSCs. The oscillations appeared when a train entered regenerative braking, which triggered a natural resonance of the traction network.

In event RW6 [44], parasitic frequency components also originated from PWM-based VSCs, which were not switching harmonics but the consequence of improper interleaving of the PWM carrier waves: with a switching frequency f_s of 450 Hz, improper interleaving produced parasitic frequency components at $2f_s \pm f_1$, i.e. 850 and 950 Hz, both being close to the first resonance frequency of the line.

Lastly, it is worthwhile noting that not only converters on-board the trains can emit frequency components susceptible to be amplified by natural resonances, but also off-board converters (supplying loads along the RW lines such as signalization, automation and telecommunication) may be the cause of undesired switching components. This was the case in event RW7 [47], where the single-phase thyristor bridge of an uninterruptible power supply emitted undesired harmonic components amplified by a network resonance after being triggered by harmonic disturbances from a train in operation.

4.3. Interactions among train converters and with the railway network

Events RW10 [43,48], RW11 [43,49], RW12 [44], RW13-17 [10, 50,51], RW18 [52,53] and RW19 [10] constitute a third type of issue reported from electrical RW systems, which is usually referred to as the "depot problem" or "low frequency-oscillations without rotary converter" for RW10-RW17, and as "harmonic instabilities" for RW18-RW19. In this type of phenomenon, interactions occurred among train converters or between train converters and the RW network. More specifically, undesired frequency components appeared when multiple trains were at a standstill in depots, stations or workshop areas while their converters were kept active to supply the auxiliary on-board equipment, or were operating during light-load conditions [10].

In event RW10 [43,48], the problem manifested itself in the form of "low-frequency power oscillations" when a large number of locomotives were in operation. While many disturbances occurred at standstill in stations, protective shutdowns and unusual vibrations were also reported during acceleration. Recordings show unstable SSOs and evidence of interference between converters of different bogies within

Table 3

Events involving railway systems.

Context	ID	Ref.	Trigger	Outcome	$f_{\rm osc.}$ [Hz]	f_1 [Hz]	Terminology in references
interactions with rotating	RW1	[43]	change of power direction (regenerative braking)	electromech. SSOs (non-torsional)	1.6, 1.9	50/3	"low-frequency oscillations and interaction"
machines	RW2	[10]	rapid power changes due to slippery rails	electromech. SSOs (non-torsional)	1.6	50/3	"interaction between electric rail vehicles and rotary converter"
	RW3		not known or given	electromech. SSOs (non-torsional)	3	25	
	RW4	[44,45]	switching harmonics during acceleration	electr. supersynchr. osc.	≈1 k	50	"repetitive distortion with over voltages" "harmonic interactions between rolling stock and network impedance"
harmonics amplified	RW5	[46]	switching harmonics during regenerative braking	electr. supersynchr. osc.	2.55 k	50	"voltage oscillations"
by grid resonances	RW6	[44]	improper interleaving	electr. supersynchr. osc.	0.85-0.95 k	50	"harmonic overvoltages"
	RW7	[47]	switching harmonics (on-board converter first, off-board converter next)	electr. supersynchr. osc.	1.05 k	50	"harmonics amplification due to resonance phenomena"
	RW8	[10]	not given or known	electr. supersynchr. osc.	0.9 k	50	-
	RW9		train operation	electr. supersynchr. osc.	2.5 k	50	-
	RW10	[43,48]	high impedance, multiple trains	electrical SSOs	5	50/3	"low frequency power oscillations
	RW11	[43,49]	operation in system fed by a static converter	electrical SSOs	7	50	"low-frequency interactions"
	RW12	[44]		electrical SSOs	5	50	"low-frequency interaction" "low-frequency instability"
interactions with the	RW13	[10,50]	multiple trains in	electrical SSOs	2–4	50	"low-frequency oscillation (LFO)"
railway	RW14		energized stand-by	electrical SSOs	5	50	"depot problem"
network	RW15		mode	electrical SSOs	5	50	
	RW16	[10,50,51]		electrical SSOs	6–7	50	
	RW17			electrical SSOs	0.6-2	50	
	RW18	[52,53]	new PWM-based trains	electr. supersynchr. osc.	100, 165	50/3	"these converters can interact with each other via the supplying network" "harmonic interaction"
	RW19	[10]	PWM-based trains	electr. supersynchr. osc.	1.8 k	50	_

the same locomotives. Similarly, in event RW12 [44], trains at a standstill were supplied by the same substation but located in two depots 25 km apart. Both were simultaneously involved in a "low-frequency instability". For such events, it was shown that the oscillation frequencies and amplitudes were related to the number of trains locally connected, the grid strength as well as the control strategy of the onboard GSC in the locomotives [10,51].

While events RW10-RW17 featured oscillations at subsynchronous frequencies, events RW18 and RW19 involved oscillations at supersynchronous frequencies. In particular, event RW18 involved oscillations at 100 Hz and 165 Hz in a system with a fundamental frequency f_1 of 16.7 Hz [52,53]. The event followed the introduction of new locomotives using PWM-based converters with a switching frequency f_s of 1.6 kHz on the Swiss RW system. The phenomenon explaining the 165 Hz oscillation was described as an interaction between the controller of the GSCs of the trains and a natural grid resonance. More specifically, the control delay caused the input impedance of the locomotives to present a non-passive small-signal behavior at several frequencies, in particular at 165 Hz. In [10], this event is referred to as an example of "harmonic instability".

In summary, three main types of phenomena have been observed in RW systems:

- SSOs resulting from interactions between converter controls onboard trains interacting with the mechanical oscillatory modes of rotary frequency converters;
- Supersynchronous oscillations resulting from the amplification of harmonic emissions from converters (on- or off-board trains) by natural grid resonances;
- Subsynchronous or supersynchronous oscillations resulting from interactions between converters on-board trains and/or with the traction network, sometimes resulting in converters tripping.

5. Overview of LCC-HVDC system events

The first LCC-HVDC link was the Swedish Gotland link built in 1954, originally based on mercury arc valves and refurbished in 1970 to become the first thyristor-based LCC-HVDC system [67]. Since then, different types of phenomena have been reported for both generations of the technology.

In this section, real-life events involving LCC-HVDC converters are reviewed. A selection of events is presented in detail, and a complete list is provided in Table 4.

5.1. Interactions between LCC-HVDC converters and rotating machines

A first type of phenomenon that was reported in the literature and in which LCC-HVDC converters were involved, consists of a form of

Table 4
Events involving LCC-HVDC systems

Context	ID	Ref.	Trigger	Outcome	$f_{ m osc.}$ [Hz]	f_1 [Hz]	Terminology in references
	LCC1	[56]	inter-area oscillation damping control, change in AC grid topology	electromech. SSOs (torsional)	11.5	60	"interacting in an adverse way with an 11.5 Hz torsional mode"
interactions with rotating machines	LCC2	[57–59]	increase in transmitted power	electromech. SSOs (torsional)	≈20	50	"SSTI, but with different characteristics from conventional SSTI", "over-threshold subsynchronous oscillations"
	LCC3	[60]	change of DFIGs rotor speed, change of HVDC-link operation mode	electromech. SSOs (torsional)	1.5–2.6	50	"SSTI"
	LCC4	[61,62]	weak grid	electr. supersynchr. osc.	100, 150-200	50	"waveform-distortion instability" "a form of harmonic instability or magnification"
interactions	LCC5	[63]	weak grid, DC-side natural resonance	electr. supersynchr. osc.	600	50	"core saturation instability"
with the grid	LCC6		not given or not known	electr. supersynchr. osc.	120	60	"core saturation instability"
	LCC7	[64]	AC-side natural resonance	electr. supersynchr. osc.	120	60	"second harmonic resonance problems"
	LCC8	[65]	weak grid	electr. supersynchr. osc.	150	50	"undesirable phenomena at frequencies close to the third harmonic"
harmonics amplified by grid resonances	LCC9	[66]	shift of natural resonance due to cables replacing overhead lines, switching harmonics	electr. supersynchr. osc.	550	50	"harmonic amplification"

adverse interaction between the controls of an LCC-HVDC converter and the torsional modes of nearby rotating machines. For instance, in event LCCI [56], such interactions were observed on two occasions in 1977. The event involved a converter of the Square Butte LCC-HVDC link and the 11.5 Hz torsional mode of a steam turbine generator (STG). The first occurrence of the interaction was related to the inter-area oscillation damping control of the link, while the second occurrence was triggered by the switching of a transmission line. The phenomenon was described as an "interaction between the STG shaft and the converter controls". In particular, it was explained that the DC current control contributed to the negative damping of the rotor oscillations. The interaction was found to be dependent on the AC system configuration and strength [68], on the DC link load level, and on the characteristics and control of the LCC-HVDC link.

Similar interactions were also observed more recently in event LCC2 [57–59], in which an LCC-HVDC converter, SCTLs and SGs of multiple thermal power plants were involved. In [57], the phenomenon was referred to as a "subsynchronous torsional interaction (SSTI) between the generators and the HVDC converter".

While SSOs arose in both LCC1 and LCC2 when torsional modes of SGs were excited by converter controllers, the same type of phenomenon was observed with DFIG WTs in event LCC3 [60]. In the reported event, the variations in the frequency of the SSOs were in agreement with the variations of DFIGs torsional modes, which depend on the rotor speed. It was also shown that the frequencies of the oscillations were influenced by the operational mode of the LCC-HVDC link.

5.2. Interactions among LCC-HVDC converters and with the grid

A second type of phenomenon in which LCC-HVDC converters have been involved is related to the interaction between the controls of LCC-HVDC converters and the grid impedance. For instance, LCC4 [61,62] refers to a set of events in which abnormal harmonics (i.e. other than orders $n{\cdot}k{\pm}1$ for an $n{\cdot}$ -pulse LCC-HVDC converter) were observed. In particular, oscillations occurred at $2f_1$ and between $3f_1$ and $4f_1$ at the Cross-Channel link (UK-FR), and oscillations occurred at $3f_1$ at the Inter-Island link (NZ). Back in 1967, a distinction was already made between the phenomenon at hand and ordinary low-frequency loop instability, describing the issue as a "waveform-distortion instability" or "a form of harmonic instability or magnification", involving a positive feedback loop between the AC voltage distortion and the control system, which aggravated the original distortion [61]. It was shown that this "harmonic instability" can occur in weak AC systems, and in systems of moderate short circuit ratio (SCR) with a natural resonance.

A similar type of interaction was reported in events LCC5 and LCC6 [63], although in these cases, the harmonic instability involved an additional amplifying effect from transformer saturation, which was referred to as "core saturation instability". Specifically in LCC5, the instability occurred when the AC system was weak and a DC-side resonance was present near the AC grid fundamental frequency. Then, a parallel resonance amplified the 12th AC-side harmonic component of the distorted transformer magnetizing current. Comparable unstable harmonic oscillations were also reported in events LCC7 [64] and LCC8 [65].

5.3. LCC-HVDC converter harmonics amplified by natural grid resonances

Although the above-described events LCC4-LCC8 display many characteristics of classical harmonic amplification by natural resonances,

Table 5
Events involving VSC-HVDC and STATCOM systems

Context	ID	Ref.	Trigger	Outcome	$f_{\rm osc.}$ [Hz]	f_1 [Hz]	Terminology in references
	VSC1	[11]	increase in transmitted power	electrical SSOs	20-30	50	"subsynchronous oscillations"
	VSC2	[11]		electrical SSOs	20-30	50	subsynctrionous oscinations
	VSC3	[69,70]	change in AC grid topology	electr. supersynchr. osc.	451	50	"harmonic instability" "harmonic interactions"
	VSC4	[71]	fault	electr. supersynchr. osc.	830	50	"overvoltage phenomena"
	VSC5	[72]	change in AC grid topology	electr. supersynchr. osc.	≈ 1500	50	"excitation of resonance frequency"
interactions	VSC6	[73]		electr. supersynchr. osc. converter tripping	1700	50	"control instability" "harmonic interactions"
with the AC grid		[74,75]		electr. supersynchr. osc.	1270	50	"instability phenomena" "high-frequency resonance" "harmonic resonance"
	VSC8	[11]	HVDC control mode switch	electr. supersynchr. osc.	> 1000	50	"oscillations in the range of high frequency"
	VSC9	[76]	increased time delay	electr. supersynchr. osc.	700, 1800	50	"high frequency resonances" "resonant instability"
	VSC10	[77]	STATCOMs in weak grid configuration	elec. sub. & super. osc.	2.5, 97.5	50	"sub- and super-synchronous interactions"
interactions with the DC grid	VSC11	[78,79]	HVDC control mode switch	elec. osc.	550	0	"high frequency resonances" "resonant instability"
	VSC12	[80,81]	increase in transmitted power	elec. osc.	23.6–25.2	0	"subsynchronous oscillations"

the involvement of converter controls is the fundamental difference with respect to the latter phenomenon. On the contrary, in event LCC9 [66], the 11th voltage harmonic amplification that was observed after the energization of a high-voltage underground cable did not involve converter controls. The impedance of the cable caused a shift of the natural grid resonances, which amplified the harmonics emitted by the LCC-HVDC converters.

In summary, three types of events have been observed in LCC-HVDC systems:

- SSOs resulting from interactions between LCC-HVDC controls and torsional modes of rotating machines (namely grid-connected SGs in thermal power plants and DFIGs in WFs);
- Supersynchronous oscillations resulting from interactions between LCC-HVDC controls, weak grids and/or natural grid resonances;
- Supersynchronous oscillations resulting from the amplification of LCC-HVDC converter harmonic emissions by natural grid resonances

6. Overview of VSC-HVDC and STATCOM events

The first commercial VSC-HVDC link was introduced at the historic Gotland island interconnection with Sweden in 1999 [67]. The increased flexibility, reduced converter footprint and lower harmonic generation of VSC-HVDC technology make it a preferred solution with respect to LCC-HVDC technology. Nowadays, STATCOMs based on the VSC technology also provide flexibility and services to the power network.

In this section, real-life events involving VSC-HVDC converters and VSC-based STATCOMs are reviewed. A selection of events is presented in detail, and a complete list is provided in Table 5.

6.1. Interactions among VSCs and with the AC grid

In event VSC1 [11], SSOs caused by converter-grid interactions were observed at the Nanhui modular multilevel converter (MMC)-based VSC-HVDC link connecting a DFIG-based offshore wind farm (OWF) to shore. Voltage and current oscillations occurred at early testing stage and depended on variations of transmitted power. Similar SSOs were

also observed in event VSC2 [11], again in an MMC-based VSC-HVDC link.

While events VSC1 and VSC2 were concerned with SSOs, other events presented oscillations at supersynchronous frequencies. For instance, event VSC3 [69] referred to a type of "harmonic instability" at a German VSC-HVDC link connecting an OWF to shore. This instability was observed after a switching operation which was intended to connect a second OWF to the same HVDC station. The mechanisms behind these "harmonic instabilities" are discussed in the case of link BorWin1 connecting a DFIG-based OWF in [70]. In particular, the risk of interactions between control loops of the VSC-HVDC converter and grid resonant frequencies is described as an interaction between critical resonant frequencies and control loops such as the current control loop or the PLL of the converter.

Events VSC4 [71] and VSC5 [72] also featured supersynchronous oscillations in VSC-HVDC links connecting OWFs to shore. In VSC4, both the offshore station and the WTs controls were involved in the incident, while in VSC5, the oscillations appeared at the onshore station.

Yet, not all cases of interactions involving VSC-HVDC systems were related to the connection of OWFs. In event VSC6 [73], a high-frequency oscillation was recorded and led to tripping of the INELFE France-Spain MMC-based VSC-HVDC link. The 1.7 kHz oscillatory phenomenon was described as an "interaction between the HVDC link and the surrounding AC network". Post-event analysis showed that the "control instability" depended on the AC line parameters, the SCR, and the AC grid configuration.

Similarly, in event VSC7 [74,75], 1.27 kHz oscillations were reported at the Luxi asynchronous back-to-back HVDC link in China. The back-to-back system is composed of one MMC-based VSC-HVDC link in parallel with two LCC-HVDC links. The high-frequency oscillations, termed "harmonic resonance" in [75], occurred when the LCC converters were shut down, their AC filters were disconnected, and one out of three AC lines was in service. The instability appeared to be caused by non-passivity due to the control delay and the instantaneous voltage feedforward of the AC current controller. Events VSC8 [11] and VSC9 [76] are comparable to events VSC6 and VSC7, as they featured supersynchronous oscillations in VSC-HVDC systems not connected to OWFs.

Table 6

Overview of identified mechanisms

Overview of identified inechanisms.		
CONVERTER OR CONTROL LIMITATIONS	POWER QUALITY DEGRADATION	CONTROL INTERACTIONS
(A1) limited under/over- voltage ride-through capability (A2) limited under/over- freq. ride-through capability (A3) limited over- current ride-through capability (B2) limited/inadequate frequency support frequency support	(D) nonlinear converter or control behavior (E) amplification of converters emissions by passive grid components	 (F) electrical interactions among converter controls and/or with passive grid components (G) electrical interactions between converter-controlled rotating machines and passive grid components (H) electromechanical interactions between converter controls and rotating machines
fundamental frequency phenomena	non-fundamental	frequency phenomena

While all previous events were characterized by either subsynchronous or supersynchronous oscillations, a phenomenon called "suband supersynchronous interaction" was reported in event VSC10 [77]. These oscillations were frequently observed in a system with three VSC-based STATCOMs connected between an LCC-HVDC converter and SCTLs, as a result of dynamic interactions between the STATCOMs and the weak AC grid. The oscillations appeared even when the series capacitors were bypassed, but ceased as soon as the STATCOMs were (partially) disconnected.

6.2. Interactions among VSC-HVDC converters and with the DC grid

Although the above-described VSC-HVDC/STATCOM events are specifically related to interactions with the AC grid, interactions with the DC grid have been reported as well. For instance, event VSC11 [78, 79] covers a 550 Hz oscillation on the DC side of the Xiamen project, a bipolar MMC-based VSC-HVDC link with a cable length of 10 km. Post-event analysis in [79] showed that the oscillations were caused by an interaction between the converter controls and the DC resonances related to the cable impedance and DC inductors. The oscillation of DC voltage and current was triggered by a control mode switch. Lastly, event VSC12 [80,81] refers to DC-side current oscillations, which were also observed at the aforementioned Xiamen VSC-HVDC link. The frequency of the oscillations (23.6 Hz and 25.2 Hz) depended on the transmitted power. To explain the event, [80] refers to [82], where it is pointed out that when the VSC station that controls the DC voltage injects active power into the DC line, the converter presents a negative resistance, and the risk of system oscillation is increased.

In summary, a single type of event has been observed in VSC-HVDC/STATCOM systems:

 Sub- and/or supersynchronous oscillations resulting from interactions between the controls of VSC-HVDC converters (or VSC-based STATCOMs) and the AC or DC grid impedance.

7. Identification of underlying mechanisms

The previous sections have provided an overview of problematic real-life events in which PE converters were directly or indirectly involved. In this section, patterns are identified among these events in order to pinpoint their fundamental underlying mechanisms. Precisely, a *mechanism* is defined in this paper as the intermediate process between the initial trigger, e.g. a fault, and the eventual outcome of the event, e.g. supersynchronous oscillations. Proceeding by elimination, a total of 11 underlying mechanisms are established in this section. The mechanisms are sorted into three main types: (1) converter or control limitations, (2) power quality degradation and (3) control interaction mechanisms. All mechanisms are summarized in Table 6, where they are displayed according to type and frequency.

In the following, the term *electrical* always refers to an electromagnetic phenomenon. Additionally, the expression *passive grid components* refers to, for instance, filters and compensation devices, but may also refer to larger systems such as a WF collection system.

7.1. Converter or control limitations

This subsection identifies underlying mechanisms related to converter or control limitations.

7.1.1. Mechanism A1

A common feature of events WF10 and PV1-PV3 is that converters were tripped after the voltage amplitude at fundamental frequency became too high or too low with respect to the rated voltage amplitude, or when such voltage deviations occurred too many times within a given period of time. In these events, the protection control of converters generally operated as expected, but the fact that the predefined limits had been reached caused the converters to trip or cease current injection, which in turn negatively impacted the network.

In this paper, this mechanism is referred to as *limited under/over-voltage ride-through capability*.

7.1.2. Mechanism A2

A common feature of events PV1 and PV2 is that converters were tripped after the fundamental frequency of the grid voltage was identified to be too low or too high with respect to the rated fundamental frequency. In these events, the protection control of converters generally operated as expected, but the fact that the predefined limits had been reached led to converters tripping or ceasing current injection, which in turn negatively impacted the network.

In this paper, this mechanism is referred to as *limited under/over-frequency ride-through capability*. It mirrors the mechanism of limited under/over-voltage ride-through capability, but is concerned specifically with deviations in terms of frequency instead of voltage amplitude.

7.1.3. Mechanism A3

A common feature of events WF8 and PV1-PV3 is that converters were tripped after the current amplitude at fundamental frequency (50/60 Hz for AC systems, 0 Hz for DC systems [9]) became too high with respect to the rated current amplitude. In these events, the protection control of converters generally operated as expected, but the fact that the predefined limits had been reached led to converters tripping or ceasing current injection, which in turn negatively impacted the network.

In this paper, this mechanism is referred to as *limited over-current ride-through capability*. It also mirrors the mechanism of limited under/over-voltage ride-through capability, but is concerned specifically with current amplitude instead of voltage amplitude.

7.1.4. Mechanism B1

A particular feature of event WF9 is that a converter-based plant was unable to provide adequate or sufficient voltage support in the form of reactive power generation or consumption to avoid a voltage collapse.

In this paper, this mechanism is referred to as *limited or inade-quate voltage support capability*, which describes the fact that converters have a limited short-circuit power capability, and/or inadequate voltage support control algorithms.

It is worthwhile noting that cases of classical voltage instability (not listed in this paper) can also be considered as indicators of limited or inadequate voltage support capability from converters, more specifically when converter-based power plants were operating within the grid before it collapsed, but were unable to contribute to voltage containment when this was necessary.

7.1.5. Mechanism B2

A common feature of events WF8 and WF10 is that the tripping of converter-based power plants, or a reduction of their active power output, directly or indirectly led to a frequency collapse. While it is apparent that the converter tripping or active power reduction prior to the frequency collapse was generally caused by another mechanism (such as a limited under/over-voltage ride-through capability), these events hint towards a mechanism in which converter-based power plants have not been able to provide a sufficient amount of active power in order to maintain the fundamental grid frequency within acceptable limits.

In this paper, this mechanism is referred to as *limited or inadequate frequency support capability*, which describes the situation in which converters have limited energy reserves or inadequate frequency support control algorithms. It mirrors the mechanism of limited or inadequate voltage support capability, but is concerned specifically with variations of the fundamental frequency instead of the voltage amplitude at the fundamental frequency.

7.1.6. Mechanism C

A common feature of events PV1 and PV2 is that grid disturbances led to an incorrect operation of synchronization controls of converters, such as PLLs misreading the fundamental grid frequency and causing converters to trip

In this paper, this mechanism is referred to as *limited synchroniza*tion capability. Unlike the mechanisms of limited under/over voltage and frequency ride-through capabilities, the incorrect PLL response is not an expected control behavior in this mechanism.

Up to this point, identified mechanisms A1-A3, B1 and B2 are related to fundamental frequency phenomena, while mechanism C is also related to non-fundamental frequency phenomena. All mechanisms of types A, B and C correspond to intrinsic limitations of PE converters, i.e. limitations that are a consequence of the fundamental characteristics or principles of operation of PE converters (for instance, the use of semiconductor switches or the lack of inherent energy storage), or extrinsic limitations, i.e. limitations that can theoretically be resolved by means of improved controlled algorithms.

7.2. Power quality degradation

In this subsection, underlying mechanisms related to power quality degradation are identified.

7.2.1. Mechanism D

A common feature of events WF5, PV4, RW4-RW9 and LCC9 is that converters emitted non-fundamental frequency components, either harmonics or inter-harmonics. Based on the events, three mechanisms are identified in which converters are susceptible to generating undesired non-fundamental frequency components:

- Semiconductor switching: in events PV4, RW4, RW5, RW7-RW9 and LCC9, harmonics of the switching frequency were generated as a consequence of the switched behavior of the converters.
- Frequency couplings caused by modulation issues: in event RW6, the improper interleaving of PWM carrier waves caused undesired components to appear at 2f_s ± f₁ with f₁ the fundamental grid frequency and f_s the switching frequency.
- Frequency couplings caused by control nonlinearities [83]: in event WF5, undesired frequency components were propagated to the network when the PLLs and Park's transformation were disturbed by SSOs. Although this particular example involves the PLL, it is not a case of limited synchronization capability, but illustrates the response of a control nonlinearity to an external perturbation.

The common denominator of the three above-mentioned mechanisms lies in the nonlinear behavior of the converter itself, or of its control functions. In this paper, these mechanisms are collectively referred to as *nonlinear converter or control behavior*.

It is noted that this mechanism should be distinguished from mechanisms A, B and C, as they reflect different concepts. Mechanisms A to C refer to the inability of converters to operate properly outside predefined ranges of values, while mechanism D is concerned with the impact of nonlinearity.

It is also noted that network nonlinearities, such as transformer saturation, also cause harmonics of the fundamental frequency to appear. However, they are not covered by this mechanism as they are not specifically related to PE converter operation.

7.2.2. Mechanism E

A common feature of events PV4, RW4-RW9 and LCC9 is that non-fundamental frequency components emitted by converters were amplified by natural grid resonances. It is emphasized, however, that the grid resonance alone was responsible for the amplification effect, while controls of converters did not contribute to the amplification effect in these particular events.

In this paper, this mechanism is referred to as *amplification of converters emissions at non-fundamental frequencies by passive grid components*. This mechanism corresponds to the traditional resonance phenomenon, where natural grid resonances amplify non-fundamental frequency components in a steady-state manner. It is worthwhile noting that the passive components of converters also have an impact on the grid impedance and, therefore, on the existence of natural grid resonances.

Both mechanisms D and E are examples of ways in which converters may contribute to a degradation of power quality. While closely related, mechanisms D and E are distinct from each other: the first one describes how nonlinear converter or control behavior leads to the generation of undesired frequency components, while mechanism E describes the amplification of these components.

7.3. Control interactions

In this subsection, underlying mechanisms related to control interactions are identified.

7.3.1. Mechanism F

A common feature of events WF5-WF8, PV5-PV10, RW10-RW19, LCC4-LCC8 and VSC1-VSC12 is that an oscillatory phenomenon resulted as a consequence of a control interaction between converters and the grid, or among converters via the grid.

In this paper, this mechanism is referred to as an electrical interaction among converter controls and/or with passive grid components.

Unlike cases of classical resonance where undesired components coincide with a natural frequency of the network, converter controls play a role in amplifying frequency components in this mechanism. For this reason, cases of "harmonic instabilities" reported from LCC-HVDC systems also fall within this category.

Table 7 Summary of events per mechanism

ID	Mechanism	Events
A1	Limited under/over-voltage ride-through capability	WF10, PV1-PV3
A2	Limited under/over-frequency ride-through capability	PV1, PV2
A3	Limited over-current ride-through capability	WF8, PV1-PV3
B1	Limited/inadequate voltage support	WF9
B2	Limited/inadequate frequency support	WF8, WF10
C	Limited synchronization capability	PV1, PV2
D	Emission of non-fundamental frequency components by converters	WF5, PV4, RW4-RW9, LCC9
E	Amplification of converters emissions by passive grid components	PV4, RW4-RW9, LCC9
F	Electrical interactions among converter controls and/or with passive grid	WF5-WF8, PV5-PV10, RW10-RW19,
	components	LCC4-LCC8, VSC1-VSC12
G	Electrical interactions between converter-controlled rotating machines and passive	WF1-WF4
	grid components	
Н	Electromechanical interactions between converter controls and rotating machines	WF5, RW1-RW3, LCC1-LCC3

7.3.2. Mechanism G

A common feature of events WF1-WF4 is that the rotor-side converter of induction machines, and more specifically the controls of such converter, led to an aggravation of the negative-resistance effect of these machines at subsynchronous frequencies. Fundamentally, this is an accentuated form of the IGE, enabling interaction with passive grid components such as SCTLs.

While this phenomenon is a form of electrical resonance, the involvement of converter controls implies that it should be distinguished from the traditional amplification of frequency components by natural resonances.

Consequently, in this paper, this mechanism is referred to as an electrical interaction between converter-controlled rotating machines and passive grid components, where the rotating machines can be seen as a medium enabling interactions between converter controls and passive grid components. It is worthwhile noting that, despite the involvement of rotating machines, no mechanical oscillatory modes are involved in this mechanism a priori.

7.3.3. Mechanism H

A common feature of events WF5, RW1-RW3 and LCC1-LCC3 is that mechanical oscillatory modes of rotating masses (such as SGs, rotary frequency converters, ...) were excited and the resulting oscillations were sustained or amplified as a consequence of an adverse interaction with the controls of converters.

In this paper, this mechanism is referred to as an *electromechanical interaction between converter controls and rotating machines*. It is noted that the mechanical mode can be torsional or non-torsional. Additionally, the frequency of the resulting oscillations is generally low_i , which is explained by the torsional or mechanical characteristics of the involved rotating masses.

Mechanisms F, G and H are examples of interactions between controls of converters on one side, and passive components, rotating machines or other converters on the other side.

8. Discussion

The observation of common patterns among real-life events has led to the identification of underlying mechanisms in which PE converters play a direct or indirect role. Four aspects are further discussed in this section: (1) the identified mechanisms, (2) the initial triggers of the phenomena, (3) the modeling requirements for the study of the events, and (4) the original terminology used in the references reporting the events. For clarity, the mechanisms identified in Section 7 and the corresponding events are summarized in Table 7.

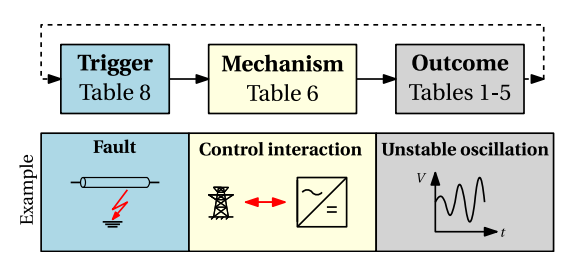


Fig. 2. Illustration of the relationship between triggers, mechanisms and outcomes. The provided example corresponds to the first set of trigger-mechanism-outcome of event WF8.

8.1. Discussion of identified mechanisms

It is apparent from Table 7 that multiple mechanisms were involved in some of the events. More precisely, several mechanisms can happen simultaneously as a response to the same trigger, or consecutively when the outcome of one mechanism acts as a trigger to one or several other mechanisms, as depicted in Fig. 2. For example, in event WF5, the interaction between the controls of the WTs converters and the weak grid caused SSOs. Next, these oscillations triggered torsional modes of turbine-generator shafts of thermal power plants. In that regard, the identified mechanisms ought not to be seen as mutually-exclusive categories. It is also expected that more converter-related events have involved a combination of mechanisms than what has been reported in the literature so far

Furthermore, Table 7 shows that the same mechanisms can occur in different types of systems. The most prominent example is that of mechanism F, which has been observed in all five types of systems considered in this paper. On the other hand, mechanism G has exclusively been observed in WFs involving DFIG-based wind turbines. Similarly, mechanism H necessarily involves grid-connected rotating machines. Nevertheless, this mechanism can be triggered by converters from different types of systems in the vicinity of the rotating machines.

Within the category of converter or control limitations mechanisms, issues related to limited synchronization capabilities (mechanism C) have only been observed in PV systems. However, incorrect determination of the fundamental frequency can technically happen with all types of PLL-based converters. Consequently, it is expected that unreported events from other types of systems have also involved this mechanism. A similar observation holds for mechanisms A2, B1 and B2, which also have been reported in only one type of system, respectively.

Within the category of power quality degradation mechanisms, all converters emit non-fundamental frequency components due to switching and comprise passive components that influence the grid impedance

 $^{^{1}}$ Among the reported events involving this mechanism, the highest mechanical oscillation frequency was 30.6 Hz, in event WF5.

(and therefore the existence of natural grid resonances). Consequently, all types of systems are potentially subject to mechanisms D and E, even if no events involving these mechanisms were reported for VSC-HVDC systems.

While the identified mechanisms exclusively rely on the overview of real-life events, other theoretically relevant mechanisms have not been included, lacking evidence or clarity from the literature. For instance, a common feature of (at least) events WF7, WF8, PV1, PV2, PV4, RW18 and VSC6 is that non-fundamental grid disturbances led to the tripping of the converters. Yet, in most events, the non-fundamental frequency oscillations have caused the converters to trip by setting off fundamental-frequency protection features such as over-voltage, over-current or under-frequency protection. Consequently, these events have been considered to involve mechanisms of type A, although non-fundamental disturbances were involved. For this reason, no mechanism describing a limited non-fundamental disturbance ride-through capability was included in Table 6.

It is also expected that more events featuring non-fundamental disturbances have caused converters to trip. However, the available references do not always specify whether the sub- or supersynchronous oscillations actually caused the converters to trip. Overall, the boundary between fundamental and non-fundamental frequency phenomena remains unclear. Newly reported real-life events and further research may support an evolution of the number and definition of identified mechanisms. In particular, not only the inability of converters to remain connected during a non-fundamental disturbance, but also the inability to perform active filtering to contribute to eliminating such disturbances could be seen as a control limitation in the future.

While this paper focuses exclusively on converter-related issues, parallels can be established between the identified mechanisms and the traditional stability concepts defined for systems dominated by the dynamics of SGs [7]. In particular, mechanisms B1 and B2 (limited/inadequate voltage and frequency support) are closely related to classical voltage and frequency instability concepts and express the way in which PE converters can contribute to classical forms of instabilities. Additional similarities can be seen between mechanism C (limited synchronization capability) and classical rotor angle instability, although the definition of mechanism C concerns the PE converters themselves, and not their possible involvement in SG rotor angle instabilities. Lastly, mechanisms G (electrical interactions between converter-controlled rotating machines and passive grid components) and H (electromechanical interactions between converter controls and rotating machines), have the particularity of occurring in systems where both PE converters and rotating machine dynamics are jointly relevant.

8.2. Identification of triggers

In addition to the identification of underlying mechanisms, the overview of real-life events enables establishing a list of disturbances that are responsible for triggering the mechanisms. These disturbances are referred to as triggers and are noted T1 to T7 according to Table 8:

- Events with T1 triggers were initiated by faults.
- Events with T2 triggers were initiated by switching lines or capacitor banks, or other grid topology changes.
- Events with T3 triggers were initiated by variations in power generation or power consumption, sometimes leading to voltage fluctuations. Specifically in event WF9, fluctuations of wind power generation led to large voltage variations. This class of triggers also covers the loss of load or generation.
- Events with T4 triggers were initiated by a change of control mode.

- Events with T5 triggers were initiated by non-fundamental frequency components. In some events, the non-fundamental frequency components were the outcome of another mechanism. For instance, in event WF5, an electrical interaction between converter controls and passive grid components (mechanism F) led to SSOs, which triggered the emission of additional non-fundamental frequency oscillations due to control nonlinearities (mechanism D), in turn setting off electromechanical interactions between converter controls and rotating machines (mechanism H). In other events, the switching harmonics resulting from the nonlinear (switched) behavior of PE converters (mechanism D) were amplified by natural resonances of the network (mechanism F)
- Events with T6 triggers were initiated by a normal converter operation at low load, in a weak grid configuration or in the presence of a natural grid resonance.
- For the remaining events, no initial trigger was identified, either because of limited measurement data at the time of the event, or limited information provided in the original references. Unknown triggers are referred to as T7 triggers.

To summarize, triggers can take the five following forms:

- Changes of power or voltage at fundamental frequency, which translates into amplitude and/or phase angle variations of voltages and currents at fundamental frequency;
- Changes of grid impedance as seen by the converters. This class of triggers also comprises the (dis)connection of passive appliances such as filter banks and SCTLs, which have an impact on the impedance of the grid;
- · Changes of converter control mode;
- Non-zero non-fundamental frequency components in voltages or currents, for instance as a consequence of a fault;
- A normal converter operation at low load, in a weak grid and/or in the presence of a natural grid resonance.

The following section discusses modeling requirements based on the identified mechanisms and triggers.

8.3. Discussion of modeling requirements

In the literature, power system instabilities are typically categorized according to the size of the trigger, or initial disturbance [7], as this information indicates modeling requirements and analysis techniques that are applicable to study the event they initiate. As a general rule, events following a small disturbance can be studied in a linearized mathematical framework, while nonlinear aspects must be retained when studying events following large disturbances.

On the one hand, triggers such as faults are commonly considered as large disturbances, since they generally cause significant variations with respect to rated values of electrical quantities. The switching and energizing of lines, resulting in a new grid configuration characterized by a different impedance, are also considered as large disturbances.

On the other hand, triggers such as power variations can be considered as either small or large disturbances, depending on amplitude and rate of change: slow variations of aggregated demand can generally be considered as small disturbances. In contrast, the loss of a generation unit will be considered as a large disturbance. Similarly, control mode changes can also be seen as small or large disturbances.

Just as their triggers, the mechanisms in Table 6 can be related to different modeling requirements and analysis techniques. A distinction is also made between linear and nonlinear frameworks.

In the category of converter or control limitations, mechanisms A, B and C are generally studied within a nonlinear framework, as the mechanisms involve nonlinear operations such as control mode switch, saturation, and other nonlinear functions.

Table 8

Summ	ary of events per trigger.	
ID	Trigger	Events
T1	Faults	WF2, WF6, WF8, WF10, PV1-PV3, PV5 and VSC4
T2	Switching of lines or capacitor banks	WF1, WF3, WF7, PV6, LCC1, VSC3 and VSC5-VSC7
Т3	Power variations/fluctuations	WF4, WF8-10, RW1, RW2, LCC2, LCC3, VSC1, VSC2, VSC9 and VSC12
T4	Change of control mode	LCC3, VSC8 and VSC11
T5	Non-fundamental frequency components	WF5, WF8, WF10, PV4, RW4, RW5-RW7 and LCC9
Т6	Normal operation with low load, weak grid or natural grid resonance	PV7, RW9-RW19, LCC4, LCC5, LCC7, LCC8 and VSC10
T7	Not given or known	WF5, PV8-PV10, RW3, RW8 and LCC6

In the category of power quality degradation, mechanism D is intrinsically related to the nonlinear characteristics of the converter (semiconductor switching) and its controller (nonlinear functions and saturation). On the other hand, mechanism E is more traditionally studied in a linearized framework with small-signal analysis of grid resonances.

In the category of control interactions, linearized models and smallsignal analysis techniques are typically used to assess the interactions between converter control and grid resonances or rotating machines.

The above considerations can be illustrated based on the example of event WF8, which is broken down as follows:

- First, a fault (Trigger T1) initiated an interaction between the WF controls and a poorly-damped natural grid resonance (Mechanism F), which resulted in growing voltage oscillations (outcome). These steps are illustrated in Fig. 2.
- Next, the oscillations (Trigger T5) set off the over-current protection control (Mechanism A3), causing the converters to trip (outcome).
- Finally, the reduced power generation (Trigger T3) associated with limited frequency-support capabilities (Mechanism B2) resulted in a frequency collapse (outcome).

Although the fault at the origin of the event can be considered as large perturbation, the interaction between converter controllers and grid resonances is typically analyzed in a linearized framework. Next, the activation of protection features and the tripping of converters are nonlinear operations. Hence, the nonlinear dynamics related to the second part of the event may impose other modeling requirements, which complicates the overall analysis of the incident. The third part of the event is related to frequency stability and is triggered by a large disturbance.

The example illustrates that not only the type of trigger, but also the mechanisms involved have an influence on modeling requirements for the study of problematic events.

8.4. Discussion of terminology

According to the terminology used in the references to describe the different real-life events (summarized in Tables 1–5), it appears that the terminology is often diverse and system-specific, even when it concerns the same underlying mechanism. For example, electrical interactions among converter controls and/or with passive grid components (mechanism F) are frequently referred to as subsynchronous oscillation or subsynchronous control interaction in WF systems. However, the same mechanism is called low-frequency interaction or depot problem in RW systems, and harmonic instability in LCC-HVDC systems. In addition, the expressions subsynchronous oscillations and harmonic instability are used multiple times in PV and VSC-HVDC systems. This example also indicates that terminology generally relies on the frequency of oscillations involved in the events, describing whether they appear above or below the fundamental frequency, and whether they occur at multiples of the fundamental frequency.

To gain further insights, Fig. 3 provides an overview of the real-life events per mechanism as a function of the observed oscillation frequencies.2 The figure shows that mechanism F actually leads to a large variety of oscillation frequencies. In this case, the use of terminology related to a specific frequency range could lead to the misconception that the corresponding events are a consequence of different mechanisms. On the other hand, applying frequency-based terminology can be beneficial in some cases in order to provide additional information on the characteristics of the underlying mechanisms: for mechanisms G and H, which both involve rotating machines, all the observed oscillations occurred in the subsynchronous frequency range, as shown in Fig. 3. This results from the oscillatory and torsional mode characteristics of rotating machines and from the basic principles of IGE. Additionally, frequency-based terminology is not generally applicable to all types of mechanisms, as is the case for converter or control limitations (mechanism A, B and C), which do not necessarily feature oscillatory

Finally, Table 5 shows that expressions such as harmonic interaction, harmonic instability, harmonic resonance and resonant instability have been used interchangeably in the context of VSC-HVDC events when referring to supersynchronous phenomena, even though these expressions are not equivalent. For instance, an instability can be an outcome of an interaction, whereas an interaction does not necessarily lead to instability. Moreover, a resonance is commonly considered a steady-state phenomenon causing a constant amplification of an oscillation, while an instability is a dynamic phenomenon that typically involves growing oscillations. Lastly, in the aforementioned expressions, the term harmonic normally indicates an oscillation at a multiple of the fundamental frequency, which was, however, not the case for events VSC3 and VSC7

The above discussion suggests that standardized definitions applicable across multiple systems are necessary to harmonize terminology concerning problematic converter-related phenomena.

² For clarity, the definitions of the mechanisms are repeated here:

ID	Mechanism
A1	Limited under/over-voltage ride-through capability
A2	Limited under/over-frequency ride-through capability
A3	Limited over-current ride-through capability
B1	Limited/inadequate voltage support
B2	Limited/inadequate frequency support
С	Limited synchronization capability
D	Emission of non-fundamental frequency components by converters
E	Amplification of converters emissions by passive grid components
F	Electrical interactions among converter controls and/or with
	passive grid components
G	Electrical interactions between converter-controlled rotating
	machines and passive grid components
Н	Electromechanical interactions between converter controls and
	rotating machines

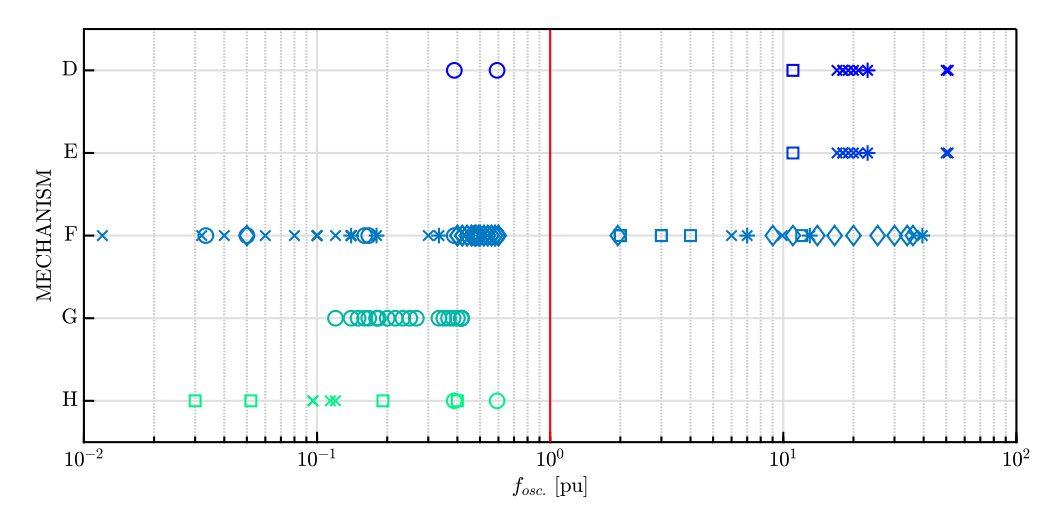


Fig. 3. Overview of oscillation frequencies observed for mechanisms D to H. Mechanisms A to C are not included in the figure as no oscillation frequencies could be associated based on the real-life events. A link to the system type is provided by the marker symbols: WF (\bigcirc) , PV (*), RW (\times) , LCC-HVDC: (\bigcirc) and VSC-HVDC (\bigcirc) .

Table 9

Events, references and mechanisms

ID	Location	Year	References	Mechanism(s)	ID	Location	Year	References	Mechanism(s)
WF1	USA	2007	[16,17]	G	RW11	DEU	2006	[43,49]	F
WF2	USA	2009	[18-22]	G	RW12	FRA	2008	[44]	F
WF3	USA	2017	[21,23]	G	RW13	CHN	2008	[10,50]	F
WF4	CHN	2012-13	[24,25]	G	RW14	CHN	2010	[10,50]	F
WF5	CHN	2014-15	[26-28]	D, F, H	RW15	CHN	2010	[10,50,51]	F
WF6	USA	2013&15	[21]	F	RW16	CHN	2011	[10,50,51]	F
WF7	USA	~2011	[29]	F	RW17	CHN	2015	[10,50,51]	F
WF8	GBR	2019	[30]	A3, B2, F	RW18	CHE	1995	[52,53]	F
WF9	USA	2010-11	[4]	B1	RW19	CHN	2015	[10]	F
WF10	AUS	2016	[31]	A1, B2	LCC1	USA	1977	[56]	H
PV1	USA	2016	[33]	A1, A2, A3, C	LCC2	CHN	2011	[57-59]	H
PV2	USA	2017	[34]	A1, A2, A3, C	LCC3	CHN	2014	[60]	H
PV3	USA	2018	[35]	A1, A3	LCC4	GBR, ITA, NZL	~1966	[61,62]	F
PV4	NLD	2004	[36]	D, E	LCC5	GBR	1977	[63]	F
PV5	AUS	2019	[37]	F	LCC6	USA	1987	[63]	F
PV6	CAN	2018	[38]	F	LCC7	CAN	1992	[64]	F
PV7	DEU	2014	[39]	F	LCC8	RUS-FIN	1994	[65]	F
PV8	CAN	2018	[38]	F	LCC9	DNK	2017	[66]	D, E
PV9	CAN	2018	[38]	F	VSC1	CHN	2011	[11]	F
PV10	CAN	2018	[38]	F	VSC2	CHN	2014	[11]	F
RW1	DEU	1991	[43]	H	VSC3	DEU	2013	[69,70]	F
RW2	NOR	1996	[43]	Н	VSC4	DEU	2016	[71]	F
RW3	USA	2006	[43]	Н	VSC5	DEU	2014-17	[72]	F
RW4	FRA	1990s	[44,45]	D, E	VSC6	FRA-ESP	2015	[73]	F
RW6	FRA	2006	[44]	D, E	VSC7	CHN	2016	[74,75]	F
RW7	ITA	2011	[47]	D, E	VSC8	CHN	2016	[11]	F
RW5	CHN	2011	[46]	D, E	VSC9	CHN	2018-19	[76]	F
RW8	CHN	2008	[10]	D, E	VSC10	CHN	2018	[77]	F
RW9	CHN	2011	[10]	D, E	VSC11	CHN	2015	[78,79]	F
RW10	CHE	2004	[43,48]	F	VSC12	CHN	2015	[80,81]	F

9. Conclusion

This paper demonstrated the value of a comprehensive cross-system overview to support the construction of more-encompassing classifications of issues related to power system stability. For the first time, by drawing analogies between problematic converter-related events that have been observed in different applications ranging from electrical railway systems to wind farms, three main types of underlying mechanisms were identified. Firstly, converter or control limitation

mechanisms refer to intrinsic limitations of PE converters, or to extrinsic limitations that can theoretically be resolved by means of improved control algorithms. Secondly, power quality degradation mechanisms correspond to the generation and amplification of undesired frequency components in steady-state. Lastly, control interaction mechanisms refer to interactions between controls of converters on one side, and passive components, rotating machines or other converters on the other side.

The overview of events in this study showed that (i) multiple mechanisms were involved in some of the events, (ii) the same mechanisms

can occur in different types of systems, and (iii) outcomes of mechanisms may trigger other mechanisms. By associating the mechanisms with either fundamental or non-fundamental frequency phenomena, it appeared that the boundary between the two types of phenomena remains unclear, and an evolution of the number and definition of identified mechanisms may be supported by new reported real-life events and further research.

The decomposition of events in a series of triggers and mechanisms showed that both aspects impact the choice of mathematical modeling requirements. Lastly, the study illustrated that the employed terminology is often diverse and system-specific, relying mostly on frequency-dependent considerations. Further research and standardization are regarded as necessary to define clear and uniform terminology in the field of problematic converter-related phenomena.

Declaration of competing interest

The authors declare that they have no known competing financial interests or personal relationships that could have appeared to influence the work reported in this paper.

Data availability

No data was used for the research described in the article.

Acknowledgments

The authors would like to thank Dr. ir. Adedotun Agbemuko and Dr. ir. Willem Leterme from KU Leuven/Energyville for their insightful comments. The work of P. De Rua has received funding from the Research Foundation–Flanders (FWO), Belgium [grant number 11E8720N]. The work of T. Roose has received funding from the Research Foundation–Flanders (FWO), Belgium and VITO [grant number 1182521N]. The work of Ö. C. Sakinci has received funding from the Neptune project, supported by the Energy Transition Fund, FOD Economy, Belgium. The work of N. de Morais Dias Campos has received funding from the European Union's Horizon 2020 research and innovation program under the Marie Sklodowska-Curie Grant agreement [grant number 765585].

References

- ENTSO-E. Completing the map Power system needs in 2030 and 2040. Tech. rep., 2020.
- [2] ENTSO-E. PowerFacts: Europe 2019. Tech. rep., ENTSO-E; 2019, p. 1–49.
- [3] ENTSO-E. Interactions between HVDC systems and other connections: ENTSO-E guidance document for national implementation for network codes on grid connection. Tech. rep., ENTSO-E; 2018, p. 1–13.
- [4] NERC. Integrating inverter-based resources into low short circuit strength systems. Tech. rep., 2017.
- [5] Eftekharnejad S, Vittal V, Heydt GT, Keel B, Loehr J. Small signal stability assessment of power systems with increased penetration of photovoltaic generation: A case study. IEEE Trans Sustain Energy 2013;4(4):960–7.
- [6] IEEE Subsynchronous Resonance Working Group. Terms, definitions and symbols for subsynchronous oscillations. IEEE Trans Power Appar Syst 1985;PAS-104(6):1326-34.
- [7] Kundur P, Paserba J, Ajjarapu V, Andersson G, Bose A, Canizares C, et al. Definition and classification of power system stability. IEEE Trans Power Syst 2004;19(2):1387-401.
- [8] IEEE PES Power System Dynamic Performance Committee. Stability definitions and characterization of dynamic behavior in systems with high penetration of power electronic interfaced technologies. Tech. rep., IEEE; 2020.
- [9] Shair J, Li H, Hu J, Xie X. Power system stability issues, classifications and research prospects in the context of high-penetration of renewables and power electronics. Renew Sustain Energy Rev 2021;145:111111.
- [10] Hu H, Tao H, Blaabjerg F, Wang X, He Z, Gao S. Train-network interactions and stability evaluation in high-speed railways – Part I: Phenomena and modeling. IEEE Trans Power Electron 2018;33(6):4627–42.
- [11] Yin C, Xie X, Xu S, Zou C. Review of oscillations in VSC-HVDC systems caused by control interactions. J Eng 2019;2019(16):1204–7.

- [12] Virulkar VB, Gotmare GV. Sub-synchronous resonance in series compensated wind farm: A review. Renew Sustain Energy Rev 2016;55:1010-29.
- [13] Shair J, Xie X, Wang L, Liu W, He J, Liu H. Overview of emerging subsynchronous oscillations in practical wind power systems. Renew Sustain Energ Rev 2019;99:159–68.
- [14] Shah R, Mithulananthan N, Bansal R, Ramachandaramurthy V. A review of key power system stability challenges for large-scale pv integration. Renew Sustain Energy Rev 2015;41:1423–36.
- [15] Karimi M, Mokhlis H, Naidu K, Uddin S, Bakar A. Photovoltaic penetration issues and impacts in distribution network – a review. Renew Sustain Energy Rev 2016;53:594-605.
- [16] Mulawarman A, Mysore PG. Detection of undamped sub-synchronous oscillations of wind generators with series compensated lines. In: Proceedings of the 2011 minnesota power systems conference. Minnesota. USA: 2011.
- [17] Narendra K, Fedirchuk D, Midence R, Zhang N, Mulawarman A, Mysore P, et al. New microprocessor based relay to monitor and protect power systems against sub-harmonics. In: Proceedings of the 2011 IEEE electrical power and energy conference. 2011. p. 438–43.
- [18] Gross LC. Sub-synchronous grid conditions: New event, new problem, and new solutions. In: Proceedings of the 37th annual western protective relay conference. Sookane. Washington: 2010.
- [19] Kidd D, Hassink P. Transmission operator perspective of sub-synchronous interaction. In: Proceedings of the IEEE PES transmission and distribution conference and exposition. Orlando. USA: 2012.
- [20] Adams J, Carter C, Huang S. ERCOT experience with sub-synchronous control interaction and proposed remediation. In: Proceedings of the IEEE PES transmission and distribution conference and exposition. Orlando, USA; 2012.
- [21] Campbell Z, Andov K, Coppel S. AEP experience with sub-synchronous oscillation phenomena. In: Proceedings of the 72nd annual georgia tech protective relaying conference. Atlanta, USA; 2018.
- [22] Irwin GD, Jindal AK, Isaacs AL. Sub-synchronous control interactions between type 3 wind turbines and series compensated AC transmission systems. In: Proceedings of the 2011 IEEE PES general meeting. Detroit, USA; 2011.
- [23] Li Y, Fan L, Miao Z. Replicating real-world wind farm SSR events. IEEE Trans Power Deliv 2020;35(1):339–48.
- [24] Wang L, Xie X, Jiang Q, Liu H, Li Y, Liu H. Investigation of SSR in practical DFIG-based wind farms connected to a series-comp. Power system. IEEE Trans Power Syst 2015;30(5):2772-9.
- [25] Xie X, Zhang X, Liu H, Liu H, Li Y, Zhang C. Characteristic analysis of SSR in practical wind farms connected to series-compensated transmissions. IEEE Trans Energy Conv 2017;32(3):1117–26.
- [26] Bi T, Li J, Zhang P, Mitchell-Colgan E, Xiao S. Study on response characteristics of grid-side converter controller of PMSG to sub-synchronous frequency. IET Renew Power Gener 2017;11(7):966–72.
- [27] Xu Y, Cao Y. Sub-synchronous oscillation in PMSGs based wind farms caused by amplification effect of GSC controller and PLL. IET Renew Power Gener 2018;12(7):844–50.
- [28] Liu H, Xie X, He J, Xu T, Yu Z, Wang C, et al. Subsynchronous interaction between direct-drive PMSG based wind farms and weak AC networks. IEEE Trans Power Syst 2017;32(6):4708–20.
- [29] Huang S, Schmall J, Conto J, Adams J, Zhang Y, Carter C. Voltage control challenges on weak grids with high penetration of wind generation: ERCOT experience. In: Proceedings of the IEEE PES general meeting. 2012.
- [30] Ørsted. Ørsted technical report for national grid ESO on the events of 9 August 2019 (appendix of Ofgem technical report). Tech. rep., Ørsted; 2019, p. 1–9.
- [31] Australian Energy Market Operator. Black system South Australia 28 september 2016. Tech. rep., AEMO; 2017, p. 1–271.
- [32] Blaabjerg F, Yang Y, Ma K. Power electronics key technology for renewable energy systems - status and future. In: Proceedings of the 3rd international conference on electric power and energy conversion systems. 2013.
- [33] NERC. 1,200 MW fault induced solar photovoltaic resource interruption disturbance report. Tech. Rep., 2017.
- [34] NERC. 900 MW fault induced solar photovoltaic resource interruption disturbance report. Tech. Rep., 2018.
- [35] NERC. April and May 2018 fault induced solar photovoltaic resource interruption disturbances report. Tech. Rep., 2019.
- [36] Enslin JH, Heskes PJ. Harmonic interaction between a large number of distributed power inverters and the distribution network. IEEE Trans Power Electron 2004;19(6):1586–93.
- [37] Australian Energy Market Operator. Power system limitations in North Western Victoria and South Western New South Wales. Tech. Rep., AEMO; 2019, p. 1–9.
- [38] Li C. Unstable operation of photovoltaic inverter from field experiences. IEEE Trans Power Deliv 2018;33(2):1013-5.
- [39] Ruester C, Hoppert S, Blum J. Power quality and stability issues in modern distribution grids: Identification and mitigation. In: Proceedings of the 2014 CIRED workshop. Rome, Italy; 2014.
- [40] Fan L, Kavasseri R, Miao ZL, Zhu C. Modeling of DFIG-based wind farms for SSR analysis. IEEE Trans Power Deliv 2010;25(4):2073–82.
- [41] Cheng Y, Fan L, Rose J, Schmall J, Huang F, Ramamurthy JR. Wind energy systems sub-synchronous oscillations: Events and modeling. Tech. Rep., (July):2020, p. 1–155.

- [42] Masson G. Snapshot of global PV markets 2020. Report T1-37, IEA PVPS; 2020.
- [43] Danielsen S. Electric traction power system stability Low-frequency interaction between advanced rail vehicles and a rotary frequency converter (Ph.D. thesis), NTNI: 2010.
- [44] Andres Suarez Diaz J. Etude et modélisation des interactions électriques entre les engins et les installations fixes de traction électrique 25kv/50hz (Ph.D. thesis), INP Toulouse; 2014.
- [45] Frugier D, Ladoux P. Voltage disturbances on 25kV-50 Hz railway lines Modelling method and analysis. In: Proceedings of the 2010 international symposium on power electronics, electrical drives, automation and motion. 2010, p. 1080–5.
- [46] Liu J, Yang Q, Zheng TQ. Harmonic analysis of traction networks based on the CRH380 series EMUs accident. In: Proceedings of the 2012 IEEE transportation electrification conference and exposition. 2012.
- [47] Brenna M, Capasso A, Falvo M, Foiadelli F, Lamedica R, Zaninelli D. Investigation of resonance phenomena in high speed railway supply systems: Theoretical and experimental analysis. Electr Power Syst Res 2011;81(10):1915–23.
- [48] Menth S, Meyer M. Low frequency power oscillations in electric railway systems Elektrische Bahnen 2006;104(5):216–21.
- [49] Pröls M, Strobl B. Stabiltätskriterien für wechselwirkungen mit umrichteranlagen in bahnsystemen. Elektrische Bahnen 2006;104(11):542–52.
- [50] Wang H, Mingli W, Sun J. Analysis of low-frequency oscillation in electric railways based on small-signal modeling of vehicle-grid system in dq frame. IEEE Trans Power Electron 2015;30(9):5318–30.
- [51] Li J, Wu M, Liu Q. Measurement and simulation on low-frequency oscillation in the traction network of Xuzhou north railway hub. In: Proceedings of the 12th world congress on intelligent control and automation. 2016, p. 1797–802.
- [52] Meyer M. Netzstabilität in grossen bahnnetzen. Eisenbahn-Revue 1999;(7–8):312–7.
- [53] Möllerstedt E, Bernhardsson B. Out of control because of harmonics An analysis of the harmonic response of an inverter locomotive. IEEE Control Syst Mag 2000:20(4):70-81.
- [54] Danielsen S, Molinas M, Toftevaag T, Fosso OB. Constant power load characteristic's influence on the low-frequency interaction between advanced electrical rail vehicle and railway traction power supply with rotary converters. Electromotion 2010;17(1):61–9.
- [55] Cespedes M, Xing L, Sun J. Constant-power load system stabilization by passive damping. IEEE Trans Power Electron 2011;26(7):1832–6.
- [56] Bahrman M, Larsen EV, Piwko RJ, Patel HS. Experience with HVDC turbine-generator torsional interaction at Square Butte. IEEE Trans Power Appar Syst 1980;PAS-99(3):966-75.
- [57] Luo C, Xiao X, Lu J, Zhang J, Yuan C. Analysis and mitigation countermeasures of a new SSO phenomenon. In: Proceedings of the 1st international future energy electronics conference. 2013, p. 553–7.
- [58] Wenhui Q, Jianguo J, Qian Z, Yu Z. Subsynchronous oscillation and its practical mitigation project at the Hulun Buir power plant. IET Gener Transm Distrib 2016;10(4):949–54.
- [59] Xiao X, Luo C, Zhang J, Yang W, Wu Y. Analysis of frequently over-threshold subsynchronous oscillation and its suppression by subsynchronous oscillation dynamic suppressor. IET Gener Transm Distrib 2016;10(9):2127–37.
- [60] Qu W, Jiang J. SSTI and its mitigation in wind farms connected with an HVDC line. Proc Comput Sci 2017;111:399–405.
- [61] Ainsworth JD. Harmonic instability between controlled static convertors and a.c. networks. Proc Inst Electr Eng 1967;114(7):949–57.
- [62] Hazell PA, Flower JO. Theoretical analysis of harmonic instability in a.c.-d.c. convertors. Proc Inst Electr Eng 1970;117(9):1869–78.
- [63] Chen S. Analysis of HVDC convertor transformer core saturation instability, and design of a data acquisition system for its assessment (Ph.D. thesis), University of Canterbury; 1996.

- [64] Hammad AE. Analysis of second harmonic instability for the chateauguay HVDC/SVC scheme, IEEE Trans Power Deliv 1992;7(1):410–5.
- [65] Kazachkov Y, Boyarsky A, Kraichik Y. The third harmonic in the DC Russia-Finland interconnection. IEEE Trans. Power Deliv 1994;9(4):2009–17.
- [66] Kwon JB, Hansen CS, Flytkjaer CF. System-wide amplification of background harmonics due to the integration of high voltage power cables. In: Proceedings of the CIGRE E-session 2020. Paris. France: 2020.
- [67] Kim C-K, Sood VK, Jang G-S, Lim S-J, Lee S-J. HVDC transmission: power conversion applications in power systems. Wiley-IEEE Press; 2009.
- [68] Bahrman MP, Larsen EV, Piwko RJ, Patel HS, Hauth RL, Breuer GD. HVDC-turbine generator torsional interactions a new design consideration. In: Proceedings of the international conference on large HV electric systems. Paris, France; 1980.
- [69] Buchhagen C, Greve M, Menze A, Jung J. Harmonic stability Practical experience of a TSO. In: Proceedings of the 15th wind integration workshop, Vienna, Austria. 2016.
- [70] Buchhagen C, Rauscher C, Menze A, Jung J. BorWin1 First experiences with harmonic interactions in converter dominated grids. In: Proceedings of the 2015 international ETG congress. Bonn, Germany; 2015, p. 27–33.
- [71] Erlich I, Paz B, Zadeh MK, Vogt S, Buchhagen C, Rauscher C, et al. Overvoltage phenomena in offshore wind farms following blocking of the HVDC converter. In: Proceedings of the IEEE PES general meeting. 2016.
- [72] Koochack Zadeh M, Rendell T, Rathke C, Menze A. Operating experiences of HVDC links - Behaviour during faults and switching events. In: Proceedings of the CIGRE B4 colloquium. Winnipeg, Canada; 2017.
- [73] Saad H, Vernay Y, Dennetière S, Rault P, Clerc B. System dynamic studies of power electronics devices with real-time simulation - a TSO operational experience. In: Proceedings of the 2018 CIGRE session. Paris. France. 2018.
- [74] Zou C, Rao H, Xu S, Li Y, Li W, Chen J, et al. Analysis of resonance between a VSC-HVDC converter and the AC grid. IEEE Trans Power Electron 2018;33(12):10157–68.
- [75] Zhang Y, Hong C, Tu L, Zhou T, Yang J. Research on HF resonance mechanism and active harmonic suppression strategy of power systems with power electronics. In: Proceedings of the 2018 international conference on power system technology. 2018, p. 2350-6.
- [76] Li Y, Pang H, Kong M, Lu J, Ji K, Tang G. Compensation control and parameters design for high frequency resonance suppression of MMC-HVDC system. CSEE J Power Energy Syst 2020. Early access.
- [77] Shu D, Xie X, Rao H, Gao X, Jiang Q, Huang Y. Sub- and super-synchronous interactions between STATCOMs and weak AC/DC transmissions with series compensations. IEEE Trans Power Electron 2018;33(9):7424–37.
- [78] Guo X, Liu Z, Li Y, Lu Y. Characteristic analysis of high-frequency resonance of flexible high voltage direct current and research on its damping control strategy. Proc Chin Soc Electr Electron Eng 2020;40(1):19–40.
- [79] Ding H, Wu Y, Zhang Y, Ma Y, Kuffel R. System stability analysis of Xiamen bipolar MMC-HVDC project. In: Proceedings of the 12th IET international conference on AC and DC power transmission. Beijing, China; 2016.
- [80] Congqi Y, Xiaorong X, Hui L, Xiao W, Zhibing W, Yongning C. Analysis and control of the oscillation phenomenon in VSC-HVDC transmission system. Power Syst Technol 2018;44(4):1117–23.
- [81] Ji K, Pang H, Yang J, Tang G. DC side harmonic resonance analysis of MMC-HVDC considering wind farm integration. IEEE Trans Power Deliv 2021:36(1):254-66.
- [82] Pinares G, Bongiorno M. Modeling and analysis of VSC-based HVDC systems for DC network stability studies. 31, (2):2016, p. 848–56.
- [83] Wang X, Blaabjerg F. Harmonic stability in power electronic-based power systems: concept, modeling, and analysis. IEEE Trans Smart Grid 2019;10(3):2858– 70.

Publication IV

N. M. D. Campos, T. Sarnet, and J. Kilter, "A gramian-based tool for modeling converter-dominated power systems," in 2024 IEEE PES Innovative Smart Grid Technologies Europe (ISGT Europe), 2024, pp. 1–5

A Gramian-based modelling and stability analysis tool for converter-dominated power systems

Nathalia de Morais Dias Campos
Tanel Sarnet
Jako Kilter
Department of Electrical Power Engineering and Mechatronics
Tallinn University of Technology
Tallinn, Estonia
{nathalia.campos, tanel.sarnet, jako.kilter}@taltech.ee

Abstract-The increasing integration of renewable energy sources and high voltage direct current (HVDC) connections has led to a proliferation of power electronic devices within the grid, thereby transforming the power system dynamics. The applicability of traditional power system modeling approaches, based on the distinction between fast and slow dynamics, became limited due to the introduction of power converter dynamics. Consequently, it becomes critical to determine the minimum level of modeling details required for accurately representing these systems. The paper aims to demonstrate how a Gramianbased model reduction method can be used to develop a tool for MATLAB/Simulink that allows visualizing and identifying the model components most relevant for a given oscillation phenomenon under study. This tool is beneficial when analyzing power system oscillations where the cause is poorly understood. The proposed approach is especially relevant given the new categories of interactions introduced in converter-dominated power systems.

Index Terms—controllability and observability, Gramians, MATLAB tool, power system modelling, stability analysis

I. INTRODUCTION

Power systems have undergone changes driven by the increasing adoption of renewable energy sources, government policies incentivizing sustainable practices, and the growing interconnectivity of power grids. These developments are part of the global commitment to combat climate change and enhance the grid infrastructure. To achieve these goals, renewable energy sources are expected to supply a substantial 90% of electricity by the year 2050, with wind and photovoltaic technologies contributing up to 63% of the total electricity generation needs [1].

At the same time, power systems are witnessing increased interconnectivity caused by the expansion of cross-border transmission capacity. Europe, for example, anticipates an increase of 35 GW in cross-border transmission capacity by 2025, with a further addition of 93 GW by 2040 [2]. The HVDC technology is becoming more relevant, offering greater

Submitted to the 23rd Power Systems Computation Conference (PSCC 2024).

operational flexibility for long-distance transmission and integrating renewable energy sources compared to traditional AC transmission methods.

A common thread connecting these trends is the increase of power electronic devices within the power systems. However, incorporating these devices into stability studies poses a challenge. Despite diligent studies conducted during the planning and operation of new interconnections, the power industry has witnessed several incidents of instability in recent years.

For instance, in 2017, the Electric Reliability Council of Texas (ERCOT) observed three subsynchronous oscillation (SSO) events involving wind farms. These wind farms had undergone stability studies and were equipped with SSO damping controls, as recommended by studies. Nevertheless, these measures proved insufficient for predicting and mitigating the instability risks [3]. Similarly, in 2019, the Australian Energy Market Operator (AEMO) reported five instances of solar farms experiencing sustained voltage oscillations under credible contingencies. These incidents led to months of generation curtailment and delayed commissioning of new units, highlighting the criticality of stability assessment in an evolving grid powered by renewables [4].

These occurrences highlight the need to improve our understanding of power electronic device behavior within the broader grid context. Unpredictable interactions between power electronic devices and the surrounding power system and a limited understanding of their dynamic behavior contribute to the risks of undetected instability issues during project studies. Conventional root mean square (RMS) simulation practices increase these risks by assuming that all system signals are steady-state or near steady-state, potentially leading to incorrect stability assessments, particularly for oscillation phenomena far from the steady-state frequency.

On the contrary, Electromagnetic Transient (EMT) simulations offer the potential for highly accurate stability assessments. However, they raise an important question: to what extent should each component within a complex system be detailed in the model? High levels of detail in modeling can introduce computational complexities that are challenging to manage. Furthermore, it may require data that is often unavailable, as manufacturers may not have provided detailed EMT

models of their devices. This gap in modeling capabilities was evident in past incidents, such as the sub-synchronous oscillation incident involving wind farms in 2009, where the ERCOT lacked the necessary wind farm EMT models for thorough studies [5].

Therefore, understanding the minimum modeling details required for various stability studies becomes critical. This knowledge allows Transmission System Operators (TSOs) to demand the appropriate studies and models to ensure reliable operation of power systems.

The main contribution of this paper is demonstrating how a Gramian-based model-order reduction method can be used to create a tool to analyze the modeling of converter-dominated power systems. A practical MATLAB/Simulink tool was implemented based on the method, which enables users to identify the sources of observed oscillations. The tool provides a straightforward visualization of the power system components that contribute the most to the oscillation phenomena, thereby offering insights into which parts of the system must be modeled in detail and which ones can be simplified.

This paper is organized as follows. Section III describes the main concepts of model-order reduction and the Gramian-based method utilized. The details of the tool implementation are described in Section III. The mathematical modeling of a modified 9-bus system test case is detailed in Section IV while Section V demonstrates the application of the tool to analyze converter interactions arising in the test case system. Finally, Section VI discusses the findings and limitations of the proposed tool.

II. MODEL-ORDER REDUCTION METHOD

Model-order reduction (MOR) is used to derive simplified models that are accurate enough for given phenomena of interest. For this reason, MOR techniques are especially valuable for determining the minimum modeling details required for different system studies [6]. A reduced-order model is obtained by eliminating or simplifying parts of the system that are less relevant to the study. The accuracy of the results depends on appropriately choosing which system components are important for the study and must, therefore, be represented by detailed models.

The problem of finding a reduced-order model of a linear system represented in state space consists of identifying which states are relevant and which ones can be discarded while ensuring the results remain within an acceptable error margin.

Consider a high-dimensional system that is linear time-invariant (LTI) with n states, m inputs, and r outputs defined in state space by

$$\dot{\boldsymbol{x}}(t) = \boldsymbol{A}\boldsymbol{x}(t) + \boldsymbol{B}\boldsymbol{u}(t) \tag{1}$$

$$y(t) = Cx(t) \tag{2}$$

where $\boldsymbol{u}(t) \in \mathbb{R}^m$ is a vector of system inputs, $\boldsymbol{y}(t) \in \mathbb{R}^r$ is a vector of system outputs and $\boldsymbol{x}(t) \in \mathbb{R}^n$ are the state variables and $\boldsymbol{A} \in \mathbb{R}^{n \times n}$, $\boldsymbol{B} \in \mathbb{R}^{n \times m}$ and $\boldsymbol{C} \in \mathbb{R}^{r \times n}$ are the state-space matrices.

The controllability operator $\Psi_c: L_2(-\infty,0] \to \mathbb{C}^n$ is mathematically defined as [7]

$$\boldsymbol{u} \mapsto \int_{-\infty}^{0} e^{-\boldsymbol{A}\tau} \boldsymbol{B} u(\tau) d\tau.$$

This operator can be interpreted as a mapping between inputs in the past $(t \le 0)$ to the initial condition x_0 at t = 0. Similarly, the definition for the observability operator Ψ_o : $\mathbb{C}^n \to L_2[0,\infty)$ is given by [7]

$$x_0 \mapsto \begin{cases} Ce^{At}x_0, & \text{for } t \ge 0\\ 0, & \text{otherwise} \end{cases}$$
 (3)

It maps the initial condition x_0 to the system's output when no input is applied for t > 0.

From the definitions of the controllability and observability operators, it is possible to define Gramians. These matrices measure the controllability and observability of a state.

The controllability Gramian \mathcal{P} is associated with the minimal energy needed to drive the states from $\mathbf{0}$ to x and is specified [7] as

$$\mathcal{P} = \Psi_c \Psi_c^* = \int_{t_1}^{t_2} e^{\mathbf{A}t} \mathbf{B} \mathbf{B}^* e^{\mathbf{A}^* t} dt. \tag{4}$$

where $\Psi_c^*: L_2(-\infty,0] \to \mathbb{C}^n$ and \mathbf{A}^* denotes the complex conjugate transpose of matrix \mathbf{A} .

Similarly, the observability Gramian Q measures the maximum amount of energy obtained from the outputs due to the initial condition x_0 and is defined [7] as

$$Q = \Psi_o^* \Psi_o = \int_{t_1}^{t_2} e^{A^* t} C^* C e^{At} dt.$$
 (5)

where $\Psi_o^*: L_2[0,\infty) \to \mathbb{C}^n$.

An approach for reducing the order of a model is based on measuring the relevance of a state in the model input-output response using their relative controllability and observability [8]. These are measured using the Gramians and combined into a participation index that ranks the importance of individual states to the oscillation observed. This approach preserves the connection between the states and the physical system, unlike other methods that rely on the transformation of the coordinate system in order to evaluate which states are the most relevant [9], [10], [11].

Mathematically, the participation $p^{(k)}$ of the k-th state variable in the system input-output behavior is defined as

$$p^{(k)} = \frac{\sqrt{\mathcal{Q}^{(k,k)}\mathcal{P}^{(k,k)}}}{\sum_{i=1}^{n} \sqrt{\mathcal{Q}^{(i,i)}\mathcal{P}^{(i,i)}}},$$
 (6)

where Q and P and the observability and controllability Gramians, respectively and n is the number of state variables in the system.

Equation (6) allows ranking the importance of individual states. Because each state is associated with a physical component of the power system, the participation $p^{(k)}$ highlights

not only the most important states but also the most important components of the system. The next sections use this property to illustrate how a tool can be created to visualize the most significant components contributing to the system dynamics.

III. TOOL DESCRIPTION

Based on the method from the previous section, a MAT-LAB/Simulink tool was developed from (6), allowing the visualization and immediate identification of the power system components most relevant for the oscillation phenomenon under study. The steps illustrated in Fig. 1 are used to apply the model-reduction method and obtain a visualization of which parts of the system contribute the most to the oscillation. This section discusses how each step is implemented to create the tool.

A. Model linearization

First, the power system non-linear model should be linearized around an operating point. The system's inputs and outputs are specified in Simulink by defining the linear analysis points. They should be selected according to the study intended to be performed or based on the application the model will have.

Since the model-order reduction method calculates the participation of the states based on the input-output behavior, the choice of inputs and outputs choice is essential as it directly affects the results. This is because the controllability is highly dependent on the inputs since it is a measure of how those inputs can drive the system. Similarly, the observability is dependent on the choice of outputs because it measures the response observed from those outputs. A consequence of this fact is that the tool cannot be used to analyze instability due to states that are neither observable nor controllable.

Finally, the "linearize' function [12] in MATLAB is utilized to obtain the linear state-space model.

B. Gramian calculation

Once the matrices of the state-space model are obtained, the tool determines the observability and controllability Gramians. These matrices are calculated by solving the corresponding Lyapunov equations. For the controllability Gramian \mathcal{P} , the following continuous-time Lyapunov equation must be solved:

$$A\mathcal{P} + \mathcal{P}A^T = --BB^T. \tag{7}$$

Similarly, the observability Gramian Q is obtained by solving the Lyapunov equation

$$A^T Q + Q A = -C^T C. (8)$$

In practical terms, this calculation is performed with the assistance of the "gram' [12] function from the MATLAB Control System toolbox. It is important to mention that the tool's algorithmic complexity and performance is limited by the complexity of calculating the controllability and observability Gramians.

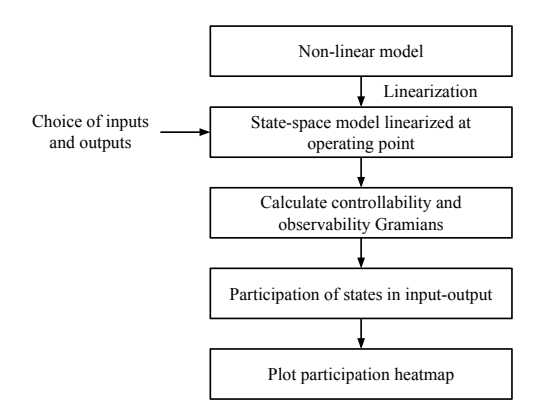


Fig. 1. Flowchart of the tool's operational steps.

Computing the solution of the Lyapunov equations is an approach that has a high computational cost of $\mathcal{O}(n^3)$ [13] and does not scale well to realistically large systems. However, there are methods in the literature that can be used to decrease this computational cost [14], [15]. For example, low-rank Gramian approximations are able to compute the Gramians efficiently by obtaining an approximate Gramian matrix both in the time and frequency domain.

C. Participation of states

Once the Gramians are computed, each state's participation is calculated using (6). For this step, the system should preferentially be modeled using p.u. values to avoid the occurrence of ill-conditioned matrices. This problem has been observed during the practical implementation of the tool.

D. Results visualization

Finally, the participation of each component in the system is calculated by taking into account the participation of all state variables in that component's model. The resulting value is normalized and used to create a heatmap that indicates which parts of the power system are mostly involved in the oscillation phenomenon observed.

IV. MODELING OF A CONVERTER-DOMINATED 9-BUS SYSTEM

This section presents the modeling description for the 9-bus system based on [16] used in this paper as a case study. The main modification to the original system was substituting two synchronous generators with two-level VSC converters, thus turning the test system into a converter-dominated system. The full system contains 84 state variables, and details of how each component was modeled are provided in the remainder of this section.

A. Generator modelling

The generator in the system was modeled using the classical model, which is a simple model consisting of a constant voltage source behind a transient reactance. This model is commonly used in screening studies to obtain a first idea about the system behavior and to represent generators located far from the point where the disturbance is applied. The classical model neglects all electromagnetic dynamics and considers the field voltage constant, resulting in a constant electromotive force. An X/R ratio value of 15 was employed. Therefore, the system can be considered relatively strong.

B. Network modelling

To accurately represent the behavior of the transmission lines, a lumped-parameter pi-circuit model was chosen, which takes into account the phase resistance, phase self-inductance, line-line mutual inductance and resistance, line-line capacitance, and line-ground capacitance. This model is recommended for short to medium-length transmission lines. It assumes that the total line resistance, inductance, and capacitance are lumped as if they were located in a single point, ignoring the effects of electromagnetic traveling waves. The parameters are evaluated at the nominal frequency.

For the loads, the static model was used. This model expresses the active and reactive power at any instant of time as functions of bus voltage magnitudes and frequency.

C. VSC modelling

An averaged-value model is used for the VSC according to details provided in [17]. Table I describes the parameters used for the controls of both VSCs. In this model, controlled voltage and current sources at nominal frequency represent the converter AC and DC sides, neglecting the switching harmonics.

TABLE I VSC parameters for the case study.

Name	Symbol	Values		
	•	VSC 1	VSC 2	
Rated apparent power	S_{rated}	1 GW	1 GW	
DC bus voltage	U_{dc}	640 kV	640 kV	
AC bus voltage	U_{pcc}	192 kV	192 kV	
VSC equivalent inductance	L_{vsc}	50 mH	50 mH	
VSC equivalent resistance	R_{vsc}	0.05Ω	0.05Ω	
Equivalent grid resistance	R_{qrid}	10.19Ω	10.19Ω	
Equivalent grid inductance	L_{qrid}	324.3 mH	324.3 mH	
AC current control time constant	τ_{idq}	10 ms	1 ms	
AC current control damping ratio	ζ_{idq}	0.7	0.7	
PLL time constant	$\hat{ au_{PLL}}$	27 ms	6 ms	
PLL damping ratio	ζ_{PLL}	0.7	0.7	
Active/reactive power control time constant	$ au_{PQ}$	100 ms	10 ms	

The converter AC-side dynamics is modeled in the dq0 frame according to the following equations:

$$\boldsymbol{U}_{AC}^{dq} - \boldsymbol{U}_{pcc}^{dq} = R_{vsc}\boldsymbol{I}_{AC}^{dq} + L_{vsc}\frac{d\boldsymbol{I}_{AC}^{dq}}{dt} + j\omega L_{vsc}\boldsymbol{I}_{AC}^{dq} \quad (9)$$

where U_{pcc}^{dq} is the voltage at the point of common coupling (PCC), U_{AC}^{dq} is the AC-side controlled voltage source, I_{AC}^{dq} is the AC current and R_{vsc} and L_{vsc} are the converter resistance and inductance, respectively.

The control system consists of active and reactive power controls; decoupled AC current control implemented in dq reference frame; voltage feed-forward filters; and an $\alpha\beta$ phase-locked loop (PLL).

The active and reactive power controls are described by the equations:

$$I_{AC}^{d*} = (P_{AC}^* - P_{AC}^{meas})(K_{p,P} + \frac{K_{i,P}}{s})$$
 (10)

$$I_{AC}^{q*} = -(Q_{AC}^* - Q_{AC}^{meas})(K_{p,Q} + \frac{K_{i,Q}}{s})$$
 (11)

where P_{AC}^* and Q_{AC}^* are the active and reactive power reference values, respectively, while P_{AC}^{meas} and Q_{AC}^{meas} are the measured active and reactive power values.

The inner current controller is implemented in the dq-frame, and the main equations describing the control loop are:

$$U_{AC}^{d*} = (I_{AC}^{d*} - I_{AC}^{d,meas})(K_{p,d} + \frac{K_{i,d}}{s}) + U_{pcc}^{d} + I_{AC}^{q,meas}L_{vsc}\omega \ \ (12)$$

$$U_{AC}^{q*} = (I_{AC}^{q*} - I_{AC}^{q,meas})(K_{p,q} + \frac{K_{i,q}}{c}) + U_{pcc}^{q} - I_{AC}^{d,meas} L_{vsc}\omega$$
 (13)

where $K_{p,d}$, $K_{p,q}$ are the controller's proportional gains and $K_{i,d}$ and $K_{i,q}$ are the integral gains.

The $\alpha\beta$ -PLL is implemented according to [18] as follows:

$$\omega_{\alpha\beta PLL} = \left(K_p + \frac{K_i}{s}\right) sin(\theta_{grid} - \theta_{\alpha\beta PLL}) \qquad (14)$$

$$\theta_{\alpha\beta PLL} = \frac{\omega_{\alpha\beta PLL}}{s} \tag{15}$$

where θ_{grid} is the grid voltage angle, $\theta_{\alpha\beta PLL}$ is the grid angle measured by the PLL, and $\omega_{\alpha\beta PLL}$ is the measured grid frequency in rad/s.

Finally, a first-order low-pass voltage-feedforward filter was used. The filter's transfer function $G_{ff}(s)$ is given by:

$$G_{ff}(s) = \frac{\omega_{ff}}{s + \omega_{ff}} \tag{16}$$

where ω_{ff} represents the filter's cutoff frequency.

This model was implemented in MATLAB/Simulink, and a state-space representation was obtained from the linearized system considering the arbitrarily selected active and reactive power setpoints of $P=0.9~\mathrm{p.u.}$ and $Q=0.2~\mathrm{p.u.}$, respectively. The correspondence between states and the physical system was maintained to derive practical modeling insights from the analysis.

V. TOOL APPLICATION AND RESULTS

The proposed tool is used to investigate the converter interaction in the 9-bus system case study described in the previous section.

Fig. 2 presents the system's eigenvalues, and the highlighted blue region shows the eigenvalues with damping lower or equal to 10%, which can be considered poorly damped. The initial analysis of the eigenvalues indicates that the system may oscillate due to these poorly damped eigenvalues. However, it is uncertain whether any eigenvalues will be excited by a change in the operation point of the system.

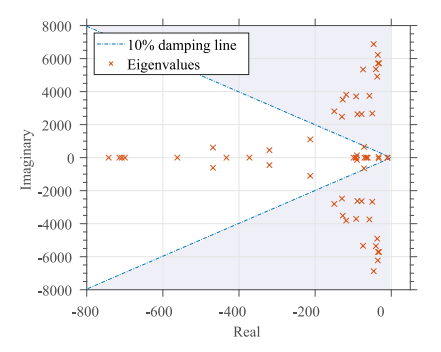


Fig. 2. System eigenvalues and 10% damping line.

To evaluate the time-domain response of the system, we applied a 5% step change to the reactive power reference of VSC2. The result was an oscillatory response, as shown in Fig. 3.

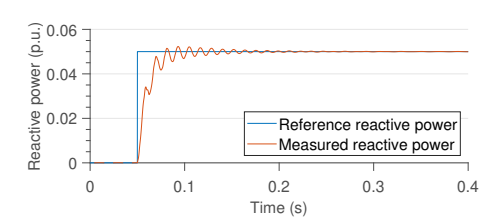


Fig. 3. Response to a 5% step in the VSC 2 reactive power reference.

By analyzing only the system eigenvalues based on their damping, it is not possible to directly predict which specific components are causing the oscillation.

The tool proposed in this paper aims at solving this issue by simplifying the analysis. In order to identify the relevant states for the observed phenomena, we applied the proposed tool according to the steps in Fig. 1. We linearized the model by selecting the reactive power reference as an input and the measured reactive power as an output. Using the state-space model, we calculated the Gramians, which were then used to determine the overall participation of each component using (6).

Fig. 4 presents the participation of the most significant states in the input-output response of the system obtained from the analysis. The participation not only measures the state's relevance but also that component's relevance in the system response since the states are associated with the physical components of the power system. Preserving the state's physical nature enables the tool's results to be directly interpretable to decide which parts of the system are causing the observed oscillation.

To make the analysis more intuitive, the tool presents an alternative view of the results found in Fig. 4 by creating a color gradient overlay in MATLAB/Simulink model that indicates the most relevant parts of the system to the phenomenon under study.

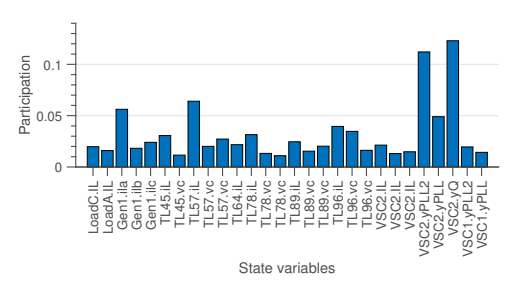


Fig. 4. Participation of states in input-output behavior.

The visualization results are shown in Fig. 5. The red colors indicate a higher participation level, while colors closer to yellow indicate a lower level of participation. This color map, along with the results in Fig. 4, makes drawing conclusions about a system's behavior easier. It shows that the VSC 2 reactive power control and the VSC 2 PLL interaction with the network are the main factors contributing to the response.

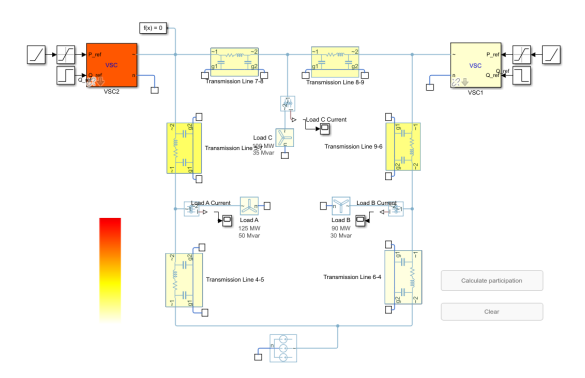


Fig. 5. Tool developed for MATLAB/Simulink showing the contribution of different parts of the system in a converter interaction case.

The results also indicate that each transmission line has relatively low participation. However, when considering their combined contribution, they significantly influence the system's behavior. Furthermore, the color map can be used to identify which areas of the model should be modeled in high detail and which parts could be simplified. This is particularly useful when analyzing more complex systems.

The proposed tool has some limitations as it is only suitable for analyzing oscillatory phenomena that can be studied using small-signal analysis.

VI. CONCLUSIONS

This paper presents a MATLAB/Simulink tool that was developed for modeling and analyzing the stability of power systems with a large number of power electronic devices based on a model-reduction method proposed by the authors.

The tool was applied to investigate an instance of converter oscillation in a converter-dominated modified 9-bus system. It identified the interaction between PLL and grid, and provided a clear visualization of the power system components that contributed to the oscillation. The results offer valuable insights into how to correctly model the different components and address the instability problem.

However, the proposed tool has certain limitations. It can only analyze stable oscillations and cannot be used for instability caused by unobservable or uncontrollable states.

Future research could focus on implementing methods to accelerate the calculation of Gramians to deal with the computational challenges of large power systems. The tool and model-reduction method can also be extended to address unstable systems.

REFERENCES

- IRENA, "World Energy Transitions Outlook: 1.5° Pathway," International Renewable Energy Agency, Abu Dhabi, Tech. Rep., 2021.
- [2] ENTSO-E, "Completing the map Power system needs in 2030 and 2040," European Network of Transmission System Operators for Electricity, Tech. Rep. August, 2020.
- [3] Y. Cheng and L. Fan, "Wind Energy Systems Sub-Synchronous Oscillations: Events and Modeling," IEEE Power & Energy Society, Tech. Rep. July, 2020.
- [4] AEMO, "Power System Limitations in North Western Victoria and South Western New South Wales," Australian Energy Market Operator, Tech. Rep. December, 2019.
- [5] J. Adams, C. Carter, and S. Huang, "ERCOT experience with subsynchronous control interaction and proposed remediation," in *Proc. IEEE PES Trans. and Distr. Conf.*, Orlando, USA, May 2012.
- [6] Q. Cossart, F. Colas, and X. Kestelyn, "A novel event- and non-projection-based approximation technique by state residualization for the model order reduction of power systems with a high renewable energies penetration," *IEEE Transactions on Power Systems*, vol. 37, no. 4, pp. 3221–3229, 2022.
- [7] G. E. Dullerud and F. G. Paganini, A Course in Robust Control Theory: A Convex Approach. New York: Springer-Verlag, 2000.
- [8] N. d. M. D. Campos, T. Sarnet, and J. Kilter, "Novel gramian-based structure-preserving model order reduction for power systems with high penetration of power converters," *IEEE Transactions on Power Systems*, pp. 1–11, 2022.
- [9] D. Chaniotis and M. A. Pai, "Model reduction in power systems using Krylov subspace methods," *IEEE Transactions on Power Systems*, vol. 2, no. 2, p. 1412, 2005.
- [10] H. R. Ali and B. C. Pal, "Model order reduction of multi-terminal directcurrent grid systems," *IEEE Transactions on Power Systems*, vol. 36, no. 1, pp. 699–711, 2021.
- [11] Y. G. I. Acle, F. D. Freitas, N. Martins, and J. Rommes, "Parameter preserving model order reduction of large sparse small-signal electromechanical stability power system models," *IEEE Transactions on Power Systems*, vol. 34, no. 4, pp. 2814–2824, 2019.

- [12] "MATLAB Control System Toolbox," Release 2022a, The MathWorks, Inc., Natick, MA, USA.
- [13] A. Antoulas, "Approximation of large-scale dynamical systems: An overview," *IFAC Proceedings Volumes*, vol. 37, no. 11, pp. 19–28, 2004.
- [14] P. Benner, P. Ezzatti, D. Kressner, E. S. Quintana-Ortí, and A. Remón, "A mixed-precision algorithm for the solution of Lyapunov equations on hybrid CPU-GPU platforms," *Parallel Computing*, vol. 37, no. 8, pp. 439-450, 2011, follow-on of ISPDC'2009 and HeteroPar'2009.
- [15] F. D. Freitas, J. Rommes, and N. Martins, "Low-rank Gramian applications in dynamics and control," in *International Conference on Communications, Computing and Control Applications*, 2011, pp. 1–6.
- [16] P. M. Anderson and A. A. Fouad, Power Systems Control and Stability, 2nd ed., 2003.
- [17] CIGRE, "Technical Brochure 604: Guide for the development of models for HVDC converters in a HVDC grid," CIGRE Working Group B4.57, Tech. Rep. December, 2014.
- [18] Z. Ali, N. Christofides, L. Hadjidemetriou, E. Kyriakides, Y. Yang, and F. Blaabjerg, "Three-phase phase-locked loop synchronization algorithms for grid-connected renewable energy systems: A review," Renewable and Sustainable Energy Reviews, vol. 90, no. February, pp. 434–452, 2018.

Appendix B — Transformations

This appendix presents relevant transformations involving the abc, dq0, and $\alpha\beta\gamma$ coordinate frames, which are essential for analysing and controlling power systems.

abc to dq0 and its Inverse

The transformation from the abc reference frame to the dq0 frame is based, in part, on an arbitrary rotation defined by an angle θ . If the rotation occurs at speed ω , which may be constant or variable, the rotation angle can also be expressed by ωt . This assumption will be utilized in the following discussion. There are several variations of this transformation, depending on whether the active and reactive powers are preserved and how the axes of the two reference frames are aligned. The following is a summary of the existing variations.

• The **power variant** transformation with **a-axis aligned with q-axis** is given by:

$$\begin{bmatrix} x_d \\ x_q \\ x_0 \end{bmatrix} = \frac{2}{3} \begin{bmatrix} \sin(\omega t) & \sin(\omega t - \frac{2\pi}{3}) & \sin(\omega t + \frac{2\pi}{3}) \\ \cos(\omega t) & \cos(\omega t - \frac{2\pi}{3}) & \cos(\omega t + \frac{2\pi}{3}) \\ \frac{1}{2} & \frac{1}{2} & \frac{1}{2} \end{bmatrix} \begin{bmatrix} x_a \\ x_b \\ x_c \end{bmatrix}. \tag{183}$$

Its inverse is given by:

$$\begin{bmatrix} x_a \\ x_b \\ x_c \end{bmatrix} = \begin{bmatrix} sin(\omega t) & cos(\omega t) & 1 \\ sin(\omega t - \frac{2\pi}{3}) & cos(\omega t - \frac{2\pi}{3}) & 1 \\ sin(\omega t + \frac{2\pi}{3}) & cos(\omega t + \frac{2\pi}{3}) & 1 \end{bmatrix} \begin{bmatrix} x_d \\ x_q \\ x_0 \end{bmatrix}.$$
(184)

• The power invariant transformation with a-axis aligned with q-axis is given by:

$$\begin{bmatrix} x_d \\ x_q \\ x_0 \end{bmatrix} = \sqrt{\frac{2}{3}} \begin{bmatrix} \sin(\omega t) & \sin(\omega t - \frac{2\pi}{3}) & \sin(\omega t + \frac{2\pi}{3}) \\ \cos(\omega t) & \cos(\omega t - \frac{2\pi}{3}) & \cos(\omega t + \frac{2\pi}{3}) \\ \sqrt{\frac{1}{2}} & \sqrt{\frac{1}{2}} & \sqrt{\frac{1}{2}} \end{bmatrix} \begin{bmatrix} x_a \\ x_b \\ x_c \end{bmatrix}.$$
(185)

 The power variant transformation with a-axis aligned with d-axis (known as Park transformation) is given by:

$$\begin{bmatrix} x_d \\ x_q \\ x_0 \end{bmatrix} = \frac{2}{3} \begin{bmatrix} \cos(\omega t) & \cos(\omega t - \frac{2\pi}{3}) & \cos(\omega t + \frac{2\pi}{3}) \\ -\sin(\omega t) & -\sin(\omega t - \frac{2\pi}{3}) & -\sin(\omega t + \frac{2\pi}{3}) \\ \frac{1}{2} & \frac{1}{2} & \frac{1}{2} \end{bmatrix} \begin{bmatrix} x_a \\ x_b \\ x_c \end{bmatrix}. \tag{186}$$

Its inverse is given by:

$$\begin{bmatrix} x_a \\ x_b \\ x_c \end{bmatrix} = \begin{bmatrix} \cos(\omega t) & -\sin(\omega t) & 1 \\ \cos(\omega t - \frac{2\pi}{3}) & -\sin(\omega t - \frac{2\pi}{3}) & 1 \\ \cos(\omega t + \frac{2\pi}{3}) & -\sin(\omega t + \frac{2\pi}{3}) & 1 \end{bmatrix} \begin{bmatrix} x_d \\ x_q \\ x_0 \end{bmatrix}.$$
 (187)

Another variation of the **Park transformation** defines that the **q-axis is ahead of the d-axis** and that ωt is the angle between phase-a and q-axis. It is given by:

$$\begin{bmatrix} x_d \\ x_q \\ x_0 \end{bmatrix} = \frac{2}{3} \begin{bmatrix} \cos(\omega t) & \cos(\omega t - \frac{2\pi}{3}) & \cos(\omega t + \frac{2\pi}{3}) \\ \sin(\omega t) & \sin(\omega t - \frac{2\pi}{3}) & \sin(\omega t + \frac{2\pi}{3}) \\ \frac{1}{2} & \frac{1}{2} & \frac{1}{2} \end{bmatrix} \begin{bmatrix} x_a \\ x_b \\ x_c \end{bmatrix}. \tag{188}$$

• The power invariant transformation with a-axis aligned with d-axis is given by:

$$\begin{bmatrix} x_d \\ x_q \\ x_0 \end{bmatrix} = \sqrt{\frac{2}{3}} \begin{bmatrix} \cos(\omega t) & \cos(\omega t - \frac{2\pi}{3}) & \cos(\omega t + \frac{2\pi}{3}) \\ -\sin(\omega t) & -\sin(\omega t - \frac{2\pi}{3}) & -\sin(\omega t + \frac{2\pi}{3}) \\ \sqrt{\frac{1}{2}} & \sqrt{\frac{1}{2}} & \sqrt{\frac{1}{2}} \end{bmatrix} \begin{bmatrix} x_a \\ x_b \\ x_c \end{bmatrix}.$$
(189)

Its inverse is given by:

$$\begin{bmatrix} x_a \\ x_b \\ x_c \end{bmatrix} = \sqrt{\frac{2}{3}} \begin{bmatrix} \cos(\omega t) & -\sin(\omega t) & \sqrt{\frac{1}{2}} \\ \cos(\omega t - \frac{2\pi}{3}) & -\sin(\omega t - \frac{2\pi}{3}) & \sqrt{\frac{1}{2}} \\ \cos(\omega t + \frac{2\pi}{3}) & -\sin(\omega t + \frac{2\pi}{3}) & \sqrt{\frac{1}{2}} \end{bmatrix} \begin{bmatrix} x_d \\ x_q \\ x_0 \end{bmatrix}. \tag{190}$$

Power Calculation

This section illustrates how to calculate power considering the previously discussed transformations. The instantaneous power in a three-phase circuit, represented in the *abc* reference frame, is determined as:

$$P_{3\Phi} = v_a i_a + v_b i_b + v_c i_c. {191}$$

Based on the analysis presented in [131], Equation (191) can be reformulated as follows:

$$P_{3\phi} = \begin{bmatrix} v_a & v_b & v_c \end{bmatrix} \begin{bmatrix} i_a \\ i_b \\ i_c \end{bmatrix}. \tag{192}$$

Let T_{θ} represent a transformation from the abc to the dq0 frame and let T_{θ}^{-1} denote its inverse. The three-phase power $P_{3\phi}$ can be calculated in the dq0 frame using the following expression:

$$P_{3\phi} = \begin{bmatrix} v_d & v_q & v_0 \end{bmatrix} (T_{\theta}^{-1})^T T_{\theta}^{-1} \begin{bmatrix} i_d \\ i_q \\ i_0 \end{bmatrix}.$$
 (193)

The transformation will be power invariant only if T_{θ} is unitary. For example, when considering the Park transformation represented by the transformation in Equation (186),

$$(T_{\theta}^{-1})^T T_{\theta}^{-1} = \frac{3}{2} \begin{bmatrix} 1 & 0 & 0 \\ 0 & 1 & 0 \\ 0 & 0 & 2 \end{bmatrix} .$$
 (194)

The three-phase power is calculated by substituting Equation (194) into (193), resulting in the following expressions:

$$P_{3\phi} = \frac{3}{2} \begin{bmatrix} v_d & v_q & v_0 \end{bmatrix} \begin{bmatrix} 1 & 0 & 0 \\ 0 & 1 & 0 \\ 0 & 0 & 2 \end{bmatrix} \begin{bmatrix} i_d \\ i_q \\ i_0 \end{bmatrix}.$$
 (195)

$$P_{3\phi} = \frac{3}{2}(v_d i_d + v_q i_q + 2v_0 i_0)$$
(196)

Thus, it can be concluded that the Park transformation is not power invariant. A similar approach can be taken to derive the power expressions for the other transformations.

abc to $\alpha\beta\gamma$ and its Inverse

In this section, the transformations from the abc frame to the $\alpha\beta\gamma$ frame are introduced, including both power variant and invariant versions.

• The **power variant** transformation (known as **Clarke transformation**) is given by:

$$\begin{bmatrix} x_{\alpha} \\ x_{\beta} \\ x_{\gamma} \end{bmatrix} = \frac{2}{3} \begin{bmatrix} 1 & -\frac{1}{2} & -\frac{1}{2} \\ 0 & \frac{\sqrt{3}}{2} & -\frac{\sqrt{3}}{2} \\ \frac{1}{2} & \frac{1}{2} & \frac{1}{2} \end{bmatrix} \begin{bmatrix} x_{a} \\ x_{b} \\ x_{c} \end{bmatrix}.$$
(197)

This transformation preserves the amplitude of the electrical variables to which it is applied. Its inverse is given by:

$$\begin{bmatrix} x_a \\ x_b \\ x_c \end{bmatrix} = \begin{bmatrix} 1 & 0 & 1 \\ -\frac{1}{2} & \frac{\sqrt{3}}{2} & 1 \\ -\frac{1}{2} & -\frac{\sqrt{3}}{2} & 1 \end{bmatrix} \begin{bmatrix} x_\alpha \\ x_\beta \\ x_\gamma \end{bmatrix}.$$
 (198)

• The power invariant transformation is given by:

$$\begin{bmatrix} x_{\alpha} \\ x_{\beta} \\ x_{\gamma} \end{bmatrix} = \sqrt{\frac{2}{3}} \begin{bmatrix} 1 & -\frac{1}{2} & -\frac{1}{2} \\ 0 & \frac{\sqrt{3}}{2} & -\frac{\sqrt{3}}{2} \\ \frac{1}{\sqrt{2}} & \frac{1}{\sqrt{2}} & \frac{1}{\sqrt{2}} \end{bmatrix} \begin{bmatrix} x_{a} \\ x_{b} \\ x_{c} \end{bmatrix}.$$
 (199)

Its inverse is given by:

$$\begin{bmatrix} x_a \\ x_b \\ x_c \end{bmatrix} = \sqrt{\frac{2}{3}} \begin{bmatrix} 1 & 0 & \frac{1}{\sqrt{2}} \\ -\frac{1}{2} & \frac{\sqrt{3}}{2} & \frac{1}{\sqrt{2}} \\ -\frac{1}{2} & -\frac{\sqrt{3}}{2} & \frac{1}{\sqrt{2}} \end{bmatrix} \begin{bmatrix} x_\alpha \\ x_\beta \\ x_\gamma \end{bmatrix}.$$
 (200)

$\alpha\beta\gamma$ to dq0 and its Inverse

The transformation from the stationary $\alpha\beta\gamma$ reference frame to the dq0 reference frame is achieved by applying a rotation at an arbitrary speed ω . The rotation of the $\alpha\beta$ components into dq components is based on the rotation matrix from linear algebra. The component γ is equivalent to the component 0. The resulting transformation can be expressed as:

$$\begin{bmatrix} x_d \\ x_q \\ x_0 \end{bmatrix} = \begin{bmatrix} cos(\omega t) & sin(\omega t) & 0 \\ -sin(\omega t) & cos(\omega t) & 0 \\ 0 & 0 & 1 \end{bmatrix} \begin{bmatrix} x_{\alpha} \\ x_{\beta} \\ x_{\gamma} \end{bmatrix}. \tag{201}$$

The inverse of this transformation is obtained by applying a similar rotation in the opposite direction. This is mathematically represented by substituting the rotation angle with $-\omega t$, resulting in sign changes for the sine terms. The resulting matrix for the inverse transformation is given by:

$$\begin{bmatrix} x_{\alpha} \\ x_{\beta} \\ x_{\gamma} \end{bmatrix} = \begin{bmatrix} \cos(\omega t) & -\sin(\omega t) & 0 \\ \sin(\omega t) & \cos(\omega t) & 0 \\ 0 & 0 & 1 \end{bmatrix} \begin{bmatrix} x_d \\ x_q \\ x_0 \end{bmatrix}. \tag{202}$$

Appendix C — Eigendecomposition

Eigendecomposition is a fundamental concept in linear algebra that facilitates the analysis and simplification of linear transformations represented by matrices. For a linear time-invariant system described by the state equation

$$\dot{\boldsymbol{x}}(t) = \boldsymbol{A}\boldsymbol{x}(t) + \boldsymbol{B}\boldsymbol{u}(t). \tag{203}$$

The system matrix \mathbf{A} can be examined through its eigenvalue properties. Specifically, the following relationship holds:

$$AV = V\Lambda, \tag{204}$$

where V is the matrix of right eigenvectors, with each column representing an eigenvector, and Λ is a diagonal matrix containing the eigenvalues along its diagonal.

This leads to the expression of the matrix \mathbf{A} in terms of its eigenvectors and eigenvalues:

$$A = V\Lambda V^{-1}. (205)$$

In this equation, V^{-1} denotes the matrix of left eigenvectors, where each row corresponds to an eigenvector. By substituting $W = V^{-1}$, the definition of eigendecomposition is established:

$$A = V \Lambda W. \tag{206}$$

This framework provides valuable insight into the properties of the system and is widely applied in the study of power system dynamics.

Appendix D — Singular Value Decomposition

This appendix presents the definition of Singular Value Decomposition, a tool from linear algebra that allows the factorization of a matrix $\mathbf{A} \in \mathbb{R}^{n \times m}$ into a product of three matrices, as described in [86]:

$$A = U\Sigma V^*, \tag{207}$$

where V^* denotes the conjugate transpose (or simply the transpose for real matrices) and U and V are unitary matrices (or orthogonal matrices for real matrices). This implies that $UU^* = U^*U = I_n$ and $VV^* = V^*V = I_m$. Additionally, the following points can be noted:

- The *left singular vectors* u_i correspond to the elements of $\mathbf{U} = (u_1, u_2, ..., u_n)$;
- The right singular vectors v_i correspond to the elements of $\mathbf{V} = (v_1, v_2, ..., v_n)$;
- The singular values σ_i correspond to the nonnegative diagonal entries of the matrix $\Sigma = \text{diag}(\sigma_1, \sigma_2, ..., \sigma_n)$.

Based on the above, the dyadic decomposition of A can be expressed as:

$$\mathbf{A} = \sigma_1 u_1 v_1^* + \sigma_2 u_2 v_2^* + \dots + \sigma_n u_n v_n^*. \tag{208}$$

If the matrix \mathbf{A} is symmetric, its singular value decomposition can be derived from the eigendecomposition, following the instructions provided in [132].

Appendix E — Hardy Spaces

This appendix provides a brief overview of Hardy spaces, which play a fundamental role in control theory and signal processing. In particular, the spaces \mathbf{H}_2 and \mathbf{H}_∞ are commonly used to characterize signals and system transfer functions, respectively. Their associated norms offer useful interpretations in terms of signal energy and system gain.

Hardy Space H_2

The Hardy space H_2 is the set of complex-valued functions F(s), defined over a complex variable s, that satisfy the following properties:

- F(s) is analytic in the open right half-plane (Re s > 0);
- F(s) satisfies the boundedness condition [117]:

$$\left[\sup_{\xi>0} \frac{1}{2\pi} \int_{-\infty}^{\infty} |F(\xi+j\omega)|^2 d\omega\right]^{1/2} < \infty. \tag{209}$$

H_2 Norm

The H_2 norm is given by the expression on the left-hand side of the bounding condition above. The integrand can be interpreted as the mean square value of the function F. In the special case where F is a real rational function, that is, stable and strictly proper, then $F \in \mathbf{R}H_2$, and the norm simplifies to:

$$||F||_2 = \left[\frac{1}{2\pi} \int_{-\infty}^{\infty} |F(j\omega)|^2 d\omega\right]^{1/2}.$$
 (210)

Properties

Let x(t) be a signal defined for $t \in [0, \infty)$, and let $\hat{x}(s)$ denote its Laplace transform. According to Plancherel's theorem [117]:

$$||x(t)||_2^2 = \int_0^\infty x(t)^2 dt.$$
 (211)

This integral represents the energy of the signal x(t).

The \mathbf{H}_{∞} norm of a transfer function F(s) provides an upper bound on the system gain in response to \mathbf{H}_2 inputs:

$$||F||_{\infty} = \sup\{||Fx||_2 : x \in \mathbf{H}_2, ||x||_2 = 1\}.$$
 (212)

Hardy Space H_{∞}

The Hardy space H_{∞} is the set of complex-valued functions F(s) that are:

- Analytic in the open right half-plane (Re s > 0);
- Bounded, i.e., there exists b > 0 such that

$$|F(s)| < b \quad \text{for all Re } s > 0. \tag{213}$$

H_{∞} Norm

The H_{∞} norm is defined as the infimum of all such bounds b:

$$||F||_{\infty} = \sup\{|F(s)| : \operatorname{Re} s > 0\}.$$
 (214)

Properties

The \pmb{H}_{∞} norm satisfies the following key properties [133]:

• Submultiplicativity:

$$||FG||_{\infty} \le ||F||_{\infty} \cdot ||G||_{\infty}.$$
 (215)

• Triangle Inequality:

$$||F + G||_{\infty} \le ||F||_{\infty} + ||G||_{\infty}.$$
 (216)

Appendix F — Control Tuning

This appendix outlines the procedures used to tune the control loops of the Voltage Source Converters (VSCs). The tuning methods are based on classical control theory and aim to achieve the desired dynamic performance.

Inner Current Control

The tuning of the inner current control is based on the closed-loop transfer function:

$$\frac{I_{ac}^{d}}{I_{ac}^{d*}} = \frac{1 + \frac{K_{p,d}}{K_{i,d}}s}{1 + \frac{K_{p,d} + R_{vsc}}{K_{i,d}}s + \frac{L_{vsc}}{K_{i,d}}s^{2}}.$$
(217)

Method 1: Pole Placement via Second-Order Approximation

This method compares the characteristic polynomial of the closed-loop system with a standard second-order system:

$$P(s) = 1 + \frac{2\zeta}{\omega_n} s + \frac{1}{\omega_n^2} s^2.$$
 (218)

The system poles are then given by:

$$s = \omega_n(-\zeta \pm \sqrt{1 - \zeta^2}). \tag{219}$$

By matching the polynomials, the natural frequency ω_n and damping ratio ζ are related to the control parameters as:

$$\omega_n = \sqrt{\frac{K_{i,d}}{L_{vec}}},\tag{220}$$

$$\zeta = \frac{K_{p,d} + R_{vsc}}{2\sqrt{K_{i,d}L_{vsc}}}.$$
 (221)

The desired ω_n and ζ are selected according to dynamic performance specifications. For instance:

$$\omega_n = \frac{3}{t_{r,5\%}} \qquad \text{for } \zeta = 0.7, \tag{222}$$

$$\omega_n = \frac{5}{t_{r.5\%}} \qquad \qquad \text{for } \zeta = 1. \tag{223}$$

The corresponding PI gains are computed as:

$$K_{i,d} = L_{vsc} \, \omega_n^2, \tag{224}$$

$$K_{p,d} = 2\zeta \omega_n L_{vsc} - R_{vsc}. \tag{225}$$

Method 2: Zero-Pole Cancellation

In this method, the controller is tuned such that the system reduces to a first-order response via zero-pole cancellation. The characteristic equation roots are:

$$s_{1,2} = \frac{-\frac{K_{p,d} + R_{vsc}}{K_{i,d}} \pm \sqrt{\left(\frac{K_{p,d} + R_{vsc}}{K_{i,d}}\right)^2 - 4\frac{L_{vsc}}{K_{i,d}}}}{2\frac{L_{vsc}}{K_{i,d}}}.$$
 (226)

The system zero is located at:

$$z_1 = -\frac{K_{i,d}}{K_{p,d}}. (227)$$

Zero-pole cancellation requires two conditions:

1. Real poles: $\zeta \geq 1$, implying:

$$K_{p,d} > 2\sqrt{K_{i,d}L_{vsc}} - R_{vsc}.$$
 (228)

2. The system zero must coincide with one of the poles.

Phase-Locked Loop

The linearized PLL transfer function is expressed as:

$$\frac{\Delta \theta_{pll}}{\Delta U_{grid}^{q}} = \frac{\frac{K_{p,pll}}{U_{grid}^{d} K_{i,pll}} s + \frac{1}{U_{grid}^{d}}}{\frac{U_{base}}{U_{grid}^{d} K_{i,pll}} s^{2} + \frac{K_{p,pll}}{K_{i,pll}} s + 1}.$$
 (229)

This transfer function can be compared to a second-order system:

$$P(s) = 1 + \frac{2\zeta}{\omega_n} s + \frac{1}{\omega_n^2} s^2.$$
 (230)

From this comparison, the PLL controller gains are obtained as:

$$K_{p,pll} = \frac{2\zeta \omega_n U_{base}}{U_{grid}^d},\tag{231}$$

$$K_{i,pll} = \frac{\omega_n^2 U_{base}}{U_{grid}^d}.$$
 (232)

The bandwidth of the PLL controller is:

$$\omega_b = \omega_n \sqrt{1 - 2\zeta^2 + \sqrt{4\zeta^4 - 4\zeta^2 + 2}}.$$
 (233)

Active and Reactive Power Control

The active and reactive power controllers share the same PI structure and tuning logic. The closed-loop transfer function is:

$$\frac{P_g}{P_g^*} = \frac{1 + \frac{K_{p,P}}{K_{i,P}}}{1 + \frac{1 + K_{p,P}}{K_{i,P}}}.$$
 (234)

The gains are selected to yield a first-order system with desired response time τ_r :

$$K_{p,P} = K_{p,O} = 0,$$
 (235)

$$K_{i,P} = K_{i,Q} = \frac{1}{\tau_r}.$$
 (236)

Voltage Feed-Forward Filter

The voltage feed-forward filter is tuned to avoid interference with the inner current control loop. If the current loop bandwidth is defined as:

$$\omega_{idq} = \frac{3}{\tau_{idq}},\tag{237}$$

then the feed-forward filter bandwidth ω_{ff} is chosen as:

$$\omega_{ff} = K \,\omega_{idg},\tag{238}$$

where K = 10 ensures sufficient separation between the two bandwidths.

Curriculum Vitae

1. Personal data

Name Nathalia de Morais Dias Campos
Date and place of birth 25 February 1992 João Pessoa, Brazil

E-mail mdc.nathalia@gmail.com

2. Education

2021-... Tallinn University of Technology, School of Engineering,

Electrical Power Engineering and Mechatronics, PhD studies

2016-2017 University of Lille 1

Electrical Engineering for Sustainable Development, MSc

2014–2015 University of Manitoba

Exchange Program in Electrical Engineering, BSc

2011–2018 Federal University of Campina Grande

Electrical Engineering, BSc

3. Language competence

Portuguese native English fluent

French intermediate
German beginner

4. Professional employment

2024-... Fraunhofer IEE, Research Associate

2020–2024 Tallinn University of Technology, Early Stage Researcher

2018–2020 Elia System Operator, Ph.D. Researcher

5. Computer skills

Simulation tools PSCAD, EMTP, RTDS, PowerFactory, MATLAB/Simulink, ATP

Programming languages Python, JavaScript, TypeScript, Go, C, C++

6. Honours and awards

- 2018, Marie Skłodowska-Curie InnoDC Scholarship
- 2017, First place in the Master's ranking
- 2016, Erasmus Mundus EBW+ Scholarship
- 2014, Science Without Borders Scholarship
- 2011, 2012, 2013, Scientific Initiation Scholarship
- 2008, 2009, 2010, Junior Scientific Initiation Scholarship
- 2008, 2009, First place in the Mathematical Olympiad of João Pessoa
- 2007, 2008, 2009, 2010, Bronze medal in the Brazilian Mathematical Olympiad

7. Defended theses

- 2017, Modular Multilevel Converters Connected by an Inductive Link, MSc, supervisors Prof. François Gruson, Prof. Xavier Guillaud and Prof. Philippe Delarue, Université de Lille, sciences et technologies.
- 2018, Analysis of the Application of Controlled Switching of Double-Circuit Transmission Lines (Análise da Aplicação do Chaveamento Controlado em Linhas de Transmissão de Circuito Duplo), supervisor Prof. Karcius Dantas, Universidade Federal de Campina Grande.

8. Scientific work

- 1. N. M. D. Campos, T. Sarnet, and J. Kilter, "A gramian-based tool for modeling converter-dominated power systems," in 2024 IEEE PES Innovative Smart Grid Technologies Europe (ISGT Europe), 2024, pp. 1–5.
- N. M. D. Campos, T. Sarnet, and J. Kilter, "Novel gramian-based structure-preserving model order reduction for power systems with high penetration of power converters," *IEEE Transactions on Power Systems*, vol. 38, no. 6, pp. 5381–5391, 2023.
- 3. G. Grdenić, F. J. C. García, N. M. D. Campos, F. Villella, and J. Beerten, "Model order reduction of voltage source converters based on the ac side admittance assessment: From EMT to RMS," *IEEE Transactions on Power Delivery*, vol. 38, no. 1, pp. 56–67, 2023.
- P. De Rua, T. Roose, O. C. Sakinci, N. M. D. Campos, and J. Beerten, "Identification of mechanisms behind converter-related issues in power systems based on an overview of real-life events," *Renewable and Sustainable Energy Reviews*, vol. 183, pp. 1–16, 2023.
- 5. ——, "Report on dynamic converter interactions and the feasibility of different software routines to represent the problems," Innovative tools for offshore wind and DC grids (InnoDC), Tech. Rep., 2019.
- W. Liu, J. Liang, N. M. D. Campos, V. Bhardwaj, J. Beerten, D. Van Hertem, H. Ergun, S. Dadjo Tavakoli, E. Prieto, O. Gomis, E. Maggioli, and H. Leite, "Report on the review and evaluation of DC and AC grid operation and interactions in different time frames," Innovative tools for offshore wind and DC grids (InnoDC), Tech. Rep., 2018.

Elulookirjeldus

1. Isikuandmed

Nimi Nathalia de Morais Dias Campos Sünniaeg ja -koht 25.02.1992, João Pessoa, Brasiilia E-post mdc.nathalia@gmail.com

2. Haridus

2021-... Tallinna Tehnikaülikool, Inseneriteaduskond,

Elektroenergeetika ja mehhatroonika, doktoriõpe

2016-2017 Lille'i Ülikool 1

Elektrotehnika säästva arengu jaoks, magistriõpe

2014–2015 Manitoba Ülikool

Vahetusprogramm elektrotehnikas, bakalaureuseõpe

2011–2018 Campina Grande Föderaalülikool

Elektrotehnika, bakalaureuseõpe

3. Keelteoskus

portugali keel emakeel inglise keel kõrgtase prantsuse keel kesktase saksa keel algtase

4. Teenistuskäik

2024-... Fraunhofer IEE, teadustöötaja

2020–2024 Tallinna Tehnikaülikool, nooremteadur 2018–2020 Elia System Operator, doktorantuuriteadur

5. Arvutioskus

Simulatsioonitarkvarad PSCAD, EMTP, RTDS, PowerFactory, MATLAB/Simulink, ATP

Programmeerimiskeeled Python, JavaScript, TypeScript, Go, C, C++

6. Autasud

• 2018, Marie Skłodowska-Curie InnoDC stipendium

• 2017, Esikoht magistriõppe pingereas

• 2016, Erasmus Mundus EBW+ stipendium

• 2014, Teadus ilma piirideta stipendium

• 2011, 2012, 2013, Teadusliku tegevuse algatamise stipendium

• 2008, 2009, 2010, Noorte teadustöö algatamise stipendium

• 2008, 2009, Esikoht João Pessoa matemaatikaolümpiaadil

• 2007, 2008, 2009, 2010, Pronksmedal Brasiilia matemaatikaolümpiaadil

7. Kaitstud lõputööd

- 2017, Modulaarset tüüpi multitasemel muundurite ühendamine induktiivse lingi kaudu, magistritöö, juhendajad prof. François Gruson, prof. Xavier Guillaud ja prof. Philippe Delarue, Lille'i Ülikool, teadus ja tehnoloogia.
- 2018, Topeltliinide juhitud lülitamise rakenduse analüüs (Análise da Aplicação do Chaveamento Controlado em Linhas de Transmissão de Circuito Duplo), juhendaja prof. Karcius Dantas, Campina Grande föderaalülikool.

8. Teadustegevus

Teadusartiklite, konverentsiteeside ja konverentsiettekannete loetelu on toodud ingliskeelse elulookirjelduse juures.